UNIVERSITÀ DEGLI STUDI DI TRIESTE

XXXI CICLO DEL DOTTORATO DI RICERCA IN FISICA

NATURE OF GRAVITY FROM THE MASS PROFILES OF GALAXY CLUSTERS

Settore scientifico-disciplinare: **FIS/05 ASTRONOMIA E ASTROFISICA**

DOTTORANDO / A
LORENZO PIZZUTI

COORDINATORE
PROF. LIVIO LANCERI

SUPERVISORI DI TESI

PROF. STEFANO BORGANI

DR. BARBARA SARTORIS

ANNO ACCADEMICO 2017/2018

UNIVERSITÀ DEGLI STUDI DI TRIESTE
DEPARTMENT OF PHYSICS

PHYLOSOPHER DOCTOR DEGREE IN PHYSICS

NATURE OF GRAVITY FROM THE MASS PROFILES OF GALAXY CLUSTERS

Supervisor: Prof. Stefano Borgani
Co-supervisor: Dott. Barbara Sartoris
Candidate: Lorenzo Pizzuti

CYCLE: XXXI

"Our imagination is stretched to the utmost,
not as in fiction, to imagine things which are not really there,
but just to comprehend those things which are there."
R. P. Feynman

This Thesis is dedicated to my loved ones, and to all those people who made me discover the beauty of Trieste in totally unespected ways. You gave me the clarity about the choices in my future.

A special thanks to my supervisors, Stefano and Barbara, who guided me with patience and determination through the wonderful world of cosmology.

Contents

List of Figures

List of Tables

Introduction

The discovery of the late-time accelerated expansion of the Universe (refs. [2, 3]) at the turn of the XX century has posed one of the most challenging problems in modern physics. In the current picture of cosmological studies, the standard ΛCDM model seems to be the most suitable to describe the expansion history, constrained with a wide range of observations (e.g. ref. [4]). In this scenario, the nature of Dark Energy, which is invoked to explain the current accelerating expansion (e.g. ref. [2]) and which should represent about 70% of the total density of the Universe, is still unknown. In the last decade several alternatives have been proposed to explain the origin of the acceleration; a possible solution is to modify the theory of General Relativity (GR hereafter), assumed in the Standard Cosmological model, on large scales by introducing new degrees of freedom which can reproduce the same effect of a cosmological constant (see e.g. refs. [5, 6]) and at the same time propagate a new force. Even when considering theories where the predicted expansion history is identical to that of the ΛCDM model, the evolution of the perturbations can be significantly different from ΛCDM. A possible evidence of modified gravity (hereafter MG) should also involve a change into the relation between the scalar potentials Φ and Ψ which appear in the perturbed Friedmann-Lemaitre-Robertson-Walker (hereafter FLRW) metric and the fluctuations in the matter density field both at linear and non-linear level (ref. [7]). These deviations can be constrained with a broad range of observational probes, such as Cosmic Microwave Background anisotropies (refs. [8, 9, 1]), Barionic Acoustic Oscillations (e.g. ref. [10]), redshift space distortions (e.g. ref. [11, 12]), galaxy clusters (e.g. refs. [13, 14]) and gravitational waves (e.g. ref. [15, 16]). Since GR is tested at high precision at Solar System scales (see e.g. ref. [17] and references therein), MG models must match the standard theory of gravity in this regime. Solar System constraints on modification of gravity can be accounted for a screening mechanism which suppresses the modifications restoring GR in high density environments (see e.g. ref [18] for a review). Alternatively, local gravity constraints can be escaped by assuming that baryons are

decoupled (ref. [19]).

The study of the mass profiles of galaxy clusters, the most massive gravitationally bound structures in our Universe, offers interesting possibilities to investigate deviation from GR at intermediate scales, where the effects of modification of gravity start to become important. Indeed, while internal processes are governed by baryonic physics, the overall dynamics of a cluster is dominated by gravitational interactions and reconstructions of the total mass profile depend on the assumed model of gravity.

In this Thesis I constrain deviations from GR by comparing mass profiles of galaxy clusters as derived from gravitational lensing and from a kinematic analysis of member galaxies. In fact, galaxies moving within clusters under the action of gravity only feel the time-time part of the perturbed FLRW metric, which is expressed by the potential Φ. On the other hand, the geodesics along which photons propagate within clusters reflect the contribution of both time-time and space-space components of the linear metric perturbations, i.e. they feel the sum of the two potentials $\Phi + \Psi$. Since in standard gravity $\Phi = \Psi$ at first order perturbation theory with non-relativistic matter sources and in the post-Newtonian approximation on a Robertson-Walker background, mass profiles obtained from kinematic and lensing analyses, under the assumption of GR, should coincide as long as GR itself is valid [1]. In other words, under the assumption that astrophysical and observational systematics are well understood for both the kinematic and lensing analyses, any deviation of mass profiles based on using either photons or galaxies as tracers of the metric perturbations should reflect a deviation from GR. The idea to combine lensing and kinematic mass profile determinations of galaxy clusters was first applied on real data by ref. [20] and later by ref. [21] to constrain the equation of state for Dark Matter under the assumption that GR is valid.

In the first part of this work, published in ref. [22], I present the results from the analysis of MACS J1206.2-0847 (hereafter MACS 1206) a galaxy cluster at redshift $z = 0.44$ for which high-quality imaging and spectroscopic data have been analyzed in detail as part of the Cluster Lensing And Supernova survey with Hubble (CLASH, ref. [23]) and the spectroscopic follow-up with the Very Large Telescope (CLASH-VLT, ref. [24]) programs. By using the reconstructed mass density profiles from kinematic analysis of ref. [25] and combined strong-weak lensing measurements of ref. [26], I derive a relation between the mass profiles and the metric scalar potentials Φ and Ψ to estimate their ratio $\eta(r, z = 0.44)$, which parametrize

[1] Note that the above statement is valid only if second order effects in standard perturbative expansion and relativistic corrections to the post-Newtonian approximation are negligible

generic departures from standard gravity, under the assumption of spherical symmetry of the cluster mass distribution. The possibility of measuring η from observations and therefore to detect deviations from the GR was discussed in ref. [27, 28], where it was pointed out that by combining constraints on the metric potentials ratio η and on the evolution of density perturbations, it is in principle possible to distinguish modifications of gravity from non-standard dark energy models. Other possible cluster-scale tests search for signatures of departures from GR looking at changes in the dynamical potential alone, as discussed in [29].

In order to translate the bounds on η in constraints on the free parameters of specific classes of modified gravity models, the second part of the Thesis considers the Horndeski Lagrangian (ref. [30]), the most general theory of massless gravity and a single scalar field with second-order equations of motion. In the quasi-static regime, i.e. when the wave nature of the scalar degree of freedom can be neglected, the extra force carried by the scalar field manifests itself as a Yukawa correction to the Newtonian potential, characterized by two parameters, a strength Q and a range λ. To simplify our task, I focus on a sub-class of Horndeski models, the so-called $f(R)$ models, in which case it turns out that $2Q^2 = 1/3$ and also that the lensing dynamics is not affected by modification of gravity. The new force is suppressed in high density regions by a non-linear mechanism that quenches deviations from GR, as required by consistency with the current observations, known as chameleon screening (ref. [31]). I will aim at constraining the interaction range λ by performing a joint kinematics and lensing analysis of the galaxy clusters MACS 1206 and RXC J2248.7-4431 (hereafter RXJ 2248) at $z = 0.35$, which is another cluster analyzed within the CLASH and CLASH-VLT collaborations. I determine the dynamic mass profiles in $f(R)$ gravity under the assumptions of spherical symmetry and dynamical relaxation of the clusters by using a modified version of the *MAMPOSSt* code of ref. [32], in which I included a parametric expression of the gravitational potential valid for generic MG models. This expression is obtained by imposing a Navarro-Frenk-White profile (NFW hereafter, ref. [33]) for the matter density perturbation. With a Maximum Likelihood approach I constrain the free parameters in our analysis, namely the scale radius r_s, the radius r_{200} (a proxy for the virial radius), the parameter describing the velocity anisotropy profile $\beta(r)$ and the interaction range λ. I assume a constant value for the scalaron mass $m_{f_R} = 1/\lambda$, which means we are neglecting the change in m_{f_R} due to the environmental density. This can be translated as dealing with models where the screening mechanism takes place at scales much smaller than the cluster size (e.g. few kpc), but also with models for which the screening is so effective that maintains the field mass nearly constant to the value inside the overdensity.

In this case, the results we obtain on λ refer to an effective "screened" $f_{,R}$, which is much smaller than the background field (ref. [34]). I discuss also the explicit effect of the chameleon screening for the Hu& Sawicki functional form of $f(R)$ (ref. [5]), assuming an instantaneous transition between the screened and non-screened regime, in order to place constraints on the background field value $|\bar{f}_R|$. I further combine the *MAMPOSSt* Likelihood with the posterior probability distribution of the NFW parameters r_s and r_{200} obtained by the joint strong+weak lensing analysis of ref. [35] in order to improve our results on λ.
The results of this analysis, published in ref. [36], will invoke the necessity to revise the assumption on which the method relies. In particular, deviations from spherical symmetry and lack of dynamical relaxation state of the cluster introduce systematic effects which can produce a spurious detection of modified gravity. The calibration of these systematics has important implications in view of upcoming and future large imaging and spectroscopic surveys (e.g Euclid, LSST), that will deliver lensing and kinematic mass reconstruction for a large number of galaxy clusters but with an expected signal-to-noise ratio much lower than for the two CLASH clusters.
The last part of this Thesis is thus devoted to the study of synthetic cluster-size dark matter halos simulated assuming GR, aimed at evaluating and calibrating the impact of systematics. In order to investigate what kind of constraints can be obtained in the most ideal situation, I have first developed a code that generates isolated spherically symmetric self-gravitating halos of collisionless particles for which all the assumptions of our method are met. The code is thought to work in any viable modified gravity framework which produces a change in the dynamical gravitational potential; for the purposes of this Thesis, I will produce and analyze synthetic halos assuming GR only. I then perform a detailed analysis of clusters from a set of N-body ΛCDM cosmological simulations performed with the GADGET-3 code of ref. [37]. I define two observational criteria which are related to the main systematics of this analysis; the first one parametrizes deviation from gaussianity of the line-of-sight velocity distribution, which has been shown to be a good proxy for the dynamical relaxation state of the cluster (see e.g. ref. [38]). The second criterion is the χ^2 obtained from the fit of the projected number density profile of the galaxies with a NFW profile, which takes into account several effects, including deviation form spherical symmetry and the parametric modeling of unknown quantities. The results of this analysis will be included in a paper in preparation.

The study developed within this Thesis presents a competitive method to constrain devi-

ation from GR which requires few selected objects in order to produce stringent bounds on the free parameters of viable modified gravity models. Notwithstanding, the high precision reachable with our method demands an accurate control of possible systematics, which can be achieved with the analysis of cosmological simulations both in ΛCDM and in non-standard frameworks (e.g. ref. [39]). It is worth to notice that this work can be easily applied to test a broad class of models simply adapting the parametrization of the metric potentials thus offering a powerful tool to deepen our knowledge of the Universe.

The Thesis is organized as follows: in Part I the basic notions of the ΛCDM cosmolgical model are discussed (Chapter 1); in Chapter 2 I also present a brief overview on modified gravity models further deriving the general parametrization of the metric potentials adopted in my analysis. Part II is devoted to describe galaxy clusters highlighting the connection between mass profile reconstructions and departures from GR. More specifically, in Chapter 3 I discuss general properties of galaxy clusters and the determination of cluster mass profiles using the dynamics of the member galaxies; I further present the modified version of the *MAMPOSSt* code developed within this Thesis. Chapter 4 is devoted to explain the basic theory of gravitational lensing and how it can be used to infer cluster mass profiles.

Finally, in Part III the results of the Thesis are presented and extensively discussed. In particular, Chapter 5 presents the data-set of the two clusters on which our analysis is based. The leading results discussed above are included in Chapter 6, 7 and 8 respectively; I then summarize the work carried out in this Thesis and I deliver my main conclusions.

Part I

Basics of Cosmology

Chapter 1

Standard Cosmology

In this Chapter I briefly review the basic principles of standard cosmology, focusing in particular on the background expansion history of the Universe and the evolution of linear perturbations in the Newtonian and relativistic regime. I further discuss some aspects of gravitational collapse of non-linear structures; in particular, I introduce the Navarro Frenk White density profile, which has been shown to provide a good description for Dark Matter halos in CDM simulations (ref. [40]) and which will be extensively used within this Thesis. A detailed treatment of these topics can be found in several textbooks of basic cosmology; for this part I refer to Chapters 14, 15 of ref. [41] and Chapters 3,4 and 6 of ref. [42]

1.1 The ΛCDM cosmological model

Our current understanding of the structure and evolution of our Universe can be formalized in the so called ΛCDM concordance model, which is so far the simplest model providing an excellent description of observational data. It is based on the theory of General Relativity (GR hereafter, see Appendix A for a quick review of the basic notions) and relies upon two main principles:
The **Cosmological Principle**. *Over sufficient large scales, the Universe can be considered as homogeneous and isotropic*;
The **Copernican Principle**. *There are no privileged observers in the Universe*.

The cosmological principle is nowadays well tested to hold on very large scales thanks to

the analyses of the Cosmic Microwave Background (CMB) radiation (e.g. ref. [4]). In terms of space-time geometry, the metric describing a homogeneous and isotropic Universe is the Friedmann-Lemaitre- Robertson-Walker metric (FLRW hereafter), whose line element can be expressed in spherical coordinates as:

$$ds^2 = -c^2dt^2 + a(t)^2\left[\frac{dr^2}{1-kr^2} + r^2d\Omega^2\right]. \tag{1.1}$$

In the above equation, $a(t)$ is the (dimensionless) scale factor which identifies the change in the physical distance between two objects as a consequence of the expansion of the Universe; (r, θ, ϕ) are the *comoving* coordinates independent of the expansion, $d\Omega^2$ is the solid angle in terms of θ, ϕ, t is the cosmological time as measured by an observer at rest in the comoving system and c is the speed of light. Finally, $k = 1, 0, -1$ determines the spatial curvature of the Universe (closed, flat and open Universe respectively).
It is often useful to define a *conformal time* $d\tau = dt/a(t)$ measuring the comoving distance traveled by a photon in the cosmological time dt. By introducing the coordinate transformation:

$$r \to f_k(\chi) = \begin{cases} \frac{1}{\sqrt{k}}\sin(\sqrt{k}\chi) & k > 0, \\ \chi & k = 0, \\ \frac{1}{\sqrt{-k}}\sinh(\sqrt{-k}\chi) & k < 0, \end{cases}$$

in the new system $(\tau, \chi, \theta, \phi)$ eq. (1.1) reads:

$$ds^2 = a(\tau)^2\left[-c^2d\tau^2 + \left(d\chi^2 + f_k(\chi)^2d\Omega^2\right)\right]. \tag{1.2}$$

For a light ray propagating along a radial null geodesics in this metric $ds^2 = 0$ and so:

$$c^2d\tau^2 \equiv \frac{c^2dt^2}{a(t)^2} = \frac{dr^2}{1-kr^2} \equiv d\chi^2,$$

one can define the proper distance of an observer at the point (t_1, r_1, θ, ϕ) from the origin $(t_0, r_0 = 0, \theta, \phi)$ as

$$l = a(t_1)\int_0^{r_1}\frac{dr}{\sqrt{1-kr^2}} = a(t_1)\int_{t_0}^{t_1}\frac{cdt}{a(t)} \equiv a(t_1)\chi. \tag{1.3}$$

For a light ray emitted at $t_0 \to 0$, in eq. (1.3) χ is a measure of the comoving distance traveled

by the photon within the age of the Universe, thus it represents the maximum observable region of the Universe at time t_1; this quantity is called *particle horizon* or *cosmological horizon*.

In an expanding spacetime described by the metric of eq. (1.1), photons suffer a shift in the frequency due to the dependence on the scale factor. Considering a light ray emitted by a source with a frequency ν_e and received by an observer in the origin with a frequency ν_o, the *redshift* z is defined through the relation:

$$1 + z = \frac{\nu_e}{\nu_o} = \frac{a(t_o)}{a(t_e)}, \tag{1.4}$$

which depends only on the value of the scale factor at the time of emission and at the time of observation. In an expanding Universe where $a(t)$ is a monotonic function of t, the redshift z is an alternative measurement of cosmological time.

1.1.1 The Friedmann Equations

In GR, the relation between the geometrical structure of the space-time and its energy density content is expressed through the Einstein's field Equations:

$$R_{\mu\nu} - \frac{1}{2} g_{\mu\nu} R + \Lambda g_{\mu\nu} \equiv G_{\mu\nu} + \Lambda g_{\mu\nu} = \frac{8\pi G}{c^4} T_{\mu\nu}, \tag{1.5}$$

where $R_{\mu\nu}$ is the Ricci tensor, which (in GR) is a function of the first and second derivatives of the metric $g_{\mu\nu}$, $R = R^{\mu}_{\mu}$ is the Ricci curvature scalar, G is the gravitational constant and $T_{\mu\nu}$ is the energy momentum tensor which describes the energy content of the Universe. The term Λ is called cosmological constant, and was first introduced by Einstein in order to find a solution reproducing a static Universe. The implications of the cosmological constant in the ΛCDM model will be discussed below.
Eq. (1.5) can be derived in the Lagrangian formalism from the variation of the general action:

$$S = \frac{c^4}{16\pi G} \int \sqrt{-g}[R - 2\Lambda] d^4x + S_m[\Psi_m, g_{\mu\nu}], \tag{1.6}$$

assuming that $g_{\mu\nu}$ is the only independent variable. In eq. (1.6) S_m is the action of the matter field Ψ_m and

$$S_{EH} = \frac{c^4}{16\pi G} \int \sqrt{-g} R d^4x \tag{1.7}$$

is called *Einstein-Hilbert* action. This formalism is particularly convenient to derive modified field equations in the context of non-standard theories of gravity, as I will show in Chapter 2.

The energy content of the Universe is described by a perfect fluid, characterized by an energy momentum tensor:

$$T_{\mu\nu} = p\, g_{\mu\nu} + c^2 \left(\frac{p}{c^2} + \rho\right) u_\mu u_\nu, \tag{1.8}$$

where p and ρ are the pressure and the density of the fluid respectively, $u^\mu = dx^\mu/d\tau$ is the 4-velocity of the fluid element in unit of c such that $u_\mu u^\mu = -1$. The time component of the conservation equation $\nabla_\mu T^{\mu\nu} = 0$ (where ∇_μ is the covariant derivative) for a FLRW metric is given by:

$$\dot{\rho} + 3\frac{\dot{a}}{a}\left(\rho + \frac{p}{c^2}\right) = 0, \tag{1.9}$$

where the dot indicates derivative with respect to the cosmological time t. Given a proper equation of state (EoS hereafter) connecting density and pressure, such that $p/c^2 = w\,\rho$, the solution of eq. (1.9) reads

$$\rho(a) \propto a^{-3(1+w)}. \tag{1.10}$$

By comparing eq. (1.5) with eq. (1.8), it is easy to show that the cosmological constant can be interpreted as a fluid characterized by an EoS with $w = -1$. The *vacuum energy* or *Dark Energy* density associated to Λ is defined as:

$$\rho_\Lambda = \frac{c^2}{8\pi G}\Lambda. \tag{1.11}$$

Note that if $\Lambda > 0$ also the vacuum density is positive, and so the pressure associated with this fluid is negative.
The solution of eq. (1.5) for an expanding Universe where $g_{\mu\nu}$ is the FLRW metric and $T_{\mu\nu}$ is given by eq. (1.8) leads to the *Friedmann equations* (ref. [43]):

$$\left(\frac{\dot{a}}{a}\right)^2 = \frac{8}{3}\pi G\rho - \frac{k}{a^2} + \frac{\Lambda}{3}, \tag{1.12}$$

$$\frac{\ddot{a}}{a} = -\frac{4\pi G}{3}\left(\rho + 3\frac{p}{c^2}\right) + \frac{\Lambda}{3}. \tag{1.13}$$

Eqs. (1.12) and (1.13), determine the evolution of the scale factor $a(t)$ as a function of the energy content of the Universe and its curvature k. In the Standard Model of cosmology, the density ρ reflects the contribution of a relativistic (radiation) and non-relativistic (matter) components ρ_r, ρ_m. Note that with the definition of eq. (1.11), one can absorb the last term of both Friedmann equations into a total density which accounts for the contribution of the vacuum energy: $\rho = \rho_r + \rho_m + \rho_\Lambda$. Each component evolves independently according to eq. (1.10), where the parameter w is given by:

$$w = \begin{cases} 0 & \text{matter;} \\ \frac{1}{3} & \text{radiation;} \\ -1 & \text{cosmological constant.} \end{cases}$$

Thus, the density associated to the relativistic component (photons and neutrinos) scales with a^{-4}, the density of non-relativistic matter decreases as a^{-3} while the density associated to Λ is independent of the scale factor. This means that in an expanding Universe the contribution of a positive cosmological constant will always be dominant in the late time expansion for any values of ρ_r, ρ_m. From eq. (1.13) it follows that if the total density is dominated by a component with $w < -1/3$ (as the case of a positive Λ) $\ddot{a} > 0$ and the universe is in a phase of *accelerated expansion*. In general, all those theories which introduce an additional component to the energy density of the Universe producing an accelerated expansion close to the effect of the cosmological constant are called *Dark Energy models* (see Chapter 2).

The evolution of the density components can be equivalently expressed as a function of the redshift, eq. (1.4): $\rho_r(z) \propto (a+z)^4,\ \rho_m(z) \propto (1+z)^3,\ \rho_\Lambda(z) = const.$

Figure 1.1 from ref. [44] shows how the densities scale with z in the case matter (black line), radiation (red line) and cosmological constant (light blue line). The light blue shaded area represents all the Dark Energy models where $w = 1 \pm 0.2$.

Note that at very early times the relativistic component dominates over the others up to $1 + z_{eq} = 2.4 \times 10^4 \Omega_m h^2$ where the matter density equals the radiation density[1]. For $z < z_{eq}$ the relevant contribution to the total density is then given by ρ_m.

The quantity

$$\frac{\dot{a}}{a} = H(t),$$

[1]The value of z_{eq} can be directly estimated from the present values of the densities imposing $\rho_m(z_{eq}) = \rho_r(z_{eq})$.

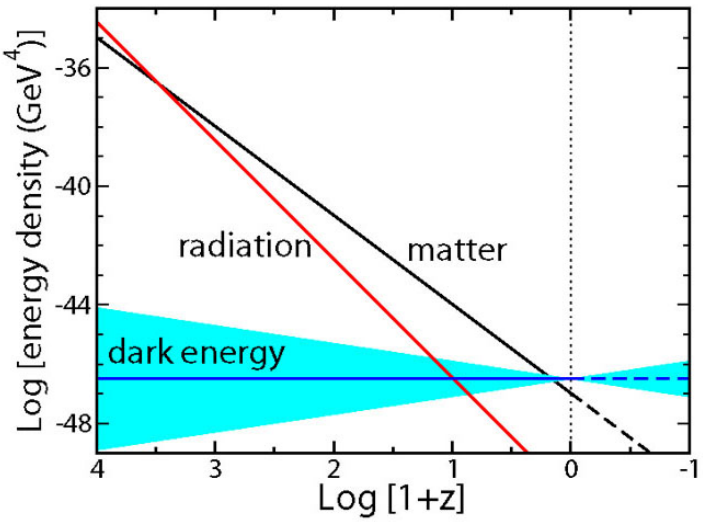

Figure 1.1: Evolution of density components as a function of redshift z. Red line: radiation. Black line: matter. Light blue line: cosmological constant. The colored region indicates Dark Energy models with $w = 1 \pm 0.2$. From ref. [44]

is called Hubble parameter and expresses the rate at which the scale factor changes in time. The present value of the Hubble parameter $H_0 = H(t_o)$ gives an an approximate estimate of the age of the Universe. Indeed, its inverse $t_H = 1/H_0$ corresponds to the age of a constant-rate expanding Universe. The latest (global) measurements of the present-day Hubble parameter made by CMB observations (ref. [4]) have constrained $H_0 = (67.4 \pm 0.5)\, km\, s^{-1}\,\mathrm{Mpc}^{-1}$, while the value found by local distance indicators (e.g. refs. [45, 46]), $H_0 = (73.52 \pm 1.62)\, km\, s^{-1}\,\mathrm{Mpc}^{-1}$, shows a $\sim 3.8\sigma$ tension with the global determination. This tension has been not fully understood yet and it represents a challenging problem of the standard cosmological model. For the purposes of this Thesis, I will not discuss this issue; the interested reader can find more details in e.g. ref. [47] and references therein.
Generally, cosmological scales are expressed in unit of the *reduced Hubble constant*, given by:

$$h = \frac{H_0}{(100\ \mathrm{km\ s^{-1}\ Mpc^{-1}})}. \tag{1.14}$$

From eq. (1.12) it is possible to define a critical density $\rho_{crit}(t)$ as the total energy density of

a flat Universe at the cosmological time t:

$$\rho_{crit}(t) = H^2(t)\frac{3}{8\pi G}. \tag{1.15}$$

The density components of the Universe are often given in units of the critical density by defining the dimensionless cosmological parameters:

$$\Omega_x(t) = \frac{\rho_x(t)}{\rho_{crit}(t)},$$

where $x = m, r, \Lambda$. The sum of these parameters $\Omega(t) = \Omega_m(t) + \Omega_r(t) + \Omega_\Lambda(t)$ is related to the spatial curvature of the universe $\Omega_k(t) = -k/H(t)^2a^2 = 1 - \Omega(t)$.
With the above definitions, the first Friedmann equation can be rewritten as:

$$H^2(t) = H_0^2\left[\Omega_m(1+z)^3 + \Omega_r(1+z)^4 + \Omega_\Lambda + (1-\Omega)(1+z)^2\right], \tag{1.16}$$

where all the dimensionless density are computed at present day (i.e. $\Omega_x = \Omega_x(t_o)$).
Eqs. (1.12), (1.13) admit several solutions, depending on the values of ρ_m, ρ_r, ρ_Λ and k, which can be found in any textbook of cosmology.

1.1.2 The ΛCDM concordance model

The study of the light curves of type Ia Supernovae (SNe Ia) by ref. [48] and ref. [49] provided in 1999 the first evidence that the expansion of the Universe is accelerated. This result has been further confirmed in the last two decades by a broad number of observations, such as improved wider supernova samples, CMB spectrum, Baryon Acoustic Oscillation (BAO), galaxy clusters, weak lensing (see e.g. refs. [4, 50, 51, 52, 53], ref. [54] for a review). In particular, combined analyses of SNe Ia, BAO and CMB data (e.g. refs. [55, 56]) have shown that the Universe has passed from a phase of deceleration, where the dominant contribution to the density was given by ρ_m, to a phase of accelerated expansion around $z = z_{DE} \sim 0.6$.
As discussed above, in the framework of General Relativity a positive acceleration $\ddot{a} > 0$ can be obtained by introducing an additional "Dark Energy" component, which dominates the late time expansion, characterized by an equation of state $w < -1/3$. Current observations are consistent with a time independent density for Dark Energy $w(z) = const = -1$ (i.e. a cosmological constant) which represents about the 70% of the total composition of the Universe at present time.

More specifically, the recent analyses of ref. [4], which is the state-of-art of the current constraints on the cosmological parameters, provided $\Omega_\Lambda = 0.6689 \pm 0.0058$, $\Omega_m = 0.3111 \pm 0.0056$ and $1 - \Omega = \Omega_k = 0.001 \pm 0.002$.
This means that observations are consistent with a spatially flat universe at present time (so that the total density equals the critical density $\rho_{crit,0}$), dominated by a Dark Energy component compatible with a cosmological constant and with a negligible contribution of the relativistic component ($\Omega_r \sim 10^{-5}$, see e.g. ref. [53]).
Moreover, the fraction of the matter density associated with baryons is constrained to be $\Omega_b\, h^2 = 0.02242 \pm 00014$, with h defined in eq. (1.14) with $H_0 = (67.4 \pm 0.5)\, km\, s^{-1}\,\mathrm{Mpc}^{-1}$. Thus, only $\sim 5\%$ of the total density of the Universe is in the form of ordinary matter. Evidences of the presence of a collisionless non-luminous dominant matter component, dubbed as *Dark Matter*, have been obtained from several astrophysical and cosmological probes (see e.g. ref. [57] for a review). First suggested by Zwicky in 1933 as a possible solution for the problem of the missing mass in the Coma cluster, Dark Matter is a necessary ingredient of the current cosmological model in order to explain different issues, such as the rotational curves of spiral galaxies, the small temperature fluctuations in the CMB spectrum, the hierarchical formation of structures in the Universe and the total mass profiles of galaxy clusters. In agreement with the present observational picture, Dark Matter should be dominated by a "cold" component, that is non-relativistic at time of decoupling in order to guarantee a correct timing for the assembly of cosmic structures from initial density fluctuations even if the perturbations in the baryonic component are suppressed (see Sec. 1.2).
The Standard Cosmological model, or ΛCDM Concordance model, sums up all the concepts I have introduced so far. The model assumes that the Universe is spatially flat and contains a cosmological constant Λ, which is currently dominating the energy density driving the observed accelerated expansion, while the matter content is mostly given by a cold Dark Matter component (CDM), plus baryons and a small (but not negligible) contribution of neutrinos. As shown in Figure 1.2, from ref. [58], the theoretical predictions of the Concordance model are in excellent agreement with a broad compilation of data-sets, obtained from different probes spawning a wide range of redshifts and three order of magnitudes in scale.
The expansion history predicted by the Standard model can be summarized as follows.

- Shortly after the initial singularity ($t \sim 10^{-33}\, s$), the Universe enters in phase of exponential expansion called inflation. In the simplest model, the expansion is driven by a single scalar field with a potential energy much larger than the kinetic energy; during

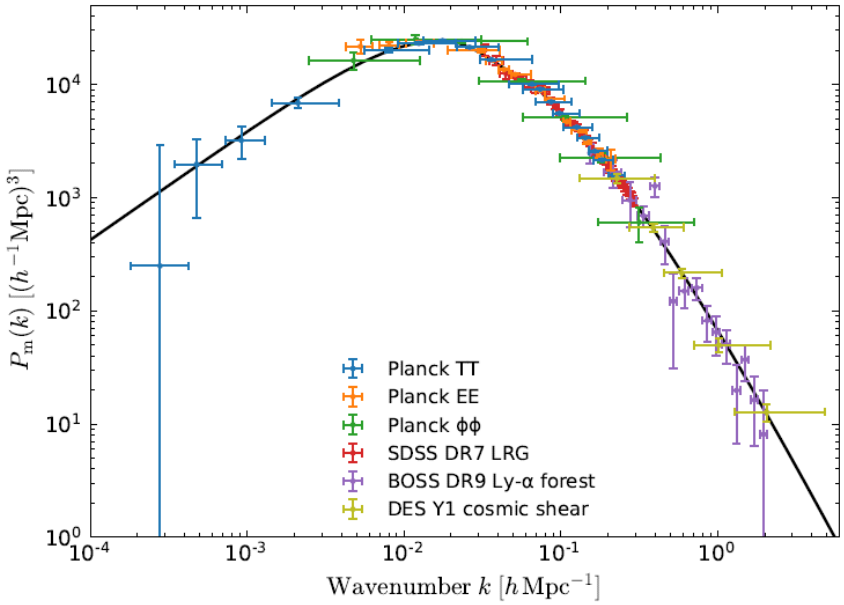

Figure 1.2: The linear power spectrum of matter density fluctuation $P(k) =< |\delta_k|^2 >$ at redshift $z = 0$ as predicted by the Concordance ΛCDM model (black solid line) compared to the power spectrum inferred by several observations Credit: Planck collaboration, ref. [58]

this phase small primordial density fluctuations are formed.

- As the inflation ends, the original field decays into particles and the temperature rises up (reheating phase); the relativistic component dominates the total density and the Universe expand decelerating. Primordial nucleii of the lightest elements form in the first three minutes trough the Big Bang Nucleosynthesis (BBN).

- At $1 + z_{eq} = 2.4 \times 10^4 \Omega_m h^2$ the radiation density component becomes equal to the matter component. The Universe enters in the matter-domination era.

- At $1+z_{ls} = 1082[1+0.0188(\Omega_b/\Omega_m)] \simeq 1100$, where Ω_b the baryon density parameter today, photons decouple from baryons and the Universe becomes transparent to radiation. The last-scattered photons are now observable as the CMB.

- At $z \simeq 0.6$ the Dark Energy associated to the cosmological constant starts to dominate the total density and the expansion enters the current phase of acceleration.

1.2 Evolution of cosmological perturbations

In the previous section I have described the background expansion history, as predicted by the Standard cosmological model, assuming that the Universe is homogeneous and isotropic. However, the cosmological principle is valid only on very large scales; on smaller scales the Universe is filled by a filamentary "cosmic web" of structures (see Fig. 1.3) which have thought

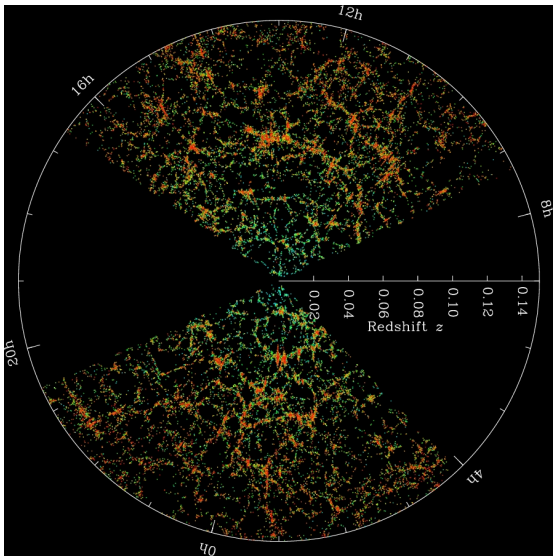

Figure 1.3: Slice of the 3D map of the distribution of galaxies in the local Universe as seen by the Sloan Digital Sky Survey (SDSS) with the Earth located at the center. Galaxies are observed within -1.25 and 1.25 degrees declination, color-coded in function of the age of their stars (redder points identify early-type galaxies). Credit: M. Blanton and the Sloan Digital Sky Survey

to assemble from the growth of tiny density fluctuations, generated during the inflation. These perturbations are observable in the CMB spectrum as small anisotropies in the temperature of the photons of the order $\delta T/T \sim 10^{-5}$, as shown in Fig. 1.4.

According to the ΛCDM picture, the components of the Universe are perfect fluids with density $\rho(\vec{x}, t)$, connected to the pressure p through the equation of state and characterized by a velocity $\vec{u}(\vec{x}, t)$. We can express the density as a background mean value $\bar{\rho}(t)$ plus a

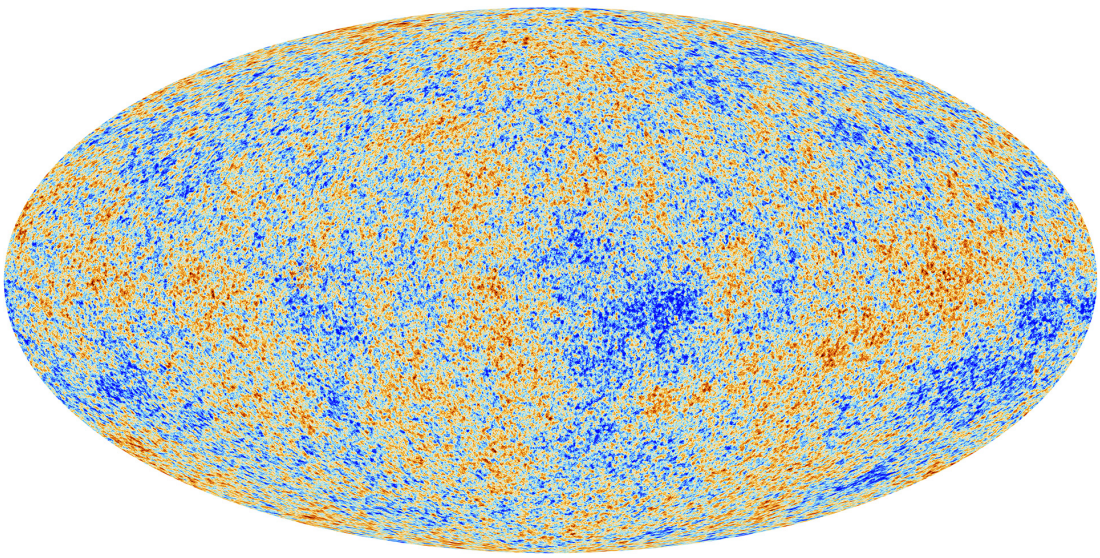

Figure 1.4: Map of the CMB temperature obtained by the Planck Mission (credit: ref. [59]). Red and blue spots indicate small fluctuations from $-300\,\mu K$ (bluer regions) to $300\,\mu K$ (redder regions) with respect to the average temperature $T = 2.72548 \pm 0.00057K$.

perturbation $\delta\rho(\vec{x},t) = \rho(\vec{x},t) - \bar{\rho}(t)$:

$$\rho(\vec{x},t) = \bar{\rho}(t)[1 + \delta(\vec{x},t)]\,, \tag{1.17}$$

where $\delta = \delta\rho/\rho$ is called *density contrast*. A qualitative description of the perturbations growth can be made assuming that the scale of those fluctuations is much smaller than the horizon $\lambda \ll R_H = (aH)^{-1}$ and the fluid can be treated as non-relativistic. In this case we can work in a Newtonian framework, where the fluid evolution is determined by the *continuity equation*:

$$\frac{D\rho}{Dt} + \rho\nabla\cdot\vec{u} = 0, \tag{1.18}$$

where $\frac{D}{Dt} = \frac{\partial}{\partial t} + (\vec{u}\cdot\nabla)$ is the convective derivative; the *Euler equation*:

$$\frac{D\vec{u}}{Dt} = -\frac{1}{\rho}\nabla p - \nabla\Phi, \tag{1.19}$$

which is the equivalent of the second Newtonian law expressing the momentum conservation. The gravitational potential Φ is related to the density through the Poisson equation:

$$\nabla^2\Phi = 4\pi G\rho. \tag{1.20}$$

The set of equations is then completed with the fluid equation of state $p = p(\rho, S)$ where S is the entropy. Observations suggest that the evolution of density perturbations is adiabatic, i.e. $dS/dt = 0$; in this case the pressure depends only on the energy density.
In an expanding Universe the proper coordinates is given by $\vec{x} = a(t)\vec{y}$, where $\vec{y}$ is the comoving coordinate. Thus the velocity reads:

$$\frac{d\vec{x}}{dt} \equiv \vec{u} = \dot{a}\vec{y} + a\dot{\vec{y}} = aH\vec{y} + a\vec{v} = H\vec{x} + a\vec{v},$$

where the first term is related to the expansion of the Universe, while the second term is due to peculiar motions different from the general cosmic expansion. The quantity $a\vec{v}$ is called *peculiar velocity* and represents the velocity of the fluid element as measured by a comoving observer at $\vec{y}$.
Fluctuations in the density field $\delta\rho$ are connected to perturbations in the gravitational potential ϕ, the pressure and δp and the velocity field $\vec{v}$. Under the assumption that the density contrast is small $\delta \ll 1$, the above set of equations can be combined keeping only the linear terms in the perturbed quantities. In Fourier space, the time evolution of the density fluctuations is given by the following relation:

$$\ddot{\delta}_k + 2\frac{\dot{a}}{a}\dot{\delta}_k + \delta_k \left[\frac{k^2 v_s^2}{a^2} - 4\pi G\bar{\rho}\right] = 0, \tag{1.21}$$

where $k = 2\pi/y$ is the comoving wavenumber and

$$\delta_k = \int \frac{d^3\vec{k}}{(2\pi)^3}\delta(\vec{y})e^{-i\vec{k}\cdot\vec{y}}$$

is the Fourier transform of the density field in comoving coordinates. The quantity $v_s^2 = \left(\frac{\partial p}{\partial \rho}\right)_{S=const}$ is the fluid sound speed. An interesting scale in eq. (1.21) is given by

$$k_J = \sqrt{\frac{4\pi G\bar{\rho}a^2}{v_s^2}}, \tag{1.22}$$

for which the term in the square brackets vanishes; the associated wavelength $\lambda_J = 2\pi/k_J$ is called *Jeans' length*. It represents the limit below which the pressure dominates over the gravitational instability, preventing the growth of perturbations that oscillate and decay in time for the effect of the Hubble drag term $2H\dot{\delta}_k$.

During the radiation-dominated era ($z > z_{eq}$) the Jeans' length for the baryon-radiation fluid is larger than the size of the horizon, thus the fluctuation in the baryonic component can not grow. Also perturbations on the pressureless Dark Matter component inside the horizon cannot grow before the equivalence due to the fact that the Hubble drag $2H\dot{\delta}_k$ prevails on the source term $\delta_k 4\pi G\bar{\rho}_m$; in this case fluctuations in the Dark Matter fluid are frozen to a constant value (Meszaros effect, ref. [60]).
After the equivalence and before recombination $z_{rec} < z < z_{eq}$, perturbations in the baryon-photon fluid are still oscillating while Dark Matter perturbations can now grow through gravitational instability. In particular, writing the density field as:

$$\delta_k(t) = D(t)\delta_{k,in}, \tag{1.23}$$

where $D(t)$ is called *linear growth factor*, it is possible to identify a growing-mode and a decaying-mode solution $D_{\pm}(t)$ in eq. (1.21). Assuming a flat matter dominated Universe ($\Omega_m \simeq 1$):

$$D_-(t) \propto H(t) \sim t^{-1},$$

$$D_+(t) \propto H(t) \int_0^t \frac{dt'}{a^2(t')H^2(t')} \propto a \sim t^{2/3}. \tag{1.24}$$

Thus, the growing mode of DM fluctuations inside the horizon evolves as the scale factor at the linear level. Note that the integral expression in eq. (1.24) is in general a solution of eq. (1.21) only for pressureless matter perturbations, and only if the relativistic component is negligible and the Dark Energy EoS parameter $w = -1$. It is worth to point out that, even if a collisionless fluid is not affected by the pressure contribution, the fluid elements move along timelike geodesics in the FLRW metric with a typical velocity v_{fs} which defines a *free streaming* length λ_{fs}, as the distance traveled by a DM particle within a Hubble time. Any perturbation with $\lambda < \lambda_{fs}$ is damped; thus, the free streaming scale defines a cutoff for the structure formation in the Universe at a given time. According to the current observational scenario, cosmological structures assemble through gravitational interaction following hierarchical bottom-up process, where smaller structures form earlier. This is possible only if Dark Matter is *cold*, i.e. it is characterized by a sufficiently small velocity v_{fs} (meaning a large mass of DM particles), so that the free streaming length is much below the size of a galactic halo (see e.g. ref. [61]).
Note that the second of eqs. (1.24) depends on the background expansion through the Hubble

rate $H(a)$; therefore, how the amplitude of the initial fluctuations scales in time is sensitive to the underlying cosmological model, providing an excellent tool to constrain cosmological parameters. The left panel of Figure 1.5 shows the growth factor $D(z)$ for and Einsten-de Sitter (EdS) Universe (red line), characterized by $\Omega_m = 1$, $\Omega_\Lambda = 0$ and $\Omega_k = 0$, an open Universe with $\Omega_m = 0.3$ (green line) and the ΛCDM Universe (blue dotted line), all normalized at the present time $z = 0$. In the ΛCDM scenario and in an open Universe the growth of structures is suppressed with respect to the EdS case, due to the larger expansion rate. This is further highlighted in the right panel of the same Figure, where two snapshots of a cosmological N-body simulations are shown. The upper panels refer to a flat ΛCDM Universe while the bottom panels are for an EdS Universe; yellow circles identify galaxy clusters which would show a temperature of X-ray emission larger than 3 keV. Note that in the EdS model structures grow much more rapidly across the same cosmic time.

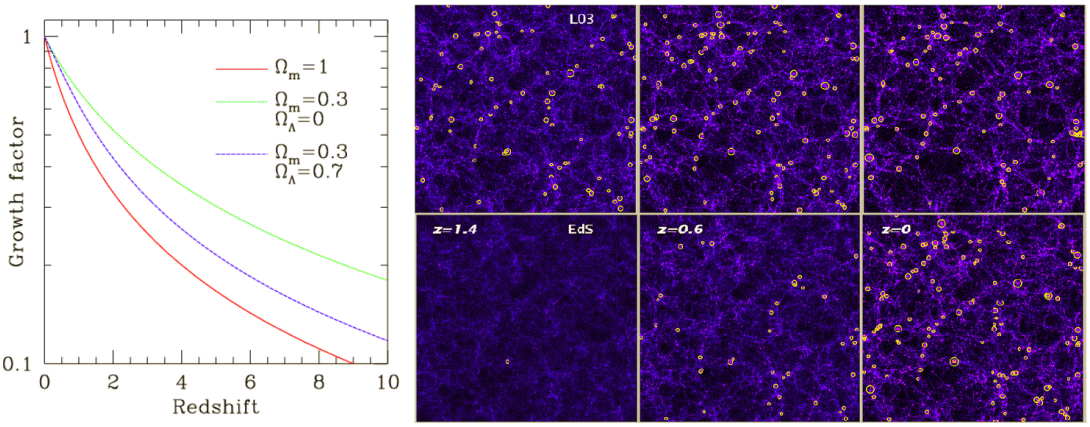

Figure 1.5: Right plot: evolution of the growth factor $D(z)$ as a function of the redshift z for an EdS Universe (red solid line), an open Universe with $\Omega_m = 0.3$ (green line) and a ΛCDM Universe ($\Omega_m = 0.3$, $\Omega_\Lambda = 0.7$, blue dotted line). Left plot: snapshots from a cosmological N-body simulation in a ΛCDM scenario (upper line) and in an EdS scenario (bottom line); each snapshot shows a region $250\,h^1$Mpc side and $75\,h^1$Mpc thick. The yellow circles mark clusters as would be identified in X-rays observations with a temperature $T > 3keV$. From ref. [62].

The linear growth factor, or its logarithmic derivative:

$$f(a) = \frac{d\log D(a)}{d\log a}, \tag{1.25}$$

can be used to test non-standard cosmologies. In particular, as I will discuss in the next Chapter,

modifications of gravity or additional interacting Dark Energy fields generally introduce a scale dependence $D(a) \to D(k, a)$ which changes the linear evolution of perturbations with respect to the ΛCDM scenario (see e.g. ref. [63]).

1.2.1 Relativistic perturbation theory

A correct description for the linear evolution of cosmological perturbations requires a general relativistic treatment, where fluctuations in the background FLRW metric are connected to perturbations in the density field through the linearized Einstein's equation:

$$(\delta G)_{\mu\nu} = \frac{8\pi G}{c^4}(\delta T)_{\mu\nu}, \tag{1.26}$$

together with the conservation of the energy-momentum tensor $\nabla_\nu T^{\mu\nu} = 0$. Given the above equations, one can follow the linear evolution of generic density contrast at any cosmological scale.

Starting from a flat FLRW metric, eq. (1.2) with $f(\chi) = \chi$, in cartesian coordinates we have:

$$\bar{g}_{\mu\nu} = a^2(\tau) \begin{bmatrix} -1 & \vec{0} \\ \vec{0} & \delta_{ij} \end{bmatrix}. \tag{1.27}$$

An arbitrary small perturbation δg of the metric $\bar{g}$ such that

$$\bar{g}_{\mu\nu} \to g_{\mu\nu} = \bar{g}_{\mu\nu} + \delta g_{\mu\nu},$$

can be generally written as:

$$\delta g_{\mu\nu} = a^2(\tau) \begin{bmatrix} -2\phi/c^2 & w_i \\ w_i & -2e\delta_{ij} + 2h_{ij} \end{bmatrix}, \tag{1.28}$$

where w_i, ϕ e h_{ij} are functions of $\vec{x}$, t and h is traceless.Eq. (1.28) can be decomposed into a scalar, vector and tensor part:

$$\delta g_{\mu\nu} = \delta g^S_{\mu\nu} + \delta g^V_{\mu\nu} + \delta g^T_{\mu\nu} =$$

$$= a^2(\tau) \left(\begin{bmatrix} -2\phi/c^2 & \partial_i w \\ \partial_i w & -2(\psi/c^2)\delta_{ij} + 2D_i D_j h \end{bmatrix} + \right.$$

$$+\begin{bmatrix} 0 & w_i^{\perp} \\ w_i^{\perp} & 2h_{(i;j)} \end{bmatrix} + \begin{bmatrix} 0 & 0 \\ 0 & 2h_{ij}^{\top} \end{bmatrix}\Bigg), \tag{1.29}$$

where h, w are scalar fields defined from h_{ij} and w_i respectively, $w_i^{\perp}$ is the divergence-free part of w_i and $h_{ij}^{\top}$ is the component of h_{ij} perpendicular to the gradient $\vec{\nabla}$. Finally, $\psi/c^2 = e + \frac{1}{3}\nabla^2 h$. The symbol D_i indicates the covariant derivative with respect to the spatial index i (see eq. (A.2)), while $(i;j)$ denotes the symmetrized covariant derivative.

Scalar modes are related to gravitational potential and are the relevant quantities to describe the formation of cosmic structures. Vector modes trace rotational effects while tensor perturbations identifies gravitational waves. For the purposes of this Thesis, I will focus only on scalar perturbations; in order to remove the additional components one can consider that in GR perturbation theory there are some extra degrees of freedom in the choice of the coordinate system. These degrees of freedom arises form the fact that the correspondence between points in the background space-time and in the perturbed space-time is not unique. This means that different coordinate systems can be chosen to describe the evolution of perturbations without changing the physics; the transformation between two different coordinate systems is called *gauge transformation*.

Since physical quantities can assume different values for any choice of the system (gauge), it is useful to define gauge-invariant variables and describe the evolution of those quantities in a suitable gauge. In particular, the scalar perturbations ϕ and ψ can be rephrased in terms of the gauge-invariant *Bardeen potentials* (ref. [64]):

$$\Phi = \phi + \frac{1}{a}\left[(w - h')a\right]',$$

$$\Psi = \psi - \frac{a'}{a}(w - h'), \tag{1.30}$$

where the prime indicates derivative with respect to the conformal time coordinate $c\tau$. As will be shown in the next Chapters, the Bardeen potentials are the fundamental quantities on which the analysis developed within this Thesis is based; the physical meaning of Φ and Ψ can be understood by fixing a convenient gauge, called the **Conformal Newtonian Gauge** where

$w_i = 0$ and $h_{ij} = 0$. In this case, the fluctuation δg reduces to:

$$\delta g^S = \begin{bmatrix} -2\Phi/c^2 & 0 \\ 0 & -2\Psi/c^2 \end{bmatrix}.$$

Note that in this gauge ϕ and ψ coincides with Φ and Ψ respectively. Thus, the distance element in the total linearly perturbed FLRW metric $g_{\mu\nu} = \bar{g}_{\mu\nu} + \delta g_{\mu\nu}$ can be written as:

$$ds^2 = g_{\mu\nu} dx^\mu dx^\nu = a^2(\tau) \left[-\left(1 + 2\frac{\Phi}{c^2}\right) c^2 d\tau^2 + \left(1 - 2\frac{\Psi}{c^2}\right) \delta_{ij} dx^i dx^j \right]. \tag{1.31}$$

Eq. (1.31), up to the conformal factor $a^2(\tau)$, is equivalent to the line element in the Newtonian limit of gravity[2] where $\Psi = \Phi \equiv \Phi_N$ is the Newtonian potential. Therefore, as mentioned before, the Bardeen potentials play the role of the *gravitational potential* times the scale factor; if GR theory is valid the Bardeen potentials should coincide, at least at linear level. This could be seen by solving the linearized eq. (1.26), which connects the metric of eq. (1.31) to perturbations in the energy momentum tensor of a perfect fluid; it can be shown that the difference between the Bardeen potentials obeys the following equation in Fourier space:

$$k^2(\Psi - \Phi) = -8\pi G a^2 \bar{P}\Pi, \tag{1.32}$$

with

$$\bar{P}\Pi = \frac{3}{2}\left(\frac{k_i k_j}{k^2} - \frac{1}{3}\delta_{ij}\right)\left(T^i{}_j - \frac{1}{3}\delta_{ij} T\right)$$

the stress tensor of the fluid. Thus, in the absence of anisotropic stresses, which is true for perfect fluids and minimally coupled scalar field, $\Pi = 0$ and

$$\Phi = \Psi. \tag{1.33}$$

Since it has been obtained from the Einstein's Equation, the validity of the above relation depends on the assumption that GR is the correct theory to describe the gravitational interaction, but this is no more true in a generic modified gravity framework where the two Bardeen potential are generally different, as I will discuss in Chapter 2. This implies that independent measurements of Φ and Ψ, or of their combination, are a good probe to test alternative theories

[2]Note that for a generic value of the curvature in the background metric, the spatial part of eq. (1.31) is given by the spatial part of eq. (1.2) times the factor $\left(1 - 2\frac{\Psi}{c^2}\right)$

to GR. In this Thesis I will focus on mass profiles reconstructions as a tool to constrain the Bardeen potential and therefore to obtain information about the nature of gravity.
It is worth to point out that eq. (1.33) is derived in linear perturbation theory, i.e. assuming that all the quantities involved are much smaller than unity and second-order effects are negligible. One can argue that this relation cannot hold in the case of a galaxy cluster, where the measured gravitational potential is linear, generally of the order of $\sim 10^{-4}c^2$ (see Chapter 3), but the density contrast δ is orders of magnitude larger than unity. However, this situation is better described by the post-Friedmann approximation (see ref. [65] and references therein) - which is the expansion of the metric and the Einstein's equations over a FLRW background in powers of $1/c$ - rather than by linear relativistic perturbation theory. It can be shown that, keeping only the leading order terms in the post-Friedmann expansion (referred as Newtonian approximation), the two (linear) scalar potentials that appears in the perturbed metric coincides in GR independently of the fact that the density field δ is linear too. It is nevertheless important to remind that tiny departures form $\Psi = \Phi$ can be sourced by non-linear effects in GR and not by a modification of gravity; these higher-order corrections should be taken into account as systematic effects for future applications of the method proposed within this Thesis.

1.2.2 Non-linear evolution

The linear theory presented above provides a good description for the evolution of density perturbations when they are much smaller than unity. However, observations of the present-day Universe reveal that the majority of observable structures, such as galaxies and cluster of galaxies, have formed in collapsed environments where $\delta\rho \gg \bar{\rho}$. Thus, in order to fully understand the assembly history of those structures we need to analyze the gravitational collapse of overdensities in non-linear regime. Unfortunately, an exact solution of the equations describing the non-linear evolution is generally not available, although several simple analytical approximations are very insightful and they have been widely used in literature to determine the qualitative behavior of gravitationally bound systems. For example, the spherical top-hat collapse model (ref. [66]) is a fundamental simplified model to describe the non-linear growth of cosmic structure, applied in a broad range of studies, such as calculation of the halo mass function (e.g. the Press & Schechter formalism, ref. [67]), or the description of gravitational collapse in the ΛCDM model and in several extensions (e.g. refs. [68, 69]). In this analytical framework, a spherical isolated overdense region with a constant density initially evolves with the expanding background universe, then it slows down and it decouples from the Hubble flow

turning from expanding to collapsing, eventually virializing in a relaxed state.
Other analytical approaches, such as the Zel'dovich approximation (ref. [70]) or, more in general, Lagrangian perturbation theory at different orders, provide valuable hints to explain the formation of the skeleton of large-scale structure (see Figure 1.6 which shows a comparison between a full N-body simulation and the result of the Zel'dovich approximation in the left and right panels respectively). Nevertheless, a full treatment of the non-linear growth of per-

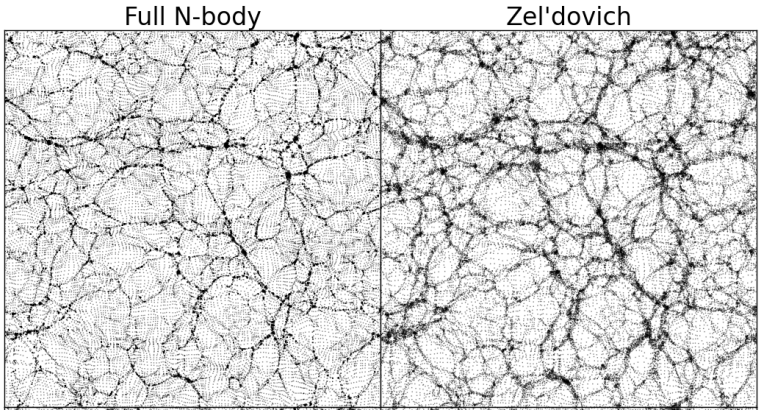

Figure 1.6: Comparison between a snapshot of a full N-body simulation at $z = 0$ (left panel) and a simulation performed with the Zel'dovich approximation (right panel). Both plots show the positions of particles in a sheet extracted from a 256^3-particles ΛCDM simulations. As shown in the plot, the position of the cosmological structures is reproduced also with the approximated method, even if with a much lower accuracy. Credit: ref. [71]

turbations requires numerical methods; in particular, formation of galaxies and clusters reflects complex dynamical processes which should account also for the baryonic physics involved and which spawn a range of scales from tens kpc for a single galaxy to few Gpc for a population of galaxy clusters. In the last 25 years, the implementation of cosmological N-body and hydrodynamical simulations has been greatly improved thanks to the speed-up of computational technologies and the improvements in the efficiency of simulation codes. Nowadays, numerical techniques are one of the most powerful tools for cosmological and astrophysical studies (see e.g. refs. [72, 73] for reviews); simulation codes have been principally developed in Newtonian limit for the computation of the gravitational force (e.g. ref. [37]), but recently full general relativistic schemes have been presented (e.g. refs. [74, 75]).
A detailed study of structure formation and cosmological simulations is beyond the aim of this Thesis; here I will only discuss a specific result obtained from the analysis of cold dark matter halos in N-body simulations that will be broadly adopted in the next Chapters.

The Navarro-Frenk-White model

In a seminal series of papers (refs. [76, 77, 33]) by J. Navarro, C. Frenk and S. White it has been shown that CDM simulated halos in equilibrium configuration follow an universal density profile, independently of the halo mass, the redshift and the underlying cosmological model. In particular, ref. [33] presented a double-power low radial profile, proportional to r^{-1} in the innermost region and to r^{-3} at large radii, which provides a good fit for halos in N-body simulations over two decades in radius (see Figure 1.7). They found the fitting formula:

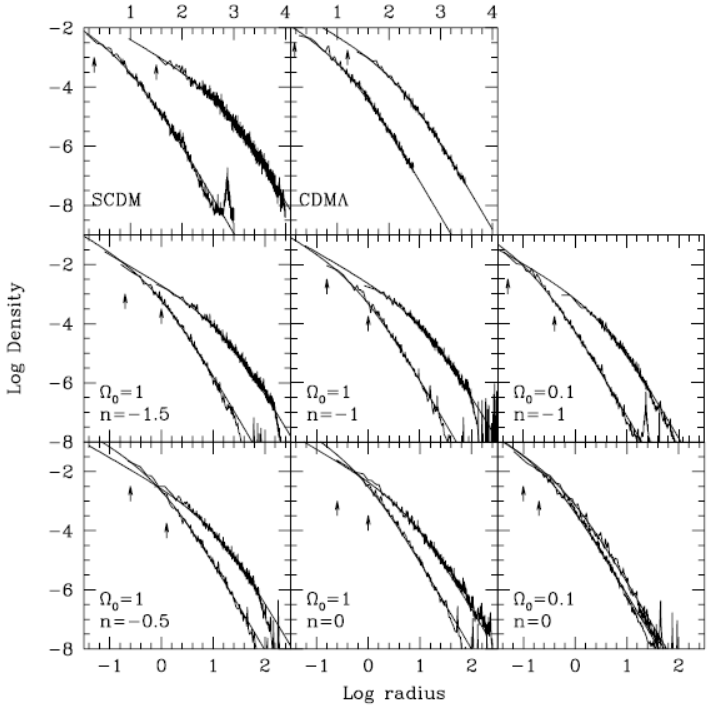

Figure 1.7: Density profiles of one of the most (rightmost curve in each plot) and one of the least massive (leftmost curve in each plot) halos in a set of cosmological N-body simulations performed in different cosmologies, specified by the values of $\Omega = \Omega_0$ and of the index n of the power spectrum of initial density fluctuations. In the Standard CDM (SCDM, $\Omega_m = \Omega_0 = 1$) and ΛCDM models radii are given in kpc and densities are in units of $10^{10} M_\odot / kpc^3$. In all plots the arrows indicate the value of the gravitational softening. From ref. [33].

$$\rho(r) = \rho_c(z) \frac{\delta_c}{\left(\frac{r}{r_s}\right)^\gamma \left(1 + \frac{r}{r_s}\right)^{3-\gamma}}, \tag{1.34}$$

with the shape $\gamma = -1$, which is called Navarro-Frenk-White (NFW hereafter) density profile. In the above equation, $\rho_c(z) = 3H^2(z)/8\pi G$ is the critical density of the Universe at redshift z, $r_s \equiv r_{-2}$ is the scale radius corresponding to the point at which the logarithmic derivative of the profile equals -2; finally, δ_c is a characteristic overdensity given by:

$$\delta_c = \frac{\Delta_{vir}}{3} \frac{c^3}{\log(1+c) - c/(1+c)}, \tag{1.35}$$

where $c = r_{vir}/r_s$ is called *concentration* and r_{vir} is the radius enclosing a mean overdensity Δ_{vir} times the critical density. In this Thesis I will always refer to $\Delta_{vir} = 200$ (and so $r_{vir} = r_{200}$), which is close to the density at virialization predicted by the spherical collapse model in a EdS universe $\Delta_{sc} = 178$.

Note that eq. (1.34) depends only on two parameters, which can be chosen to be e.g. r_{200} and r_s , or $M_{200} = \frac{4}{3}\pi\ 200\rho_c r_{200}^3$ and $c = c_{200}$, and which are strongly correlated. Indeed, ref. [33] showed that the earlier a halo has formed, the larger is the value of its concentration. Since on average, according to the hierarchical structure assembling paradigm, more massive halos formed later, this leads to an inverted mass-concentration relation. Given the large scatter in the assembling history of Dark Matter halos, the mass-concentration relation exhibits a notable scatter too. In particular, it has been shown that at a fixed mass the concentration parameter follow a log-normal distribution with a typical standard deviation $\sigma_{\log c} \sim 0.25$ (e.g. ref. [78]). Figure 1.8 from ref. [79] shows the mass-concentration relation extended over 15 order of magnitudes in CDM halo mass; the black solid line represent a model to compute the mean concentration proposed by ref. [80] with a scatter $\sigma_{\log c} \sim 0.14$ (gray area), while the dotted line is the model of ref. [81]; the violet-filled and blue circles with the relative errorbars represent the result from the MultiDark and Bolshoi simulations respectively.

Numerical studies on the mass-concentration ($c - M$) relation by ref. [82] indicated that $c(M, z)$ is a decreasing function of both mass and redshift. Moreover, they found that at high redshift the mass dependency is significantly reduced. More recently, the analysis of refs. [80, 83] showed instead an upturn in the $c - M$ relation at high redshift, which however has been shown to disappear when selecting only the most relaxed clusters in the sample.

The dynamical relaxation state, which will be a fundamental assumption for the analysis presented in this Thesis (as I will discuss in Chapter 3), has been demonstrated to be correlated with the concentration. Indeed, from both simulations (e.g ref. [84]) and observations (e.g ref [85]) it has been found that more relaxed clusters are on average also more concentrated.

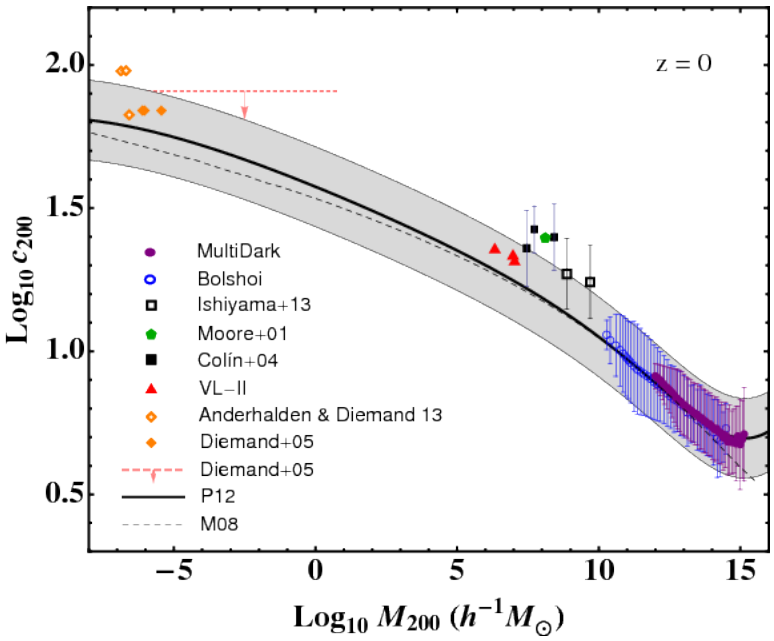

Figure 1.8: Mass-concentration relation in a CDM scenario for halos in the mass range $[10^{-6}\,h^{-1}M_{\odot}, 10^{15}\,h^{-1}M_{\odot}]$. Violet-filled circles with the relative errorbars are from the MultiDark the blue circles are the results from the Bolshoi simulation. The solid black line shows the mass-concentration model from ref. [80] while the gray band represent the scatter within $1\,\sigma_{\log c} \sim 0.14$. The dotted line represent the model of ref. [81]. Credit: ref. [79]

From the observational point of view, several studies of galaxy clusters at low and intermediate redshift confirm the predictions of theoretical analysis about the anti-correlation between c and M (see e.g. refs [85, 86, 87]). However, a generally steeper slope and a higher normalization has been found compared to the simulations-derived relation. According to e.g. ref. [88] the discrepancy can be explained in terms of bias in the selection of the observed sample. For example, in strong lensing-selected clusters elongated along the line of sight higher mass and concentration are measured, while the opposite effect is obtained in clusters which are elongated in the direction perpendicular to the line of sight.

In this Thesis I will consider two galaxy clusters from the CLASH and CLASH-VLT collaborations, within which a total sample of 25 galaxy clusters has been analyzed. 20 clusters in the CLASH sample has been selected by their X-ray morphology (see Chapter 5). The CLASH mass-concentration relation is shown in Figure 1.9 from ref. [87] (solid lines and shaded purple area), where each data-point represents one of the selected clusters. Both models and data are color-coded according to their redshift. Ref. [87], which analyzed 19 of the X-ray selected clusters with redshift between 0.19 and 0.89, derived the $c - M$ relation adopting the

parametrization of ref. [82]:

$$c(M_{200}, z) = A \times \left(\frac{1.37}{1+z}\right)^{B} \times \left(\frac{M_{200}}{8 \times 10^{14} M_{\odot}/h}\right)^{K}, \tag{1.36}$$

with

$$A = 3.66 \pm 0.16, \quad B = 0.14 \pm 0.52, \quad K = 0.32 \pm 0.18. \tag{1.37}$$

The study of ref. [87] is in excellent agreement with the $c - M$ relation derived from cosmological simulations when clusters are selected by 2D X-ray images; this confirms that X-ray morphology-based selections reduce the bias due to elongation and shape of the strong lensing selection.

The gray contours in the plot indicate the results derived by ref. [89] from the stacked weak-shear analysis of 16 CLASH X-ray selected clusters, referred to a redshift $z \sim 0.35$. The results of the two analyses are in agreement within the errors, even if the stacked contours are slightly above the value predicted by the relation of ref. [87].

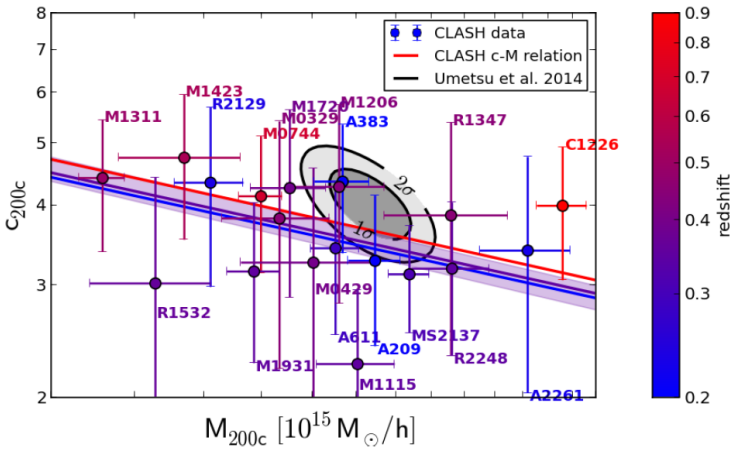

Figure 1.9: Solid lines: the best-fit c-M relation to the CLASH data in the $M_{200} - c_{200}$ plane for $z = 0.2$ (blue), $z = 0.35$ (purple) and $z = 0.9$ (red). The labeled data points in the top panel show each CLASH cluster color-coded according to redshift. The shaded area around the purple line shows the 1σ error on the normalization of the CLASH $c - M$ relation. Grey contours refer to the 1σ and 2σ confidence levels, respectively, for the $c - M$ stacked analysis of ref. [89] at $z \sim 0.35$. Credit: ref. [87].

Given its relative simplicity, the NFW profile has been widely adopted in literature to describe the mass profile of gravitationally bound structures such as galaxy clusters, where it has been shown to provide a generally good fit to observational data (e.g. refs. [25, 35], see also Chapter 5); nonetheless, some discrepancies between different sets of simulations and

observations have been found regarding the inner shape of Dark matter halo mass profiles. More specifically, the analysis of ref. [90] on cosmological N-body simulations showed that the central region of CDM halos follows a steeper (cusp) profile with $\gamma = 1.5$ (Moore profile). Around the same years, observational studies of dwarf and low-surface brightness galaxies (e.g ref. [91, 92]) revealed a shallower Dark matter profile (i.e. $\gamma \to 0$) towards the center; this is usually referred as the cusp-core problem. More recent works (e.g. ref. [93]) indicate that the presence of baryons can flatten or steepen the Dark Matter halo profile with respect to a pure CDM paradigm; in particular, ref. [93] demonstrated that Supernova feedback in the central region of dwarf galaxies can be responsible of the generation of the inner core in the profile. As for the debate about the simulated halos, the analysis of ref. [94], which studied the central regions of DM halos in high-resolution N-body simulations, indicates that the density profile for $r \to 0$ is actually shallower than the value $\gamma = 1.5$ of the Moore model; at the same time, the NFW profile tends to underestimate the density below the scale radius. Ref. [94] found that the inner profile is better described by an exponential law (Einasto profile):

$$\rho(r) = \rho(r_s) \exp\left\{ \frac{-2}{\alpha} \left[\left(\frac{r}{r_s} \right)^{\alpha} - 1 \right] \right\},$$

where $0.12 \lesssim \alpha \lesssim 0.25$ (e.g ref. [95]).

Despite the controversies about the inner shape (both between data and simulations and different sets of simulations) are still open, the NFW profile remains a good model to characterize the overall distribution of matter in cosmological structures. Moreover, the parametric nature of the profile makes it suitable to describe the equilibrium configuration of density perturbations also in non-standard frameworks such as modified gravity theories, as I will discuss in the next Chapter.

Chapter 2

Beyond the Concordance Model: Modified Gravity

In this Chapter I will present a general overview of modified gravity models which have been introduced to explain the accelerated expansion of the Universe as a possible alternative to the Concordance ΛCDM model where GR is assumed along with the introduction of the cosmological constant. I will briefly discuss the Horndeski parametrization, a general class of scalar-tensor theories with second order equations of motion; I will then focus on a viable subclass of the Horndeski Lagrangian, the $f(R)$ models of gravity, which will be used as a case study within this Thesis. Finally, in the last part of the Chapter, I will discuss the state-of-art of cosmological constraints of modified gravity, further highlighting the role of the work presented here for the investigation of the nature of gravity. Throughout this Chapter, unless not explicitly specified, I will assume $c = 1$.

2.1 Modified Gravity and Cosmology

GR is without doubt a successful theory in describing the gravitational interaction, and it has been shown to be valid by a broad range of observations at small and intermediate scales, such as Solar System and stellar tests, gravitational waves (e.g. refs. [96, 97]); however, tests of GR at cosmological scales have been much less precise so far. Attempts to modify and extend GR were made already few years later its formulation, mostly motivated by purely academic interest (e.g. ref. [98]); later on, the introduction of higher order terms in the action of GR

has been proposed to solve theoretical issues related to quantum corrections in strong gravitational regime (i.e. effects becoming relevant at scales close to the Planck scale, as the very early universe or near black hole singularities). Only after the discovery of the late-time accelerated expansion modified gravity models have became a popular subject of study as a viable alternative to the presence of the cosmological constant in the Standard ΛCDM model. Indeed, even if the Concordance model has been proved to outstandingly fit the large amount of observational data-sets, with excellent agreement at different scales and redshifts (as discussed in the previous Chapter), it suffers several problems. For example, the observed value of the energy associated to the cosmological constant is small: $\rho_\Lambda \sim (10^{-3}\,\mathrm{eV})^4$; according to quantum field theory, vacuum energy affects the dynamics in GR producing a non-negligible contribution which can in principle explain the presence of a positive Λ in the Einstein's equation. However, the predicted value of the vacuum energy density is expected to be of the order of the Planck energy density, and therefore many orders of magnitude larger than ρ_Λ inferred by observations, requiring a exceptional fine-tuning at any perturbative order in the quantum corrections (see e.g. ref. [99]). Another challenging issue related to the cosmological constant is the so called *Why now*- problem, or coincidence problem, concerning the remarkable fact that the density parameters Ω_m and Ω_Λ are roughly of the same order at the present time. The equivalence between matter and dark energy densities occurs at very low redshift, and thus it seems that we live in a special period of the cosmic history just by coincidence.

In the last 25 years, several alternatives to the cosmological constant has been proposed in order to explain the late-time expansion of the Universe; one possibility is to replace ρ_Λ with a generic dark energy component ρ_{DE} characterized by an EoS $p_{DE} = w(a)c^2\rho_{DE}$, where $w_0 = w(a_0) < -1/3$ in order to have acceleration. Dark energy can be interpreted as the energy density of some new fields with a potential term dominating over the kinetic term (e.g. quintessence models, ref. [100]). At the background level, w is often parametrized as a linear function of the scale factor $w(a) = w_0 + (1-a)w_a$, known as Chevallier-Polarski-Linder (CPL) parametrization. In Figure 2.1 the contours in the plane w_0, w_a for the analysis of ref. [1] are shown. Different colors indicate different combinations of data-sets, including CMB data, expansion probes (Type Ia Supenrovae, BAO and local measurement of H_0) and growth rate probes (redshift space distortion and weak lensing data). Note that the contours from CMB and Weak lensing analyses (green shaded regions) show a $\sim 2\sigma$ tension with the ΛCDM predictions, while when considering the combination of Planck CMB data, SNe type Ia, BAO

and local measurements of H_0 (Planck+BSH, blue shaded areas in the plot), the constraints are in agreement with the expectations of the Concordance model $w_a = 0\, w_0 = -1$. I will come back to this apparent tension in Section 2.3.

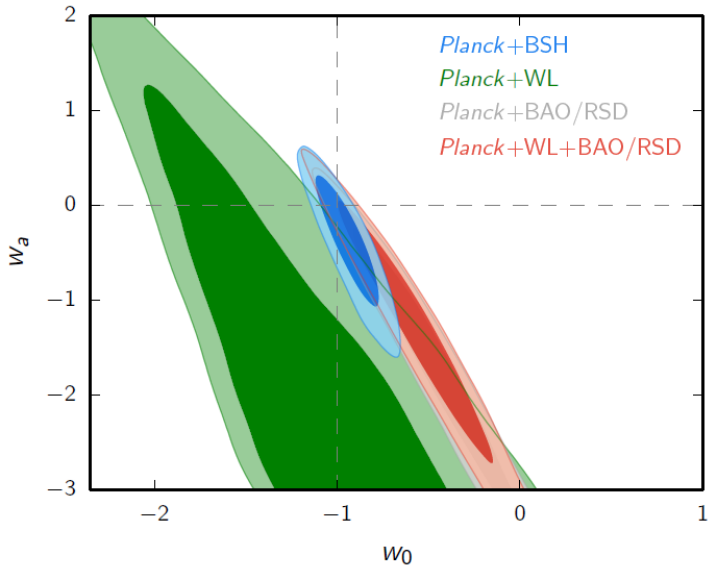

Figure 2.1: 1σ and 2σ contours in the plane (w_0, w_a) as obtained by various combinations of data-sets. The intersection of the dashed lines corresponds to the ΛCDM model $(-1, 0)$.

The simplest models assume that dark energy is smooth, i.e. it doesn't cluster on sub-horizon scales and is totally described in term of the EoS parameter $w(a)$. More sophisticated options allow for clustering dark energy having a speed of sound $c_s^2 = \delta p_{DE}/\delta\rho_{DE} < c^2$ (e.g. ref. [101]). Nevertheless, the effects on structure formation are generally very small and vanish when $w \to -1$; according to ref. [102], deviations from c_s to the speed of light are very difficult to be constrained with present and upcoming data-sets. For a recent review on Dark Energy model, see ref. [103].

Another alternative approach to explain the late-time acceleration of the Universe is to break down the assumption that GR is the correct theory to describe the large-scale gravitational interaction. Possible modifications of the Einstein's field equations can indeed produce an accelerated expansion without the explicit contribution of the cosmological constant, mimicking the expansion history of the ΛCDM model. All the extensions of the Concordance

model based on a different theory of the gravitational interaction are called *modified gravity* (MG) models (see e.g. refs. [104, 105] for reviews).

It is worth to notice that modifying GR is not an easy task. According to Lovelock's theorem (ref. [106]), GR is the only four-dimensional local theory of gravity with second-order derivatives of the metric in the equations of motion. This means that any departure from GR should introduces either non-locality, additional degrees of freedom, higher-order derivatives or higher dimensional spacetimes (e.g. the braneworld gravity, ref. [107]), giving rise to possible theoretical issues related to the consistency of the theory. I will not focus on this topic within the Thesis; more details can be found in e.g. ref. [108] and references therein.

A second important point to discuss is an effective definition for modified gravity. As I will show below, the effect of modifications of gravity can be rephrased in terms of additional fields which contribute to the total energy momentum tensor; in this view, modified gravity models are indistinguishable from Dark Energy models. An operative classification can be made by analyzing how the new degrees of freedom couple to the metric; I define modified gravity models as those models where the additional degrees of freedom are coupled non-minimally to the metric.

Over the last decades several modified gravity models have been proposed; in the following I will consider only the class of scalar-tensor theories, which are the most studied modified gravity models so far, especially in the cosmological context, as they encompass a wide phenomenology given a relatively simple structure.

2.1.1 Scalar-tensor theories

With scalar-tensor theories we commonly define all those models where both a scalar field (or several scalar fields) and a tensor field are included. The general action of a scalar-tensor theory with a single scalar field ϕ coupled to the gravitational field $g_{\mu\nu}$ can be written as:

$$S = \int d^4x\sqrt{-g}\left[\frac{R}{16\pi G}\phi - \frac{W(\phi)}{\phi}\nabla_\mu\phi\nabla^\nu\phi - 2V(\phi) - \mathcal{L}_m(\Psi_m, g_{\mu\nu})\right], \tag{2.1}$$

where $W(\phi)$ is a differentiable function of the scalar field and $\mathcal{L}_m$ is the Lagrangian of the matter fields Ψ_m. Variation of the action with respect to the metric and to the scalar field leads to the modified Einstein's equations and to the equation of motion of the scalar field

respectively:

$$\phi\left(R_{\mu\nu}-\frac{1}{2}g_{\mu\nu}R\right)+\left[\frac{W(\phi)}{2\phi}\nabla_\mu\phi\nabla^\mu\phi+\Box\phi+V(\phi)\right]g_{\mu\nu}-$$

$$-\nabla_\mu\nabla_\nu\phi-\frac{W(\phi)}{\phi}\nabla_\nu\phi\nabla_\mu\phi=8\pi GT_{\mu\nu}\,,$$

$$(2W(\phi)+3)\Box\phi+W'(\phi)\nabla_\mu\phi\nabla^\mu\phi+4V(\phi)-2\phi V'(\phi)=8\pi GT, \tag{2.2}$$

together with the energy momentum conservation equation $\nabla_\mu T^{\mu\nu}=0$. In the above relations, the prime indicates derivative with respect to ϕ and the energy momentum tensor refers to the matter fields. If we consider now a metric $\tilde{g}_{\mu\nu}$, related to $g_{\mu\nu}$ by a conformal transformation:

$$g_{\mu\nu}=\Omega^2(\phi)\tilde{g}_{\mu\nu},$$

it can be shown that the action of eq. (2.1) in terms of the new metric takes the form:

$$S_E=\int d^4x\sqrt{-g}\left[\frac{\tilde{R}}{16\pi G}-\frac{1}{2}\tilde{\nabla}_\mu\Phi\tilde{\nabla}^\mu\Phi-U(\Phi)-\mathcal{L}_m(\Psi_m,\Omega^2(\Phi)\tilde{g}_{\mu\nu})\right], \tag{2.3}$$

with the tilde indicating that quantities are computed with respect to $\tilde{g}_{\mu\nu}$. Note that I have introduced the scalar field Φ which is related to ϕ by:

$$\frac{d\Phi}{d\ln\Omega}=\sqrt{12+8\Omega^2(\phi)W(\phi)}.$$

In this particular frame, called the *Einstein Frame* and indicated by the subscript E, the scalar degree of freedom is coupled minimally to the metric, analogous to a pure dark energy model such as Quintessence, but now the matter fields are coupled to Φ via the conformal function Ω. This leads to Einstein's field equations which are GR-like:

$$\tilde{R}_{\mu\nu}-\frac{1}{2}g_{\mu\nu}\tilde{R}=8\pi G\tilde{T}^{(tot)}_{\mu\nu}, \tag{2.4}$$

where:

$$\tilde{T}^{(tot)}_{\mu\nu}=\tilde{T}_{\mu\nu}+\tilde{\nabla}_\mu\Phi\tilde{\nabla}_\nu\Phi-\left(\frac{1}{2}\tilde{\nabla}_\sigma\Phi\tilde{\nabla}^\sigma\Phi+V(\Phi)\right)\tilde{g}_{\mu\nu} \tag{2.5}$$

is the total energy momentum tensor of the matter field plus an additional fluid component expressed in terms of Φ. However, the matter energy-momentum tensor is no longer conserved and this produces an additional fifth force in the geodesic equation proportional to the gradient of the scalar field $\vec{\nabla}\Phi$.
In conclusion, a modified gravity model of the scalar-tensor type is identified in term of the metric $g_{\mu\nu}$ (usually dubbed as the *Jordan frame*) by manifestly non-GR Einstein's equations, but matter particles fall along geodesics in spacetime. In the Einstein frame instead, the metric field equations are GR-like with an enhancement of the gravitational force, driven by the new scalar field, appearing in the geodesic equation.

The most general class of scalar-tensor theories with second order equations of motion in four dimensions and with an universal coupling between matter and gravity is incorporated in the so-called *Horndeski* action (ref. [30]), which can be written as:

$$S_H = \int d^4x\sqrt{-g}\left[\frac{1}{8\pi G}\sum_{i=2}^{5}\mathcal{L}_i(g_{\mu\nu},\phi) + \mathcal{L}_m(g_{\mu\nu},\Psi_m)\right]. \tag{2.6}$$

The Lagrangian densities $\mathcal{L}_i$ are expressed in terms of four generic functions $\mathcal{G}_i$ of the field ϕ and of its kinetic term $X = \nabla_\mu\phi\nabla^\mu\phi$:

$$\mathcal{L}_2 = \mathcal{G}_2(\phi, X),$$

$$\mathcal{L}_3 = -\mathcal{G}_3(\phi, X)\Box\phi,$$

$$\mathcal{L}_4 = \mathcal{G}_4(\phi, X)R + \frac{\partial}{\partial X}\mathcal{G}_4(\phi, X)\left[(\Box\phi)^2 - \nabla_\mu\nabla_\nu\phi\nabla^\mu\nabla^\nu\phi\right],$$

$$\mathcal{L}_5 = \mathcal{G}_5(\phi, X)G_{\mu\nu}\nabla^\mu\nabla^\nu\phi - \frac{1}{6}\frac{\partial}{\partial X}\mathcal{G}_5(\phi, X)\left[(\Box\phi)^3 +\right.$$

$$\left. +2\nabla_\mu\phi^\nu\nabla_\nu\phi^\sigma\nabla_\sigma\phi^\mu - 3\nabla_\mu\nabla_\nu\phi\nabla^\mu\nabla^\nu\phi\Box\phi\right]. \tag{2.7}$$

The Horndeski framework includes as subclasses several popular modifications of gravity studied in literature, such as covariant Galileion, Brans-Dicke theory, $f(R)$ gravity (see below), but also Dark energy models as the above mentioned Quintessence or more general k-essence models (ref. [109]). The recent detection of a gravitational wave (GW) event and its electro-

magnetic counterpart emitted by the merging of two neutron stars (GW170817) by ref. [97] provided strong constraints on the speed of GWs $|c_{GW} - c|/c < 10^{-15}$, narrowing the allowed habitable zone for the Horndeski models (see e.g. refs. [16, 110]). In particular, a severe fine-tuning required to set the speed of GW equal to c can be avoided if $\mathcal{G}_5 = 0$ and $\mathcal{G}_4 = \mathcal{G}_4(\phi)$ should be a function of the scalar field only. In this case, the most general viable Horndeski Lagrangian density assumes the form:

$$\mathcal{L} = \mathcal{G}_4(\phi)R + \mathcal{G}_2(\phi, X) - \mathcal{G}_3(\phi, X)\Box\phi. \tag{2.8}$$

The $f(R)$ models of gravity, which I will discuss in Section 2.2, are included in eq. (2.8) by setting $\mathcal{G}_3 = 0$ and $\mathcal{G}_2(\phi, X) = \mathcal{G}_2(\phi)$.

2.1.2 Linear perturbations in Modified Gravity

As discussed in Chapter 1, linear perturbations over a FLRW background can be written in terms of the scalar Bardeen potentials Φ and Ψ when the conformal Newtonian gauge choice (see ref. [111]) is adoped. In spherical coordinate, for generic value of the curvature K we have:

$$ds^2 = a^2(\tau)\left\{\left(1 + 2\frac{\Phi}{c^2}\right)d\tau^2 - \left(1 - 2\frac{\Psi}{c^2}\right)[d\chi^2 + f_K^2(\chi)d\Omega^2]\right\}, \tag{2.9}$$

This metric is formally equivalent to the one obtained in the post-Friedman expansion keeping only the leading-order terms, as already mentioned in Chapter 1, where Ψ and Φ are two scalar conformal-Newtonian components which coincide with the Bardeen potential only when first-order relativistic corrections to the expansion are negligible. Note that through this Thesis I will refer to "Bardeen potential" to indicate the Newtonian metric components.

In the Newtonian approximation, assuming $\Phi, \Psi \ll c^2$ does not automatically implies that the matter perturbations should be small too. In galaxy clusters, for example, the average gravitational potential is of the order of $10^{-4}c^2 \div 10^{-5}c^2$ while the density perturbations $\delta\rho$ are highly non-linear.

I have already shown that in General Relativity, under the assumption of no anisotropic stresses in the Energy Momentum Tensor $T_{\mu\nu}$, the two Bardeen potentials are equal, $\Phi = \Psi \equiv \Phi_N$, where Φ_N is the usual Newtonian potential obeying the Poisson equation (in Fourier space):

$$k^2\Phi_N = -\frac{3}{2}\Omega_m(t)\delta_m H^2. \tag{2.10}$$

In the expression above $k = k_{com}/a$ is the physical wavenumber, $\Omega_m(t)$ is the time dependent matter density parameter, H is the Hubble parameter, $\delta_m = (\rho_m - \rho_{bg})/\rho_{bg}$ the matter density contrast, where ρ_{bg} is the background matter density at that time. Here I have already assumed spherical symmetry, i.e. $\Phi_N = \Phi_N(k)$, $\delta_m = \delta_m(k)$. In a general modified gravity scenario, Φ is no longer equal to Ψ, and the Poisson equation should be changed as (see e.g. refs. [112, 113]):

$$k^2\Phi = -\frac{3}{2}Y(k,a)\Omega_m(t)\delta_m H^2, \tag{2.11}$$

together with the equation for the lensing potential:

$$k^2(\Phi+\Psi) = -\frac{3}{2}Y(k,a)\left[1+\eta(k,a)\right]\Omega_m(t)\delta_m H^2. \tag{2.12}$$

Here $Y(k,a)$ is the effective gravitational constant and $\eta(k,a) = \Psi/\Phi$ is the *anisotropic stress*, or gravitational slip, in Fourier space, both equal to unity in standard gravity. As shown in ref. [112], in the Horndeski framework these quantities can be expressed in terms of five parameters introduced in ref. [113]:

$$Y(k,a) = h_1\left(\frac{1+k^2h_5}{1+k^2h_3}\right), \qquad \eta(k,a) = h_2\left(\frac{1+k^2h_4}{1+k^2h_5}\right). \tag{2.13}$$

Here, $h_1...h_5$ are functions of time only and can be considered constant for small redshift ranges, as the one spanned by the clusters used within this Thesis. Note that the above mentioned constraints from the speed of GW here imply $h_2 = 1$.
It is useful to define $Q^2 = (h_5 - h_3)/2h_3$ and $\hat{Q}^2 = (h_4 - h_3)/2h_3$ such that:

$$Y\eta = h_1h_2\left(1+\frac{2\hat{Q}^2k^2}{m^2+k^2}\right), \qquad Y = h_1\left(1+\frac{2Q^2k^2}{m^2+k^2}\right), \tag{2.14}$$

which are in the form of Yukawa potentials with strength $\hat{Q}^2$ and Q^2 respectively and characteristic mass $m^2 = 1/h_3$. Scale-independent standard gravity is recovered for $m \to \infty$ and $h_1, h_2 \to 1$. Fourier-inverting eq. (2.11) in real space one obtains:

$$\frac{1}{r^2}\frac{\partial}{\partial r}r^2\frac{\partial}{\partial r}\Phi = 4\pi G\sigma(r), \tag{2.15}$$

where I have defined

$$\sigma(r) = \frac{V}{(2\pi)^3}\int e^{i\mathbf{k}\mathbf{r}}Y(k)\delta\rho_m(k)d^3k. \tag{2.16}$$

The general solution of eq. (2.15) can be written as

$$\Phi(r) = -2\pi G h_1 \int_0^\infty \int_{-1}^1 \frac{1 + 2Q^2 e^{-m|\mathbf{y}-\mathbf{r}|}}{|\mathbf{y}-\mathbf{r}|} \delta\rho_m(y) y^2 dy dz \,, \tag{2.17}$$

with $z = cos\theta$. In the above equation, one can split the integral into two contributions:

$$\Phi(r) = -2\pi G h_1 \left[\int_0^\infty \int_{-1}^1 \frac{\delta\rho_m(y)}{|\mathbf{y}-\mathbf{r}|} y^2 dy dz + \int_0^\infty \int_{-1}^1 \frac{2Q^2 e^{-m|\mathbf{y}-\mathbf{r}|}}{|\mathbf{y}-\mathbf{r}|} \delta\rho_m(y) y^2 dy dz \right]$$

$$= h_1 \left[\Phi_N + \Phi_{MG}\right], \tag{2.18}$$

where the first term is the usual Newtonian potential while the second part reflects the additional contribution given by deviations from GR. The constant h_1 encodes modification of the gravitational constant and could be absorbed into the definition of G as $G_{eff} = h_1\, G$.

I now parametrize the mass density perturbations as a Navarro-Frenk-White model which, as already discussed in Chapter 1, represents a good fit of the mass distribution in simulated Dark Matter Halos. As I will discuss in Chapter 5, the NFW mass profile provides the highest likelihood in the kinematic and lensing analyses of the two galaxy clusters considered in this work. Solving the first double integral in the right hand side (RHS) of eq. (2.18) we obtain the expression for the Newtonian potential sourced by a spherical distribution of mass:

$$\Phi_N(r) = G \int_{r_0}^r \frac{dy}{y^2} M_{NFW}(y), \tag{2.19}$$

in terms of the standard-gravity NFW profile:

$$M_{NFW}(r) = M_{200} \left[\log(1 + r/r_s) - r/r_s(1 + r/r_s)^{-1}\right] \times \left[\log(1 + c) - c/(1 + c)\right]^{-1} \tag{2.20}$$

described in terms of the scale radius r_s and the radius r_{200}. I recall that $r_s \equiv r_{-2}$ is the radius at which the logarithmic derivative of the density profile equals -2 and r_{200} is the radius enclosing an overdensity 200 times the critical density of the universe at the redshift of the object, as defined in Chapter 1. $c = r_{200}/r_s$ is the concentration.
For this particular mass density model it is possible to derive an analytical expression for the

modified gravity contribution. Focusing on the second part on the RHS of (2.18):

$$-2\pi G\int_0^\infty\int_{-1}^1\frac{2Q^2e^{-m|\mathbf{y}-\mathbf{r}|}}{|\mathbf{y}-\mathbf{r}|}\delta\rho_m(y)y^2dydz$$

$$=-2\pi G\int_0^\infty\int_{-1}^1\frac{2Q^2e^{-m\sqrt{y^2+r^2-2ryz}}}{\sqrt{y^2+r^2-2ryz}}\delta\rho_m(y)y^2dydz$$

$$=-4\pi GQ^2\int_0^\infty F(r,y)y^2\delta\rho(y)dy, \tag{2.21}$$

where

$$F(r,y)=\frac{1}{mry}\begin{cases}e^{-m(y-r)}-e^{-m(y+r)} & y>r,\\ e^{m(y-r)}-e^{-m(y+r)} & y<r.\end{cases}$$

Substituting $\delta\rho_m(y)=\rho_0(r_{200},r_s)\left[y/r_s(1+y/r_s)^2\right]^{-1}$ and integrating over dy, we get:

$$\Phi_{MG}(r)=\frac{2\pi G\rho_0}{r}r_s^3\Big\{e^{-m(r_s+r)}\left[\mathrm{Ei}(m\,r_s)-\mathrm{Ei}(m(r_s+r))\right]$$

$$-e^{m(r_s+r)}\mathrm{Ei}\left[-m(r_s+r)\right]+e^{m(r_s-r)}\mathrm{Ei}(-m\,r_s)\Big\}=2Q^2\phi_{MG}(r), \tag{2.22}$$

so that the final expression for the time-time Bardeen potential in configuration space reads

$$\Phi(r)=h_1\left[G\int_{r_0}^r\frac{dx}{x^2}M(x)+2Q^2\phi_{mg}(r)\right]. \tag{2.23}$$

I now recast eq. (2.23) in terms of an *effective dynamical mass*

$$M_{dyn}(r)=h_1\left[M_{NFW}(r)+2Q^2\frac{d\phi_{mg}}{dr}\right], \tag{2.24}$$

which generates the Bardeen potential Φ according to:

$$\Phi(r)=G\int_{r_0}^r\frac{dx}{x^2}M_{dyn}(x). \tag{2.25}$$

As $m\to 0$, the additional contribution $\phi_{mg}(r)$ reduces to

$$\phi_{mg}(r)\to-\frac{4\pi G\rho_0r_s^3}{r}\log\frac{r_s+r}{r_s}, \tag{2.26}$$

which coincides with the expression of the Newtonian potential $\Phi_N(r)$ when the integral in eq. (2.19) is explicitly computed. This means also $M_{dyn}(r) \to h_1 M_{NFW}(r)(1+2Q^2)$ for a given r . In Figure 3.5 of Chapter 3 I will show the behavior of the modified mass profile M_{dyn} for different values of the parameter $\lambda = 1/m$ in the case of $f(R)$ gravity (where, as shown below, $2Q^2 = 1/3$).

Combining eq. (2.11) and eq. (2.53), we obtain a similar expression for the space-space potential Ψ:

$$\Psi(r) = h_1 h_2 \left[G \int_{r_0}^{r} \frac{dx}{x^2} M_{NFW}(x) + 2\hat{Q}^2 \phi_{mg}(r) \right] . \tag{2.27}$$

The effect of modifications of gravity is thus completely determined by the choice of the parameters $h_1, h_2, Q, \hat{Q}, m$. In the general case they are totally independent from each other, but, as I will discuss in the next paragraph, fixing a particular model allows us to establish relations among these parameters, reducing the number of degrees of freedom.

As I will discuss in Chapter 3, since in a galaxy cluster the typical velocities of the galaxies are non-relativistic ($\sim 10^3\, km/s \ll c$), the motion of the galaxies is determined only by the time-time component of the metric; it is thus possible to infer the Bardeen potential Φ, and consequently the dynamical mass M_{dyn}, by the dynamical analysis of the observed galaxies in a cluster. The combination of Ψ and Φ can instead be determined through gravitational lensing observations. Indeed, photons perceive the gravitational potential due to the contribution of both time-time and space-space metric components. In Chapter 4 I will define at leading order in Ψ, Φ a lensing potential $\Phi_{lens} = (\Psi + \Phi)/2$, which is related to the lensing mass density profile through the Poisson equation

$$\nabla^2 \Phi_{lens} = 4\pi G \rho_{lens} \, . \tag{2.28}$$

Hence, gravitational lensing analysis gives at the linear level sum of the Bardeen potentials.

2.2 $f(R)$ gravity

One of the simplest and most investigated alternatives to General Relativity (GR) is the class of theories known as $f(R)$ gravity, proposed by ref. [114], in which the Einstein-Hilbert action is modified by adding a general non-linear function of the Ricci curvature scalar R.

In the Jordan frame the total action reads:

$$S = \frac{1}{16\pi G}\int \sqrt{-g}[R + f(R)]d^4x + S_m[\Psi_m, g_{\mu\nu}], \tag{2.29}$$

where S_m is the action of the matter field Ψ_m. Note that for $f(R) = \text{const} \equiv -2\Lambda$ one recovers GR in presence of a cosmological constant. I will work in the so-called *metric* formalism of $f(R)$ gravity, i.e. I assume that the metric is the only independent variable on which apply the variational principle in order to derive Einstein's equations. There is another possible approach, dubbed *Palatini* formalism, in which both the metric $g_{\mu\nu}$ and the connection $\Gamma^{\lambda}_{\mu\nu}$ are independent variables and should be taken into account in the variation, under the assumption that the matter action $S_m[\Psi_m, g_{\mu\nu}]$ does not depend on the connection. In standard General Relativity, where the action is linear in R, the two procedures are equivalent and lead to the same field equations. However, this is no more true in modified gravity scenarios with a more general action, and a distinction between the two formalisms should be made. For completeness, I mention also a third version of gravity theories called *metric affine* formalism where the assumption of $\frac{\delta S_m}{\delta \Gamma} = 0$ is relaxed; metric affine gravity is a generalization of the Palatini approach. A more detailed description of those aspects could be found in e.g. ref. [115] and references therein.

Variation of eq. (2.29) with respect to the metric $g_{\mu\nu}$ gives rise to the modified Einstein equations:

$$(1 + f_{,R})R_{\mu\nu} - \frac{1}{2}g_{\mu\nu}[f(R) + R] + (g_{\mu\nu}\Box - \nabla_\mu\nabla_\nu)f_{,R} = 8\pi G T_{\mu\nu}. \tag{2.30}$$

The quantity

$$f_{,R} = \frac{df(R)}{dR},$$

usually known as the scalaron, is a new degree of freedom which can be interpreted as a scalar field, mediating an additional fifth force with a characteristic range described by the physical Compton length λ (see below). Thus, $f(R)$ models are actually a sub-class of scalar tensor theories where the scalaron field is coupled to gravity; this can be explicitly shown defining a conformal transformation:

$$f_{,R}(R) = e^{\sqrt{\frac{16\pi G}{3}}\tilde{\phi}}, \tag{2.31}$$

from which the action of eq. (2.29) becomes identical to the action of a scalar-tensor theory in the Einstein frame for the field $\tilde{\phi}$ with a potential (see e.g. ref. [116]):

$$U(\tilde{\phi}) = \frac{Rf_{,R} - f(R)}{16\pi G f_{,R}^2}. \tag{2.32}$$

In the case of flat FLRW universe, the Ricci scalar is given by

$$R_b = 6\left(\frac{\ddot{a}}{a} + H^2\right) = 3H_0^2\Omega_m\left[(1+z)^3 + 4\frac{\Omega_\Lambda}{\Omega_m}\right], \tag{2.33}$$

where the subscript b indicates background value, $a(t)$ is the scale factor, Ω_m is the matter density parameter today, and $H = \dot{a}(t)/a(t)$ is the Hubble parameter; overdot means derivative with respect to the cosmic time t. Under the assumption of the cosmological principle, from eq. (2.30) we can further derive the Friedmann equation:

$$H^2 + \frac{1}{6}f(R) - \frac{\ddot{a}}{a}f_{,R} + H\dot{f}_{,R} = \frac{8\pi G}{3}\rho_{m,b}. \tag{2.34}$$

The trace of eq. (2.30) shows explicitly the role of the field $f_{,R}$. Indeed we have:

$$\Box f_{,R} = \frac{1}{3}\left[R - f_{,R}R + 2f(R) - 8\pi G\rho_m\right], \tag{2.35}$$

which can be seen as the equation of motion for the scalaron, with a canonical kinetic term and an effective potential

$$\frac{\partial V_{eff}}{\partial f_{,R}} = \frac{1}{3}\left[R - f_{,R}R + 2f(R) - 8\pi G\rho_m\right]. \tag{2.36}$$

For the class of viable models that in the high-curvature regime satisfy $|f_{,R}| \ll 1$ and $|f(R)/R| \ll 1$ (see e.g. refs. [117, 118]), V_{eff} has an extremum at the general-relativistic value

$$R = \frac{8\pi G}{3}\rho_m.$$

The concavity of the potential in the extremum is given by its second-order derivative:

$$m_{f_R}^2 \equiv \frac{\partial^2 V_{eff}}{\partial f_{,R}^2} = \frac{1}{3}\left(\frac{1 + f_{,R}}{f_{,RR}} - R\right), \tag{2.37}$$

where $f_{,RR} = df_{,R}/dR$; m_{f_R} represents the scalaron mass and its inverse $\lambda = 1/m_{f_R}$,

the Compton length, gives the typical interaction range of the fifth force. In the limit of $|Rf_{,RR}|, |f_{,R}| \ll 1$ one has

$$m^2_{f_R} \sim \frac{1}{3f_{,RR}}. \tag{2.38}$$

Constraining the scalaron mass means therefore to constrain the second derivative of $f(R)$, rather than just $f_{,R}$. Notice also that, in this approximation, in order to have a stable minimum, $f_{,RR} \geq 0$ is thus required. Ref. [119] argued that this is a critical constraint to avoid short timescale instabilities in the high curvature regime. Physically, the condition means a non-tachyonic scalaron field.

Looking to perturbations in the FRW background, under the quasi-static approximation for which $\nabla f_{,R} \gg \dot{f}_{,R}$ (which is achieved for scales $k/aH \gg 1$), it is possible to rearrange the field equation (2.35) in a Poisson-like form for the fluctuations, as shown in [120]:

$$\nabla^2 \delta f_{,R} = \frac{1}{3}\delta R(f_{,R}) - \frac{8}{3}\pi G \delta\rho_m, \tag{2.39}$$

where I am working in physical coordinates and the perturbed quantities are defined as $\delta X = X - X_b$. Solving the linearized modified Einstein equations in the Newtonian gauge of eq. (2.9) one can furthermore derive the Poisson equation for the Bardeen potential Φ:

$$(1 + f_{,R})\nabla^2\Phi = \frac{16\pi G}{3}\delta\rho_m - \frac{1}{6}\delta R(f_{,R}). \tag{2.40}$$

In the linear regime, the curvature perturbations are everywhere small compared to the GR value $\delta R \ll 8\pi G\delta\rho_m$. This happens for example if $|f_{,R(b)}| \gg |\Phi_N|$, where $\Phi_N \sim 10^{-5}$ is the typical Newtonian potential for a galaxy cluster. Following e.g. ref. [117] and references therein I expand the curvature perturbation as:

$$\delta R \simeq \left(\frac{\partial R}{\partial f_{,R}}\right)_{R_b} \delta f_{,R} = 3\bar{m}^2_{f_R}\delta f_{,R}, \tag{2.41}$$

where $\bar{m}^2_{f_R}$ refers to the background scalaron mass. Combining the last three equations and writing the result in Fourier space, we obtain an expression for the time-time Bardeen potential:

$$\Phi(k) = -\frac{4\pi G\delta\rho_m}{1 + f_{,R}}\frac{1}{k^2}\left(1 + \frac{1}{3}\frac{k^2}{\bar{m}^2_{f_R} + k^2}\right), \tag{2.42}$$

which is the same as eq. (2.11) with:

$$2Q^2 = 1/3, \quad h_1 = (1 + f_{,R})^{-1} \simeq 1, \quad m = \bar{m}_{f_R}. \tag{2.43}$$

A similar equation can be derived for Ψ:

$$\Psi(k) = -h_1 h_2 \frac{4\pi G\delta\rho_m}{k^2}\left(1 - 2\hat{Q}^2\frac{k^2}{\bar{m}_{f_R}^2 + k^2}\right) = -\frac{4\pi G\delta\rho_m}{1 + f_{,R}}\frac{1}{k^2}\left(1 - \frac{1}{3}\frac{k^2}{\bar{m}_{f_R}^2 + k^2}\right), \tag{2.44}$$

where $2\hat{Q}^2 = -1/3\,, h_2 = 1$. In real space, for a NFW mass density profile, we finally get:

$$\Phi(r) = \left[G\int_{r_0}^{r}\frac{dx}{x^2}M(x) + \frac{1}{3}\phi_{mg}(r, \bar{m}_{f_R})\right] + O(f_{,R}); \tag{2.45}$$

$$\Psi(r) = \left[G\int_{r_0}^{r}\frac{dx}{x^2}M(x) - \frac{1}{3}\phi_{mg}(r, \bar{m}_{f_R})\right] + O(f_{,R}). \tag{2.46}$$

We are now left with only one free parameter, i.e. the background scalaron mass $\bar{m}_{f_R}$ (or, equivalently, the interaction range λ), related to the background $f_{,R}$ through eq. (2.37). The maximum enhancement of gravity due to the effect of the fifth force is $1/3$ with respect to GR on scales $k \gg \bar{m}_{f_R}$. Eq. (2.45) is what I will use in the analysis of the cluster dynamics in order to constrain $\lambda = 1/m$.

It is straightforward to compute the lensing potential form eqs. (2.45), (2.46):

$$\Phi_{lens}(r) = \frac{1}{2}(\Phi + \Psi) = G\int_{r_0}^{r}\frac{dx}{x^2}M(x) + O(f_{,R}). \tag{2.47}$$

In $f(R)$ models photons perceive only the Newtonian part of gravity except for a correction of order $\sim f_{,R}$. Thus, for models with $|f_{,R}| \ll 1$, geodesics of photons are unchanged by the presence of the new degree of freedom. This feature is physically related to the property that $f(R)$ and scalar-tensor theories in general can be generated by a conformal rescaling of the metric, together with the conformal invariance of electromagnetism (see e.g. [29]).

For small field values $|f_{,R(b)}| \ll |\Phi_N|$, the characteristic mass becomes larger and the contribution of the force modification is suppressed. Moreover, if one considers an overdensity such as a galaxy cluster (assumed to be spherically symmetric), in the interior the field is close to the minimum of the effective potential, given by the GR limit $\delta R \simeq 8\pi G\delta\rho_m$; in this case field gradients are negligible except for a shell at the boundary where the overdensity matches

the cosmological background. The thickness of this shell is given by

$$\Delta r = r_{match} - S. \tag{2.48}$$

In the above equation, r_{match} indicates the boundary of the overdensity and S is dubbed the *screening radius*. For $r < S$ gravity is described by standard GR and eq. (2.40) becomes the usual Poisson equation for the Newtonian potential.

In order to use the same formalism of eq. (2.42), derived by linearizing the curvature perturbations, inside the overdensity, one has to replace $\bar{m}_{f_R}$ with an effective mass $m_{eff}(k)$, which depends on the environmental density, and is related to the scalaron minimum value inside the overdensity. If in the region enclosed within the screening radius S we have full screening, m_{eff} becomes so large that the field does not propagate and the additional terms in eqs. (2.42),(2.44) tend to zero. The mechanism to recover GR in high density regions by using an environment-dependent field is known as the chameleon mechanism (ref. [31]).

Assuming a constant value for m_{eff} in this picture (i.e. neglecting the dependence on the environment) is equivalent to assume a screening mechanism so efficient (or so inefficient) that the transition of the scalaron field to its background value takes place at scales much larger (much smaller) than the cluster size.

2.2.1 The Hu & Sawicki model

One of the most common viable functional forms for $f(R)$ is the popular Hu & Sawicki model of ref. [5] (H&S hereafter), in which $f(R)$ is expressed as a power law:

$$f(R) = -M^2 \frac{c_1 (R/M^2)^n}{c_2 (R/M^2)^n + 1}, \tag{2.49}$$

where $M^2 = H_0^2 \Omega_m$; n, c_1, c_2 are free parameters that can be suitably related to each other in order to reproduce the expansion history of the ΛCDM model. Indeed, by requiring

$$\frac{c_1}{c_2} = 6\frac{\Omega_\Lambda}{\Omega_m}, \qquad c_2 \left(\frac{R}{M^2}\right)^n >> 1, \tag{2.50}$$

it is possible to expand eq. (2.49) as:

$$\lim_{(M^2/R)\to 0} f(R) \simeq 6\Omega_\Lambda - \frac{f_{,R0}}{n}\frac{R_{0,b}^{n+1}}{R^n}, \tag{2.51}$$

with

$$f_{,R0} = f_{,R}(z=0) = -n\frac{c_1}{c_2^2}\left(\frac{M^2}{R_{0,b}}\right)^{n+1}$$

the background value of the scalar field at present time. For $|f_{,R0}| \ll 1$ eq. (2.51) reduces to a cosmological constant; moreover, since $R(z)$ is an increasing function of redshift, the approximation is valid at all cosmological times. The H&S functional form has been widely used in literature given its relatively simple parametrization, which allows to derive constraints on MG from the comparison with observational data.

2.3 Cosmological constraints on modified gravity

At the beginning of this Chapter I classified all the alternatives to the ΛCDM model in two main categories: the first one includes models in which the energy density content of the Universe is modified with the introduction of new fields (Dark Energy models), while the second one questions if our current understanding of gravity is adequate to describe the gravitational interaction at large scales (Modified Gravity models). In general, any departure from a simple cosmological constant comes at the price of additional degrees of freedom which intervene in the formation and evolution of cosmological structures (with the exception of non-clustering Dark energy models), leaving in principle a detectable imprint even if the background expansion is indistinguishable from the one predicted by the standard Concordance model. Search for such signatures, both at background and perturbed level, is a key feature to investigate the nature of the modification and distinguish viable models among the broad class of scenarios proposed in the literature (see e.g. ref. [108] and references therein for more details). In the following I present an overview of cosmological tests of modified gravity, identifying the main observables used to constrain deviations from the Concordance model. For a recent review, see ref. [121].

Departures from General Relativity on large scales modify the Friedmann equations, as I have shown for $f(R)$ gravity, altering the background expansion history of the Universe with respect to the the ΛCDM one. Therefore, a precise determination of the time evolution of the scale factor is a good way to test alternative models of gravity at cosmological scales. This can be achieved by using observables which measure quantities that directly probe cosmic expansion history, such as Type Ia SNe and BAO, related to the luminosity distance and the

angular diameter distance respectively (e.g. refs. [122, 123]), as well as model-independent probes of $H(z)$ such as cosmic chronometers (e.g. refs. [124, 125]) in combination with local measurements of H_0 (e.g. ref. [45]). As already discussed in Chapter 1 and in Section 2.1, current data-sets have shown that the background evolution of the Universe is in exceptional agreement with the one predicted by the ΛCDM model, although some tensions are still present. Expansion probes constraints are generally combined with information coming from large scale structure analysis, such as Weak Lensing surveys (e.g. refs. [126, 127]), galaxy clustering and cluster abundance (refs. [128]), redshift space distortion (RSD, e.g. ref. [129]), CMB and CMB lensing (ref. [1]).

Cosmological tests of modified gravity aim at constraining the phenomenological functions $Y(k,a)$ and $\eta(k,a)$, which define general departures from GR in the growth of cosmic structures, or their combination

$$\Sigma(k,a) = \frac{Y(k,a)[1+\eta(k,a)]}{2}, \tag{2.52}$$

which expresses modification in the lensing potential as

$$k^2\frac{(\Phi+\Psi)}{2} \equiv k^2\Phi_{lens} = -\frac{3}{2}\Sigma(k,a)\Omega_m(t)\delta_m H^2. \tag{2.53}$$

Another possibility is to infer the linear growth rate $f(a)$, eq. (1.25); as already mentioned in Chapter 1, the linear evolution of cosmic structures changes when introducing additional degrees of freedom coupled with the matter fields. Even for pure collisionless dark matter perturbations, the differential equation eq. (1.21) now exhibits an explicit scale-dependence; in terms of $f = d\log D(a)/d\log a$ it can be rewritten as:

$$\frac{df}{d\ln a} + f^2(a) + \left(\frac{\dot{H}}{H^2}+2\right)f(a) - \frac{3}{2}Y(k,a)\Omega_m = 0, \tag{2.54}$$

where the scale enters through the function $Y(k,a)$. In GR it has been shown (e.g. ref. [130]) that $f(a)$ is well described by a power-low function of Ω_m:

$$f(a) = \Omega_m(a)^\gamma,$$

where $\gamma \simeq 0.545$ is the growth index, with small correction induced by presence of Dark Energy. In modified gravity or Dark Energy frameworks γ assumes different values (e.g ref.

[131]), thus it can be used to discriminate between various models. The linear growth rate can be probed by e.g. RSD measurements, which however are sensitive to the combination $f(z)\sigma_8(z)$, where $\sigma_8(z)$ is the amplitude of matter fluctuations over a scale of $8\,h^{-1}$Mpc. RSD are distortions in the redshift space caused by peculiar velocities of cosmological objects. Since the peculiar motion follows the infall of matter toward over dense regions, RSD analysis traces the growth rate of cosmic structures. In particular, the galaxy power spectrum in redshift space reads:

$$P_g^s(k,\mu,z) = P^r(k,z)[b(z) + \mu^2 f(z)],$$

where $b(z)$ is the galaxy linear bias, μ is the cosine of the angle between the wavenumber $\vec{k}$ and the line-of-sight, $P^r(k,z)$ is the matter power spectrum in real space, which comes with its amplitude (e.g. σ_8). Thus, the linear growth function $f(z)$ inferred from RSD surveys is degenerate with the amplitude of matter fluctuations. In Figure 2.2 from ref. [132] the evolution of $f(z)\sigma_8(z)$ is shown for 6 different models (solid and dashed lines) compared with several constraints from RSD data (points with errorbars). The measurements at $z < 1$ include 6dFGS, the SDSS main galaxies, the 2dFGRS, the SDSS LRG, the BOSS LOWZ, the BOSS CMASS, WiggleZ, VVDS and VIPERS surveys. The red solid line indicates the predictions of the Concordance model with the amplitude fitted using the filled points and squares. The plot demonstrates that current RSD measurements at low-redshift are not sufficient to distinguish from various alternatives to the ΛCDM model. The inclusion of higher redshift data and the reduction of the uncertainties as expected by future surveys (e.g. DESI, Euclid) are necessary in order to discriminate the behavior of different MG models. In particular, the analysis of ref. [132] shows that the high-redshift measurement obtained from the Subaru FMOS galaxy redshift survey (red filled point in the plot) is consistent with GR but other models were found outside the 1σ region.

Constraints on the MG parameters $Y(k,a)$, $\eta(k,a)$ and $\Sigma(k,a)$ from the combined analysis of CMB data, expansion probes and growth-rate probes are presented in ref. [1]. I show in Figure 2.3 the 1σ and 2σ marginalized contours in the plane $(\eta(z=0)-1, Y(z=0)-1)$ and $(\Sigma(z=0)-1, Y(z=0)-1)$ obtained by ref. [1] (Left panel of Figure 14 and Figure 15 in the paper, respectively) when no scale dependence is assumed [1]. As a result, a tension with GR is found at $\sim 3\sigma$ C.L. when *Planck* CMB data are combined with constraints from Baryonic

[1] Note that the parameter Y is indicated as μ in ref. [1]

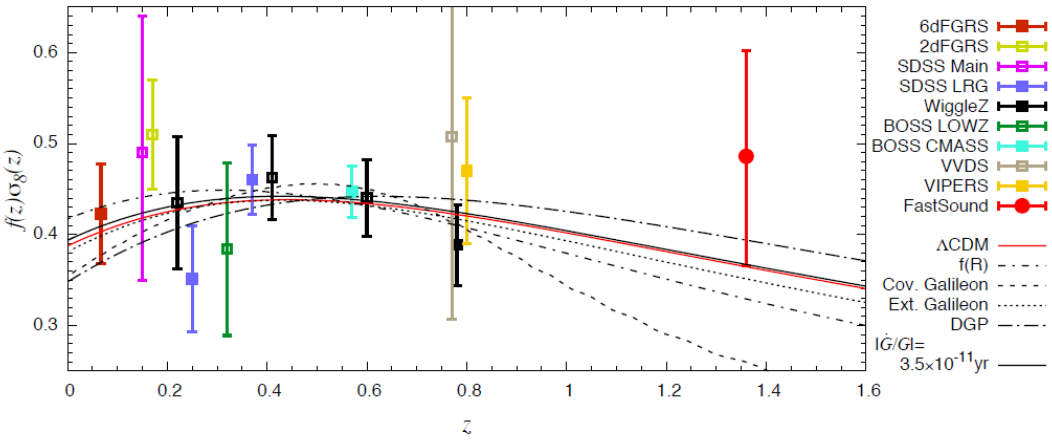

Figure 2.2: Measurements of $f(z)\sigma_8(z)$ in the redshift range $0 < z < 1.55$ compared with the predictions of 5 MG models plus the ΛCDM model. For the Concordance model (red solid line), the amplitude is determined by minimizing the χ^2 of the data indicated by the filled point and squares. Credit: ref. [132]

Acoustic Oscillations, Redshift Space Distortions and Weak Lensing data. Interestingly, the tension with ΛCDM predictions is alleviated when including in the analysis also the contribution from CMB lensing. Even if the origin of this discrepancy is still debated, the results of ref.

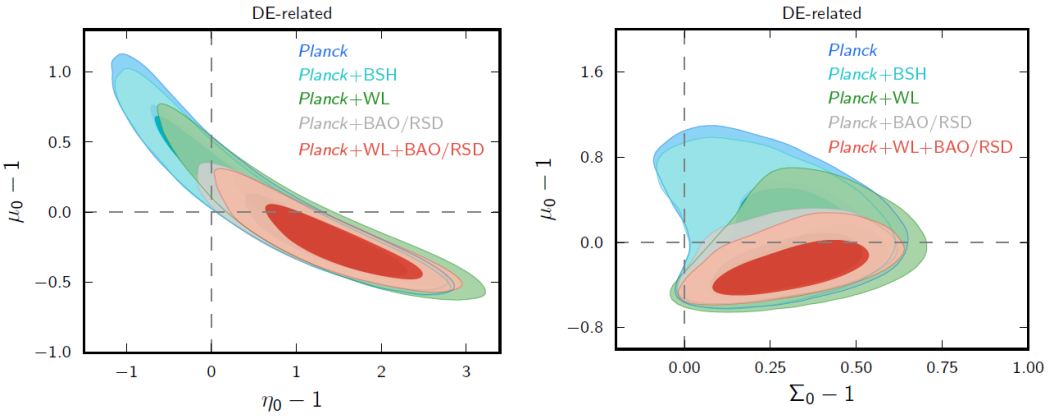

Figure 2.3: Constraints on MG parameters in the plane $(\eta(z=0)-1, Y(z=0)-1)$ (left panel) and $(\Sigma(z=0)-1, Y(z=0)-1)$ (right panel) obtained from the analysis of the Planck CMB spectrum combined with expansion probes (Planck+BSH), Weak Lensing (Planck+WL) and RSD (Planck+BAO/RSD). The inner shaded regions indicate 1σ contours while the outer lighter regions correspond to 2σ-contours. The vertical dashed lines show the GR ΛCDM values. From Figure 14 and Figure 15 of ref. [1].

[1] show that combined informations coming from several distinct observational probes are required get stringent constraints on deviations from GR. Whether the apparent tension is the effect of systematics or a true indication of new physics is a question to be investigated with the advent of future more precise data-sets from growth-rate and expansion probes. In this context, it is fundamental to find new approaches to constrain modification of gravity which are totally independent of other determinations.

As I will discuss in Chapter 6, the method I present in this Thesis, based on galaxy clusters mass profiles reconstruction, provides constraints on MG parameters quite competitive with the current determinations in literature; in particular, the bounds on the parameter η obtained from the analysis of one single galaxy cluster will be shown to be as stringent as (or even better than) the results of ref. [1]. The potential of our method, which provides a promising tool to investigate the nature of gravity in view of the next generation imaging and spectroscopic surveys, however necessarily requires a severe control of the possible systematics, as will be extensively pointed out in Chapter 8.
Nowadays, the most stringent constraint on the parameters Σ, Y in the scale-independent case has been found by ref. [133] using a combination of CMB data from Planck, cosmic shear from CFHTLenS and DES science verification data, RSD from BOSS DR12 and the 6dF galaxy survey. They obtained, at 1σ C.L.:

$$\Sigma - 1 = -0.01^{+0.05}_{-0.04}, \qquad Y - 1 = -0.06 \pm 0.18.$$

In addition to the above mentioned tests for modified gravity, it is worth to remind also the already discussed GWs, which are an excellent probe to select viable non-standard models.
As for the specific class of $f(R)$ models, current analyses performed by using distance indicators at low-redshift (ref. [134]), galaxy cluster abundance (refs. [128, 14]) and redshift space distortions (ref. [135]), have tightened the constraints on the background field up to $|\bar{f}_{,R0}| < 10^{-6}$, compatible with very small deviations from GR, although the recent results of ref. [125], obtained with the Cosmic chronometer approach, show a slight tension with standard gravity when particular functional form of $f(R)$ are used.
In conclusion, among the large variety of observational probes aimed at constraining deviations from the Concordance Model, some analyses seem to indicate possible tensions with the ΛCDM predictions whose nature is still unclear; developing new methods to test GR is crucial

to explore the origin of the apparent inconsistencies from other perspectives and to obtain a better understanding of the behavior of gravity at cosmological scales.

Part II

Galaxy clusters mass profiles as test for modified gravity

Chapter 3

Dynamics of galaxies in clusters

In this Chapter I will study the relation between the motion of galaxies in a cluster and the underlying gravitational potential; in particular, I will introduce the Jeans' equation, which is used to recover the the mass profile of a galaxy cluster under the assumption of dynamical relaxation, further discussing how cluster dynamics analyses can be used to constrain modified gravity. The Chapter is organized as follow: Section 3.1 provides a brief introduction about galaxy clusters, Section 3.2 presents the dynamics of collisionless systems in an equilibrium configuration, highlighting under what conditions it approximates the dynamics of a galaxy cluster. For this part I refer to Chapter 4 of ref. [136] and Chapter 5 of ref. [42]. In Section 3.3 I introduce the *MAMPOSSt* procedure developed in ref. [32] to determine the mass profile of a cluster from the dynamics traced by the member galaxies. I illustrate the modified version of *MAMPOSSt* implemented within this Thesis to constrain the free parameters of alternative models of gravity; the modified *MAMPOSSt* method will be applied in the framework of $f(R)$ gravity to obtain the results presented in Chapter 7 and Chapter 8.

3.1 Phenomenology of galaxy clusters

A cluster of galaxies is a massive object with typical size of $1\,\mathrm{Mpc}$, spawning approximately two order of magnitude in mass (from $10^{13}\,M_{\odot}$ to $10^{15}\,M_{\odot}$). Clusters are made of hundreds to thousands galaxies, but only a tiny fraction of the total cluster mass ($\sim 2 \div 5\%$) corresponds to galaxies (e.g ref. [137]).

The galaxy population of a cluster is mainly composed by elliptical early-type galaxies, up to

$\sim 80\%$ in regular clusters; the total projected distribution of cluster member galaxies is on average well fitted by a (projected) NFW profile (see e.g. ref. [138]), but also other models have been shown to provide adequate fit. For example, in the case of the galaxy cluster MACS 1206 ref. [25] found that even if the NFW profile gives the least χ^2 in the maximum likelihood fit to the total number density distribution, the King profile of ref. [139]:

$$n(R) \propto \frac{1}{1 + (R/r_\nu)^2},$$

where r_ν is a characteristic scale radius, is also not rejected by data; moreover, it is preferable to the projected NFW when only the star-forming galaxies are considered in the fit.

A fraction of the missing mass in galaxy clusters (from 10% to 20% of the total mass) was identified to be ordinary matter not associated with galaxies in the form of a hot ionized plasma with an average temperature of the order of $10^8\ K$ and typical densities varying from $10^{-1} cm^{-3}$ to $10^{-4} cm^{-3}$. The diffuse gas is called *Intra Cluster Medium* (ICM hereafter) and emits in the X-band with luminosity between 10^{43} and $10^{45}\ erg/s$ due to the interactions of the free electrons with the ions (mostly protons and Helium nuclei) via thermal bremsstrahlung. The ICM contains also traces of heavy elements partially ionized, such as Carbon, Oxygen and Iron, with typical abundances of one third of the solar value. From X-ray observations one can estimate the temperature map of the hot gas and its density profile from the surface brightness (see e.g. ref. [140]). The high temperature of the ICM is thought to be generated by a shock heating mechanism during the gravitational collapse of the gas. Minor contributions are also given by non-gravitational effects, such as Active Galactic Nuclei (AGN) and Supernovae, especially in the central regions and in low-mass clusters.

The majority of the matter content ($\sim 80\%$) of a galaxy cluster is contained in a halo of smoothly distributed Dark Matter, which thus dominates the global cluster dynamics.

In the hierarchical structure formation paradigm, galaxy clusters are thought to form through a series of merging events of smaller systems which assembled via gravitational interactions. In this context, galaxy clusters represent the largest gravitationally bound objects that emerge as the final step of the hierarchical formation process. They offer a fertile soil for studying a large variety of phenomena at the edge between astrophysics and cosmology; indeed, while the overall structure of a cluster and its assembling history are determined by gravity, as the physics can be almost entirely described in terms of the evolution of collisionless Dark Matter, the internal properties of clusters reflect the contribution of dissipative processes governed by

the physics of baryons.
Galaxy clusters can be used in different ways as excellent cosmological probes; for example their statistical properties, such as spatial distribution and abundance (e.g. refs. [141, 142]), clusters peculiar velocities (e.g. refs. [143, 144]) or features related to the internal structure baryon gas fraction (e.g ref. [145]), and cluster mass profiles reconstructions (e.g. ref. [146]). In particular, within this Thesis, I investigate the internal distribution of the total cluster mass (i.e. the mass profile) with two different probes, namely the dynamics of the member galaxies and the gravitational lensing effects, which in the last few years has reached an unprecedented level of precision, allowing for the possibility to constrain departures from GR in a competitive and independent way with respect to other probes, as discussed in Chapter 2.

The right panel of Figure 3.1 shows the composite X-ray and optical image of the cluster Abell 383; the ICM is identified by the violet haze. Note that the hot gas exhibits an almost concentric distribution peaked near the cluster core; also the member galaxies are spherically distributed, with no evident substructures, around the Brightest Central Galaxy (BCG) which is further located in projection close to the X-ray luminosity peak. These features are indications that Abell 383 is a *dynamically relaxed* cluster, which means that all the matter components are in an equilibrium configuration within the same total gravitational potential. This is also suggested by the fact that in regular clusters the mean quadratic velocity of the ICM particles, related to the gas temperature as

$$< v_{gas}^2 >= \frac{3k_B T}{\mu m_p}, \tag{3.1}$$

where μ is the average mass of a gas particle in terms of the proton mass m_p, is comparable to the velocity dispersion of the member galaxies σ_{gal}^2.
Dynamical relaxation is a fundamental requirement for the analysis developed within this Thesis. As I will extensively discuss in the next Sections, clusters in dynamical equilibrium show convenient properties for the reconstruction of the total cluster mass profile; in Chapter 2 I have shown that the mass profile is connected to the underlying gravitational potential and this relation is sensitive to the assumed model of gravity. Thus, relaxed clusters are interesting targets to investigate the effect of possible departures from GR.

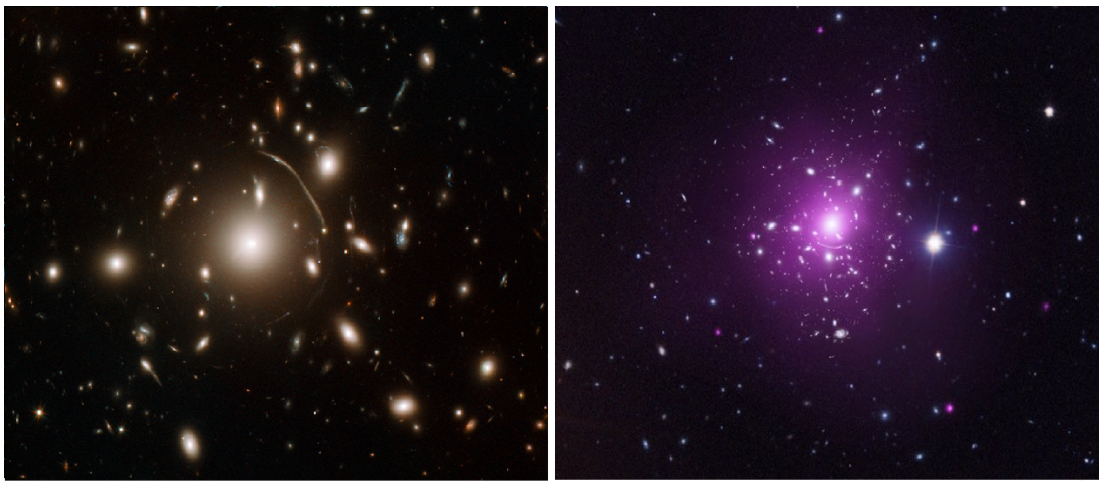

Figure 3.1: Left: Optical image of the galaxy cluster Abell 383 obtained from the Hubble Space Telescope. Credits: NASA, ESA, J. Richard (CRAL) and J.-P. Kneib (LAM). Right: composite X-ray/optical image of the same cluster; the purple area shows the ICM X-ray emission. From NASA/CXC/Caltech/A.Newman et al./Tel Aviv/A. Morandi & M. Limousin (X-ray), NASA/STScI, ESO/VLT, SDSS (optical).

3.2 Dynamics of collisionless systems

When considering astrophysical systems such as star clusters, galaxies and galaxy clusters, the relevant interaction which dominates the dynamics is the gravitational force; if single interactions and close encounters are negligible, the systems is said to be *collisionless* and each tracer (e.g. a galaxy in a cluster) experiences an acceleration caused by the overall smooth gravitational potential. At equilibrium, velocities randomize and the dynamics is determined by the evolution of the *phase-space distribution function* $f(\vec{x}, \vec{v}, t)$ through the collisionless Bolzmann equation (see below). As discussed in Chapter 2, the typical velocity dispersions in galaxy clusters are of the order of $10^{-3}\, c^2$ (e.g. refs. [25, 147]), thus the weak field limit approximation of eq. (A.16) is valid and galaxies perceive only the time-time component of the metric. Even if galaxy clusters are characterized by an average matter density fluctuation $\delta\rho$ highly non-linear, the space-time geometry perturbations are small compared to the background, and the metric of a cluster is given by eq. (2.9) in the conformal Newtonian gauge. This implies that the gravitational potential involved in the dynamics of galaxies in clusters is the Bardeen potential Φ.

Consider now a cluster made of $N \sim 10^2 \div 10^3$ members with typical masses $m \sim 10^{11}\, M_\odot$ in a configuration of dynamical equilibrium; it is easy to show that encounters are relatively

unimportant and the cluster can be treated as a system of collisionless particles. To demonstrate this, I estimate the variation of the velocity $\delta\vec{v}$ of a reference galaxy in the cluster induced by the interaction with another member. Under the approximation of a small variation in the velocity $|\delta\vec{v}/\vec{v}| << 1$, and assuming a straight line trajectory in the region of the encounter, the variation in the direction orthogonal to the motion $|\delta\vec{v}_\perp|$ is given by:

$$|\delta\vec{v}_\perp| \simeq \frac{2Gm}{bv}, \tag{3.2}$$

where b is the impact parameter of the interaction. By approximating the cluster as a sphere of radius R, one can express the mean surface density of galaxies as:

$$\nu \sim \frac{N}{\pi R^2}. \tag{3.3}$$

After one crossing of the system, the reference galaxy will have experienced a number of encounters with impact parameter in the differential interval from b and $b + db$, which is equal to

$$d\nu = \nu \times 2\pi b\, db = \frac{2N}{R^2} b\, db. \tag{3.4}$$

After each interaction the velocity changes by an amount $\delta\vec{v}_\perp$; since the direction of the variation is random, the average change is negligible when summing all the contributions $< \delta\vec{v}_\perp >= 0$. We thus consider the sum of the squared variations induced by all the encounters in one crossing:

$$(\delta\vec{v}_\perp^2)_{cross} \simeq \delta\vec{v}_\perp^2 \times d\nu = \left(\frac{2Gm}{bv}\right)^2 \frac{2N}{R^2} b\, db. \tag{3.5}$$

The total variation $(\Delta\vec{v}_\perp^2)_{cross}$ is obtained by integrating over all the values of the impact parameter $b \in [b_{min}, b_{max}]$, where $b_{max} \equiv R$ and $b_{min} = Gm/v^2$. The last statement arises from the condition $|\delta\vec{v}/\vec{v}| < 1$ which is violated for $b \lesssim Gm/v^2$. We have:

$$(\Delta\vec{v}_\perp^2)_{cross} = \int_{b_{min}}^{R} \left(\frac{2Gm}{bv}\right)^2 \frac{2N}{R^2} b\, db = 8N \left(\frac{Gm}{Rv}\right)^2 \ln\left(\frac{R}{b_{min}}\right). \tag{3.6}$$

Since I have assumed that the cluster is in dynamical equilibrium, I can apply the virial theorem $2T = |E_\phi|$, where T is the total kinetic energy and E_ϕ is the (Newtonian) gravitational

potential energy generated by all the members of the system:

$$2\frac{1}{2}Nmv^2 = \frac{G(Nm)^2}{R} \Rightarrow \frac{Gm}{v^2} = \frac{R}{N}, \tag{3.7}$$

from which one obtains:

$$\left(\frac{\Delta\vec{v}_\perp^2}{\vec{v}^2}\right)_{cross} = \frac{8}{N}\ln\left(\frac{R}{b_{min}}\right) \sim \frac{8}{N}\ln N. \tag{3.8}$$

From eq. (3.8) it follows that in order to have a variation in the velocity of order of unity, a galaxy should cross the cluster a number of times

$$n_{cross} = \frac{N}{8}\left[\ln\left(\frac{R}{b_{min}}\right)\right]^{-1}. \tag{3.9}$$

If one crossing of the systems happens in $t_{cross} \sim R/v$, I define the *relaxation time* t_{rel} as the product $t_{cross} \times n_{cross} \sim N\,R/(v\,8\ln N)$. The relaxation time expresses the timescale for which the motion of a member of the system is significantly perturbed by encounters with other members. In the case of a rich galaxy cluster, $N \sim 10^3$ and so $n_{cross} \sim 18$, with a typical crossing time of $10^9\,yrs$; this means that the relaxation time is of the order of $10^{10}\,yrs$, which is comparable to Hubble time. Thus, collisions of galaxies in clusters can be irrelevant or not, depending on the dynamical assembly history of the cluster. In galaxy clusters at equilibrium configuration (hereafter *dynamically relaxed clusters*) the effect of encounters is negligible and the dynamics is described by the evolution of the phase-space distribution function $f(\vec{x},\vec{v},t)$ under the influence of a smooth gravitational potential $\Phi(\vec{x},t)$.

3.2.1 The Vlasov equation

A self-gravitating system of N collisionless objects governed by the total potential $\Phi(\vec{x},t)$ can be described in terms of the number of particles dN which, at a specific time t, occupy the positions between $\vec{x}$ and $\vec{x} + d^3\vec{x}$ and are characterized by velocities between $\vec{v}$ and $\vec{v} + d^3\vec{v}$:

$$dN = f(\vec{x},\vec{v},t)d^3\vec{x}d^3\vec{v}, \tag{3.10}$$

where $f > 0$ is the above mentioned distribution function and it expresses the density of objects in the phase-space $\{(\vec{x},\vec{v})\}$; given a set of initial conditions at t_0, the value of f is determined for any $t > t_0$.

The dynamical quantities of the system are identified by the 6-dimensional vector $w = (\vec{x}, \vec{v})$ and its velocity

$$\dot{w} \equiv (\dot{\vec{x}}, \dot{\vec{v}}) = (\vec{v}, -\nabla\Phi), \tag{3.11}$$

with Φ the total gravitational potential related to the mass density profile trough the Poisson equation:

$$\nabla^2\Phi = 4\pi G\rho. \tag{3.12}$$

Since I am neglecting collisions, the flow of points in the phase-space is characterized by a regular "drift" motion, and the distribution function satisfies the continuity equation:

$$\frac{\partial f}{\partial t} + \sum_{i=1}^{6} \frac{\partial (f\,\dot{w}_i)}{\partial w_i} = 0, \tag{3.13}$$

where the index runs over all the 6 components. Integrating eq. (3.13) over a volume ΔV in the phase-space it is easy to show that the first term describes the rate at which the number of particles changes within this volume, while the second term expresses the rate at which particles flow in or out the same volume.
Since $\vec{x}$ and $\vec{v}$ are independent variables and Φ does not depend on $\vec{v}$, it follows that

$$\sum_{i=1}^{6} \frac{\partial \dot{w}_i}{\partial w_i} \equiv \sum_{j=1}^{3} \left[\frac{\partial v_j}{\partial x_j} - \frac{\partial}{\partial v_j} \left(\frac{\partial \Phi}{\partial x_j} \right) \right] = 0. \tag{3.14}$$

Thus, it is possible to rewrite eq. (3.13) as:

$$\frac{\partial f}{\partial t} + \sum_{i=1}^{6} \dot{w}_i \frac{\partial f}{\partial w_i} = \frac{\partial f}{\partial t} + \sum_{j=1}^{3} \left(v_j \frac{\partial f}{\partial x_j} - \frac{\partial \Phi}{\partial x_j} \frac{\partial f}{\partial v_j} \right) = 0, \tag{3.15}$$

which is called *Vlasov equation* or collisionless Boltzmann equation. In terms of the convective derivative $\frac{D}{dt} = \frac{\partial}{\partial t} + (\vec{v} \cdot \nabla)$, eq. (3.15) reads:

$$\frac{D}{dt} f(\vec{x}, \vec{v}, t) = 0, \tag{3.16}$$

and it describes the conservation of the density of points in the phase space as seen by an observer which is comoving with the flow; in other words, the Vlasov equation shows that the flow of points in phase-space is that of an incompressible fluid. When collisions become

important, an additional contribution appears in eq. (3.15):

$$\left(\frac{\partial f}{\partial t}\right)_{coll},$$

which expresses the variation of the distribution function induced by encounters between members of the system.

If the system under study exhibits symmetries, it is useful to recast the Vlasov equation in a different suitable coordinate frame. Within this Thesis I will always assume spherical symmetry, and thus the spherical coordinate system $(r,\, \theta,\, \phi,\, v_r,\, v_\theta,\, v_\phi)$ is adopted[1]. In this frame, eq. (3.15) can be written as:

$$\frac{\partial f}{\partial t} + v_r\frac{\partial f}{\partial r} + \frac{v_\theta}{r}\frac{\partial f}{\partial \theta} + \frac{v_\phi}{r\sin\theta}\frac{\partial f}{\partial \phi} + \dot{v}_r\frac{\partial f}{\partial v_r} + \dot{v}_\theta\frac{\partial f}{\partial v_\theta} + \dot{v}_\phi\frac{\partial f}{\partial v_\phi} = 0, \tag{3.17}$$

where

$$\begin{aligned}
\dot{v}_r &= \frac{v_\theta^2 + v_\phi^2}{r} - \frac{\partial \Phi}{\partial r},\\
\dot{v}_\theta &= \frac{v_\phi^2\cot\theta - v_r v_\theta}{r} - \frac{1}{r}\frac{\partial \Phi}{\partial r},\\
\dot{v}_\phi &= -\frac{v_\theta v_r + v_\theta v_\phi\cot\theta}{r} - \frac{1}{r\sin\theta}\frac{\partial \Phi}{\partial \phi}.
\end{aligned} \tag{3.18}$$

3.2.2 The Jeans' equation

I am now interested in investigating the properties of the collisionless Boltzmann equation by computing its moments. As a first step, integrating eq. (3.15) over the velocities one obtains:

$$\int \frac{\partial f}{\partial t} d^3\vec{v} + \sum_{i=1}^{3}\left[\int v_i \frac{\partial f}{\partial x_i} d^3\vec{v} - \frac{\partial \Phi}{\partial x_i}\int \frac{\partial f}{\partial v_i} d^3\vec{v}\right] = 0. \tag{3.19}$$

By introducing the *spatial density* of the particles ν and their *mean velocity* $\bar{v}_i$ as

$$\nu(\vec{x},t) = \int f(\vec{x},\vec{v},t) d^3\vec{v}; \qquad \bar{v}_i(\vec{x},t) = \frac{1}{\nu}\int v_i\, f(\vec{x},\vec{v},t) d^3\vec{v},$$

[1] I will discuss departures from spherical symmetry as possible source of systematics in Chapter 8

it is possible to rearrange eq. (3.19) to get:

$$\frac{\partial \nu}{\partial t} + \frac{\partial(\nu \bar{v}_i)}{\partial x_i} = 0, \tag{3.20}$$

where the sum over i is implied. Eq. (3.20) is the continuity equation for the spatial number density ν.

Multiplying now eq. (3.15) by v_j and then integrating again over the velocity space, one gets the first moment of the Vlasov equation, which can be written as:

$$\frac{\partial(\nu \bar{v}_j)}{\partial t} + \frac{\partial(\nu \overline{v_i v_j})}{\partial x_i} + \nu \frac{\partial \Phi}{\partial x_j} = 0, \tag{3.21}$$

where I have defined

$$\overline{v_i v_j} = \frac{1}{\nu} \int v_i v_j f \, d^3\vec{v}.$$

I now multiply eq. (3.20) for $\bar{v}_j$ and I subtract it to eq. (3.21); introducing the *velocity stress tensor*:

$$\nu \sigma_{ij}^2 = \nu \overline{(v_i - \bar{v}_i)(v_j - \bar{v}_j)} = \nu \left[\overline{v_i v_j} - \bar{v}_i \bar{v}_j \right], \tag{3.22}$$

we finally obtain the *Jeans' equation* (J. Jeans, 1919)

$$\nu \frac{\partial \bar{v}_j}{\partial t} + \nu \bar{v}_i \frac{\partial \bar{v}_j}{\partial x_i} = -\nu \frac{\partial \Phi}{\partial x_j} - \frac{\partial(\nu \sigma_{ij}^2)}{\partial x_i}. \tag{3.23}$$

Eq. (3.23) is similar to the Euler equation, eq. (1.19), where the role of the pressure is played by the velocity stress tensor.

The Jeans' equation relates observed dynamical quantity to the underlying gravitational potential Φ; for a galaxy cluster, described by the linearly perturbed FLRW metric (eq. (2.9)) in the Newtonian gauge, Φ coincides with the time-time Bardeen potential times the conformal scale factor $a(\tau)$[2].

Note that, while in the case of the Euler equation we can relate the pressure p to the density ρ through the equation of state, for the Jeans' equation there is no analogous relation connecting the 6 independent components of $\boldsymbol{\sigma}^2$ to the number density ν. One can imagine to compute the second moment of the Vlasov equation by multiplying it by $v_j v_k$ and integrating over the velocity space. In doing so we end up with a new equation containing terms $\overline{v_i v_j v_k}$ which

[2] In the Jeans' analysis I will neglect the scale factor since a galaxy cluster is actually disentangled by the Hubble flow and the dynamics of galaxies is not affected by the expansion of the Universe.

will require an additional relation, and so on. In order to close this hierarchy of equations it is possible to either truncate the system for a given order n, or making assumptions on the structure of the velocity field. As already discussed above, the results presented in this Thesis are derived assuming that the clusters are spherically symmetric. In this particular case, the Jeans' equation can be derived in spherical coordinates starting from eq. (3.17):

$$\frac{d(\nu\sigma_r^2)}{dr} + \frac{\nu(r)}{r}\left[2\sigma_r^2 - (\sigma_\theta^2 - \sigma_\phi^2)\right] = -\nu(r)\frac{d\Phi}{dr}, \tag{3.24}$$

where $\sigma^2_{r,\theta,\phi}$ are the *velocity dispersions* corresponding to the the diagonal components of the velocity stress tensor, related to v_r, v_θ, v_ϕ respectively.
I define *velocity anisotropy profile* the ratio:

$$\beta(r) = 1 - \frac{\sigma_\theta^2 + \sigma_\phi^2}{2\sigma_r^2}, \tag{3.25}$$

which is a function of the radial distance from the center of the halo r; since in spherical symmetry the velocity dispersions along the tangential and azimuthal direction are equal $\sigma_\theta^2 = \sigma_\phi^2$, the velocity anisotropy reduces to:

$$\beta(r) = 1 - \frac{\sigma_\theta^2}{\sigma_r^2}. \tag{3.26}$$

In this way, the Jeans' equation can be written as:

$$\frac{d\left[\nu(r)\sigma_r^2(r)\right]}{dr} + 2\beta(r)\frac{\nu(r)\sigma_r^2(r)}{r} = -\nu(r)\frac{d\Phi(r)}{dr}. \tag{3.27}$$

Thus, measurements of the number density profile ν, of the velocity dispersion σ_r and of the velocity anisotropy $\beta(r)$ allow us to constrain the gravitational potential through eq. (3.27). As shown in Chapter 2, Φ is related to the effective dynamical mass (see eq. (2.25)):

$$\frac{d\Phi}{dr} = \frac{G\,M_{dyn}(r)}{r^2}, \tag{3.28}$$

where M_{dyn} is the cumulative mass enclosed within the radius r. A different version of eq. (3.27) can be obtained in terms of M_{dyn}:

$$M_{dyn}(r) = -\frac{r}{G}\sigma_r^2\left[\frac{d(\ln\nu)}{d(\ln r)} + \frac{d(\ln\sigma_r^2)}{d(\ln r)} + 2\beta(r)\right], \tag{3.29}$$

which makes explicit the relation between the mass profile and the dynamical quantities.
The Jean's equation is in principle a powerful method to determine galaxy cluster mass profiles, but the application of eq. (3.27) is limited by the fact that what one can actually infer is only the velocity dispersion along the line of sight and the projected number density profile. It is in general impossible to infer independently σ_r^2 and $\beta(r)$; moreover, tangential velocities are generally small and direct measurements of the anisotropy are complicated. Different methods have been developed in the literature to reconstruct $\beta(r)$; for example, one possible solution is to assume a parametric model for the anisotropy and to determine the parameters of the profile along with the mass profile with a Maximum Likelihood fit to the data (see Sec. 3.3). Another possibility is to infer $\beta(r)$ with some non-parametric technique by inverting the Jeans' equation (e.g. refs. [148, 149]), but this generally requires additional information and assumptions. Observations of galaxy clusters (e.g. ref. [25, 150]) as well as analyses of cosmological simulations (e.g. refs. [151, 152]) indicate that generally orbits tend to be isotropic in the center (i.e. $\beta = 0$) while the anisotropy grows with radius. As an example, Figure 3.2 shows the non-parametric reconstruction of $\beta(r)$ from the analysis of the galaxy cluster MACS 1206 by ref. [25] while Figure 3.3 shows the velocity anisotropy profile of dark matter particles from 6 simulated halos taken from the set of cosmological N-body simulations I will discuss in Chapter 8. The halos considered spawn a mass range $M_{200} \in [2 \times 10^{14}, 1.7 \times 10^{15}]\, M_{\odot}$.

It is worth to mention that the Jeans' analysis is not the only possible method to determine galaxy cluster mass profiles through the dynamics of member galaxies. Moreover the assumption of dynamical equilibrium limits the validity of the Jeans' equation out to the virial radius, which at $z = 0$ corresponds to the radius r_{200} defined in Chapter 2. Other techniques for which no assumption on the dynamical state of the cluster is needed can be used to reconstruct the mass profile in more external regions $r > r_{200}$. For example, the Caustic method of ref. [153] identifies the curves $\mathcal{A}(r)$ in the projected phase space (R, v_z) (see below) of the galaxies where the phase space number density is formally infinite. The amplitude of those caustics depends on the averaged escape velocity squared along the line of sight $\left\langle v^2_{z\,esc}(r)\right\rangle$, which is in turn connected to the gravitational potential $\Phi(r)$. This technique does not require assuming dynamical equilibrium and a model for the mass profile, but comes at the price of introducing an additional function of Φ and $\beta(r)$ which relates $M(r)$ to $\mathcal{A}(r)$ and whose calibration represents the main systematics of this method (see e.g. ref. [25] which applied the Caustics technique to estimate the mass profile of the cluster MACS 1206 in the external regions). In this Thesis I apply only the Jeans' reconstruction to determine M_{dyn} assuming a parametric model

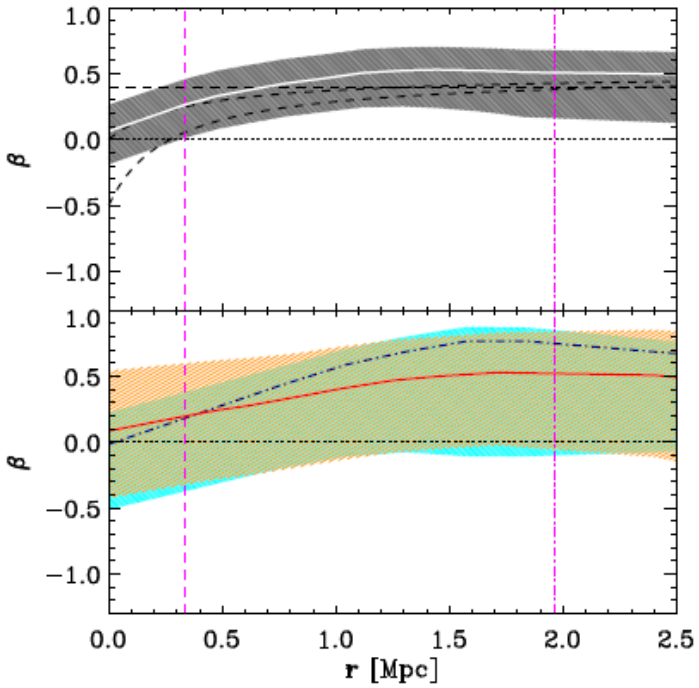

Figure 3.2: Anisotropy profile $\beta(r)$ of the galaxy cluster MACS 1206 as a function of the radial distance derived by ref. [25] inverting the Jeans' equation (white solid line in the upper panel, red solid and blue dashed line in the bottom panel) assuming the reference mass profile found by the analysis of Section 3 in ref. [25]. Top panel: all cluster members are used. The gray band indicates the 68% confidence region while the black dashed curves correspond to 3 parametric profiles of $\beta(r)$ obtained as the best fit from the *MAMPOSSt* analysis (see Sec. 3.3 and Chapter 5). Bottom panel: red line and orange shaded area show the anisotropy derived using passive galaxies only, while the blue dashed line and the light blue region correspond to the anisotropy profile of active galaxies. Both shaded intervals are the 68% confidence regions. Credits: ref. [25].

for the mass profile; this is because my analysis will be performed always within the virial radius to avoid large-scale structure contaminations (see Chapter 6). More important, parametric expressions for the Bardeen potentials eq. (2.23), eq. (2.27) are useful when one is interested in constraining specific classes of modified gravity models, as I will discuss in the next Section.

The study of the X-ray emission from the ICM is another possible way to determine the cluster mass profile under the assumption that the gas is in hydrostatic equilibrium with the total potential. Assuming spherical symmetry, the total mass enclosed in a radius r from the

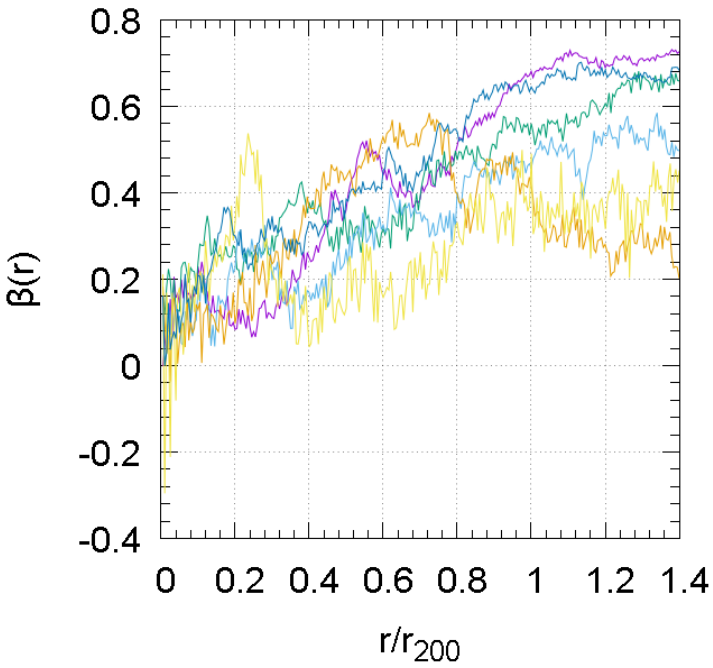

Figure 3.3: Velocity anisotropy profile of 5 dark matter halos taken from a set of cosmological N-body simulations performed with the GADGET-3 code (see Chapter 8) as a function of the radial distance from the halo center scaled for the virial radius r_{200}.

center is related to the gas density through (e.g. ref. [154]):

$$\rho_{gas}(r)\frac{dP}{dr} = \frac{G\,M(r)}{r^2}, \tag{3.30}$$

where P and ρ_{gas} are the pressure and the density of the gas respectively. If I further use the equation of state for a perfect gas:

$$P = \frac{\rho_{gas} k_B T}{\mu m_p},$$

it is possible to obtain a relation between the total cumulative mass, the density and the temperature of the gas:

$$M(r) = -\frac{k_B T(r) r}{\mu m_p G}\left[\frac{d\ln\rho_{gas}(r)}{d\ln r} + \frac{d\ln T(r)}{d\ln r}\right]. \tag{3.31}$$

Eq. (3.31) is very similar to the Jeans' equation (3.29) where the gas temperature is replaced by the velocity dispersion of the galaxies. It is worth to notice that since both galaxies and ICM

perceive the same gravitational potential, the two methods for reconstructing the mass profile are sensitive in the same way to modification of gravity. Nevertheless, diffuse gas and galaxies dynamics suffer different systematics; for instance non-thermal pressure, e.g. associated to unthermalized gas motions, leads to a biased estimate of the cluster mass from X-ray analyses compared to other methods (see e.g. ref. [155] and references therein, ref. [156]), especially in the cluster outskirts where the contribution of non-thermal pressure becomes large (e.g. ref. [157]).

In Thesis I will not use X-ray mass profiles reconstructions, as I am interested in constraining the gravitational potential out to the virial radius r_{200} while X-ray observations are generally limited to r_{500}; moreover, X-ray measurements are biased in the outskirt of galaxy clusters due to gas clumping (see e.g. ref. [158]). Clearly, combined X-ray and Jeans' analyses to infer the gravitational potential in the central region of relaxed clusters could in principle help in tightening the constraints on the inner shape of the profile (e.g. constraints on the scale radius r_s of the NFW mass model); as I will discuss in Chapter 7 and Chapter 8, having additional information on the mass profile parameters is quite important to detect possible signatures of modified gravity.

3.3 Mass profiles from the *MAMPOSSt* method

MAMPOSSt (Modelling Anisotropy and Mass Profiles of Observed Spherical Systems) is a method to derive mass profiles of galaxy clusters from the analysis of the dynamics of the member galaxies, under the assumption of spherical symmetry and dynamical relaxation. In this section I briefly describe the code, developed by ref. [32] and the modification I have made to include the effects of modified gravity models.

The *MAMPOSSt* method performs a Maximum-Likelihood fit to the distribution of the galaxies, assumed to be collisionless tracers of the gravitational potential, in the projected phase space (R, v_z), where R is the projected radius from the cluster center and v_z is the velocity measured along the line of sight (l.o.s.), given in the rest frame of the cluster (i.e. $< v_z > \sim 0$). Thus, large samples of spectroscopic redshift data for the cluster member galaxies are the key ingredient for the *MAMPOSSt* procedure. Figure 3.4 shows the projected phase spaces of the member galaxies identified for two clusters analyzed in this Thesis, namely MACS 1206 (left panel, from ref. [25]) and RXJ 2248 (right panel). Vertical solid lines corre-

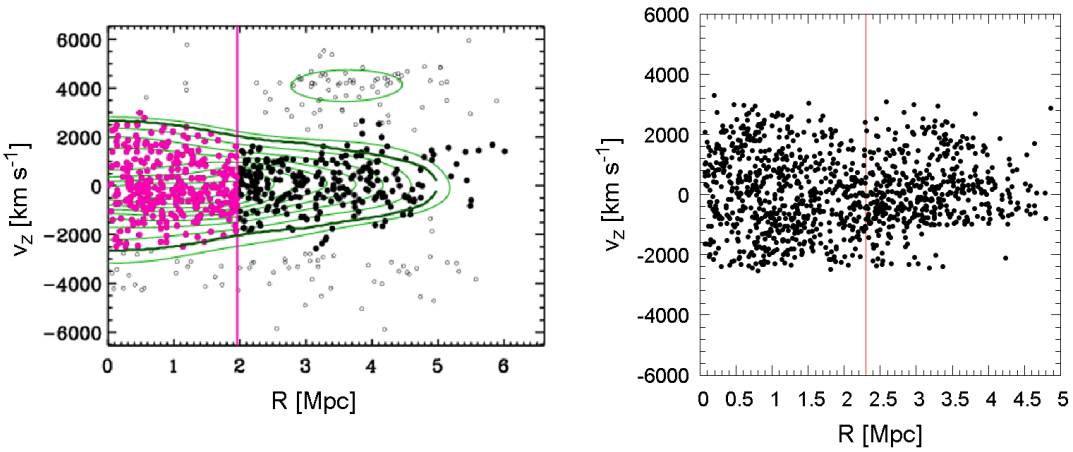

Figure 3.4: Left panel: projected phase space for the cluster MACS 1206. Filled circles show the selected member galaxies, while green curves identify the caustics; from ref. [25]. Right panel: projected phase space for the galaxy cluster RXJ 2248. In both plots the vertical lines indicate the values of r_{200} found by the lensing analysis of ref. [26] and ref. [35] respectively.

spond to r_{200} estimated by the lensing reconstruction of ref. [26] (MACS 1206) and ref. [35] (RXJ 2248). Green curves in the left panel are the caustics found by the analysis of ref. [25].

MAMPOSSt works under the assumption of a 3-dimensional Gaussian distribution for the velocities of the tracers. It is worth to point out that the method can be generally performed given any model of the 3D velocity distribution; the choice of a Gaussian is the simplest, but the code has been extensively tested and verified to work quite well on halos drawn from cosmological simulations in which the velocity distribution along the l.o.s. can have significant deviations from Gaussianity. More in detail, ref. [32] extracted 11 cluster-mass Dark Matter halos from a cosmological hydrodynamical simulation performed by ref. [159] using the parallel Tree+SPH GADGET-2 code [37]; 10 of the halos were logarithmically spaced in r_{200} while the last one was chosen to be the most massive halo in the simulation.

Ref. [32] sampled 500 dark matter particles from each halos and applied the *MAMPOSSt* procedure in combination with different interlopers[3] removal algorithms, showing that *MAMPOSSt* provides an overall good, almost unbiased, estimation of the free parameters in the dynamical analysis (see e.g. Table 4 in ref. [32]).

The *MAMPOSSt* technique solves the spherical Jeans' equation eq. (3.27) given a parametric form of the mass profile $M(r)$, the velocity anisotropy profile $\beta(r) = 1 - \sigma_\theta^2/\sigma_r^2$, and the num-

[3]I define *interlopers* particles(galaxies) which are not belonging to the cluster but whose projected radius lies within the cluster range. As discussed in ref. [160], not taking into account those objects can produces a highly biased estimation of the dynamical mass parameters.

ber density profile of the galaxies $\nu(r)$. It is worth to notice that the distribution of galaxies in clusters does not follow the total distribution of mass; in particular, ref. [138] derived the mean projected number density profile of galaxies in clusters from a catalog of the SDSS DR7 in the redshift range $0.15 < z < 0.4$, finding that the average concentration parameter is roughly a factor of two lower than that predicted for dark matter halos in N-body simulation. Also the analysis of ref. [161] on a stacked sample of 59 clusters has shown that the baryonic mass profile exhibit a smaller concentration with respect to the total mass profile; thus $\nu(r)$ generally scales in a different way with respect to the mass profile $M(r)$. Nonetheless, *MAMPOSSt* can be also run imposing that the scale radius of the two profile is equal (i.e. light follows mass assumption).

Within this Thesis, I will consider 4 parametrizations of $\beta(r)$ implemented in the *MAMPOSSt* code:

the **constant anisotropy model "C"**

$$\beta(r) = \beta_C, \tag{3.32}$$

the **Mamon&Lokas model "ML"** of ref. [162], which has been shown to provide a good fit to the average cluster-size halos anisotropy profile over a set of cosmological simulations (see e.g ref. [152])

$$\beta(r)_{ML} = \frac{1}{2}\frac{r}{r + r_\beta}, \tag{3.33}$$

where r_β is a characteristic scale radius;

the **Tiret model "T"** of ref. [163]

$$\beta(r)_T = \beta_\infty \frac{r}{r + r_c}, \tag{3.34}$$

a generalized version of the "ML" which tends to β_∞ at large radii;

the **Opposite model "O"**

$$\beta(r)_O = \beta_\infty \frac{r - r_c}{r + r_c}, \tag{3.35}$$

which allows for tangential orbits in the innermost region.

In *MAMPOSSt* the scale radius for the "T" and "O" profiles is set to be equal to the scale radius of the mass profile $r_c \equiv r_s$.

In eq. (3.27) $\Phi(r)$ is the gravitational potential which is given by the time-time Bardeen potential for the linearly perturbed FLRW metric (in Newtonian gauge); it coincides with the

Newtonian potential in standard GR. $\sigma_r(r)$ is the velocity dispersion along the radial direction.

The solution of the Jeans' equation can be written as (e.g. ref. [162]):

$$\sigma_r^2(r) = \frac{1}{\nu(r)} \int_0^\infty \exp\left[2\int_r^s \beta(t)\frac{dt}{t}\right] \nu(s)\frac{d\Phi(s)}{ds}ds. \tag{3.36}$$

Note that eq. (3.36) is the only relation in which the gravitational potential enters directly; I thus modified this expression by substituting $d\Phi/ds$ with the derivative of eq. (2.11). The solution is obtained in GR by assuming that the cluster is an isolated object. Ref. [164] showed that eq. (3.36) holds also in a cosmological ΛCDM background.

For simple models of the velocity anisotropy profile $\beta(r)$, the integral in the exponential inside eq. (3.36) has an analytical solution such that the expression for σ_r^2 becomes:

$$\sigma_r^2(r) = \frac{1}{\nu(r)K(r)} \int_0^\infty K(s)\nu(s)\frac{d\Phi(s)}{ds}ds, \tag{3.37}$$

where I have defined the kernel $K(r)$ as

$$\frac{K(s)}{K(r)} = \exp\left[2\int_r^s \beta(t)\frac{dt}{t}\right].$$

I list here below the expressions of $K(r)$ (up to an constant integration factor) for the 4 models of $\beta(r)$ adopted in this work:

$$K(r) = \begin{cases} r^{2\beta} & \beta = \text{"C"}, \\ r + r_\beta & \beta = \text{"ML"}, \\ (r + r_\beta)^{2\beta_\infty} & \beta = \text{"T"}, \\ (r + r_\beta)^{2\beta_\infty} r^{-2(1+\beta_\infty)} & \beta = \text{"O"}. \end{cases}$$

The probability density of observing an object at position (R, v_z) in the projected phase space is given by:

$$q(R, v_z) = \frac{2\pi R g(R, v_z)}{N_p(R_{max}) - N_p(R_{min})}, \tag{3.38}$$

with $N_p(R)$ the predicted number of galaxies lying at the projected distance R from the cluster center and $g(R, v_z)$ is the surface density of observed objects with l.o.s. velocity v_z; In the

case of a 3D-Gaussian velocity distribution, it takes the form:

$$g(R, v_z) = \sqrt{\frac{2}{\pi}} \int_R^\infty \frac{r\nu(r)}{\sqrt{r^2 - R^2}} \frac{dr}{\sigma_z(R, r)} \exp\left[-\frac{v_z^2}{2\sigma_z^2(R, r)}\right], \tag{3.39}$$

where $\sigma_z(R, r)$ is the velocity dispersion along the line of sight defined as:

$$\sigma_z(R, r) = \sigma_r(r)\sqrt{1 - \beta(r)\frac{R^2}{r^2}}\,. \tag{3.40}$$

steps through which the *MAMPOSSt* procedure works can be summarized as follows:

(i) For a given choice of the parameter vector $\boldsymbol{\theta} = \{r_s, r_{200}, r_\nu, \beta\}$ (see below) $\sigma_r(r)$ is computed from eq. (3.37) over a logarithmic grid of radii r_i and then performs a cubic-spline interpolation to evaluate at intermediate radii.

(ii) The solution of the Jeans' equation is then used to calculate $g(R, v_z)$ for each $(R_i, v_{z,i})$. The integral of eq. (3.39) is numerically solved by assuming a cutoff for the upper limit of $\sim 15 r_{200}$, where the velocity of the matter pushed by the Hubble flow is roughly 3σ above the mean value of the cluster. Variations of the viral radius by up to a factor of 2 do not change significantly the result of the integration (ref. [32]).

(iii) The Likelihood is computed from eq. (3.38) as:

$$-\log \mathcal{L} = -\sum_{i=1}^{n} \log q(R_i, v_{z,i}|\boldsymbol{\theta}). \tag{3.41}$$

The minimum value of $-\log \mathcal{L}$ is found by searching over a grid in the parameter space. In its original version, the *MAMPOSSt* code works with four free parameters, namely the scale radius of the tracers density profile r_ν, the parameter of the velocity anisotropy profile, the scale radius r_s and the radius r_{200} of the chosen parametric mass profile.

3.3.1 MG-*MAMPOSSt*

I have modified the *MAMPOSSt* procedure by introducing the generic form for the gravitational potential Φ of eq. (2.23):

$$\Phi(r) = h_1 \left[G \int_{r_0}^{r} \frac{dx}{x^2} M_{NFW}(x, r_s, r_{200}) + 2Q^2 \phi_{mg}(x, r_s, r_{200}, m, S)\right], \tag{3.42}$$

which accounts for a broad range of viable modified gravity models, including the $f(R)$ case. I have expanded the parameter array by introducing 4 additional parameters, which are the interaction range $\lambda = 1/m$, the conformal rescaling h_1, the coupling factor Q and the screening radius S, under the assumption of an instantaneous transition between the screened and non-screened regime (see Sec. 7.2).

For the purposes of this Thesis, I will focus on $f(R)$ models as a case study; in this framework, as already discussed in Chapter 2, Q is a constant fixed such that $2Q^2 = 1/3$. Furthermore, $h_1 = 1/(1 + f_{,R})$; I will restrict the analysis to the range $\lambda \leq 100$Mpc, which, for example, in the Hu & Sawicki model of $f(R)$ (ref. [5]) roughly corresponds to $|f_{,R}| < 10^{-3}$, so one can safely set $h_1 = 1$. It is also worth to notice that in general h_1 is totally degenerate with the observed mass of the overdensity, whose information is already encoded in the virial radius r_{200}.

The modified gravity module of the code (MG-*MAMPOSSt* hereafter) is implemented only for the case of a NFW mass density profile, which provides the highest Likelihood in the GR analysis of both clusters used in this work (see Chapter 5); an extension of the code to work with other choices for the parametrization of the mass profile in generic modified gravity models is relatively straightforward and will be implemented for future analyses.

I tested the MG-*MAMPOSSt* code in linear $f(R)$ models (i.e. $\lambda = const$) to reproduce the results of ref. [25] for MACS 1206 in the limit of standard gravity $\lambda \to 0$; as shown in Figure 3.5, for $\lambda = 0.1$ Mpc (black solid line) the contribution given by the modification of gravity is very small and, except for the innermost region, the effective mass profile is very close to the GR profile obtained by ref. [25] in the standard *MAMPOSSt* analysis (red dotted line and red shaded area). In the opposite situation ($\lambda \gg 1$) I checked that the modification in the effective mass profile reaches the maximum enhancement of $1/3$ as expected for $f(R)$ gravity. It is worth to notice that the contribution of the additional degree of freedom saturates for $\lambda \gtrsim 10$ Mpc: the overall relative difference in the effective mass profile computed for $\lambda = 10$ Mpc (blue line) and $\lambda = 1000$ Mpc (brown dotted line) is less than 1%. This is not surprising since λ determines the typical length at which the fifth force decreases; for scales much larger than the cluster size it is impossible to distinguish the effect induced by different values of the interaction range. In Fig. 3.6 I also show the enhancement in the radial velocity dispersion profile σ_r given by the solution of the Jeans' equation (3.27) for different values of the interaction range λ. Since σ_r is proportional to the square root of the effective mass profile, for $\lambda \to \infty$ I have $\sigma_r^{MG} \to 1.16\sigma_r^{GR}$.

I will apply our MG-*MAMPOSSt* code on the data of two galaxy clusters in the framework of $f(R)$ gravity for the case of a constant value of $m = 1/\lambda$, and for environment-dependent function:

$$\lambda(r) = \bar{\lambda} \times f(r; S), \tag{3.43}$$

where $\bar{\lambda}$ is the background value and $f(r; S)$ is a step function equal to 0 for $r \leq S$ and equal to 1 otherwise. The screening radius S at which the transition happens will be fixed by assuming the H&S functional form of $f(R)$ (Sec. 2.2.1). The results will be presented and discussed in Chapter 7.

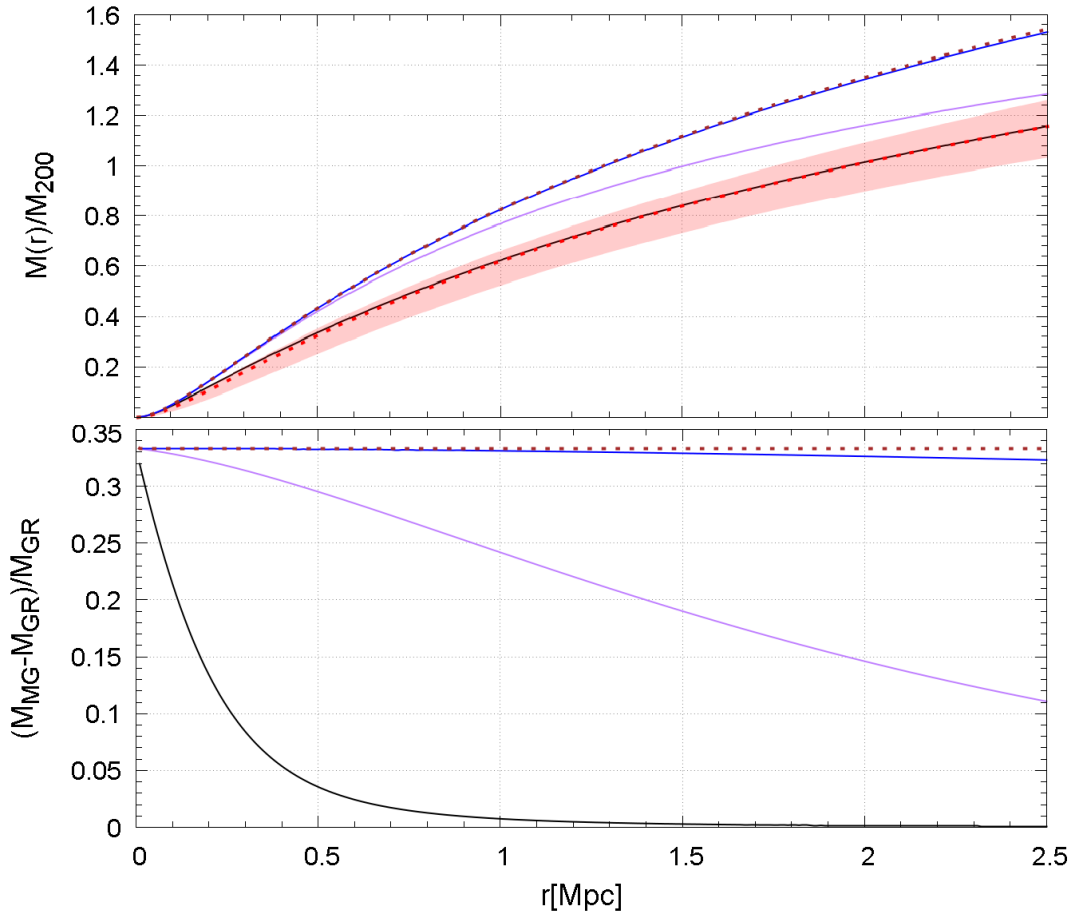

Figure 3.5: Upper panel: mass profiles in $f(R)$ gravity, expressed in unit of $M_{200} = 200H^2(z)r_{200}^3/2G$, for different values of the interaction range and $r_{200} = 1.96\,\text{Mpc}$, $r_s = 0.27\,\text{Mpc}$ (best fit values of the GR analysis of ref [25] for MACS 1206). Brown dotted line: $\lambda = 1000\,\text{Mpc}$. Blue solid line: $\lambda = 10\,\text{Mpc}$. Purple solid curve: $\lambda = 1\,\text{Mpc}$. Black solid curve: $\lambda = 0.1\,\text{Mpc}$. The red shaded area shows the GR profile within the 68% C.L. in the NFW parameters with the best fit indicated by the red dashed curve. Bottom panel: relative enhancement of the profiles with respect of the GR one, for the same value of λ as in the upper plot. For $\lambda \gg 1\,\text{Mpc}$ the profile is enhanced by a factor 1/3 with respect the GR value, while for $\lambda = 0.1\,\text{Mpc}$ the modifications of gravity are suppressed with the exception of the central regions.

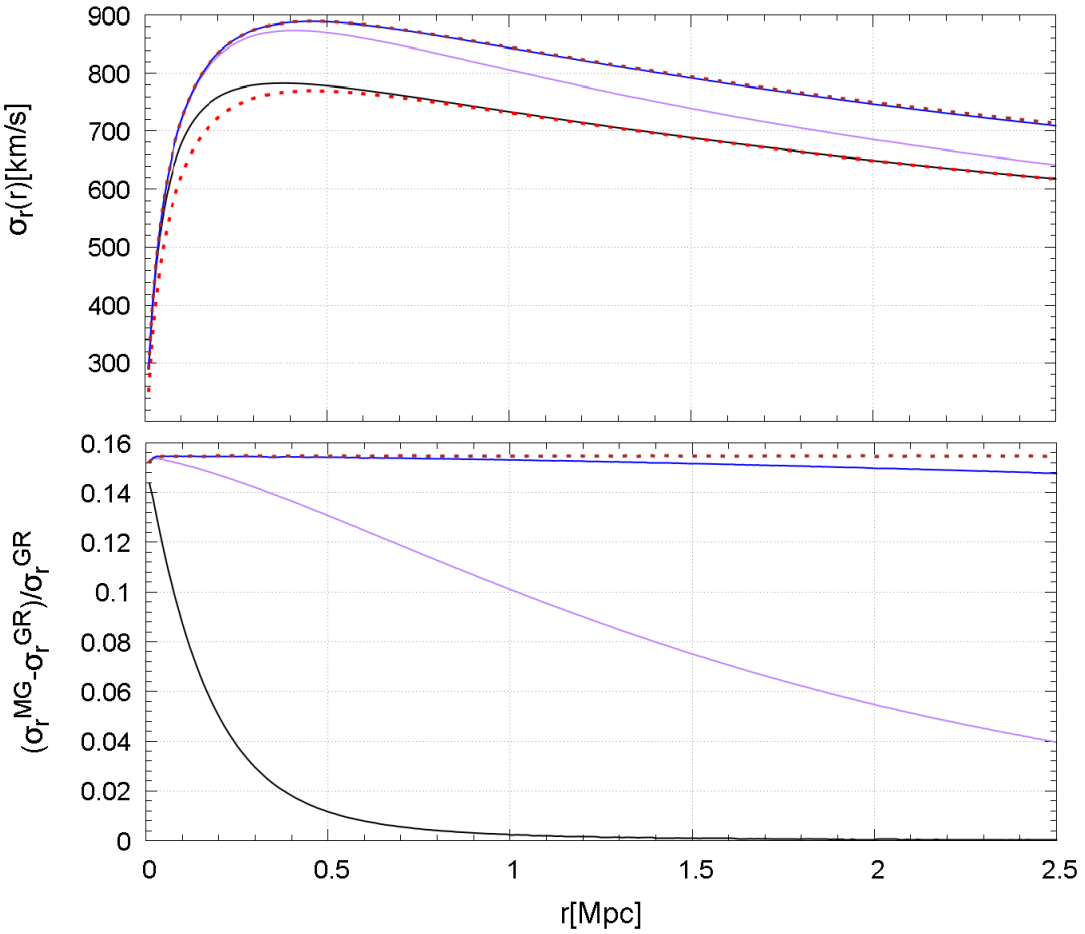

Figure 3.6: Upper panel: radial velocity dispersions in $f(R)$ gravity for different values of the interaction range and $r_{200} = 1.96\,\mathrm{Mpc}$, $r_s = 0.27\,\mathrm{Mpc}$ (best fit values of the GR analysis of ref [25] for MACS 1206). The velocity anisotropy is parametrized as a "O" model with normalization parameter $\beta_\infty = 0.5$ and the scale radius of the number density profile r_ν is set to be equal to r_s. Brown dotted line: $\lambda = 1000\,\mathrm{Mpc}$. Blue solid line: $\lambda = 10\,\mathrm{Mpc}$. Purple curve: $\lambda = 1\,\mathrm{Mpc}$. Black solid curve: $\lambda = 0.1\,\mathrm{Mpc}$. the GR profile is indicated by the red dashed curve. Bottom panel: relative enhancement of the profiles with respect of the GR one, for the same value of λ as in the upper plot For $\lambda \gg 1\,\mathrm{Mpc}$ the profile is enhanced by a factor 0.16 with respect the GR value, while for $\lambda = 0.1\,\mathrm{Mpc}$ the result is very close to standard gravity except in the cluster central regions.

Chapter 4

Gravitational Lensing with galaxy clusters

In this Chapter I briefly discuss the theory of photon propagation in curved spacetime. I will derive the lensing potential Φ_{lens} from the linearly perturbed FLRW metric, showing how it depends on both Bardeen potentials, which is a crucial point of the method for constraining modified gravity presented in this Thesis. Section 4.2 then provides an overview on galaxy cluster mass profiles reconstruction with gravitational lensing in the two regimes of Strong Lensing and Weak Lensing, highlighting what kind of data are required to perform these analyses.
For a more detailed description, I refer to the lecture notes of ref. [165] and to refs. [166, 167]

4.1 Propagation of light rays in a gravitational field

The idea that the trajectory of a light ray could be bended by the presence of a gravitational field dates back to the Eighteenth century. In 1804 Soldner, embracing the current view of corpuscular nature of light, applied the Newton's gravitational law to compute the deflection angle of a light "particle" under the influence of the gravitational potential at the surface of the Sun:

$$\tilde{\alpha} = \frac{2GM_{\odot}}{c^2 R_{\odot}} \simeq 0.83\, arcsec.$$

This results was then derived and corrected by a factor 2 by Einstein using the General Relativity principles; the value of $1.7\, arcsec$ was observationally proved during the total eclipse in

1919 by measuring the apparent displacement of a star near the Sun surface (Dyson, Eddington, Davidson, 1920) and it is considered one of the most important fundamental tests of GR in literature. The light deflection induced by the presence of mass distributions in spacetime is called gravitational lensing and it can be used to investigate properties and composition of both the region in which those bending effects are generated (the lens) and the background "lensed" sources whose light rays are distorted by the lens. In particular, gravitational lensing effects in galaxy clusters are an exceptional tool to study the structure of Dark Matter within the cluster and the nature of gravity, as well as to probe cosmology from the analysis of lensed images (e.g. ref [168] and references therein).
As already mentioned, the geometry of a galaxy cluster is described by the linearly perturbed FLRW metric. Since possible departures from GR are expected to be small, as confirmed by recent observations (see Chapter 2), the Bardeen potential Ψ should be of the same order of $\Phi \sim 10^{-4}c^2$. I am now going to define the effective refractive index $n(x)$ for light propagation in a FLRW spacetime which is linearly perturbed by the presence of a matter distribution, showing the connection between n and the two Bardeen potentials.

4.1.1 Linearly perturbed FLRW metric and effective refractive index

Propagation of electromagnetic waves in curved spacetimes are described by the covariant Maxwell equations. In vacuum, for a generic metric $g_{\mu\nu}$ we have:

$$F_{[\mu\nu;\rho]} = \frac{1}{3}\left(\nabla_\rho F_{\mu\nu} + \nabla_\nu F_{\rho\mu} + \nabla_\mu F_{\nu\rho}\right) = 0;$$

$$\nabla_\nu F^{\mu\nu} = 0, \tag{4.1}$$

where $F_{\mu\nu}$ is the electromagnetic Field-Strength tensor. Semicolon indicates covariant derivatives while comma represents partial derivatives.
By using the definition of covariant derivative and Christoffel symbols, eqs. (4.1) become:

$$F_{[\mu\nu,\rho]} = 0,$$

$$(\sqrt{-g}F^{\mu\nu}),_\nu = (g^{\mu\alpha}g^{\nu\beta}\sqrt{-g}F_{\alpha\beta}),_\nu = 0. \tag{4.2}$$

Let us now consider a conformal transformation of the metric:

$$g_{\mu\nu} \rightarrow \tilde{g}_{\mu\nu} = \Omega^2(x^\mu) g_{\mu\nu}.$$

It is straightforward to see that the first of eqs. (4.2) is invariant under such transformation, since it does not explicitly depend on the metric. For the second equation, considering that:

$$g^{\mu\nu} = \Omega^2 \tilde{g}^{\mu\nu}, \qquad \sqrt{-g} = \Omega^{-4}\sqrt{-\tilde{g}},$$

it follows that the term $g^{\mu\alpha}g^{\nu\beta}\sqrt{-g}$ is also invariant under conformal transformations. Thus, the evolution of electromagnetic fields in curved spacetime is determined only by the *conformal part* of the metric.
A linear perturbation of the FLRW background, adopting spherical coordinates in the Newtonian Gauge, is given by eq. (2.9). Dividing and multiplying by the time-time component of the metric g_{00}, we obtain a conformally equivalent version of the perturbed metric as:

$$ds^2 = a^2(\tau)\left(1 + \frac{2\Phi}{c^2}\right) d\tilde{s}^2,$$

where I have defined

$$d\tilde{s}^2 = -c^2 d\tau^2 + \frac{1 - \frac{2\Psi}{c^2}}{1 + \frac{2\Phi}{c^2}} \left[d\chi^2 + f_k^2(\chi) d\Omega^2\right], \tag{4.3}$$

and I have re-introduced for convenience the factor c. Using the fact that the Bardeen potentials are small compared to c^2, one can expand the coefficient of the spatial part in eq. (4.3) in the following way:

$$\frac{1 - \frac{2\Psi}{c^2}}{1 + \frac{2\Phi}{c^2}} \simeq \left(1 - \frac{2\Psi}{c^2}\right)\left(1 - \frac{2\Phi}{c^2}\right) \simeq 1 - \frac{2}{c^2}(\Psi + \Phi) + O(\Psi^2, \Phi^2). \tag{4.4}$$

Introducing the *lensing potential* $\Phi_{lens} = \frac{\Phi+\Psi}{2}$, we finally obtain the expression of the conformal metric:

$$d\tilde{s}^2 \simeq -c^2 d\tau^2 + (1 - \frac{4}{c^2}\Phi_{lens}) \left[d\chi^2 + f_k^2(\chi) d\Omega^2\right]. \tag{4.5}$$

Thus, light rays propagation is affected by the geometry of eq. (4.5), which depends on the sum of the two Bardeen potentials through Φ_{lens}. This means that lensing mass profile recon-

structions are sensitive to both Φ and Ψ; this is a fundamental point for the derivation of the results I wil present in Chapter 6 and Chapter 7.
Note that the spatial part of the line element $d\tilde{s}^2$ is conformally equivalent to the spatial part of the background FLRW metric. Using the definition of effective refractive index in eq. (B.8) we obtain, at first order in Φ and Ψ:

$$n = \sqrt{1 - \frac{4}{c^2}\Phi_{lens}} \simeq 1 - \frac{2}{c^2}\Phi_{lens} + O(\Phi^2, \Psi^2). \tag{4.6}$$

Eq. (4.6) coincides with the usual relation (see ref. [169]):

$$n \simeq 1 - \frac{2}{c^2}\Phi,$$

setting $\Phi = \Psi$.
The speed of a light ray which is moving under the influence of a gravitational field can then be expressed in terms of the lensing potential:

$$v_n \equiv \frac{dl}{d\tau} = \frac{c}{n} \simeq c + \frac{2}{c}\Phi_{lens}.$$

4.1.2 The deflection angle and the lens equation

I have shown that propagation of photons in curved spacetime is analogous to the classical geometrical optics; the presence of gravity plays the role of a medium with a refractive index $n > 1$[1], modifying both the speed and the path of light rays. In general, the region in which the trajectories of photons are perturbed is much smaller than the distance light travels from the source to the observer. This path can be divided in 3 distinct parts: propagation from the source to the mass distribution acting as gravitational lens, propagation through the lens and propagation from the lens to the observer. If the size of the mass distribution is negligible with respect to the total distance traveled by photons, we assume that the lens is distributed in a bi-dimensional sheet orthogonal to the line of sight (*thin screen approximation*). The plane of this sheet is called *lens plane*.
The surface mass density Σ of the lens can be expressed in terms of the 2-components vector

[1]Note that the Bardeen potentials are negative

$\vec{\xi}$ on the lens plane (see Fig. 4.1 from ref. [165]) as:

$$\Sigma(\vec{\xi}) = \int \rho(\vec{\xi}, z) dz, \tag{4.7}$$

where $\rho(\vec{\xi}, z)$ is the mass density of the lens integrated along the line of sight z. The thin screen

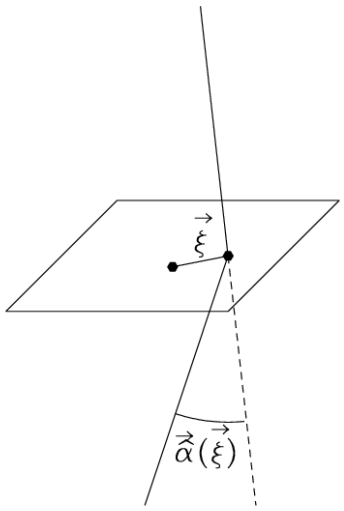

Figure 4.1: Light deflection in thin screen approximation. $\vec{\alpha}$ is the deflection angle. Credits: ref. [165].

approximation is valid also when considering structures like galaxy clusters. Indeed, typical distances of galaxy clusters, of the order of $10^2 \div 10^3$ Mpc, are generally much larger than their typical sizes ($\sim 1 \div 2$ Mpc).

In analogy with the geometrical optic, one can define the *deflection angle* with the effective refractive index:

$$\vec{\hat{\alpha}} = -\int \frac{\nabla_\perp n}{n} ds = -\int \nabla_\perp (\ln n)\, ds, \tag{4.8}$$

where the gradient is computed along the direction perpendicular to the light ray propagation and integrated over the actual light path. Inserting eq. (4.6) into eq. (4.8) and using the fact that $|\Phi_{lens}| << c^2$ it follows that:

$$\vec{\hat{\alpha}} \simeq \frac{2}{c^2} \int \nabla_\perp \Phi_{lens} dz, \tag{4.9}$$

which connects the deflection angle to the lensing potential. Note that the integral is now computed along the line of sight, which is a consequence of the fact that $\vec{\hat{\alpha}}$ is expected to be

small. For a mass distribution in thin screen approximation it can be shown that:

$$\vec{\hat{\alpha}}(\vec{\xi}) = \frac{4G}{c^2}\int \frac{(\vec{\xi}-\vec{x})\Sigma(\vec{x})}{|\vec{\xi}-\vec{x}|^2}d^2x, \tag{4.10}$$

where $\Sigma(\vec{\xi})$ is given by eq. (4.7). Note that $\vec{\alpha}$ is in general a 2-dimensional vector whose components lie in the lens plane. If the lens exhibits circular symmetry, the deflection angle is a scalar given by:

$$\hat{a}(R) = \frac{4GM(R)}{c^2 R}, \tag{4.11}$$

with R the projected radius from the center of the lens and

$$M(R) = 2\pi\int_0^R \Sigma(x)xdx$$

the total mass enclosed within the radius R.

Consider now a light ray emitted by a source S which reaches the observer located at the point O after being deflected by an angle $\vec{\hat{\alpha}}$. I want to qualitatively analyze the geometry of gravitational lensing to derive some fundamental relations used in the reconstruction of galaxy cluster mass profiles. I define $\vec{\beta}$ the angle between the optical axes of the lens and the position of the sources S and $\vec{\theta}$ the angle between the optical axes and the position of the image I (see Fig. 4.2).

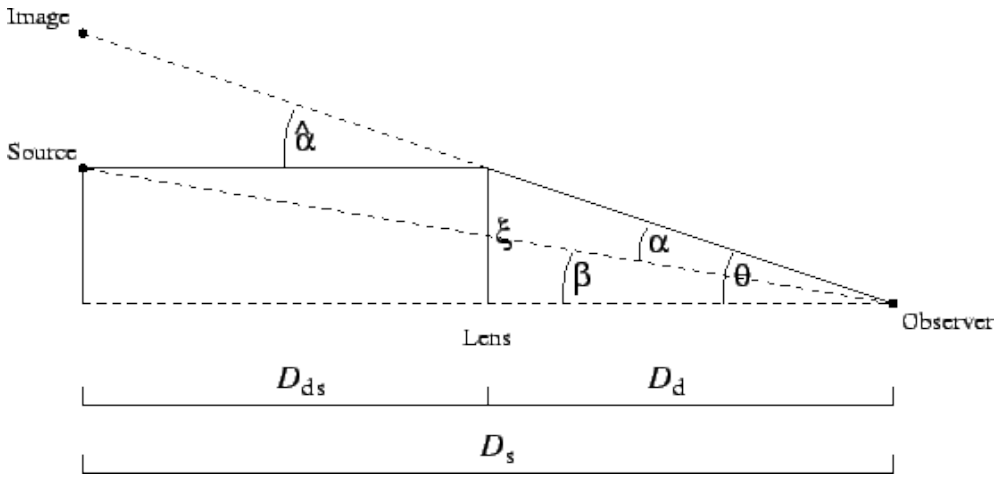

Figure 4.2: Geometrical description of gravitational lensing. ξ identifies the point of minimum distance of the light ray to the source. $\hat{\alpha}$ indicates the deflection angle, while α is the reduced deflection angle. Figure from ref. [165]

.

I introduce the reduced deflection angle as:

$$\vec{\alpha} = \frac{D_{ds}}{D_s}\vec{\hat{\alpha}}, \tag{4.12}$$

where D_{ds} e D_s are the distance between lens and source and the distance between source and observer respectively. The reduced reflection angle expresses the angular separation between source and image with respect to the observer.
Since $\vec{\theta}D_s = \vec{\beta}D_s + \vec{\hat{\alpha}}D_{ds}$, using the definition eq. (4.12) we obtain the *lens equation*:

$$\vec{\beta} = \vec{\theta} - \vec{\alpha}(\vec{\theta}). \tag{4.13}$$

This relation is generally non linear in $\vec{\theta}$, meaning that for a single source at an angle β it is possible to obtain different images located at angles θ_i, solutions of eq. (4.13). Note that despite eq. (4.13) has been derived in Euclidean space, it can be shown that it is valid also in a generic spacetime using the geodesic deviation equation (see e.g. ref. [170] and references therein), where distances should be now interpreted as angular diameter distances.
For a circularly symmetric lens with a constant surface density the reduced deflection angle is given by:

$$\alpha_r(R) = \frac{4D_{ds}G}{D_s c^2 R}\Sigma\pi R^2,$$

where I used eq. (4.11). The projected radius R is related to the angle θ through $R = D_d\theta$, thus:

$$\alpha(\theta) = \frac{4\pi G\Sigma}{c^2}\frac{D_{ds}D_d}{D_s}\theta,$$

such that the lens equation becomes

$$\beta = \theta - \frac{4\pi G\Sigma}{c^2}\frac{D_{ds}D_d}{D_s}\theta \propto \theta. \tag{4.14}$$

It will exist a critical value of the surface density Σ_{cr} defined as:

$$\Sigma_{cr} = \frac{c^2}{4\pi G}\frac{D_s}{D_d D_{ds}} = 0.35 cm^{-2}\left(1Gpc\frac{D_s}{D_d D_{ds}}\right),$$

for which $\alpha(\theta) = \theta$, so from the lens equation $\beta = 0$ for any value of θ. If $\Sigma > \Sigma_{cr}$ the lens is said to be *supercritical* and in this case multiple images of the same sources are generated. Let us focus on a circularly symmetric supercritical lens with an arbitrary mass distribution $M(\theta)$;

the lens equation reads:

$$\beta(\theta) = \theta - \frac{D_{ds}}{D_d D_s} \frac{4GM(\theta)}{c^2 \theta}. \tag{4.15}$$

If the source lies on the optical axis (i.e. $\beta = 0$) then for the symmetry of the problem the corresponding images will be a ring of radius

$$\theta_E = \sqrt{\frac{4GM(\theta_E)}{c^2} \frac{D_{ds}}{D_d D_s}}, \tag{4.16}$$

which is called the *Einstein ring*. The value of θ_E depends not only on the mass distribution but also on the distance scales, and it is one of the fundamental quantities in gravitational lensing analyses. Indeed, the Einstein radius θ_E defines the typical scale to discriminate strong lensing ($\theta < \theta_E$) and weak lensing effect ($\theta \gtrsim \theta_E$, see Sec. 4.2); it is worth to notice that the average surface density enclosed within the Einstein ring is by definition the critical density Σ_{cr}.

4.1.3 Magnification and Shear

The Liouville theorem ensures that the surface brightness of an object is preserved when the light is deflected by a gravitational field. Nevertheless, gravitational lensing changes the apparent solid angle of a source such that the flux received from an image would be amplified or decreased by the ratio between the areas occupied by the image and the source. This quantity is called *magnification* μ and for a spherically symmetric lens is given by

$$\mu = \frac{\theta \, d\theta}{\beta \, d\beta}. \tag{4.17}$$

In the case of a lens with a generic matter distribution the magnification will be described by a *magnification tensor* defined as:

$$\mathcal{M}_{ij} = \frac{\partial \theta_i}{\partial \beta_j}. \tag{4.18}$$

In order to understand the physical interpretation of the components $\mathcal{M}_{ij}$, I consider the projection on the lens plane of the rescaled lensing potential Φ_{lens}:

$$\psi(\vec{\theta}) = \frac{2}{c^2} \frac{D_{ds}}{D_d D_s} \int \Phi_{lens}(D_d \vec{\theta}, z) dz, \tag{4.19}$$

which is called effective potential. The gradient of $\psi(\vec{\theta})$ along $\vec{\theta}$ coincides with the reduced deflection angle; the Laplacian instead gives:

$$\nabla^2_{\vec{\theta}}\psi = \frac{2}{c^2}\frac{D_d D_{ds}}{D_s}\int \nabla^2_{\vec{\xi}}\Phi_{lens} dz,$$

which can be related to the lens surface density through the Poisson equation for Φ_{lens}:

$$\nabla^2_{\vec{\theta}}\psi = \frac{2}{c^2}\frac{D_d D_{ds}}{D_s}4\pi G\Sigma^{lens}(\vec{\theta}) = 2\frac{\Sigma^{lens}(\vec{\theta})}{\Sigma_{cr}} = 2\kappa(\vec{\theta}), \tag{4.20}$$

where I used the definition of Σ_{cr}. Note that in a generic modified gravity scenario Σ^{lens} is not related to the usual Newtonian potential since $\Phi_{lens} \neq \Phi_N$; nonetheless, I have already discussed that for some classes of models with a particular conformal structure (such as $f(R)$) the lensing potential coincides with the Newtonian potential due to a cancellation of the effects induced by additional degrees of freedom between Ψ and Φ.
The quantity $\kappa(\vec{\theta}) = \frac{\Sigma(\vec{\theta})}{\Sigma_{cr}}$ is called *convergence* and it describes an isotropic magnification of the source. In terms of κ, the effective potential can be derived solving eq. (4.20):

$$\psi(\vec{\theta}) = \frac{1}{\pi}\int \kappa(\vec{\theta'}) \ln|\vec{\theta} - \vec{\theta'}| d^2\theta'. \tag{4.21}$$

Let's now focus on the inverse of the magnification tensor, which gives the Jacobian of the mapping from the source to the image in the lensing process:

$$\mathcal{S}_{ij} = \frac{\partial \beta_i}{\partial \theta_j} = \mathcal{M}^{-1}.$$

Using the lens equation (eq. (4.13)) to replace β_i we obtain:

$$\mathcal{S}_{ij} = \delta_{ij} - \frac{\partial \alpha_i}{\partial \theta_j} = \delta_{ij} - \frac{\partial^2 \psi}{\partial\theta_i \partial\theta_j} = \delta_{ij} - \psi_{ij}, \tag{4.22}$$

where I have further substituted the definition of ψ in eq. (4.21). The quantity:

$$\psi_{ij} = \frac{\partial^2 \psi}{\partial\theta_i \partial\theta_j}$$

identifies the deviation from the identity induced by gravitational lensing. Using the components of $\mathcal{S}$, the convergence $\kappa(\vec{\theta})$ can be written as a combination of the diagonal elements:

$$\kappa = \frac{1}{2}(\psi_{11} + \psi_{22}) \equiv \frac{1}{2} tr(\psi_{ij}). \tag{4.23}$$

The other derivatives of the effective potential can be combined to introduce an object called *shear tensor* describing the degree of deformation of the image with respect to the source (see Figure 4.3):

$$\gamma_1(\vec{\theta}) = \frac{1}{2}(\psi_{11} - \psi_{22}) = \gamma(\vec{\theta}) \cos(2\phi(\vec{\theta})),$$

$$\gamma_2(\vec{\theta}) = \psi_{12} = \psi_{21} = \gamma(\vec{\theta}) \sin(2\phi(\vec{\theta})). \tag{4.24}$$

In the above equation $\gamma = \sqrt{\gamma_1^2 + \gamma_2^2}$ expresses the intensity of the distortion while the angle ϕ identifies the orientation in the lens plane. Combining now eq. (4.24) with eq. (4.23), the inverse magnification tensor becomes:

$$\mathcal{S} = \begin{bmatrix} 1 - \kappa - \gamma_1 & -\gamma_2 \\ -\gamma_2 & 1 - \kappa + \gamma_1 \end{bmatrix} =$$

$$(1 - \kappa) \begin{bmatrix} 1 & 0 \\ 0 & 1 \end{bmatrix} - \gamma \begin{bmatrix} \cos 2\phi & \sin 2\phi \\ \sin 2\phi & -\cos 2\phi \end{bmatrix} \tag{4.25}$$

The scalar magnification μ is now given by the determinant of the magnification tensor:

$$\mu = \det \mathcal{M} = \frac{1}{det\mathcal{A}} = \frac{1}{(1 - \kappa)^2 - \gamma^2}. \tag{4.26}$$

Thus, measurements of the convergence and of the shear are connected to the projected lensing potential and can be used to reconstruct the matter distribution of gravitational lenses. In the next section I will summarize the typical features of the so called strong and weak lensing regimes and how these effects are used to reconstruct mass profiles of galaxy clusters.

4.2 Mass profiles of galaxy clusters from lensing analyses

When considering gravitational lensing effects, two different classes of phenomena can be identified, namely strong and weak gravitational lensing. In the context of galaxy clusters, *Strong Lensing* (SL hereafter) classify all the effects associated with the production of multiple images of the same source. As already mentioned, typically this occurs when the surface den-

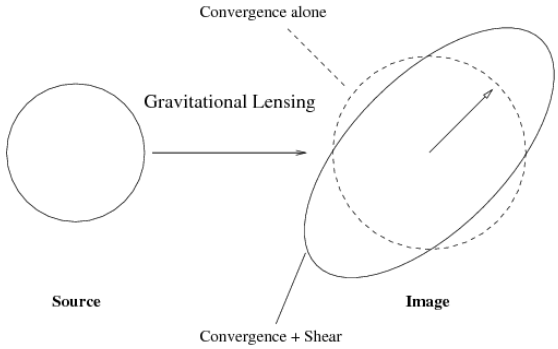

Figure 4.3: Effect of the lensing distortion on a circular source where the separate contributions of convergence $\kappa(\vec{\theta})$ (isotropic magnification) and shear $\gamma_{1,2}(\vec{\theta})$ (distortion of shape and orientation) are highlighted . Credits: ref. [165].

sity of the lens is larger than the critical density in some points (i.e. the lens is supercritical). In this case there exists critical curves γ_{crit} for which the determinant of $\mathcal{S}$, eq. (4.25), must be singular, meaning that the magnification diverges. The true angular positions $\beta(\gamma_{crit})$ of those curves with respect to the lensing map are called *caustics*. When a caustic has points with not defined derivatives (cusps), the image of nearby sources in the lens plane is strongly magnified and distorted, and generally it gives rise to spectacular giant arcs.
Note that, similarly to the caustics in the phase space of galaxies defined in Chapter 3, those curves are characterized by a quantity that tends to infinity.
Strong Lensing effects are observable in the innermost region of galaxy clusters and allow to infer the corresponding mass profile. Indeed, if one considers a caustic producing a tangential arc with respect to the lens center (tangential critical curves), it can be shown that for a spherically symmetric lens:

$$M(\theta) = \Sigma_{cr}\pi(\theta D_d)^2, \tag{4.27}$$

where $M(\theta)$ is the total projected mass enclosed within the radius $R = \theta D_d$. Despite its simplicity, eq. (4.27) illustrates the basic idea of SL mass profile reconstruction. A real mass distribution is actually asymmetric and a more detailed modeling of lensing effects is required (see e.g. ref. [171]), together with high-quality imaging and spectroscopic data to identify multiple images and arcs; Figure 4.4 from ref. [172] shows the spectroscopic confirmed multiple images for the galaxy cluster MACS 1206, obtained thanks to the combined information from CLASH and MUSE data (see also Chapter 5). Usually the mass profile is recovered assuming a parametric model (e.g. refs. [173, 35, 172]) and performing a Maximum Likelihood fit to constrain the free parameters. It is worth to notice that with excellent data sets available, SL

analyses allow not only to determine the overall cluster mass profile, but also to estimate the contribution of single substructures and clumps in the mass distribution near the cluster core (see e.g. ref. [174]).

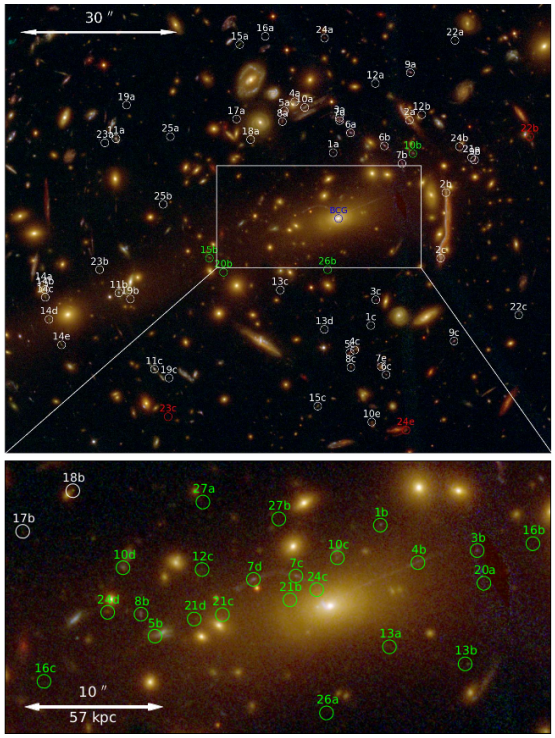

Figure 4.4: Multiple images in the core of the cluster MACS 1206 (green and white circles) spectroscopically identified by CLASH-VLT+MUSE programs observations. The image is obtained combining the information of 12 CLASH-*HST* filters. Credits: ref. [172].

The second class of lensing phenomena, named *Weak Lensing* (WL hereafter), groups all the smaller effects generated by light rays deflection in a gravitational field, which generally occur in galaxy clusters for distances from the center larger than the Einstein radius out to the outskirt. WL produces a set of weakly distorted images (typically ~ 50 objects per $arcmin^2$) called *arclets*. For each lensed galaxy the image is unique, so that the matrix $\mathcal{S}$ is always invertible, and the typical values of $\kappa, \gamma << 1$ In this case individual changes in the shape and magnitude of background sources due to the lensing mapping are much more difficult to detect, in particular for ground-based observations where the presence of turbulences in the atmosphere can change the value of the source ellipticity, totally masking the lensing distortion. Thus, mass profile reconstructions with WL analyses are performed using a statistical

approach. Considering that the average intrinsic ellipticity of galaxies is ~ 0.25 (e.g. ref. [175]) and assuming a random distribution for the orientations and intrinsic ellipticities of the unlensed sources, we can obtain the value of γ, by averaging over a large sample of galaxies.
In the case of a single isolated lens, the WL effect consists in an alignment of the lensed images in the tangential direction with respect to the lens. The resulting averaged tangential shear $< \gamma_t >$ can then be related to the surface density contrast of the matter distribution generating the gravitational lensing effects.
The first algorithm to infer the mass profile of clusters with WL analyses was developed by ref. [176] and it requires the knowledge of the shear components γ_1, γ_2 only to estimate the convergence as:

$$\kappa(\vec{\theta}) = \frac{1}{\pi} \int d^2\theta' \mathcal{R} \left[\mathcal{D}^*(\vec{\theta} - \vec{\theta'}) \Gamma(\vec{\theta'}) \right], \tag{4.28}$$

where

$$\mathcal{D}(\vec{\theta}) = \frac{(\theta_2^2 - \theta_1^2) - 2i\theta_1\theta_2}{|\vec{\theta}|^4}$$

is a convolution kernel and $\Gamma = \gamma_1 + i\gamma_2$ is the complex shear. Eq. (4.28) can be derived from the derivatives of the effective potential ψ_{ij}. More sophisticated methods combine complementary measurements of the magnification, which can be estimated for example from multi-band imaging data (see e.g. ref. [177]).

Gravitational lensing effects offer a powerful method to determine the mass distribution of a galaxy cluster independently of its dynamical state. Moreover, SL events, although they are certainly rarer than WL phenomena, allow to infer the density profile also in the very central region of clusters ($R \lesssim 0.1\,\mathrm{Mpc}$) with higher accuracy compared to other probes. Nevertheless, lensing analyses still suffer from several systematics, such as the contamination of cluster member galaxies in the lensing signal and the influence of surrounding large-scale structure which affects especially the outer regions; as I will discuss in Chapter 6, this second effect is one of the reasons to limit the analysis presented in this Thesis out to the cluster virial radius. As for SL, the number of multiple images used in the analyses as well as the number of spectroscopic redshifts available can significantly affect the accuracy in SL modeling (e.g. ref. [178]). Furthermore, it is worth to notice that the 3-dimensional mass profile is obtained by de-projecting the surface mass density, and thus it requires to make assumptions on the overall shape of the gravitational potential (such as spherical symmetry).
The general concepts introduced in this Chapter are the basis of the joint Strong and Weak

lensing mass profile reconstruction for the two galaxy clusters analyzed within this Thesis (see Chapter 5). As I will discuss in the next Part, the unprecedented level of precision reached in the determination of the two profiles - which is the key requirement for constraining tiny effects such as deviations from GR - relies on the excellent quality multi-band imaging data and spectroscopic data provided by the CLASH and CLASH-VLT collaborations.

Part III

Results

Chapter 5

Observational data sets

This Chapter is devoted to describe the two galaxy clusters whose data are used in this Thesis, namely MACS J1206.2-0847 (hereafter MACS 1206) at redshift $z = 0.44$ and RXC J2248.7-4431 (hereafter RXJ 2248) at $z = 0.35$; these objects were extensively analyzed as part of the Cluster Lensing And Supernova survey with Hubble (CLASH, ref. [23]) and the spectroscopic follow-up with the Very Large Telescope (CLASH-VLT, ref. [24]). Section 5.1 shortly describes the above mentioned programs, with particular emphasis on CLASH-VLT, which provided high-quality data-set of low and medium resolution spectroscopic redshifts for the cluster member galaxies, needed to obtain the input line of sight (l.o.s.) velocities in the *MAMPOSSt* procedure (see Chapter 3); in Section 5.2 and Section 5.3 I will introduce MACS 1206 and RXJ 2248, highlighting the properties of these two clusters which are relevant in view of the analysis presented in Chapters 6 and 7 .

5.1 The CLASH and CLASH-VLT programs

In August 2009, after NASA Service Mission 4 (SM4) of repairing and upgrading the Hubble Space Telescope (*HST*) concluded with the installation of the Wide Field Camera 3 (*WFC3*, see ref. [179]), a new class of *HST* surveys, called Multi-Cycle Treasury (MCT) Programs, was developed. In order to use the full potential of the improved instrument, more than 500 orbits of *HST* were allocated to allow projects aimed at reaching challenging scientific achievements by means of large observational time. The Cluster Lensing And Supernova survey with

Hubble (CLASH[1]) is one of three selected projects for the MCT program, approved in 2011 with Principal Investigator M. Postman; using 524 total orbits of the Hubble Space Telescope over 3 years of observations, CLASH collected high-quality panchromatic imaging data for 25 galaxy clusters. The sample, observed in 16 filters form the near-ultraviolet to the near-infrared with the *ACS* (Advanced Camera for Surveys) and the *WFC3*, encompasses a redshift range $0.15 < z < 0.9$ and a mass range from $\sim 5 \times 10^{14}\, M_{\odot}$ to $\sim 3 \times 10^{15}\, M_{\odot}$. The CLASH project accomplished four main goals:
(i) the study of the Dark Matter distribution in galaxy clusters at an extraordinary level of precision,
(ii) the analysis of the internal properties of galaxies in those clusters,
(iii) the identification of distant Type Ia Supernovae up to $z \sim 2.5$,
(iv) to find and analyze galaxies at very high redshift $z > 7$.
The 25 galaxy clusters were taken from the MAssive Cluster Survey (MACS) catalog (see e.g. ref. [180] and references therein) and from the Abell catalog (ref. [181]); 20 of these objects were selected from X-ray observations for their properties of apparent dynamical relaxation. In particular, they show a well-defined central surface brightness peak and an overall concentric distribution of the X-ray-emitting gas, with an average temperature $T_X \geq 5\,\mathrm{keV}$. Additional indications of a relaxed state for the clusters in this subsample come from the analysis of the X-ray pressure maps, which exhibit negligible departures from hydrostatic equilibrium; moreover, the projected distance of the Brightest Central Galaxy (BCG) from the X-ray peak is always less than 23 kpc. Fig. 5.1 show the X-ray images of the 20 relaxed clusters from the Archive of Chandra Cluster Entropy Profile Tables (ACCEPT[2]).
The other 5 clusters in the CLASH catalog were chosen as powerful gravitational lenses to magnify sources at very high redshift, since they are characterized by large values of the Einstein radius (from $35''$ to $55''$).

The CLASH-VLT VIMOS Large Programme is one of the follow-up of the CLASH project, approved in Period 86 (PI: P. Rosati) to carry out an exhaustive spectroscopic survey of 13 CLASH clusters observable from the Southern hemisphere. The 4-channel Visible Multi-Objects Spectrograph (VIMOS, ref. [182]), mounted on the ESO-Very Large Telescope in Chile, was used to collect data for a total of 225 hours of observation in order to achieve the

[1] http://www.stsci.edu/ postman/CLASH/Home.html
[2] //www.pa.msu.edu/astro/MC2/accept/

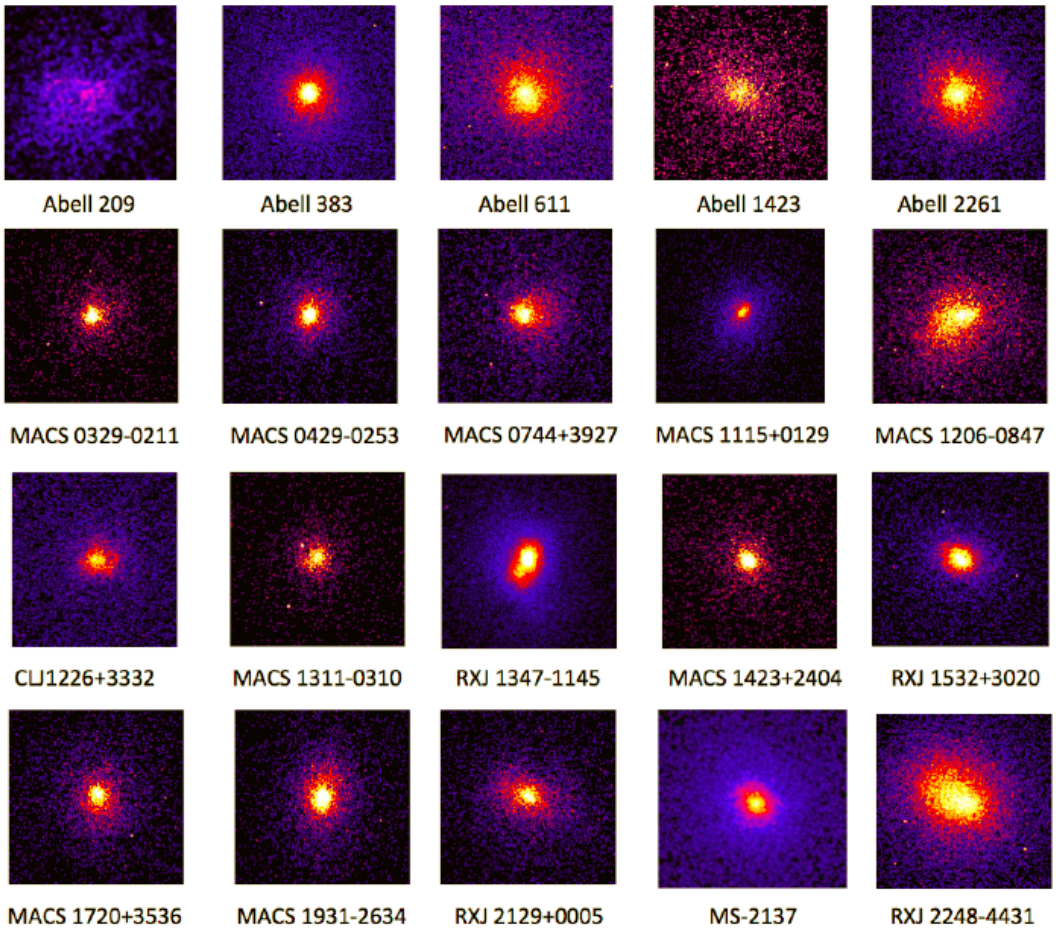

Figure 5.1: X-ray images from the ACCEPT catalog for the 20 X-ray selected clusters in the CLASH sample; each plot shows an area subtending an angle of $\sim 3.45\, arcmin^2$. From ref. [23].

following goals:
(i) Spectroscopically confirm at least ~ 500 member galaxies for every cluster, out to 2 times the virial radius in order to recover the mass profile from dynamical analysis with the same accuracy of the mass profile obtained by strong+weak lensing analysis;
(ii) Confirm the multiple imaging systems found by *HST* and the angular diameter distances for lensed sources by measuring the spectroscopic redshift of nearly 200 lensed galaxies in the cluster center;
(iii) Obtain a full high-quality set of multi-wavelength data to study galaxy population properties in different environments.
Observations were conducted using a combination of the VIMOS low resolution LR-blue grism and the medium resolution MR grism, in four pointings for each cluster, covering a total area between 15 and $20\, arcmin^2$); each pointing is chosen to have a different channel of the spectrograph aligned with the cluster central region.
The complete data-set also includes imaging data from the Suprime-Cam of the Subaru telescope for several clusters, and from ESO Wide Field Imager (WFI) for RXJ2248, which is the southernmost cluster in the sample. Fig. 5.2 from ref. [24] shows the distribution of galaxies of the cluster MACSJ0416-2403, in the field of view of Subaru/Sup-Cam R-band ($29 \times 25\, arcmin^2$). The red points are all the spectroscopically-confirmed cluster members (~ 900), whose redshift corresponds to rest-frame velocities (with respect to the median cluster redshift) $|v_{rf}| \leq 3000\, Km/s$; blue points indicate other galaxies in the redshift range $0.02 \leq z \leq 4.15$. The collection of spectroscopic redshifts was additionally used as a calibration of the photometric redshifts obtained by CLASH- HST. The joint information from VIMOS and from the 16-band HST photometry brought down the accuracy in redshift to $\Delta z/(1+z) \sim 0.03$, which is a key point for accurate lensing reconstructions.
CLASH + CLASH-VLT provides one of the best up-to-date combined imaging and spectroscopic data-set for single clusters, allowing for mass profiles reconstruction with unprecedented precision (see below); this is extremely important if one wants to investigate signatures of modification of gravity at clusters scales, which for any viable model should be very small in order to encompass all the cosmological and astrophysical constraints. Furthermore, such modest effects are in general systematics-dominated; an adequate control of the assumptions is required to obtain robust results. I will extensively discuss those points in the next Chapters.

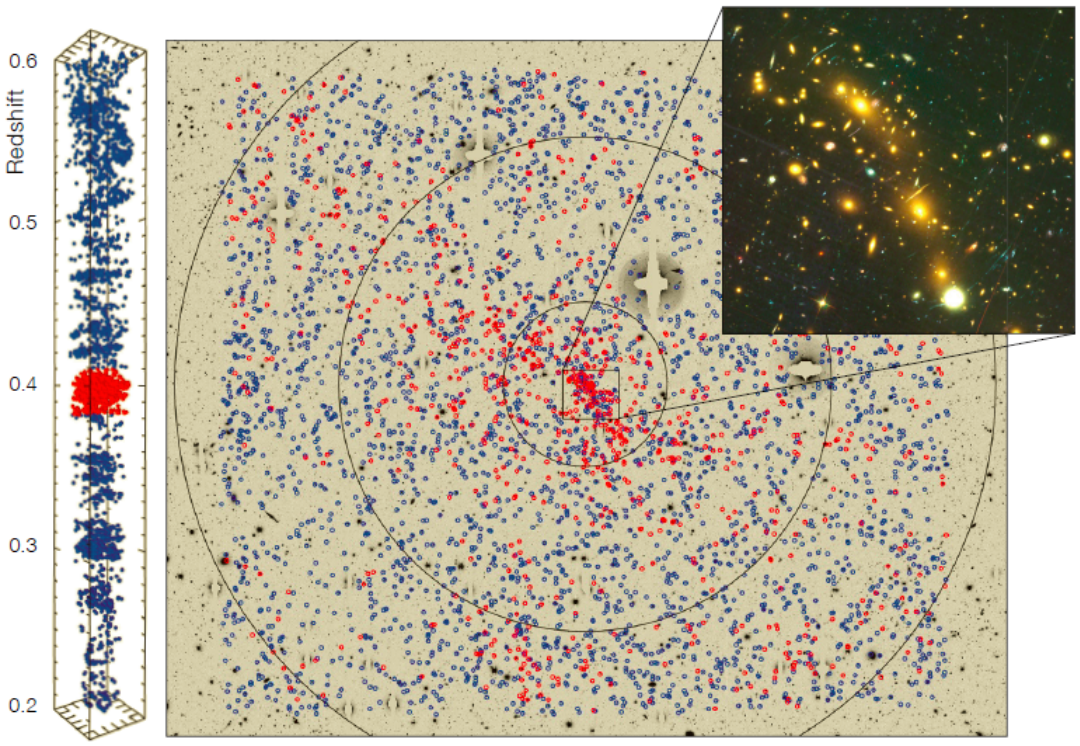

Figure 5.2: Main central plot: confirmed member galaxies (red points) of the cluster MACSJ0416-2403, analyzed within the CLASH / CLASH-VLT programs, in the field of view $29 \times 25\, arcmin^2$. Other 3307 galaxies in the range $z \in [0.02, 4.15]$ are shown as blue points.The black circles corresponds to region with projected radius of $1, 3$ and 5 Mpc centered on one of the two BCGs of the cluster. Right plot: zoomed-in ($1.8 \times 2\, arcmin^2$) view of the cluster core obtained by *HST* ACS-WFC3. Left plot: 3D redshift distribution in the range $0.2 \leq z \leq 0.6$ of the galaxies in the main plot. Credits: ref. [24].

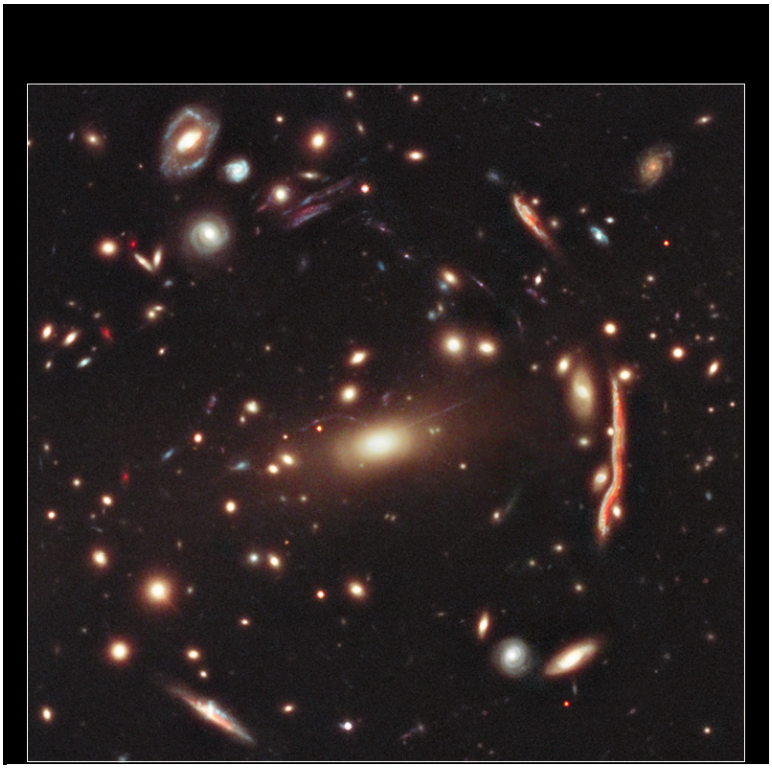

Figure 5.3: *HST* ACS+WFC3 composite image of MACS 1206. The field of view is $65 \times 65\, arcsec$, centered on the BCG. Credits: NASA, ESA, M. Postman (STScI), and the CLASH Team .

5.2 MACS 1206

The galaxy cluster MACS 1206, located at redshift $z = 0.44$, is one of the 20 X-ray selected clusters observed as part of the CLASH survey. In Fig. 5.3 I show the composite image of the cluster from *HST* ACS+WFC3 observations in a field of view $65 \times 65\, arcsec^2$.

MACS1206 appears as a large-scale relaxed object with a few minor overdensities in the two-dimensional distribution of the member galaxies (ref. [183]). This result is also supported by the analysis of ref. [184], that does not find a significant level of substructures within the cluster when the most conservative selection is used to assign the membership of cluster galaxies. The concentric distribution of the mass components (stellar, gas and dark matter, see ref. [26]) further point to a relaxed status of the cluster (see also ref. [185] who demonstrate that the projected separation of the BCG and the X-ray emission peak is a robust indicator of a system's dynamical state). Moreover, the kinematic mass profile determination is in agreement with the analysis based on the *Chandra* X-ray observations under the assumption of hydrostatic

equilibrium. As discussed in Chapter 3, mass profiles based on hydrostatic equilibrium of the intra-cluster medium and on the Jeans' equation are both sensitive to the time-time component of the metric, but they feel the lack of equilibrium in different ways. Therefore, the consistent results obtained by these methods suggest that the cluster is in an equilibrium configuration (i.e. dynamically relaxed).

A first strong lensing analysis of MACS1206 was carried out in ref. [171] using 50 multiple images of 13 background lensed galaxies. An upgrade of this analysis was presented in ref. [26], exploiting a combination of strong lensing information with weak lensing shear and magnification measurements from *Subaru* multi-band images. Taking advantage of high purity sample of background galaxies derived from extensive multicolor and spectroscopic information, a robust measurement of the cluster mass density profile was obtained out to $\sim 2\,\mathrm{Mpc}$. In the radial region between 0.3 and $0.4\,\mathrm{Mpc}$, the mass profiles derived from strong lensing and weak lensing shear and magnification analyses have been shown to be consistent with each other. The resulting mass profile is parametrized according to the Navarro-Frenk-White model. Additional lensing analyses of the CLASH clusters involving also MACS 1206 were carried out by refs. [87, 89, 186, 35]; for the first part of this Thesis, presented in Chapter 6, I refer to the joint Strong+Weak lensing analysis of ref. [26]. For the second part (see Chapter 7), I used the updated results of [35], that refined the shear-and-magnification weak-lensing analysis of ref. [89] by including *HST* strong-lensing information for a sample of 20 CLASH clusters inclusive of MACS 1206. The weak+strong lensing results take into account model-dependent systematics of their strong-lensing modelling. Their error analysis also accounts for the intrinsic variations of the projected cluster lensing signal due to variations in cluster asphericity and the presence of correlated halos (see ref. [186]).

The measurement of the kinematic mass profile is presented in ref. [25] using spectroscopy information from the CLASH-VLT project (ref. [24]). Observations with VLT/VIMOS led to a total of 2749 galaxies with reliable redshift measurements in the cluster field. After the rejection of interlopers, 592 cluster members were identified. The sample was then analyzed in the projected phase-space with the *MAMPOSSt* method, presented in Chapter 3, that solves the Jeans' equation, eq. (3.27), to provide a maximum likelihood fit for the parameters of different mass models out to the virial radius ($\sim 2\,\mathrm{Mpc}$). In eq. (3.27) the galaxy number density $\nu(r)$ is parametrized as a NFW model (see eq. (1.34)):

$$\nu(r) \propto \frac{1}{(1 + r/r_\nu)^2 r/r_\nu},$$

characterized by a scale radius $r_\nu = 0.63^{+0.11}_{-0.09}$ Mpc, obtained by fitting the projected distributions of the member galaxies $n(R)$ (see Chapter 7; σ_r indicates the radial velocity dispersion. The kinematic analysis also requires modeling the velocity anisotropy profile $\beta(r)$ of the tracers of the gravitational potential,due to the well-known mass-anisotropy degeneracy. In the original analysis of ref. [25] three models for $\beta(r)$ were considered, the "Tiret" model of eq. (3.34), the "O" model of eq. (3.35), and constant anisotropy with no radial dependence, eq. (3.32). As already discussed in Section 3.3, the parameter r_c is assumed to coincide with the scale radius r_s of the NFW mass profile. In fact, ref. [152] proved that with this value of r_c the “O" and “T" models provide a good fit to the average anisotropy profiles predicted by a set of cosmological simulations of galaxy clusters.

The NFW model gives the highest likelihood fit to the kinematic data for the mass profiles reconstructed with the MAMPOSSt method, and in combination with the anisotropy "O" model it gives the smallest product of the relative errors in the two free parameters r_s and r_{200}. Fig. 5.4 shows the projected mass profiles of MACS 1206 obtained with different method: strong+weak lensing analysis from ref. [26] (red and yellow band), dynamics analysis (gray+ green bands) of ref. [25] and the best fit X-ray hydrostatic mass from Chandra (blue dashed line). The overall excellent agreement between independent data-sets and mass profile determinations is an additional indicator of the relaxed state of the cluster; moreover, it suggests that the application of our method to constrain the anisotropic stress $\eta(r)$ (see Chapter 6) should provide bounds consistent with standard gravity $\eta = 1$.

5.3 RXJ 2248

The galaxy cluster RXJ 2248 at redshift $z = 0.35$ (first identified as Abell S1063 in ref. [181]) is another object from the sample of the 20 X-ray selected clusters for their apparent properties of dynamical relaxation. The *HST* combined image is shown in Fig. 5.5. Given the large mass of the cluster at a relatively high redshift, many lensing analyses have been performed: for the strong lensing analysis refs. [187, 188, 189, 186, 146], and for the weak lensing analyses refs. [190, 89, 191, 192, 35]. The strong lensing mass profile used in this Thesis is an improvement of the one presented in [146].They used a combination of 22 strong lensing models on a data set of 47 multiple images belonging to 16 families in a redshift range of $[0.1 - 6]$ detected down to $m_{F814W} = 26$. This data-set comes from the *HST* imaging, the spectroscopy with VIMOS-VLT, and obtained during the MUSE-VLT science verification programme (ID 60.A-

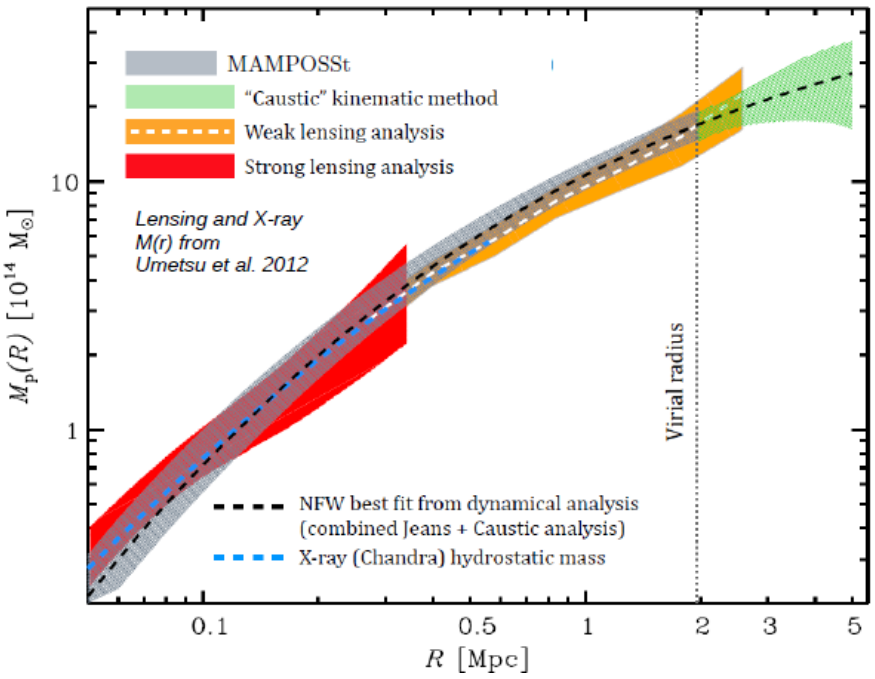

Figure 5.4: Projected mass profiles for the galaxy clusters MACS 1206. Strong lensing analysis: red band. Weak lensing analysis: yellow band and white dashed line (best fit). Dynamics analysis: gray and green areas, black dashed line (best fit). Chandra X-ray analysis: blue dashed line. All shaded regions corresponds to 1σ confidence level. From ref. [24].

Figure 5.5: *HST* WFC3+ACS image of the galaxy cluster RXJ 2248 in a field of view of $2.07 \times 2.32\,arcmin^2$

9345, P.I.:K. Caputi). As in the case of MACS1206, the results I will present in Chapter 7 are derived using the weak lensing analysis of ref. [35] that combine weak lensing shear and magnification information from WFI 2.2m images out to $\sim 2.5\,\mathrm{Mpc}$. I use the weak lensing information together with the strong lensing one from ref. [146]. The combined mass profile is parametrized with a NFW model.

As for the kinematic analysis I refer to the results obtained in Sartoris et al (in prep.) In this analysis they use a sample of 1233 galaxy members selected among more than 3700 galaxies with spectroscopic redshift provided by the VIMOS and MUSE observation out to $\sim 5\,\mathrm{Mpc}$. The MAMPOSSt technique has been applied using several anisotropy and mass profile models. Sartoris et al. find that the best combination of models is the NFW mass profile with a Tiret (eq. (3.34)) velocity anisotropy model.

According to ref. [193], RXJ 2248 has undergone a recent off-axis merger. However, moderately deep X-ray Chandra (ref. [146]) observations do not show evidence of massive substructures in the inner region, but only a regular elongated shape, orientated like a large scale filament (ref. [192]).

Chapter 6

Model-independent constraints on GR violation

In this Chapter I combine high-precision dynamic and lensing measurements of the total mass profile of the galaxy cluster MACS J1206.2-0847 to estimate the value of the ratio $\eta = \Psi/\Phi$ between the two scalar potentials in the linearly perturbed FLRW metric.

As anticipated in Chapter 1 and Chapter 2, an accurate measurement of the anisotropic stress η, could show possible, interesting deviations from the predictions of the theory of General Relativity, according to which Ψ should be equal to Φ. In Part II was pointed out that whereas the mass profile derived from the analysis of the dynamics of the members galaxies tracks only the time-time part of the perturbed metric (i.e. only Φ), the lensing mass profile reflects the contribution of both time-time and space-space components (i.e. the sum $\Phi + \Psi$). I thus express η in terms of the mass profiles and perform the analysis over the radial range $0.5\,\mathrm{Mpc} \leq r \leq r_{200} = 1.96\,\mathrm{Mpc}$ to provide new model-independent constraints of MG at cosmological scales. Both mass distributions are parametrized with a spherical Navarro-Frenk-White profile, which gives the highest probability from the fit to data (see Section 5.2); I consider the effect of assuming different functional forms for mass profiles and of the orbit anisotropy in the kinematic reconstruction as possible sources of systematics. The results shown in this Chapter, which are published in ref. [22], highlight the potential of this method to detect deviations from GR, while calling for the need of further high-quality data on the total mass distribution of clusters and improved control on systematic effects. Within this Chapter and the next one I assume a background ΛCDM model with $\Omega_m = 0.3$ for the matter density parameter and $H_0 =$

70 km s^{-1}Mpc^{-1} for the present-day Hubble constant; note that the derived constraints do not depend on the specific cosmology chosen, which is used only to convert observed angular scales into physical scales.

6.1 $\eta(r)$ from galaxy cluster mass profiles

As discussed in the previous Chapters, the spacetime geometry around a galaxy cluster is described by a linear perturbation to the FLRW metric, which can be written in the conformal Newtonian gauge, eq. (1.31), in terms of two gauge-invariant scalar quantities, the Bardeen potentials Φ and Ψ. In Section 1.2.1 I showed that the perturbed metric is related to the perturbation in the matter and energy content through the linearized Einstein's field equations which, in the absence of anisotropic stresses ($\Pi = 0$), lead to the condition that $\Phi = \Psi$. We thus define the anisotropic stress in configuration space $\eta(x)$ as the ratio $\Psi(x)/\Phi(x)$, where $x \equiv x^{\mu}$ are the spacetime coordinates; a deviation of this parameter from the value $\eta = 1$ indicates a violation of the Einstein's equations, i.e. a deviation from standard gravity.

In the following analysis, I carry out an observational determination of η by using the cluster mass profiles obtained from measurements of the velocity dispersion of the cluster galaxies and from combined strong and weak lensing measurements. These two methods to infer mass profiles from observational data are connected to the gravitational potentials in different ways. The motion of the galaxies in a cluster is determined by the metric time-time component $g_{00} = -(1 + 2\Phi/c^2)$, since their typical velocities, $\sim 10^3\,\mathrm{km\,s^{-1}}$, are non-relativistic. For example, in the case of the cluster MACS 1206, the velocity dispersion along the line of sight has been measured by ref. [25] $\sigma_{LOS} = 1087^{+53}_{-55}\,\mathrm{km\,s^{-1}} \ll \mathrm{c}$.
The Bardeen potential Φ is related to the source term by the (0,0) component of the Einstein's equations, which in this context is simply given by the Poisson equation

$$\nabla^2\Phi = 4\pi G\delta\rho_{dyn}\,, \tag{6.1}$$

where $\delta\rho_{dyn}$ is the effective dynamical mass density profile, which in Furier space is given by

$$\delta\rho_{dyn}(k) = Y(k,a)\delta\rho(k). \tag{6.2}$$

In the above equation, $Y(k,a)$ expresses the modification in the Poisson equation defined in eq. (2.11). It is worth to stress that in this first analysis I do not assume any parametric form

for Y, since I am only interested in constraining generic deviation from GR.
As for lensing mass profile, in Chapter 4 I introduced the lensing potential as $\Phi_{lens} = (\Phi + \Psi)/2$. from which it is possible to define an effective density field $\delta\rho_{lens}$ through the Poisson equation:

$$\nabla^2\Phi_{lens} = 4\pi G\delta\rho_{lens}\,. \tag{6.3}$$

Under the assumption of spherical symmetry one can integrate eq. (6.1) and eq. (6.3) over a sphere of radius r, thus obtaining

$$\frac{d}{dr}\Phi(r) = \frac{G}{r^2}M_{dyn}(r), \tag{6.4a}$$

$$\frac{d}{dr}\left[\Phi(r) + \Psi(r)\right] = \frac{2G}{r^2}M_{lens}(r)\,. \tag{6.4b}$$

In the above equations, $M_{dyn}(r)$ and $M_{lens}(r)$ are the total dynamic and lensing effective masses enclosed within a sphere of radius r. Combining eq. (6.4a) and eq. (6.4b) and integrating once more with respect to r, I derive the relation between the ratio of the Bardeen potentials and the cumulative mass profiles:

$$\eta(r) \equiv \frac{\Psi(r) - \Psi(r_0)}{\Phi(r) - \Phi(r_0)} = \frac{\int_{r_0}^{r} \frac{G}{r'^2}\left[2M_{lens}(r') - M_{dyn}(r')\right]dr'}{\int_{r_0}^{r} \frac{G}{r'^2}M_{dyn}(r')dr'}. \tag{6.5}$$

Here $\Phi(r_0)$ and $\Psi(r_0)$ are two integration constants that one can set equal to zero using the freedom in the definition of the potentials.

6.2 Results

In this section I discuss the application of eq. (6.5) to compute the anisotropic stress $\eta(r)$ for MACS 1206, using the lensing and kinematic mass profiles considered above. In our analysis, I integrated the mass profiles in the radial range $[r_0, r_{200}]$, with $r_0 = 0.55\,\mathrm{Mpc}$ and $r_{200} = 1.96\,Mpc$, where the latter is the best-fit value as obtained from both the kinematic and lensing analysis of refs. [25, 26]. At larger radii, dynamical equilibrium cannot be reliably assumed, and therefore the Jeans' equation can no longer be used to infer the gravitational potential. Moreover, at such large radii, the lensing masses become less reliable, as the weak shear signal becomes increasingly contaminated by large-scale structure filaments that might

affect the recovered mass profiles.

In spite of MACS 1206 global behavior (see Section 5.2 of Chapter 5), in the innermost regions ($r \leq 0.5\,\mathrm{Mpc}$) we do not have sufficient information to establish whether the central core is dynamically relaxed and to confirm the validity of the spherical symmetry assumption. In fact, *Chandra* X–ray observations of MACS 1206 show an inner entropy profile (see ref. [194]) which is higher than expected for a relaxed cool core cluster, thus indicating a dynamically active core. Moreover, optical photometric observations in the cluster central region ($R \lesssim 0.1\,\mathrm{Mpc}$), presented in ref. [195], show evidence for a distribution of the intracluster light (ICL) which is asymmetric with respect to the position of the BCG, with an elongation in the direction of the second brightest cluster galaxy. This suggests the presence of a tidal interaction between these two central galaxies, further questioning dynamical relaxation to hold in the central region of MACS 1206.

In this analysis I consider four parameters: r_{-2} and r_{200}, derived from the dynamics analysis in ref. [25] and r_{-2} and r_{200} derived from the lensing analysis by ref. [26][1]. For the dynamic mass profile, following ref. [25], I adopt the combination of the NFW profile, eq- (2.20), and the "O" model of eq. (3.35) for the orbit anisotropy ("NFW+O" hereafter) as the reference model, as obtained considering the scale radius of the number density profile $r_\nu = 0.63\,\mathrm{Mpc}$. In order to propagate the statistical errors from the mass profile parameters to $\eta(r)$, and following the analysis of ref. [21], I repeated the calculation of $\eta(r)$ by Montecarlo sampling with 10^4 trials the two probability distributions in the (r_{-2}, r_{200}) parameter space, as provided by the dynamics and by the lensing mass reconstructions. The results of these trials are shown in Figure 6.1 for the three models of the mass profile considered in the analysis (see the discussion about systematics below). From left to right: NFW, Hernquist (eq. (6.6)) and Burkert (eq. (6.7)) profiles, with red and blue points for the dynamics and lensing, respectively. As discussed in ref. [21], the joint distribution of the (r_{200}, r_{-2}) parameters from the kinematic analysis has nearly zero covariance, so the errors on these two characteristic radii are almost uncorrelated. On the other hand, the joint probability distribution of the parameters from the lensing analysis can be assumed to be a bi-variate Gaussian with covariance between r_{-2} and r_{200}. As expected, the iso-probability contours in the (r_{200}, r_{-2}) plane are almost elliptical in this case (see Figure 6.1). In Figure 6.2 I plot the results for $\eta(r)$ as a function of the distance from the center, r. For the reference analysis based on the NFW+O mass model, I show the

[1] In this Chapter I refer to r_{-2} instead of r_s in order to have a quantity which can be compared among different mass profile models. Indeed, $r_{-2} \neq r_s$ for Burkert and Hernquist profiles

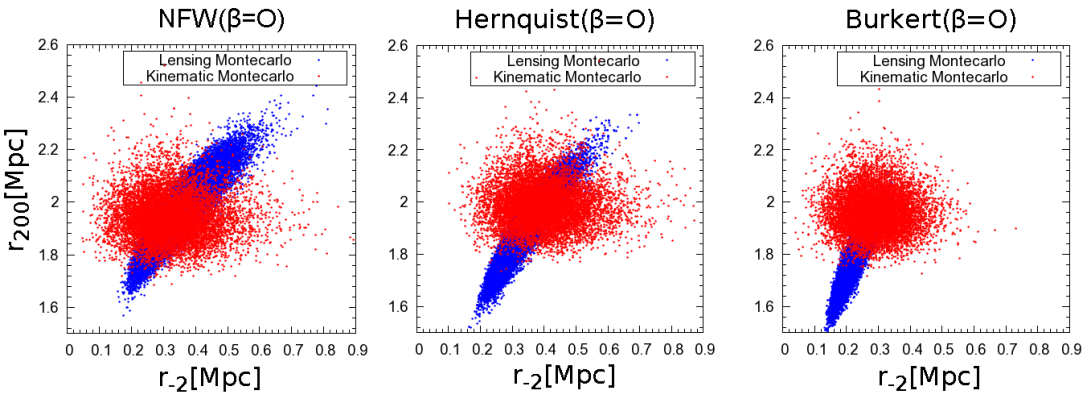

Figure 6.1: Results of the 10^4 Montecarlo simulations generated by sampling the joint probability distribution of r_{200} and r_{-2} from the dynamics analysis (red points) and from the combination of strong and weak lensing analyses (blue points). Left panel: NFW mass model of ref. [33]; central panel: Hernquist mass model of ref. [196]; right panel: Burkert mass model of ref. [197].

results in the range $0.55 - 1.96$ Mpc with the red solid line, along with the corresponding 68% C.L. (orange shaded area). The effect of starting the integration of the mass profiles in eq. 6.5 from a smaller radius, namely $r_0 = 0.07$ Mpc, is shown by the black dashed curve, with the yellow area marking the corresponding 68% C.L. The errors increase when using information from the cluster central region where the mass profile derived from strong-lensing has larger errors than the one obtained from weak-lensing (see Figure 13 of ref. [25]). Here the errors in the strong-lensing regime are dominated by model-dependent systematic uncertainties [26, 186]. The weaker constraint affects all the η profile by virtue of the correlation between errors at different radii. I also notice that the median values of $\eta(r)$ are slightly lower than those estimated when using $r_0 = 0.55$ Mpc. In both cases, the results are consistent with $\eta = 1$, thus with the predictions of GR.

Possible systematic effects could in principle affect the analysis. From an observational point of view, the cluster orientation and asphericity can affect both lensing and kinematic mass profile determinations. Ref. [183] found that the ellipticity of the galaxy distribution for MACS1206 is $\epsilon = 0.20^{+0.05}_{-0.06}$. Such value is low especially for a medium-z cluster compared with what found at low redshift by ref. [198] ($\langle\epsilon\rangle = 0.25 \pm 0.12$ in a sample 44 Abell clusters) and by ref. [199] ($\langle\epsilon\rangle = 0.4$ for a sample of 99 Abell clusters). Moreover, since the kinematic analysis is based on the Jeans equation and thus on the assumption that the cluster is in dynamical equilibrium, the presence of substructures could affect our results on η. However, as discussed in Chapter 5, MACS1206 do not show a significant level of substructures. In order

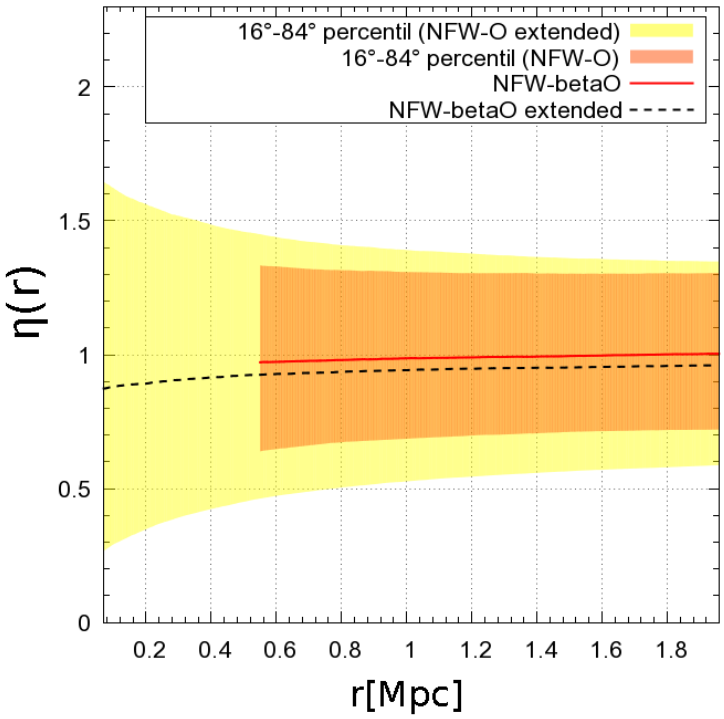

Figure 6.2: Constraints on the radial profile of the anisotropic stress $\eta(r)$ for the reference analysis based on the NFW parametrization of the density profile (see eq. (2.20)) and the O-model of eq. (3.35) for the orbit anisotropy. Results correspond to $r_0 = 0.55$ Mpc (NFW-betaO) and 0.07 Mpc (NFW-betaO extended) for the minimum radius down to which mass density profiles are considered. Solid red and black dashed curves show the median values of $\eta(r)$, while the narrower orange and broader yellow areas mark the corresponding 68 % C.L. regions.

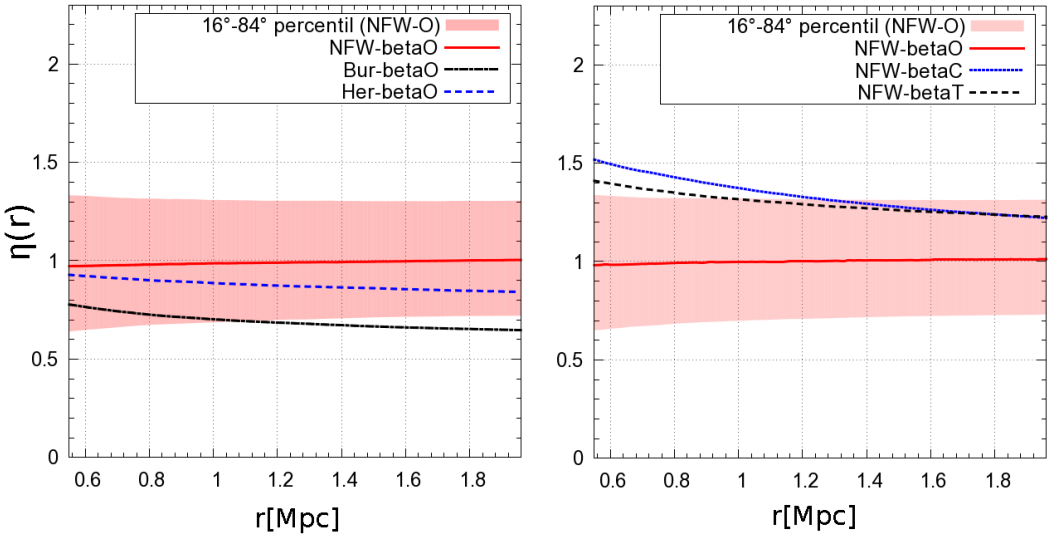

Figure 6.3: The effect of changing the reference model for the mass density profile (left panel) and the orbit anisotropy profile $\beta(r)$ (right panel) on the resulting constraints on the anisotropy stress profile $\eta(r)$. Here I assume $r_0 = 0.55$ Mpc. Left panel: three mass profile models with fixed anisotropy $\beta = "O"$. NFW model, ref. [33]: red solid curve; Hernquist model, ref. [196]: blue dashed curve; Burkert model, ref. [197]: black dash-dotted curve. Right panel: NFW mass profile for different anisotropy models. $\beta = "O"$: red solid curve; $\beta = "T"$: black dashed curve; $\beta = "C"$: blue dotted curve. In both panels the shaded area indicates the 68% C.L. errors for the reference NFW+O model.

to estimate the dependence of the $\eta(r)$ measurement eq. (6.5), on the kinematic mass profile used, I also consider the Hernquist (ref. [196], hereafter "Her") model:

$$M(r) = M_{200}\frac{(2r_{-2}+r_{200})^2}{r_{200}^2}\frac{r^2}{(r+2r_{-2})^2}, \tag{6.6}$$

and the Burkert (ref. [197], hereafter "Bur") model:

$$M(r) = M_{200}\frac{\left\{\ln[1+(r/r_B)^2]+2\ln(1+r/r_B)-2\arctan(r/r_B)\right\}}{\ln[1+(r_{200}/r_B)^2)]+2\ln(1+r_{200}/r_B)-2\arctan(r_{200}/r_B)}, \tag{6.7}$$

where $r_B \simeq \frac{2}{3}r_{-2}$. In Table 6.1, I summarize the kinematic mass models for which I derived constraints on η.

In Figure 6.3 I quantify the systematic effect on η obtained by changing all the mass and anisotropy models. I stress that all the kinematic mass and anisotropy profile combinations considered in this analysis have been proven in ref. [25] to provide acceptable fits and none of them is rejected by data. The same finding also holds for the mass profiles from the lensing analysis. In the left panel, I consider three different mass profiles (see also Table I) in both kinematic and lensing analysis, assuming in all cases $\beta =$ "O" for the orbit anisotropy. The solid, dashed and dash-dotted lines indicate the median values of the distributions for NFW, Hernquist and Burkert respectively, while the colored area indicates the 68% C.L. region for the NFW+O profile. I note that GR predictions are now slightly outside the 68% C.L. regions when using the "Bur" mass profile, thus underlining the importance of the adopted mass profile parametrization. However, it is worth to point out that the "Bur" model has been statistically disfavored by the ensemble mass profile derived from a stacked lensing analysis of the CLASH X-ray-selected sample, also including MACS J1206, based on strong–lensing, weak–lensing shear and magnification data [200].

In the right panel of Figure 6.3 I show $\eta(r)$ computed using the NFW mass profile and the three anisotropy profiles discussed in Section 5.2. The shaded areas indicate the 68% confidence regions for the reference model NFW+O while the solid, dashed and dotted lines represent the medians of the distributions. In this case, although the details of the results are sensitive to the anisotropy model adopted, the resulting η profiles always lie within the statistical uncertainties of the reference model (see also Table I).

As mentioned above, since η is obtained as a ratio of integrals depending on the mass profiles (see eq. 6.5), the errors at different radii are correlated. In fact, the determination of

Mass profile	β	η	$\Delta\eta(68\%C.L.)$	$\Delta\eta(95\%C.L.)$
NFW	O	1.00	$^{+0.31}_{-0.28}$	$^{+0.61}_{-0.54}$
NFW	C	1.22	$^{+0.45}_{-0.38}$	$^{+0.93}_{-0.68}$
NFW	T	1.23	$^{+0.33}_{-0.33}$	$^{+0.71}_{-0.61}$
Bur	O	0.65	$^{+0.26}_{-0.23}$	$^{+0.51}_{-0.44}$
Her	O	0.84	$^{+0.31}_{-0.28}$	$^{+0.66}_{-0.60}$

Table 6.1: Constraints on the anisotropic stress η for the different mass and anisotropy models. Column 1: mass model used (NFW: ref. [33]; Bur: ref. [197]; Her: ref. [196]). Column 2: model for the profile of orbit anisotropy as fitted in the kinematic mass reconstruction (O: eq. 3.35; T: eq. 3.34; C: constant β). Column 3: median values for η at r_{200}; Columns 4 and 5: errors at 68% and 95% C.L.

$\eta(r)$ at a fixed radius $\bar{r}$ is affected by the shape of the profile at $r < \bar{r}$. For this reason, I quote the values of η computed at $r_{200} = 1.96$ Mpc for all the models analyses, as reported in Table 6.1.

For the reference model (NFW with anisotropy profile 'O'), I obtain

$$\eta(1.96\,Mpc) = 1.00^{+0.31}_{-0.28}\,(\text{stat}) \pm 0.35\,(\text{syst}), \tag{6.8}$$

at 68 % C.L. where the systematic error is computed taking into account the variation in the median value of $\eta(r_{200})$, due to the different anisotropy and mass profiles used. As such, our analysis provides constraints on the anisotropic stress η which are fully consistent with the GR predictions.

6.3 Conclusions

In this Chapter I have presented a method to derive constraints on the anisotropic stress $\eta = \Phi/\Psi$ by comparing high-precision determinations of the total mass profiles of galaxy clusters from lensing and kinematic analyses. As a case study, I have applied this method to MACS 1206, a *bona fide* relaxed cluster at $z = 0.44$ with $M_{200} = (1.4 \pm 0.2) \times 10^{15}\,M_{\odot}$ (ref.[25]). Lensing masses for MACS 1206 have been derived by ref. [26] using the high-quality imaging

and photometric data obtained from HST and *Subaru* within the CLASH project. Kinematic mass profiles have been derived by ref. [25] thanks to intensive spectroscopic observations carried out within the CLASH-VLT program. Galaxy motions are sensitive only to the time-time component Φ of the metric perturbation, while lensing is sensitive to both the time-time and space-space components, i.e. to $\Phi + \Psi$. Therefore, a comparison of mass profiles based on these two independent methods allows one to set constraints on possible deviations from the prediction of General Relativity (GR), $\eta = 1$.

The results of this analysis can be summarized as follows.

- Comparing mass profiles over the range of radii from $r_0 = 0.55$ Mpc out to $r_{200} = 1.96$ Mpc, I find results to be consistent with the prediction of GR: $\eta(r_{200}) = 1.00^{+0.31}_{-0.28}$ at 68% C.L. for the reference analysis based on the NFW parametrization of the mass density profile and a specific model for the profile of orbit anisotropy.

- While the above errors refer only to statistical uncertainties, we also estimated the effects of systematic uncertainties related to changing the parametrization of the mass density and orbit anisotropy profile, as well as changing the minimum radius down to which mass profiles are considered. Within the range of models considered, these systematic uncertainties roughly double the uncertainty in the measurement of η.

- Interestingly, I find these constraints to be competitive with those obtained by combining expansion probes, cosmic microwave background anisotropies and large-scale structure observations (e.g., refs. [201, 1]). In particular, ref. [202] constrained the values of $\eta(z = 0)$ and $Y(z = 0)$; this analysis was based on WMAP-5 data combined with cosmic shear data from CFHTLenS and Integrated Sachs Wolf (ISW) data, taking into account also a possible time evolution of the two functions. They found $\eta(z = 0) = 0.98^{+0.73}_{-1.00}$ for $z_s = 1.0$ and $\eta(z = 0) = 1.30 \pm 0.35$ for $z_s = 2$, where z_s is a transition redshift at which the parameters smoothly change to their late time values, with uncertainties referring to 68% C.L.. In a similar way, ref. [203] obtained $-1.6 < \eta(0) - 1 < 2.7$ at 95% C.L. by combining CMB constraints from WMAP-5, Type-Ia SN from Union2, and cosmic shear data from CFHTLS and COSMOS surveys.

  Ref. [1] combined CMB data with different cosmological probes to study time- and scale-dependence of the modified gravity parameters η and Y, both extrapolated to $z = 0$, as already mentioned in Chapter 2. When the contribution of CMB lensing is included in the analysis, they obtain $\eta(z = 0) - 1 = 0.60 \pm 0.86$ for the scale-independent

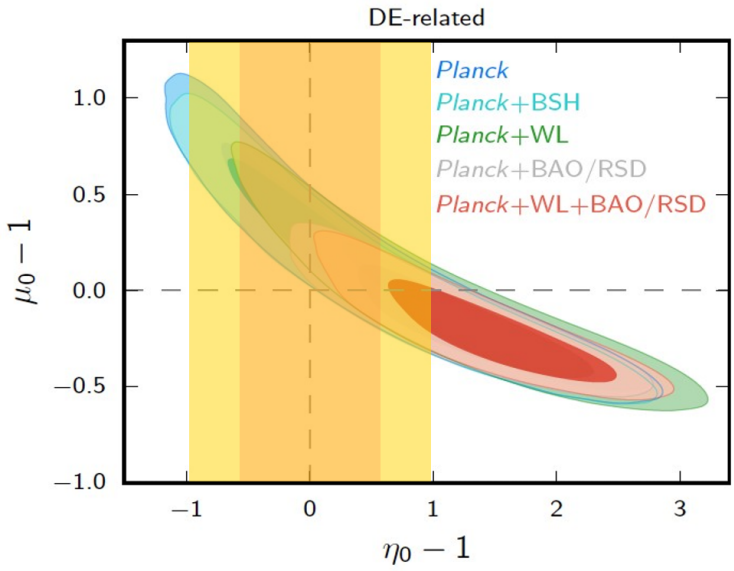

Figure 6.4: Comparison between the results of this analysis (yellow vertical bands) and joint constraints on $\eta(z=0), \mu \equiv Y(z=0)$ in the scale-independent case, obtained by ref. [1] (Fig. 14, left panel) combining CMB data, Baryonic Acoustic Oscillations, Redshift Space Distortions and Weak Lensing data. The inner darker yellow region refers to 1σ stat+syst uncertainties, while the lighter shaded area corresponds to 2σ confidence region.

determinations. They also show that the constraints become weaker when introducing the dependence on the scale.

In general, the results obtained are broadly consistent with the above constraints on deviations from GR, even if our method provides constraints only on η. The statistical uncertainty in the measurement of η is quite competitive with those obtained from CMB and large-scale structure probes. This can be seen in Figure 6.4, where I compare the bounds on $\eta(r_{200}, z=0.44)$ including also sytematics uncertainties (lighter and darker yellow regions) with the results on $\eta(z=0)$ and $\mu \equiv Y(z=0)$, shown in left panel of Figure 14 in ref. [1]. However, I emphasize once again that an accurate control of systematics in the analysis is mandatory for our proof-of-concept analysis to turn into an accurate and robust method to constrain modifications of gravity at the scales of galaxy clusters.

It is worth pointing out that the above results have been obtained from high-quality observational data of only a single galaxy cluster, thus highlighting the potential of using mass profiles of clusters as tools to probe the nature of gravity on cosmological scales. In principle, this

result should not surprise; as long as the cluster in consideration satisfies the main assumptions on which lensing and kinematic mass profiles are recovered, the precision of the derived constraints is only limited by the quality of observational data. Kinematic mass profiles are based on solving the Jeans equation for the projected phase-space distribution of cluster galaxies, assuming a spherically symmetric stationary system within which galaxies moves as tracers of the underlying potential. Even though the lensing mass profile do not rely on any assumption on the dynamical state of the cluster, its reconstruction still assumes spherical symmetry, as well as negligible contamination from the surrounding large-scale structure. In this respect, the choice of MACSJ 1206 for this case study is close to be optimal, given the overall appearance of this object as dynamically relaxed system.

MACSJ 1206 is only one of a dozen clusters of the CLASH-VLT survey for which data of comparable quality are available. The extension of this analysis to other clusters requires the combination of large redshift samples, high-quality weak and strong lensing data, as well as X-ray data on well selected clusters. A sample of at least 500 redshifts of member galaxies is needed for accurate dynamical mass profiles. Together with deep X-ray data, kinematic data are also needed to check whether the system is relaxed or whether other astrophysical systematics can play a significant role. As a complementary approach, applying the same analyses to realistic cosmological simulations of galaxy clusters should quantify the impact of systematics in the measurement of lensing and kinematic mass profiles, and, ultimately, their impact in precision tests of gravity at the scale of galaxy clusters. This aspect will be broadly discussed in Chapter 8.

Finally, it is important to notice that the analysis discussed in this Chapter does not take into account specific models of modified gravity. In order to better highlight how the bounds obtained on η compare with those derived from other cosmological probes - as well as to further investigate the constraining power of our method - it is interesting to recast them in terms of constraints on the free parameters of viable modified gravity theories.
In spite of these considerations, in the next Chapter I will focus on the specific class of $f(R)$ modified gravity models, performing a detailed kinematc mass profile reconstruction for the clusters MACS 1206 and RXJ 2248. I will then combine the information provided by the Strong+Weak lensing analyses of these two galaxy clusters to constrain the interaction range parameter λ defined in eq. (2.37).

Chapter 7

Constraints on $f(R)$ models

In this Chapter I apply the method of combining dynamics and lensing mass profile reconstructions, presented in the previous Chapter, to the specific case of $f(R)$ models of gravity; the results shown here have been published in ref. [36].

As already mentioned, the bounds on $\eta(r)$ obtained from the analysis of the galaxy cluster MACS 1206 are derived without assuming any parametrization for modified gravity; I now focus on the class of Horndeski models, for which the expression of the Bardeen potentials Φ and Ψ is given by eq. (2.23) and eq. (2.27) respectively, further restricting the analysis to $f(R)$ gravity, as a case study, where the only additional free parameter is the fifth force interaction range $\lambda = 1/m$. Using the modified version of the MAMPOSSt code introduced in Chapter 3, I perform a maximum likelihood fit to the phase-space data of the clusters MACS 1206 and RXC2248 to determine the total mass profile from dynamics in $f(R)$ framework. I assume a spherical Navarro-Frenk-White mass profile in order to obtain a constraint on λ for models in which the dependence of this parameter on the environment is negligible at the scale considered (i.e. $\lambda = const$). I then use information from lensing mass profile determinations to put a prior on the other NFW free parameters. As I will discuss, the joint kinematic+lensing analysis in the case of RXJ 2248 leads to a peculiar behavior that could in principle be explained in terms of modifications of gravity. The results are presented in Section 7.1. I will further show in Section 7.2 how the obtained constraints change when introducing a radial dependence in the interaction range (i.e. a screening effect), modeled with an analytical approximation. I discuss the impact of systematics and the limits of our analysis as well as future improvements of the results obtained in Section 7.3. This work has interesting implications in view of upcoming and

future large imaging and spectroscopic surveys, that will deliver lensing and kinematic mass reconstruction for a large number of galaxy clusters.

7.1 Results

In this section I present our results for the constraints on the interaction range λ obtained from the analysis of the galaxy clusters MACS 1206 and RXJ 2248.

I apply the *MAMPOSSt* method to constrain $\lambda = 1/m_{eff}$ using the parametric expression of eq. (2.23) for the gravitational potential in generic $f(R)$ models (i.e. setting the parameters as in eq. (2.43)) without screening, i.e. by assuming that the dependence of the environment of m_{eff} is negligible at the scales we are looking. In other words, I assume the screening radius to be much smaller - or much larger - than the cluster size. The situation could be also described in terms of a model with a strong screening mechanism where the effective mass of the scalaron remains always close to the minimum inside the overdensity.

For both clusters I include in the analysis data out to the virial radius, that is close to r_{200}, to ensure the validity of the Jeans equation. Moreover, the region below $r = 0.05\,Mpc$ is excluded since the internal dynamics of the Brightest Central Galaxy (BCG) becomes dominant (see e.g. ref. [161]).

7.1.1 MACS 1206

In the case of MACS 1206, for which 592 cluster members were identified in ref. [25], I use a sample of 345 galaxies, namely all the members lying within the radial range used in our analysis $[0.05\,\mathrm{Mpc} - 2.0\,\mathrm{Mpc}]$ in which I assume the Jeans' equation to be valid. The projected number density profile of the tracers $n(R)$ is fitted with a projected NFW (pNFW, ref. [204]) with a face value of the scale radius parameter $r_\nu = 0.63\,\mathrm{Mpc}^{+0.11}_{-0.09}$, as given by the Maximum Likelihood fit on the total sample of spectroscopic+photometric members (see Sect. 2.2 of ref. [25]).

I run the *MAMPOSSt* procedure in the modified gravity scenario with four free parameters, r_{200}, r_s, λ plus the velocity anisotropy parameter β. I use the "C" velocity anisotropy model (constant anisotropy with radius) as the reference model of the analysis, since it provides the highest probability in the *MAMPOSSt* fit in agreement with the GR results (see Table 2 of ref. [25])

In Figure 7.1 I show the marginalized likelihood distributions for the four free parameters

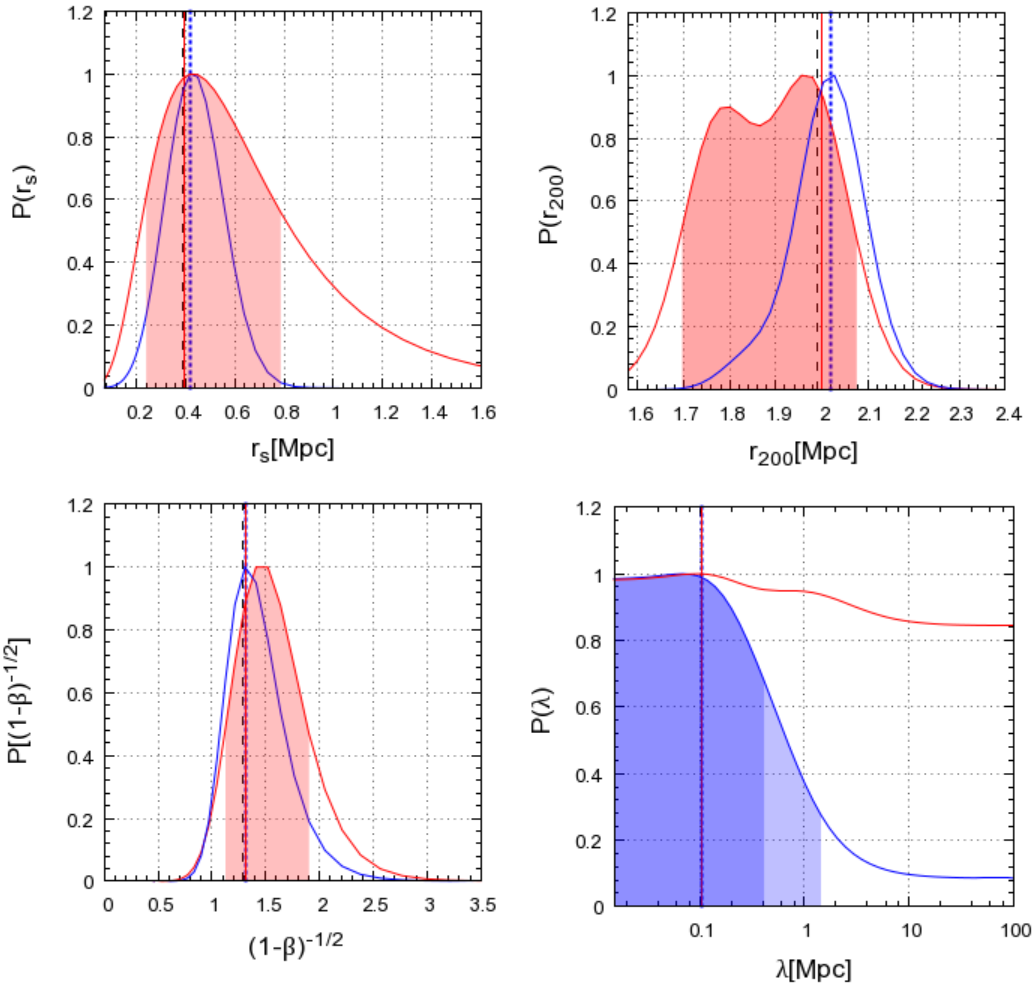

Figure 7.1: Results for MACS 1206. Marginalized likelihood distributions for the free parameters in the *MAMPOSSt* analysis obtained by integrating over the other three. Upper panels: r_s and r_{200}. Bottom panels: $\sigma_r/\sigma_\theta = 1/\sqrt{1-\beta}$ and $\lambda = 1/m_{eff}$. The red distributions are obtained from the kinematic analysis alone, while the blue curves show the joint lensing+kinematic results. Red and blue vertical lines represent the values corresponding to the maximum of the *MAMPOSSt* Likelihood and of $\mathcal{L}_{tot}$ respectively. Black solid lines are the best fit values of the GR analysis. Filled Red shaded areas in r_s, r_{200} and β indicate the 68% C.L. error from the dynamic analysis; the dark and light blue regions below the distribution of λ show the $\Delta\chi^2 = 1.0$ and the $\Delta\chi^2 = 2.1$ confidence intervals respectively.

in the case of $\beta(r) = const.$ As in ref. [25], I consider the quantity $\sigma_r/\sigma_\theta = 1/\sqrt{1-\beta}$ instead of β. The red curves are the results from the kinematic analysis while the blue curves represent the marginalized distributions when adding lensing information (see below). The vertical red solid lines indicate the best fit values given by *MAMPOSSt* for each parameter, compared with the GR best fit (black dashed lines). The red shaded regions in the r_s, r_{200} and β probability distributions show the 68% statistical errors. I obtain:

$$r_{200} = 2.00^{+0.08}_{-0.28}\,\mathrm{Mpc}, \qquad r_s = 0.39^{+0.40}_{-0.16}\,\mathrm{Mpc}, \qquad \beta \equiv \beta_C = 1.31^{+0.59}_{-0.19}, \tag{7.1}$$

at 68% C.L., consistent with the results of [25]. The constraints on the parameters r_s and β_C in GR are basically unaffected by the introduction of the modified gravity term in the dynamical analysis with the *MAMPOSSt* method. In the case of the virial radius r_{200} instead, the distribution tends to be wider with respect to the one obtained from the analysis of ref. [25], with a bimodal feature that, as explained below, is due to the degeneration with the interaction range λ.

From the red curve in the bottom right panel of Fig. 7.1 it can be seen that the distribution of λ from the dynamics alone is almost flat; in the limit of $\lambda \to 0$ (i.e. $m_{eff} \to \infty$) this is not surprising, since we are approaching the GR regime and the contribution of M_{mg} in eq. (2.23) becomes negligible. To give an example, for $\lambda \leq 0.05\,\mathrm{Mpc}$ the increase in the mass profile at $r = 0.3\,\mathrm{Mpc}$ due to the fifth force is $\sim 10^{-4}$, that is undetectable if compared to the modification induced by the statistical uncertainties in r_s and r_{200}.

More interesting is the case $\lambda \gg 1\,\mathrm{Mpc}$, associated with considerable deviations from GR. The flattening behavior of the curve for large λ is explained by looking at the degeneration directions in the two-dimensional distributions of Fig. 7.2. Each plot is obtained by marginalizing over the other two parameters; here the red and green lines indicate the dynamics contours at $\Delta\chi^2 = 2.3,\ 4.61$ (where $\chi^2 = -2\log[\mathcal{L}]$) respectively. As λ increases, the virial radius r_{200} tends to assume lower values, while the scale radius r_s shows only a slight change for $\lambda > 1$. This behavior is a consequence of the relatively small maximum gain (up to $1/3$) produced in the mass profile by the additional force in $f(R)$ gravity. In fact, the effect generated by the term M_{mg} for large values of λ can be compensated by suitably adjusting r_s (which determines the inner slope of the profile) and r_{200} (which is related to the total observed mass of the cluster) with respect to the GR values, so that the resulting modified mass profile becomes very close to the GR one. Physically, this means that in $f(R)$ gravity the galaxy dynamics is

altered in a similar way as the modification induced by a deeper potential well in GR, and even the high-quality data used are not sufficient to distinguish between the two cases.

The interaction range distribution shows a smooth peak at $\lambda = 0.1$ Mpc, corresponding to the best fit given by *MAMPOSSt*, but the excess of probability is statistically irrelevant; the presence of the peak is related to the degeneration between λ and r_s.

As discussed in Sect. 2.2, up to a conformal rescaling $(1 + f_{,R})^{-1}$, photons are affected only by the Newtonian contribution in $f(R)$ models. I thus can get additional information on the NFW parameters r_s and r_{200} by using the results of the gravitational lensing analysis presented in ref. [35].

In order to improve the derived constraints, I multiply the total likelihood distribution obtained by the *MAMPOSSt* method with the posterior probability distribution $P_{lens}(r_s, r_{200})$ given by strong+weak lensing analysis of [35] assuming flat prior in $\log(M_{200}),\ \log(c)$. Since the lensing distribution peaks at $r_s = 0.53 \pm 0.18$ Mpc, $r_{200} = 2.14 \pm 0.16$ Mpc[1], favoring larger values of the NFW parameters compared to the *MAMPOSSt* result (see left panel of Fig. 7.2), the final likelihood, defined as

$$\log(\mathcal{L}_{tot}) = \log(\mathcal{L}_{dyn}) + \log(P_{lens}), \tag{7.2}$$

explores a region in the parameter space that is in the orthogonal direction with respect to the degeneracy direction in the dynamical analysis, thus increasing the significance of small deviations from GR. The new two-dimensional contours at $\Delta\chi^2 = 2.3,\ 4.61$, obtained by including the lensing prior, are shown by the dark and light blue regions in Fig. 7.2, while the marginalized distributions of $\mathcal{L}_{tot}$ are plotted as the solid blue curves in Fig. 7.1. The blue vertical dotted lines in each panel correspond to the maximum of the total likelihood $\mathcal{L}_{tot}$ including lensing informations. Now I can put an upper limit, after marginalization, on the effective scalaron interaction range $\lambda \leq 0.49$ Mpc at $\Delta\chi^2 = 1.0$ (blue shaded area in the right bottom panel of Fig. 7.1) and $\lambda \leq 1.01\ Mpc$ at $\Delta\chi^2 = 2.71$ (light blue shaded area in the right bottom panel of Fig. 7.1), in agreement with the results presented in Chapter 6 which indicate negligible deviations from GR for this cluster.

The analysis discussed above has been performed for the best fit model, NFW and "C"

[1]Here the errors are estimated by approximating the distribution to a bivariate Gaussian around the maximum of the probability. Note that the maximum-likelihood values of r_{200} and r_s I find are slightly smaller than the values given in Table 2 of ref. [35]. This is because they quoted marginalized posterior constraints on the respective parameters obtained using the biweight location and scale estimators of ref. [205]

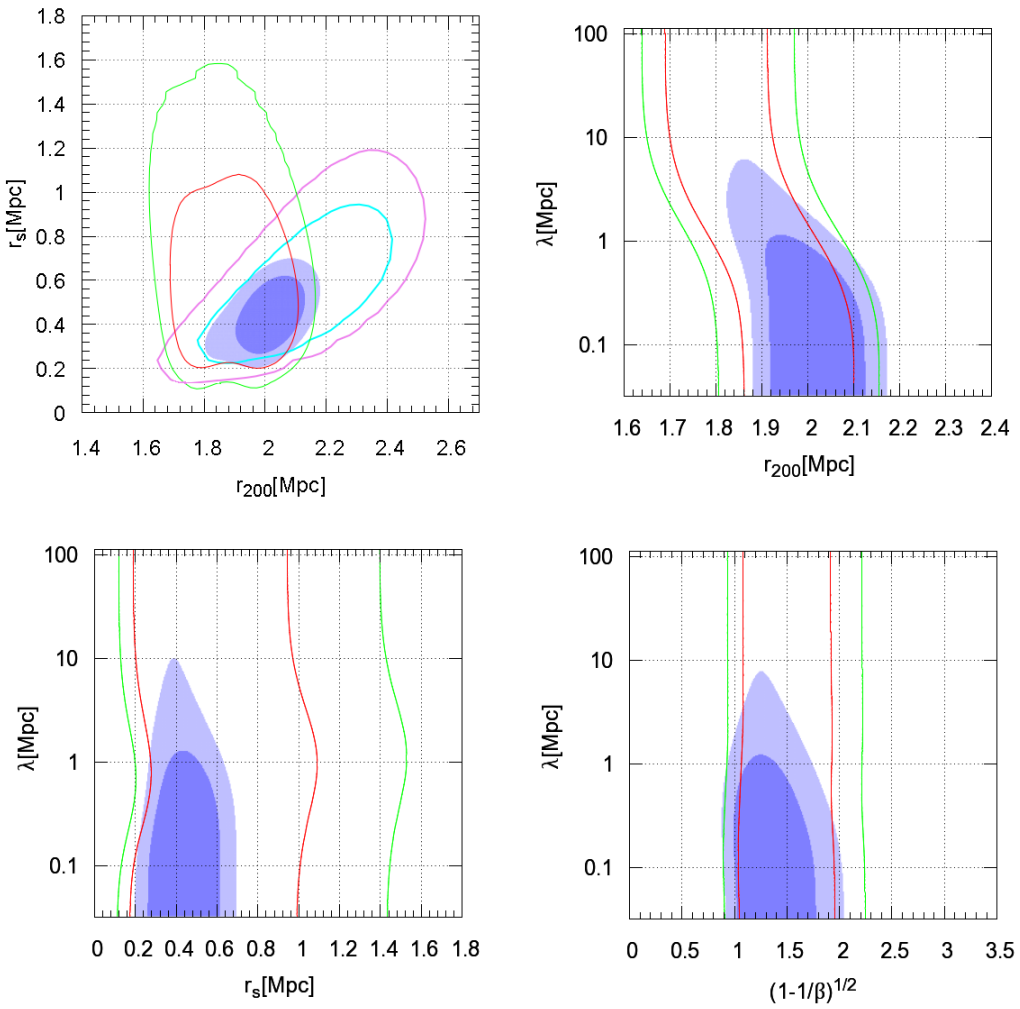

Figure 7.2: Results for MACS 1206. Two-dimensional likelihood distributions obtained from the dynamical analysis alone (red and green contours) and from the total likelihood with lensing contribution (dark and light blue shaded areas) after marginalization over the other two parameters. Upper panels: r_{200} vs r_s, r_{200} vs λ. Bottom panels r_s vs λ, β vs λ. The inner contours/shaded regions correspond to the points within $\Delta\chi^2 \leq 2.3$ from the maximum of the probability (roughly measuring the 68% C.L) while the outer contours/filled regions indicates points within $\Delta\chi^2 \leq 4.6$ (which represents the 90% C.L.). In the upper left panel the cyan and magenta lines show the $\Delta\chi^2 \leq 2.3$ and $\Delta\chi^2 \leq 4.61$ contours from the lensing analysis of ref. [35].

anisotropy profile in the dynamical analysis, by assuming a fixed value for the scale radius of the number density profile of the tracers r_ν as the best fit value given by ref. [25]. I can asses now by how much the constraints are affected by a change of the anisotropy profile and of the parameter r_ν . To this purpose, we repeat the analysis for the other two anisotropy models mentioned, "T" and "O"; moreover, for the reference model we run *MAMPOSSt* with r_ν set to the extremes of the 68% confidence region obtained by the GR analysis of ref. [25]. The results are summarized in the first 5 rows of Table 7.1 while the marginalized distributions are shown in Fig. 7.3 and Fig. 7.4.

In each plot of both figures the red lines are for the distributions obtained from the reference model "C" with $r_\nu = 0.63\,\mathrm{Mpc}$. In Fig. 7.3, the black dashed line shows the results for the "O" model, while the blue dotted curve is obtained from the "T" model. It is worth to notice that the best fit value of λ, as well as the position of the peak of the interaction range marginalized distribution, is not modified significantly by the different parametrization of the anisotropy profile. This is not surprising since λ is totally degenerate with β, as one can see from the right bottom plot of Fig. 7.2[2]. On the other hand, the shape of the distribution near the peak is affected by the changes in the anisotropy model. This is a consequence of the degeneration between λ and the scale radius r_s, which is responsible of the internal structure of the mass profile (right bottom panel of Fig. 7.2). In fact, the more the distribution in r_s is sharp, the more the peak in λ is evident. Fig. 7.4 shows the effect of changing r_ν within the 68% C.L. given by the GR analysis. The relatively small statistical uncertainties with which r_ν is known produce a negligible effect on the marginalized distributions of the free parameters in our analysis. The black dashed curves in each plot indicate the results for r_ν set at the upper limit of the 68% confidence region, while the blue dotted curves are for r_ν set to the lower value. It's interesting that this last case ($r_\nu = 0.54\,\mathrm{Mpc}$) produce a likelihood slightly higher than the best fit $r_\nu = 0.63\,\mathrm{Mpc}$ (see Table 7.1), but we stress again that the scale radius is obtained by a fit which is external to the *MAMPOSSt* procedure. The corresponding vertical lines indicate the values which maximize the likelihood $\mathcal{L}_{dyn}$.

To estimate the systematic uncertainties in our results on r_s, r_{200} and λ I take into account the variation caused by these changes. For the standard NFW parameters we obtain:

$$r_{200} = \left[2.00^{+0.08}_{-0.28}(stat) \pm 0.06(syst)\right]\,\mathrm{Mpc}, \tag{7.3}$$

[2]I verified that this statement remains valid for the other two models analyzed

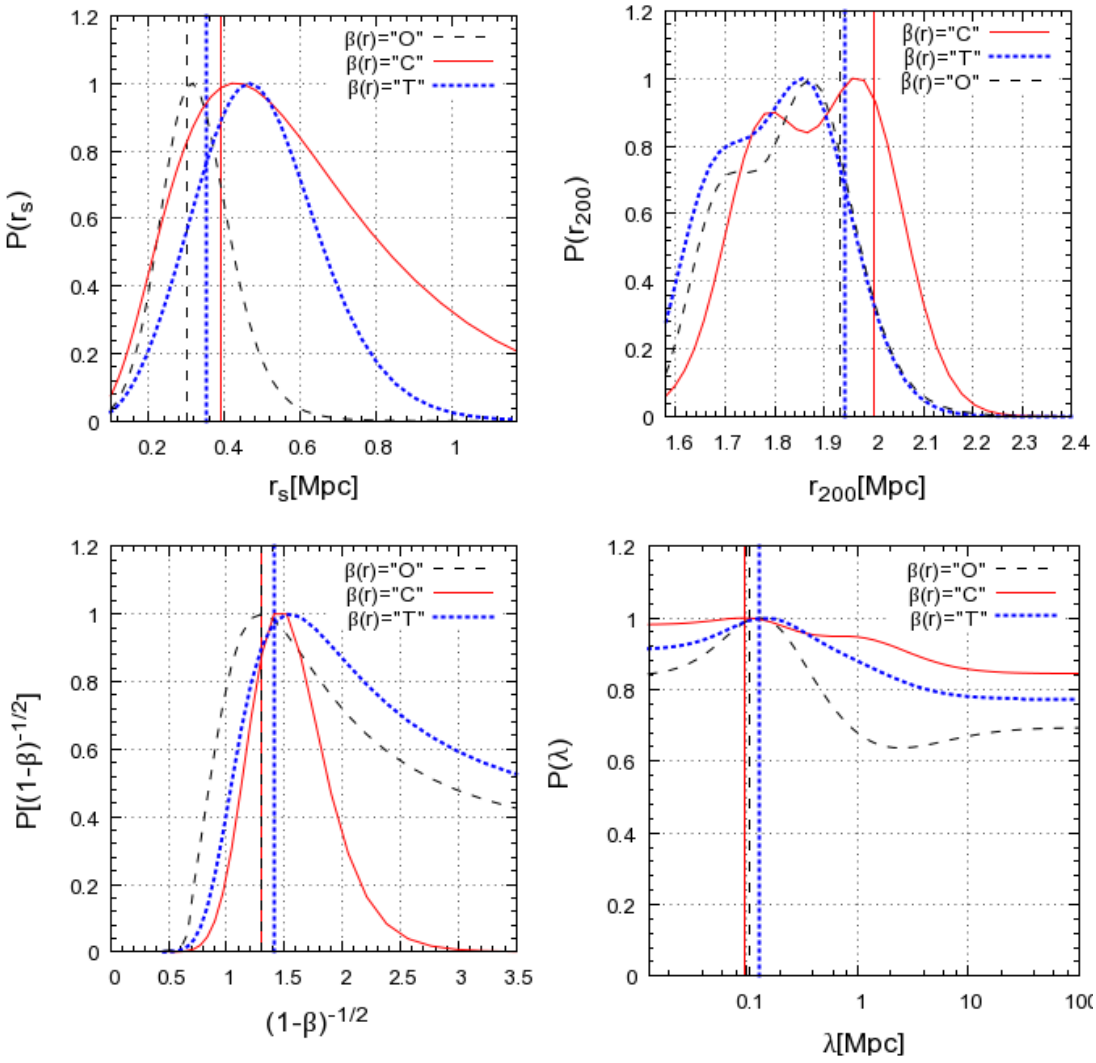

Figure 7.3: Results for MACS 1206. Marginalized likelihood distributions of r_{200}, r_s, $\sigma_r/\sigma_\theta = 1/\sqrt{1-\beta}$ and λ from the *MAMPOSSt* analysis obtained by changing the anisotropy model $\beta(r)$ for $r_\nu = 0.63\,\mathrm{Mpc}$. in the bottom left plot β indicates β_C for the "C" model and β_∞ for "T" and "O" models. Black dashed curves: "O" model. Red solid curves: "C" model. Blue dotted curves :"T" model. The corresponding vertical lines indicate the *MAMPOSSt* best fit of each free parameter.

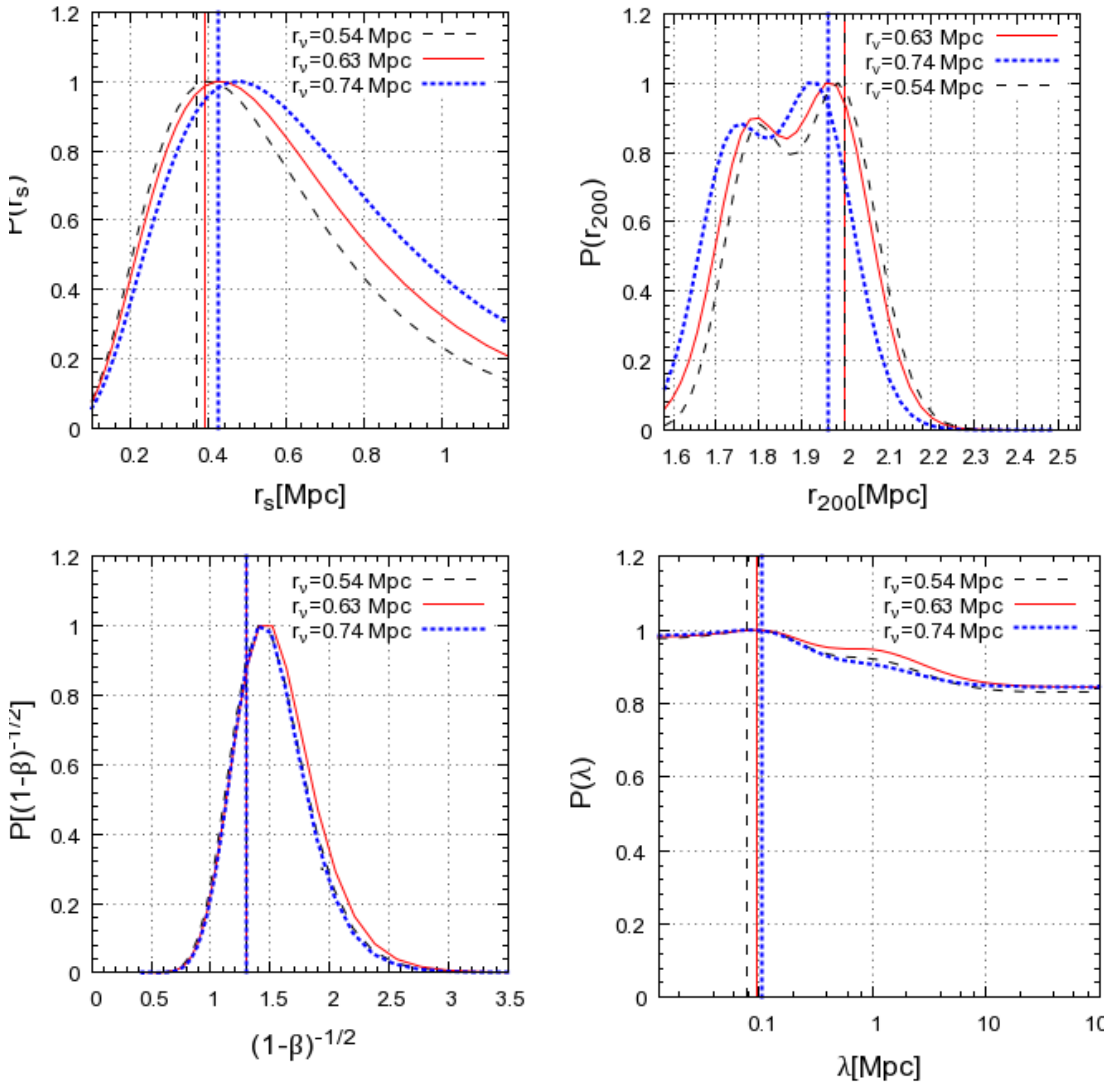

Figure 7.4: Results for MACS 1206. Marginalized likelihood distributions of r_{200}, r_s, $\sigma_r/\sigma_\theta = 1/\sqrt{1-\beta}$ and λ obtained for the reference model "C" by changing the scale radius of the number density profile of the galaxies r_ν within the 68% confidence region of the G.R. analysis. Red solid curves: r_ν fixed to the GR best fit value. Black dashed curves: r_ν fixed to the lower limit of the 68% confidence region. Blue dotted curves: r_ν (β_∞) settled to the upper limit of the 68% confidence region. The corresponding vertical lines indicate the *MAMPOSSt* best fit of each free parameter.

$$r_s = \left[0.39^{+0.40}_{-0.16}(stat) \pm 0.09(syst)\right] \text{ Mpc}, \tag{7.4}$$

where the statistical errors indicates the 68% confidence region as above, and the systematic errors are computed as the maximum difference between the best fit values (vertical lines). For $\beta \equiv \beta_C$ one can estimate only the variation induced by r_ν, since the parameter has a different meaning for each velocity anisotropy profile. As one can see from Fig. 7.4, no measurable effects are produced on the β distribution when r_ν is modified.

In the case of λ, I estimate the impact of systematics looking at the modifications in the upper bound after adding information from lensing analysis:

$$\lambda \leq [1.61 + 0.30(syst)]\text{Mpc} \qquad \Delta\chi^2 = 2.71, \tag{7.5}$$

where the systematic uncertainty is the largest difference (in absolute value) between the upper limits obtained from the models analysed. The result is still compatible with small or negligible deviations from standard gravity.

7.1.2 RXJ 2248

I perform the analysis for the cluster RXJ 2248 in the radial range $[0.05\,\text{Mpc} - 2.3\,\text{Mpc}]$, using the 981 member galaxies lying in this region out of a sample of 1233 cluster members identified (Sartoris et al., in prep.).

As for MACS 1206, I fixed the number density profile whose parameter is given by the best fit value of the standard GR study (Sartoris et al., in prep.). In particular, the projected number density profile is again a pNFW with $r_\nu = 0.59 \pm 0.08\,\text{Mpc}$, where this value is obtained by a Maximum Likelihood analysis on the spectroscopic members only. For $\beta(r)$ I use the same models discussed above; the highest probability for this cluster is given by the Tiret model "T" of eq. (3.34). The results of the *MAMPOSSt* procedure applied to the modified gravitational potential of eq. (2.23) with the velocity anisotropy model "T" are shown in Figs. 7.5 and 7.6. As before, the red and green curves in Fig. 7.5 indicate the contours at $\Delta\chi^2 = 2.3$ and $\Delta\chi^2 = 4.6$ respectively. The distributions for each parameter, obtained after marginalizing $\mathcal{L}_{dyn}$, are plotted as the red curves in Fig. 7.6.

The effective interaction range probability distribution (bottom right plot of Fig. 7.6) shows the same qualitative behavior as found from the analysis of MACS 1206: the curve flattens both for large λ and for $\lambda \to 0$, although the shape is more peaked near the *MAMPOSSt* best

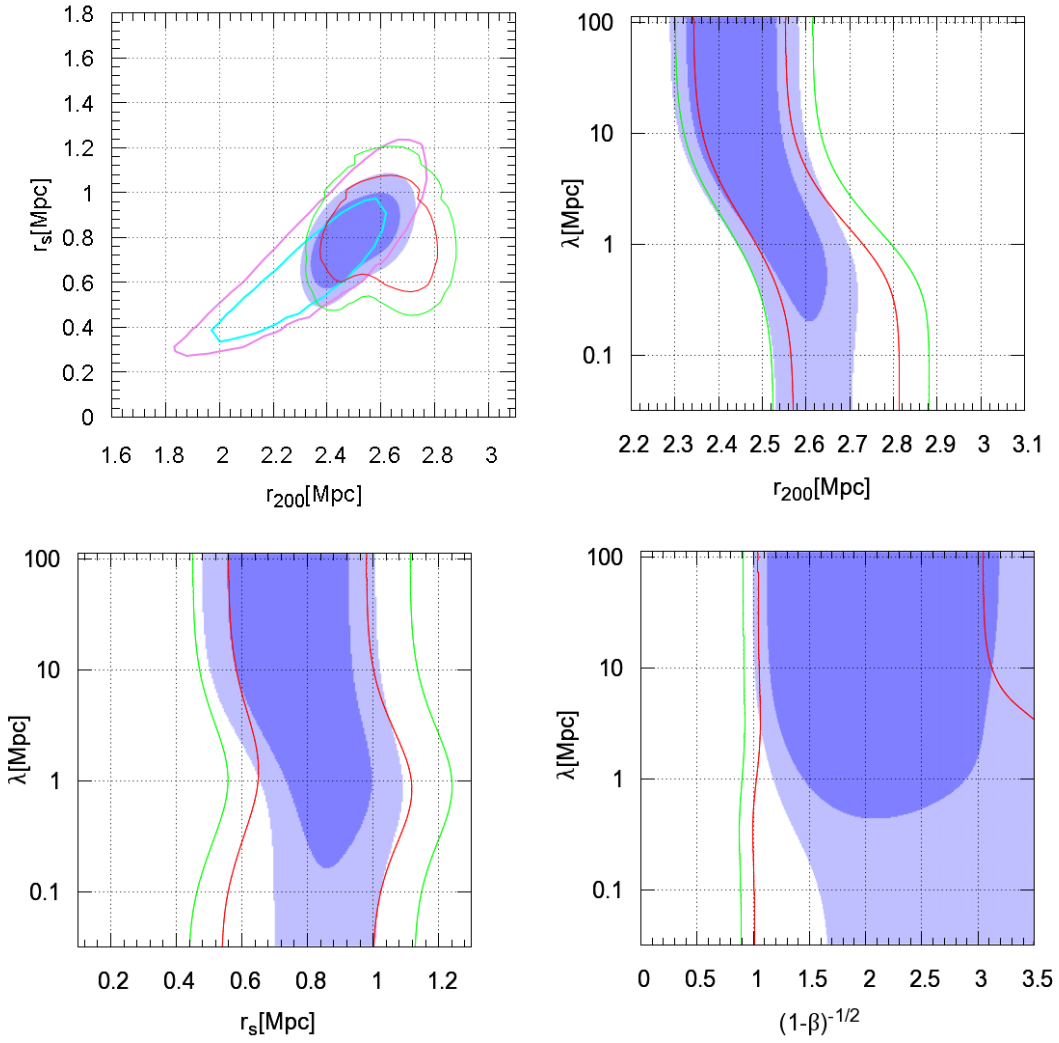

Figure 7.5: Results for RXJ 2248: two-dimensional contours at $\Delta\chi^2 \leq 2.3$ and $\Delta\chi^2 \leq 4.61$ from the maximum of the probability of the *MAMPOSSt* analysis (red and green lines respectively) and of the joint dynamics+lensing analysis (dark blue and light blue filled regions). The cyan and purple lines in the left upper panel show the lensing contours at 68% C.L. and 90% C.L.

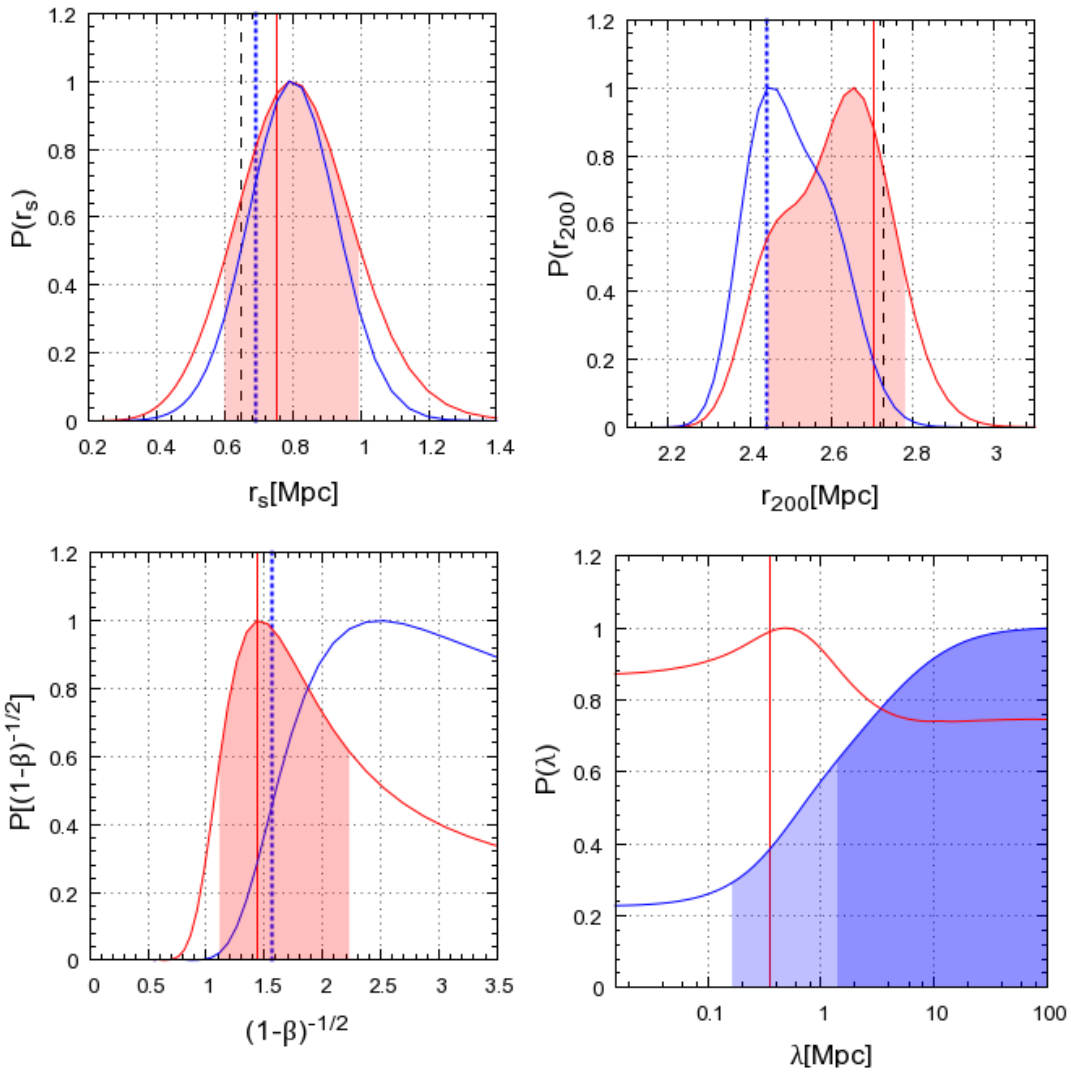

Figure 7.6: Results for RXJ 2248: single parameter distributions obtained by marginalizing the total likelihood over the other three. Upper panels: r_s and r_{200}. Bottom panels: $\sigma_r/\sigma_\theta = 1/\sqrt{1-\beta}$ and $\lambda = 1/m_{eff}$. Red curves: dynamics analysis, blue curves: lens+dyn. Vertical red solid lines indicate the *MAMPOSSt* best fit values, blue dotted lines correspond to the values maximizing the total likelihood while black dashed lines are the dynamics GR best fit. The filled areas below the marginalized distributions of r_s, r_{200} and $\beta = \beta_\infty$ represent the 68% C.L. of the dynamics results. The dark and light blue regions below the curve $P(\lambda)$ show the $\Delta\chi^2 \leq 1.0$ and $\Delta\chi^2 \leq 2.71$ confidence intervals, respectively.

fit value $\lambda = 0.91$ Mpc (red vertical solid line) compared to the previous cluster. As mentioned above, the presence of the peak is strictly related to the distribution of the scale radius r_s, which controls the inner shape of the mass profile. Also the 2-dimensional degeneration directions with r_s, r_{200} and β (Fig. 7.5) are very similar to those of Fig. 7.2. The reason for a nearly constant, non-zero probability to have large deviations form GR can be again explained in terms of the small enhancement of the mass profile produced by the fifth force, which allows λ to be large if r_s and r_{200} change in such a way to compensate the effect of the additional term. It is worth to point out that the number of galaxies used in the *MAMPOSSt* fit for this cluster is about three times larger than that of MACS 1206; this means that roughly tripling the statistics is still not sufficient to set meaningful constraints on λ from the analysis of dynamics alone.

As for the standard NFW parameters and the velocity anisotropy, I obtain the results:

$$r_{200} = 2.70^{+0.09}_{-0.24}\,\text{Mpc}, \qquad r_s = 0.75^{+0.14}_{-0.18}\,\text{Mpc}, \qquad \beta_\infty = 1.43^{+0.59}_{-0.19}, \tag{7.6}$$

at 68% C.L., where the errors are computed with respect to the best fit values of the *MAMPOSSt* procedure (red vertical solid lines in Fig. 7.6). The constraints are consistent with the results obtained from the GR analysis (Sartoris et al., in prep.) $r_{200} = 2.73^{+0.08}_{-0.09}$ Mpc, $r_s = 0.65^{+0.12}_{-0.22}$ Mpc and $\beta_\infty = 1.43^{+1.07}_{-0.24}$ (black dashed lines in Fig. 7.6). Nevertheless, as for MACS 1206, the degeneration between the virial radius and the modified gravity parameter produce a shallower marginalized distribution of r_{200}, with an excess of probability towards lower values. There is a modest difference between the GR and MG best fit values, suggesting that the impact of the interaction range λ on the total likelihood distribution is larger than for MACS 1206. Since the best fit is sensitive to every small variation in the probability, the slight preference of $\lambda \sim 0.3$ (roughly three times the value from the best fit obtained in the previous case) is sufficient to move away the other parameters from the GR values, but the excess is still not relevant enough to affect the marginalized distributions which remain in agreement with the analysis of Sartoris et al. (in prep.).

Following the same approach as in Sect. 7.1.1, I combine the likelihood distribution generated by the *MAMPOSSt* method with the lensing posterior probability distribution $P(r_{200}, r_s)$ derived from the results of [35] and Caminha et al. (in prep). The blue contours and the blue lines of Figure 7.6 show what I obtain from the analysis of $\mathcal{L}_{tot}$ defined in eq. (7.2). No upper limits can be provided for λ in this case. On the contrary, the joint kinematic+lensing study indicates a preference for large values of the effective interaction range, excluding at

$\Delta\chi^2 = 2.71$ the region $\lambda \leq 0.14$ Mpc, as one can see from the marginalized distribution in the right bottom panel.

The origin of this behavior is related to a slight tension between the lensing and dynamics probability distributions in the plane (r_s, r_{200}). Indeed, $P_{lens}(r_{200}, r_s)$ exhibits a peak for $r_{200} = 2.24 \pm 0.22$ Mpc, $r_s = 0.55 \pm 0.27$ Mpc (see the purple contours in the upper left panel of Fig. 7.6), while the 2-dimensional dynamics distribution has a maximum for $r_s = 0.81$ Mpc and $r_{200} = 2.65$ Mpc. When combining the 2 analyses, we increase the probability in the region of parameter space corresponding to relatively large λ values, while decreasing the probability for a vanishing interaction range, as can be seen from the 2 dimensional distributions of Fig. 7.5.

As before, I now study the effect of changing the scale radius of the tracers r_ν within the 68% C.L. of the GR analysis and the anisotropy model $\beta(r)$. Fig. 7.7 shows the effect on the marginalized distributions due to the different parametrization of the anisotropy profile while Fig. 7.8 displays the changes induced by r_ν. The red curves in both Figures indicate the reference model ("T" in this case) with $r_\nu = 0.59$ Mpc. Again, the largest effect on the results is obtained when changing the anisotropy model (Fig. 7.7). In this case both the position and the shape of the peak in the distribution of λ are modified as a consequence of the variations in the r_s marginalized likelihood; this is particularly evident for the model "O" which shows the largest discrepancy in the best fit value of r_s compared to the reference model (vertical lines in the upper left plot of Fig. 7.7, see also Table 7.1). Nevertheless, the tension with lensing results is not resolved when including these systematics. As shown in the five bottom rows of Table 7.1, all the runs provide a lower limit on λ which is larger than the reference model, except for the case of $r_\nu = 0.66$ Mpc where the constraint on the interaction range relaxes from $\lambda \geq 0.30$ to $\lambda \geq 0.06$ Mpc at $\Delta\chi^2 = 2.71$.

Note that the results for $r_\nu = 0.54$ Mpc is slightly preferred with respect to the case of $r_\nu = 0.59$ Mpc (last row in Table 7.1), similarly of what I found for MACS 1206. In order to take into account the variation induced on the NFW parameters r_s, r_{200} by the changes in the anisotropy profile and in the scale radius of the number density profile, I consider the maximum difference between the best fit values of each run and of the reference model:

$$r_{200} = [2.70^{+0.09}_{-0.24}(stat) \pm 0.04(syst)]\,\text{Mpc}, \qquad r_s = [0.75^{+0.14}_{-0.18} \pm 0.20(syst)]\,\text{Mpc}. \quad (7.7)$$

As I did for the previous cluster, I estimate the systematic uncertainties in β_∞ from the variation

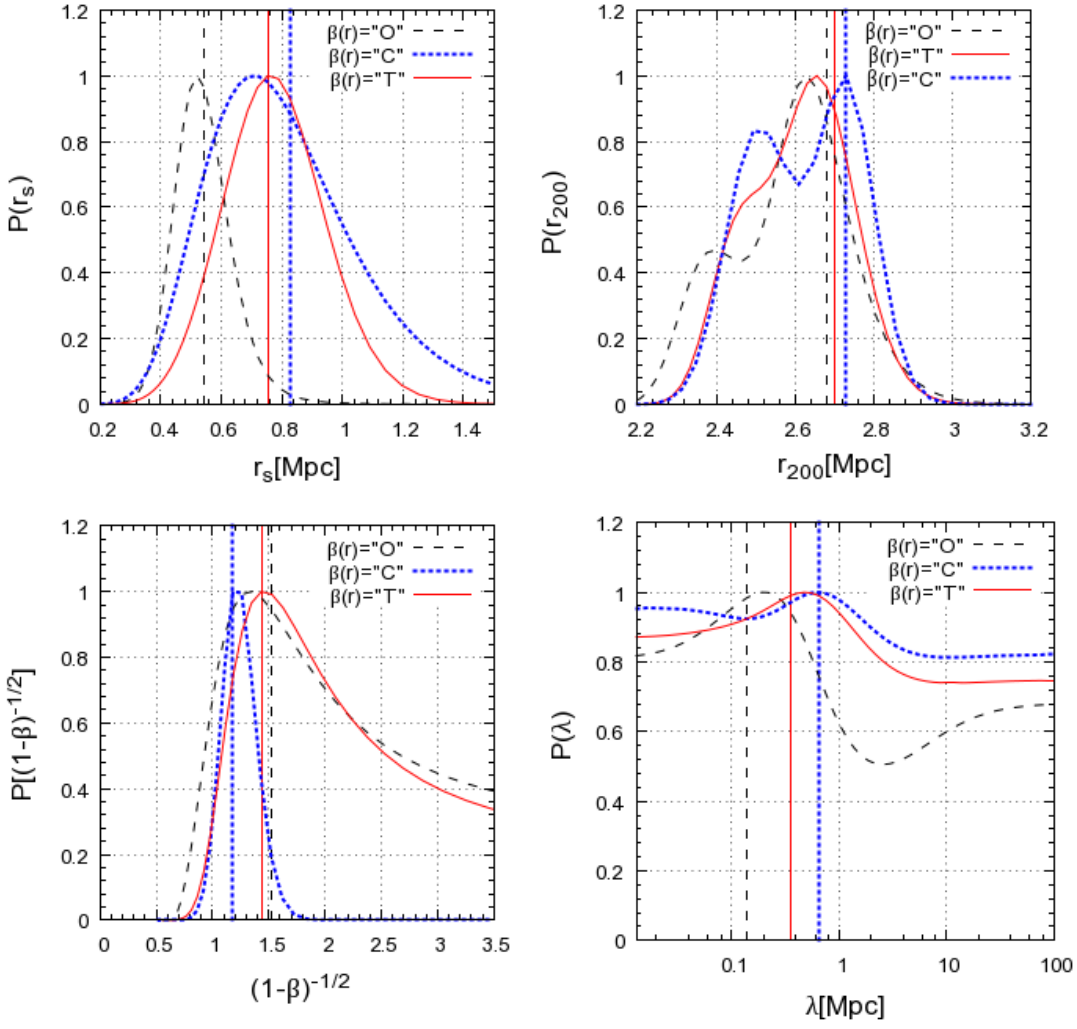

Figure 7.7: Effects on the marginalized likelihood distributions of r_{200}, r_s, $\sigma_r/\sigma_\theta = 1/\sqrt{1-\beta}$ and λ from the dynamics analysis of RXJ 2248 when changing the anisotropy model $\beta(r)$. Red solid curves: reference model "T". Black dashed curves: "O" model. Blue dotted curves: "C" model. The corresponding vertical lines indicate the *MAMPOSSt* best fit of each free parameter. In the bottom left plot, $\beta \equiv \beta_\infty$ for the "T" and the "O" models, while $\beta \equiv \beta_C$ for the "C" model.

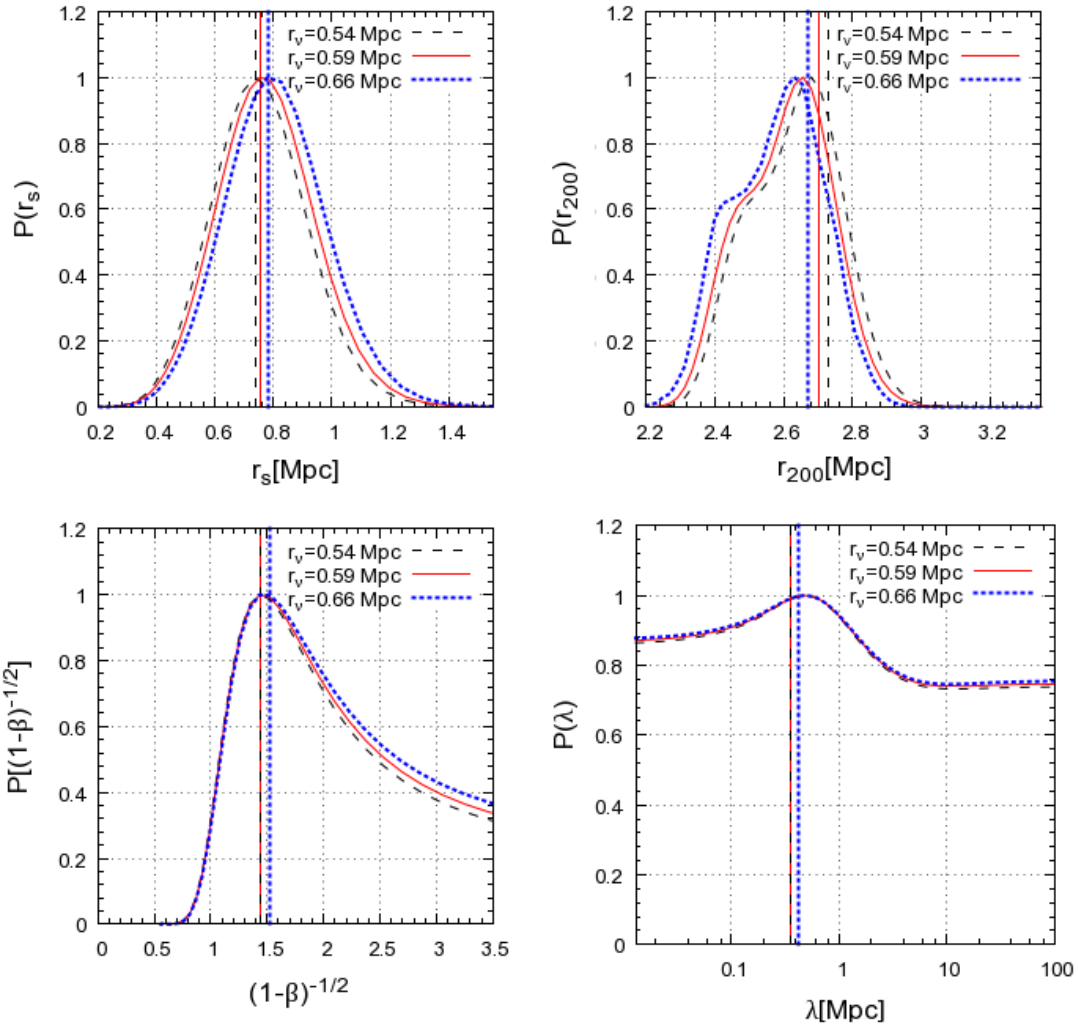

Figure 7.8: Effects on the marginalized likelihood distributions of r_{200}, r_s, $\sigma_r/\sigma_\theta = 1/\sqrt{1-\beta}$ and λ of the dynamics analysis of RXJ 2248 for the reference model "T" when changing the scale radius of the number density profile of the galaxies r_ν within the 68% confidence region of the GR analysis. Red solid curves: r_ν fixed to the GR best fit value. Black dashed curves: r_ν fixed to the lower limit of the 68% confidence region. Blue dotted curves: r_ν settled to the upper limit of the 68% confidence region. The corresponding vertical lines indicate the *MAMPOSSt* best fit of each free parameter.

induced by r_ν only, obtaining:

$$\beta_\infty = 1.43^{+0.59}_{-0.19}(stat) \pm 0.10(syst). \tag{7.8}$$

Anis. model	r_ν [Mpc]	r_{200} [Mpc]	r_s [Mpc]	$(1-\beta_{C/\infty})^{-1/2}$	λ [Mpc]	$\Delta\chi^2$
		MACS 1206				
$\boldsymbol{C}$	**0.63**	$2.00^{+0.08}_{-0.28}$	$0.39^{+0.40}_{-0.16}$	$1.31^{+0.59}_{-0.19}$	≤ 1.61	0.0
O	0.63	$1.93^{+0.04}_{-0.25}$	$0.30^{+0.14}_{-0.07}$	$1.51^{+0.69}_{-0.55}$	≤ 1.31	0.72
T	0.63	$1.94^{+0.02}_{-0.30}$	$0.35^{+0.33}_{-0.04}$	$1.41^{+1.35}_{-0.29}$	≤ 1.31	0.20
C	0.74	$1.96^{+0.06}_{-0.29}$	$0.42^{+0.42}_{-0.18}$	$1.31^{+0.59}_{-0.18}$	≤ 1.31	0.20
C	0.54	$2.00^{+0.09}_{-0.27}$	$0.42^{+0.28}_{-0.12}$	$1.31^{+0.59}_{-0.19}$	≤ 1.78	-0.14
		RXJ 2248				
$\boldsymbol{T}$	**0.59**	$2.70^{+0.09}_{-0.24}$	$0.75^{+0.14}_{-0.18}$	$1.43^{+0.79}_{-0.24}$	≥ 0.14	0.0
O	0.59	$2.68^{+0.10}_{-0.22}$	$0.55^{+0.11}_{-0.14}$	$1.53^{+0.71}_{-0.55}$	≥ 0.84	0.64
C	0.59	$2.73^{+0.07}_{-0.29}$	$0.83^{+0.21}_{-0.32}$	$1.18^{+0.25}_{-0.14}$	≥ 0.80	0.44
T	0.66	$2.67^{+0.10}_{-0.27}$	$0.78^{+0.26}_{-0.19}$	$1.53^{+0.69}_{-0.34}$	≥ 0.06	0.20
T	0.54	$2.73^{+0.08}_{-0.26}$	$0.74^{+0.24}_{-0.19}$	$1.43^{+0.66}_{-0.24}$	≥ 0.19	-0.16

Table 7.1: Results on the free parameters of our analysis for the cluster MACS 1206 (first 5 rows) and RXJ 2248 (last 5 rows). The bold characters indicate the reference models adopted for each of the two clusters. The errors in r_{200}, r_s and $\sigma_r/\sigma_\theta = 1/\sqrt{1-\beta}$ are the 68% C.L. from the *MAMPOSSt* procedure; the upper(lower) limits on λ are obtained at $\Delta\chi^2 = 2.71$ from the joint kinematic+lensing analysis. The last column indicate the logarithmic difference between the likelihood of the model analysed and the likelihood of the reference model.

7.2 Chameleon screening: constraints on $|\bar{f}_R(z)|$

As highlighted in Chapter 2, in general $\lambda = \lambda(r)$ is a function of the environment; in particular, the interaction range tends to vanish in the limit of high density regions and small scales to recover standard GR. The transition between the screened and non-screened region depends on the structure of the effective potential V_{eff} in the equation of motion of the field (2.35), which is determined by the choice of the functional form $f(R)$. It is important to point out that in this analysis I have considered only generic $f(R)$ models in which the screening mechanism works at scales smaller (or much larger) than those investigated here, so that we could neglect the dependence of $m_{f_R} = 1/\lambda$ on the local density.

In order to translate our results in a bound on the background scalaron field $|\bar{f}_{,R}|$, one has to take into account how the chameleon screening works once a particular model is fixed. As an example, I focus on the H&S model in which, as shown in Chapter 2, the functional form of $f(R)$ can be approximated by a power law:

$$f(R) \simeq 6\Omega_\Lambda - \frac{f_{,R0}}{n}\frac{R_{0,b}^{n+1}}{R^n}, \tag{7.9}$$

where I set $n = 1$; $f_{,R0} < 0$ is the background scalaron value at present day. An accurate treatment of this situation requires a full numerical solution of the nonlinear equation (2.35), which is hard to obtain due to computational issues. Indeed, the transition between the interior (screened) and the exterior linear regime is very stiff for the most common viable models, including the H&S parametrization. Bettoni et al. (in prep) tries to overcome this problem solving the equation using the full metric around a spherical distribution of mass.

As a proof-of-concept, I follow here a simple analytical approximation to describe the screening mechanism in this case, just to show what I can obtain with our method. I model the chameleon regime with an instantaneous transition between the region of full screening $r \leq S$, where $f_{,R} = 0$, and the linear region $r > S$, where the Newtonian potential is modified according to eq. (2.42). As explained in ref. [206], this can be achieved by taking $\delta f_{,R} = \min(\delta f_{,R}^{lin}, |\bar{f}_{,R}|)$, where $\delta f_{,R}^{lin}$ is the solution of the field equation, eq. (2.35), with the linearization condition (2.41).

In terms of λ, I define the effective interaction range constant and equal to the background value in the unscreened region $r > S$ and equal to zero for $r \leq S$. I define S to be the screening radius, which is given solving $\delta f_{,R}^{lin}(S) = \bar{f}_{,R}$ for each value of r_s, $r_{200}, \lambda \equiv \bar{\lambda}_{f_R}$. In Fig-

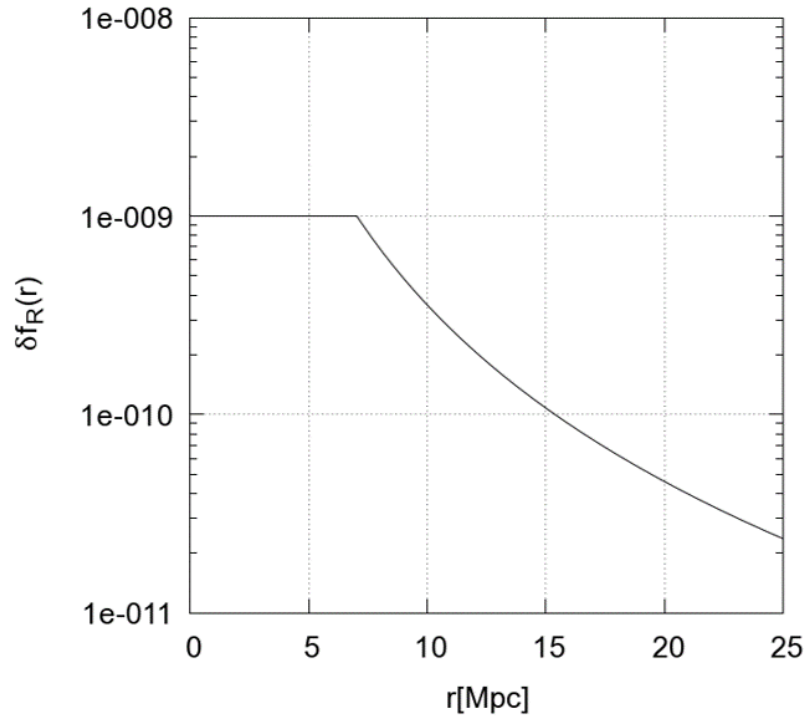

Figure 7.9: Perturbations in the scalaron field $\delta f_{,R} = f_{,R} - \bar{f}_{,R}$ as a function of the radial distance from the cluster center for $\lambda = 0.1\,\mathrm{Mpc}$ $r_s = 0.27\,\mathrm{Mpc}$, $r_{200} = 2.00\,\mathrm{Mpc}$.

ure 7.9 I show the behaviour of the field perturbation $\delta f_{,R}$ as a function of the radial distance from the cluster center for the best fit parameters of the *MAMPOSSt* analysis of MACS 1206 assuming a Hu & Sawicki functional form. As we can see, the screening mechanism is very strong for this class of models, masking the effect of the additional force up to $\sim 7\,\mathrm{Mpc}$ for $\bar{\lambda} = 0.1\,\mathrm{Mpc}$. With the method proposed in this work one would be able, in the most optimistic case, to constrain the background field only down to values for which the screening radius is smaller than the cluster size (i.e. less than $\sim 2\,\mathrm{Mpc}$) corresponding to $|\bar{f}_{,R}| \sim 10^{-8}$ for H&S model.

I run again the *MAMPOSSt* procedure computing the screening radius S, and then requiring $\phi_{mg}(r)$ of eq. (2.22) to be zero for $r \leq S$. Combining the resulting likelihood with the lensing posterior I get $\bar{\lambda}_{f_R} \leq 20\,\mathrm{Mpc}$ and $\bar{\lambda}_{f_R} \geq 12\,\mathrm{Mpc}$ at $\Delta\chi^2 = 2.71$ for MACS 1206 and RXJ 2248, respectively. Now $\bar{\lambda}_{f_R}$ is related to the background field value through eq. (2.37), which is so constrained to be $|\bar{f}_{,R}(z = 0.44)| \leq 4.0 \times 10^{-5}$ and $|\bar{f}_{,R}(z = 0.35)| \geq 1.4 \times 10^{-5}$. The first bound is in agreement with current determinations of the magnitude of

the background scalaron, obtained using distance indicators at low-redshift (ref. [134]), galaxy cluster abundance (refs. [128, 14]) and redshift space distortions (ref. [135]), which have tightened the upper limit up to $|\bar{f}_{,R0}| < 10^{-6}$, compatible with very small deviations from GR. On the other hand, it is not surprising that the effect of introducing screening for RXJ 2248 is to increase the tension I found, leading to a value of $|\bar{f}_{,R0}|$ for this particular model which is totally inconsistent with other constraints.

7.3 Discussions

In this Chapter I have presented an analysis aimed at constraining modifications of gravity at the scales of galaxy clusters by determining the time-time gravitational potential $\Phi(r)$ from the analysis of the dynamics of the galaxies in the cluster. I have focused on a particular sub-class of scalar-tensor theories, the $f(R)$ models, where the additional degree of freedom associated to the modification of gravity is expressed in terms of the interaction range λ; I have applied the method to the case of two dynamically relaxed clusters MACS 1206 at $z = 0.44$ and RXJ 2248 at $z = 0.35$, extensively analyzed within the CLASH/CLASH-VLT collaborations. Assuming spherical symmetry, I have parametrized the cluster mass density profile as a NFW profile, characterized by the scale radius r_s and the virial radius r_{200}, constraining the vector of parameters (r_s, r_{200}, λ) with the modified *MAMPOSSt* code described in Sect. 3.3. Since in $f(R)$ gravity photons are not affected by the fifth force contribution I have further combined our results with the information on the NFW parameters r_s, r_{200} from the strong+weak lensing analysis of ref. [35].

The results for the cluster MACS 1206 are in agreement with the GR predictions, confirming the previous general analysis of Chapter 6. When including lensing contribution, I obtain an upper limit of $[\lambda \leq 1.61(stat) + 0.30(syst)$ Mpc at $\Delta\chi^2 = 2.71$; the bound takes into account variations in the velocity anisotropy profile $\beta(r)$ and in the scale radius of the galaxy number density profile r_ν, which enters in the kinematic determination of the gravitational potential (or, equivalently, of the mass profile).

A peculiar behavior has instead been found in the case of RXJ 2248, where the joint kinematic+lensing analysis shows a 2σ preference for values of λ larger than 0. Including also systematics effects due to changes in the anisotropy profile $\beta(r)$ and in r_ν, I get a lower bound $\lambda \geq 0.12$ Mpc at $\Delta\chi^2 = 2.71$. This result arises from a mild tension $< 1\sigma$ between the dynamics and lensing determinations of the mass profile in GR. Larger values of r_s and r_{200}

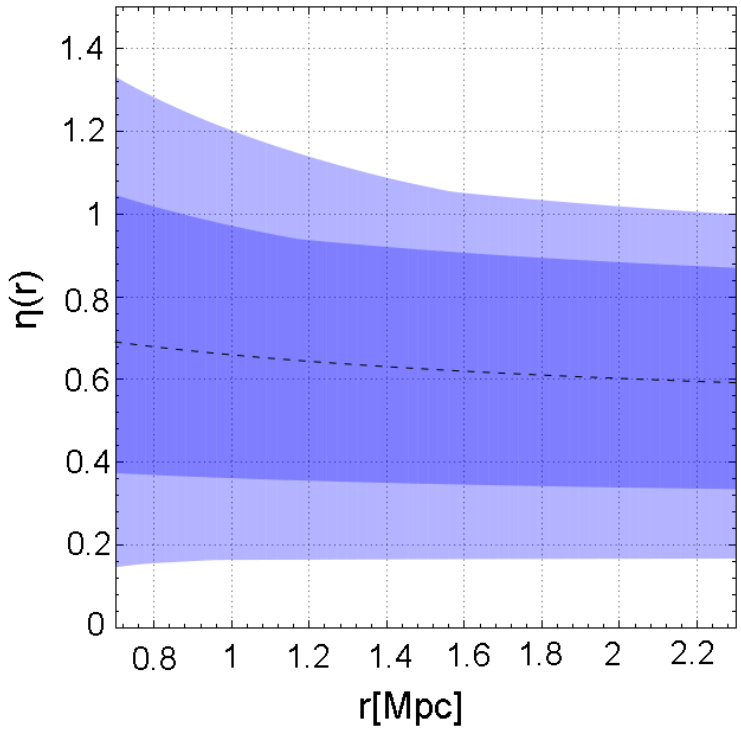

Figure 7.10: Anisotropic stress η in the radial range $[0.7\,\mathrm{Mpc} - 2.3\,\mathrm{Mpc}]$ for the cluster RXJ 2248. The blue shaded region indicates the 68% C.L. while the light blue area is the 90% C.L. The best fit profile is given by the black dashed line.

are favored by the dynamics analysis with respect to the lensing results; the discrepancy could be interpreted as the additional contribution of the fifth force which affects only the motion of non-relativistic particles. In order to better investigate the effect of this tension on the Bardeen potential Φ and Ψ, I compute the anisotropic stress $\eta = \Psi/\Phi$ in the radial range covered by our analysis, following the approach of Chapter 6. The results are shown in Fig. 7.10, where the blue and light blue areas represent the 68% and the 90% confidence regions, respectively. As we can see, the discrepancy with the GR expected value $\eta = 1$ is at more than 1σ for $r \gtrsim 1\,\mathrm{Mpc}$. For $r = 2.3\,\mathrm{Mpc}$ I obtain $\eta = 0.57 \pm 0.42$ at 90% C.L. Interestingly, this is in agreement with the prediction of $f(R)$ models, in which the anisotropic stress is smaller than 1, reaching the value $\eta = 1/2$ in the case of maximum deviations from GR.

The results from the analysis of RXJ 2248 point in the opposite direction of what I have obtained for MACS 1206 (although the constraints I have derived on λ from the 2 clusters are

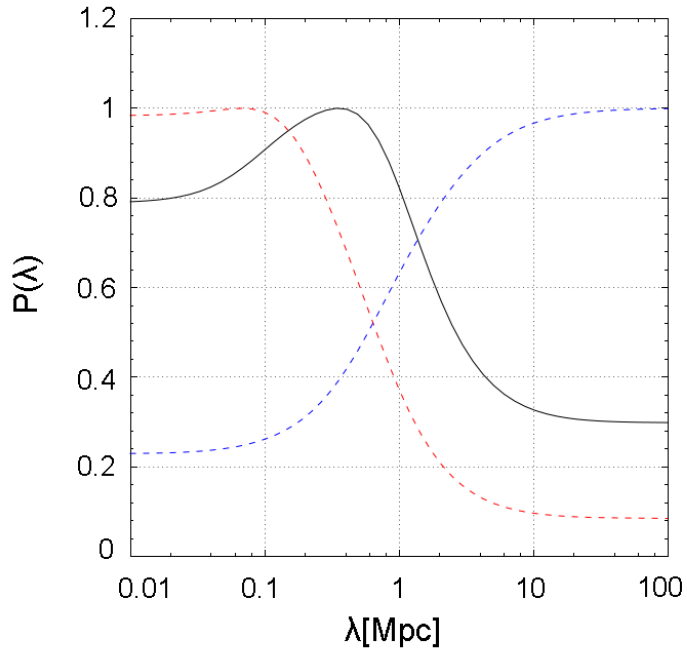

Figure 7.11: Black solid line: combined likelihood obtained by multiplying the marginalized probability distributions from the analysis of the reference model for MACS1206 (red dashed line) and for RXJ 2248 (blue dashed line).

still compatible within the 90% C.L.), highlighting the need to check the systematics associated to the assumptions on which our method relies. The presence of possible substructures and departures from spherical symmetry could in principle affect both the dynamics and lensing analyses; nonetheless, I stress again that both clusters belong to a sample of 20 X-rays selected objects for their properties of apparent dynamical relaxation.

One can in principle assume that the interaction range is constant in time between the redshifts of MACS 1206 and RXJ 2248 and combine the marginalized likelihoods of λ derived from the analysis of the reference model for each cluster. As we can see in Fig. 7.11, the apparent tension with GR is relaxed and I can still put an upper limit of $\lambda \leq 1.81$ Mpc at $\Delta\chi^2 = 1.0$.

In conclusion, although two clusters are obviously too few to produce robust constraints, they are already sufficient to show the potential of the method of combining dynamics and lensing to test gravity. On the other hand, the tension I have highlighted shows that it is necessary to model accurately the velocity anisotropy and to take into account deviations from

spherical symmetry and from virialization before the method can be claimed to provide a robust determination of the anisotropic stress η and its scale dependence. This can be achieved by studying simulated clusters, both in GR and in modified gravity, to better understand how the above mentioned effects influence our constraints. As a first step in this direction, in the next Chapter I will present the results of the analysis of a set of synthetic Dark Matter halos; the main purpose of this work is to calibrate those systematics and to find observational criteria in order to identify the suitable clusters for the application of our method.
Moreover, it is worth to notice that the analysis presented in this Chapter can be extended to all the generic scalar-tensor theories where the coupling constant Q is not fixed and the lensing potential is still given by the Newtonian potential $(\Phi + \Psi)/2 = \Phi_N$ (e.g. the Brans-Dicke k-essence (BDK) model of ref. [207]). However, the data I used here are not sufficient to get significant information on this kind of models.

Future imaging surveys, both from ground (e.g. LSST) and from space-borne telescopes (e.g. Euclid) will provide lensing mass reconstructions for thousands of clusters, although at a signal-to-noise level lower than that reached by the two clusters considered here. At the same time, the next generation of high-multiplexing spectrographs on 8m-class telescopes will allow a precise characterization of the phase-space structure for a sizable fraction of such clusters. This increase in statistics calls for the need of controlling the above mentioned systematics in the recovery of mass profiles from lensing and internal cluster dynamics, if we want to take full advantage of the their potentiality as powerful diagnostics for the nature of gravity on cosmological scales.

Chapter 8

Calibrating systematics with simulations

In the previous chapters I have presented a powerful method to constrain modifications of gravity using galaxy cluster mass profiles; nevertheless, I have already stressed that a solid control of the assumptions on which the analysis relies is required in order to draw robust conclusions. In particular, the interesting behavior found in the case of the cluster RXJ 2248 suggests that some effects, whose contribution can be negligible in the framework of General Relativity, may become relevant source of systematics when searching for small deviations, such as those induced by the additional degrees of freedom in non-standard gravity.

In this Chapter I analyze a set of cosmological simulations of galaxy clusters carried out in standard gravity, which is aimed at identifying and calibrating the impact of the above mentioned systematics. I follow two lines of investigation; in the first part I determine what kind of constraints we expect in the ideal case when applying our method to a synthetic cluster for which all the assumptions are met. This is achieved by generating equilibrium configurations of isolated self-gravitating systems made of collisionless particles distributed according to a spherical NFW profile, which are then analyzed with the *MG-MAMPOSSt* procedure in linear $f(R)$ gravity. The results indicate that the study of the dynamics of the tracers alone is not sufficient to break the degeneracy between the mass profile parameters and the interaction range $\lambda = 1/m$ even in the ideal situation, regardless of the number of particles used in the likelihood fit. Notwithstanding, combining the dynamics analysis with additional information on

the virial radius r_{200} and on the scale radius r_s with reasonable uncertainties (e.g. constraints from a lensing mass reconstruction) leads to stringent bounds on λ (or m) always in agreement with GR predictions.

In the second part I evaluate how the constraints suffer the lack of dynamical relaxation and departures from spherical symmetry by studying 29 massive Dark Matter halos taken from a set of ΛCDM N-body simulations performed with the GADGET-3 code; I determine the influence of these effects as spurious detections of $\lambda > 0$ ($m < \infty$) emerging from the analysis. I furthermore define two observational criteria which can be used to get helpful insights in identifying, among a generic population of galaxy clusters in the local Universe, those objects that are more suitable for the application of the proposed method. I discuss possible developments of this work in light of the wide collection of imaging and spectroscopic data that will be available with the next generation surveys.

8.1 Synthetic Dark Matter Halo

In order to investigate how possible systematics can affect constraints on modified gravity models obtained using a combination of lensing and kinematic information, one need first to test the reliability of our method in the case when all the assumptions are perfectly satisfied. Adopting a ΛCDM background with $H_0 = 70\,\mathrm{km\,Mpc^{-1}}s^{-1}$, $\Omega_m = 0.3$ and $\Omega_\Lambda = 0.7$ (where the cosmology enters only in the definition of the virial mass M_{200}, defined in Chapter 1), I generate a sample of spherically-symmetric, isolated halos made of collisionless particles distributed as a NFW mass profile of eq. (2.20). I populate each halo out to $\sim 7\,r_{200}$, imposing to have 1000 particles within the virial radius[1]. For each particle at a radial distance r from the cluster center, I assign a velocity whose components in spherical coordinates are Gaussian-distributed with a squared dispersion $\sigma_r^2(r)$, $\sigma_\theta^2(r)$ and $\sigma_\phi^2(r)$, respectively. The radial component σ_r^2 is given by the solution of the Jeans' equation, eq. (3.36), while the dispersion along the tangential direction is connected to the radial one through the velocity anisotropy profile $\beta(r)$:

$$\sigma_\theta^2(r) = [1 - \beta(r)]\sigma_r^2(r). \tag{8.1}$$

Since I am assuming spherical symmetry, I further impose $\sigma_\phi^2 \equiv \sigma_\theta^2$.

In the Jeans' analysis, the velocity anisotropy profile is generally unknown; as discussed in

[1]The choice of 1000 particles within r_{200} is an optimistic, although not unrealistic, expectation on of the number of cluster galaxies with accurate measured spectroscopic redshift from present and future surveys.

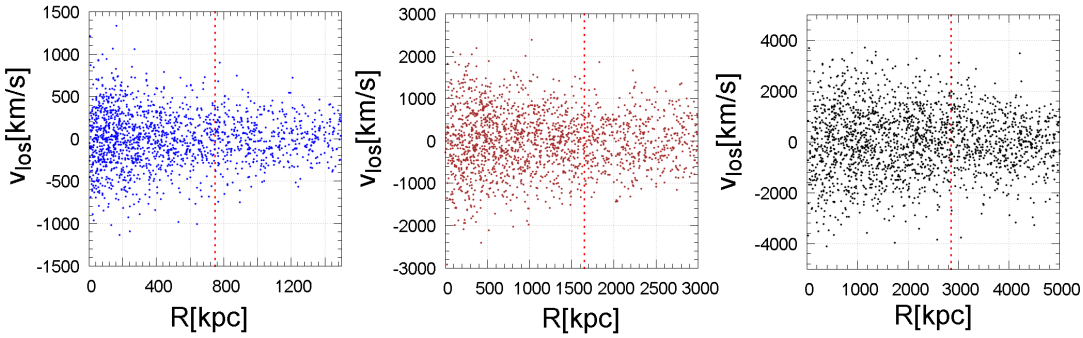

Figure 8.1: Projected phase spaces of three synthetic clusters with different masses and concentrations. Left panel: $r_{200} = 0.750\,\text{Mpc},\ r_s = 0.096\,\text{Mpc}$. Central panel: $r_{200} = 1.650\,\text{Mpc},\ r_s = 0.379\,\text{Mpc}$. Right panel: $r_{200} = 2.850\,\text{Mpc},\ r_s = 1.077\,\text{Mpc}$. The red vertical dashed line indicates $R = r_{200}$

Chapter 3, *MAMPOSSt* assumes a parametric profile for $\beta(r)$, and fits the free parameters of the chosen model together with the parameters of the mass profile and of the number density profile. I generate the synthetic clusters with a "Tiret" model, eq. (3.34), where again r_c is assumed to be equal to the scale radius of the mass profile r_s and the normalization constant β_∞ is fitted in the *MAMPOSSt* procedure. The halos are created all with $\beta_\infty = 0.5$, corresponding to a Mamon&Lokas profile, eq. (3.33), with the additional constraint $r_\beta = r_s$.

I apply the *MG-MAMPOSSt* code to a sample of 15 synthetic halos generated at $z = 0$, whose masses spawn a range from $[5.1 \times 10^{13}\ M_\odot \div 2.9 \times 10^{15}\ M_\odot]$. For each halo, I choose the scale radius r_s according to the mass-concentration relation of eq. (1.36) (extrapolated ad $z = 0$), obtained from the analysis of 19 CLASH clusters by ref. [87].

I have randomly sampled the value of the parameter A, B and K for every halo assuming that they are Gaussian-distributed around the central value with a standard deviation given by the uncertainties in eq. (1.37).

The input values of r_{200} and r_s are given in the second and third columns of Table 8.1, ordered by increasing mass. In Figure 8.1 I also show the projected phase spaces (R, v_{los}) for the first, the seventh and the last halos in the sample, on the left, central and right plots respectively. The red vertical dashed line corresponds to the value of the virial radius r_{200} of each cluster.

8.1.1 Results from the *MAMPOSSt* procedure

As a preliminary test, I analyze the 15 realizations of projected phase spaces with the standard *MAMPOSSt* procedure in GR using all particles with a projected radius $R \in [0.05\,\text{Mpc},\ r_{200}]$

ID	$r_{200}\,[Mpc]$	$r_s\,[Mpc]$	$r_\nu\,[Mpc]$	$r_{200}\,[Mpc]$(M)	$r_s\,[Mpc]$(M)	$\mathcal{A}_T$(M)
1	0.750	0.096	0.086	0.74 ± 0.02	$\mathbf{0.17^{+0.04}_{-0.03}}$	$\mathbf{> 3.5}$
2	0.900	0.115	0.110	0.91 ± 0.02	$0.18^{+0.04}_{-0.07}$	> 1.30
3	1.050	0.126	0.128	$1.06^{+0.02}_{-0.03}$	$0.14^{+0.15}_{-0.04}$	$1.09^{+0.35}_{-0.25}$
4	1.200	0.200	0.195	$1.21^{+0.03}_{-0.05}$	$\mathbf{0.31^{+0.04}_{-0.06}}$	$1.24^{+0.78}_{-0.27}$
5	1.350	0.106	0.096	$1.39^{+0.03}_{-0.04}$	$\mathbf{0.16^{+0.09}_{-0.04}}$	$1.58^{+1.17}_{-0.49}$
6	1.500	0.298	0.269	$\mathbf{1.42^{+0.06}_{-0.02}}$	$\mathbf{0.46^{+0.04}_{-0.10}}$	$\mathbf{> 1.96}$
7	1.650	0.379	0.394	$\mathbf{1.62^{+0.02}_{-0.07}}$	$0.28^{+0.15}_{-0.03}$	$1.38^{+1.47}_{-0.37}$
8	1.800	0.519	0.493	$1.83^{+0.01}_{-0.09}$	$0.38^{+0.19}_{-0.07}$	$1.55^{+1.10}_{-0.41}$
9	1.950	0.448	0.430	$1.95^{+0.02}_{-0.13}$	$0.49^{+0.15}_{-0.10}$	> 0.93
10	2.100	0.537	0.561	$2.11^{+0.04}_{-0.10}$	$0.28^{+0.32}_{-0.08}$	$0.98^{+0.63}_{-0.16}$
11	2.250	0.536	0.483	$2.29^{+0.05}_{-0.07}$	$0.50^{+0.24}_{-0.12}$	$1.24^{+0.45}_{-0.31}$
12	2.400	0.591	0.530	$2.40^{+0.02}_{-0.16}$	$0.64^{+0.13}_{-0.22}$	> 0.84
13	2.550	0.990	1.035	$2.49^{+0.09}_{-0.25}$	$0.87^{+0.31}_{-0.05}$	$1.38^{+2.11}_{-0.38}$
14	2.700	0.957	1.007	$2.81^{+0.08}_{-0.30}$	$0.90^{+0.47}_{-0.14}$	$1.23^{+0.75}_{-0.28}$
15	2.850	1.077	0.950	$2.89^{+0.04}_{-0.31}$	$1.01^{+0.37}_{-0.07}$	$1.58^{+2.11}_{-0.50}$

Table 8.1: second and third column: NFW parameters r_{200}, r_s for the sample of synthetic halos used in our analysis. The fourth column shows the values of the scale radius r_ν of the projected number density profile of the particles fitted from the phase space, which is additionally required in the *MAMPOSSt* procedure. Last three columns: constraints on the free parameters r_{200}, r_s, $\mathcal{A} = \sigma_\theta/\sigma_r$ from the *MAMPOSSt* analysis in GR. Bold numbers indicate the cases in which the true values are excluded at the 68% C.L.

in the fit; this choice has been made to be consistent with real observations, although the range on which perform the fit could be totally arbitrary in this ideal case. Indeed, for an observed cluster we cannot assume the validity of Jean's equation behind r_{200}, moreover at very small radii the dynamics is dominated by the presence of the BCG.

As already discussed in Chapter 3 and Chapter 7, the version of *MAMPOSSt* code used within this Thesis additionally requires a parametric model of the projected number density profile of the tracers[2], with a characteristic scale radius r_ν; since I am working with collisionless particles, by construction the number density profile $\nu(r)$ scales exactly as the NFW mass profile $\rho(r)$ (i.e. $r_\nu \equiv r_s$). However, the *projected* number density profile, needed to compute the probability of eq. (3.38), is obtained in *MAMPOSSt* by integrating the the 3-dimensional profile along the line of sight, assuming that it extends to infinity. This leads to a value of r_ν which can be slightly different from r_s; for this reason I fit the projected number density profile form the phase space of each clusters and I use the best fit values of r_ν as the input for the *MAMPOSSt* analysis (see the fourth column of Table 8.1). This is also more reliable from an observational point of view: as mentioned in Chapter 3, in a real cluster it is not guaranteed that the distribution of the tracers (i.e. the member galaxies) scales in the same as the total density profile. In general, the projected number density profile is determined by fitting the observed distribution of the member galaxies. I have checked that the results do not change if we fix $r_\nu = r_s$.

The last three columns of Table 8.1 show the constraints on the free parameters in the GR analysis, r_{200}, r_s and $\mathcal{A}$, defined as the ratio:

$$\left(\frac{\sigma_\theta}{\sigma_r}\right)_\infty \equiv \frac{1}{\sqrt{1-\beta_\infty}}. \tag{8.2}$$

As expected, the true values of the parameters for each halo are included within the 68% confidence level with the exception of few cases (marked in bold); this consistency check confirms that the *MAMPOSSt* method effectively recovers the dynamical parameters for ideal spherically-symmetric halos in equilibrium configuration, modulo statistical fluctuations in the sampling of the projected phase spaces. As an example, Figure 8.2 shows the marginalized probability distributions (upper plots) and the 2-dimensional contours at $\Delta\chi^2 = 2.3$ and $\Delta\chi^2 = 4.6$ (bottom plots, blue and green curves respectively), for the halo number 9. The

[2]It is important to notice that in general the *MAMPOSSt* procedure does not necessarily involve a parametrization for the physical quantities in the Jenas' equation; nevertheless, for the purpose of this Thesis a parametric approach is worthed to investigate specific class modified gravity models, as pointed out in Chapter 3.

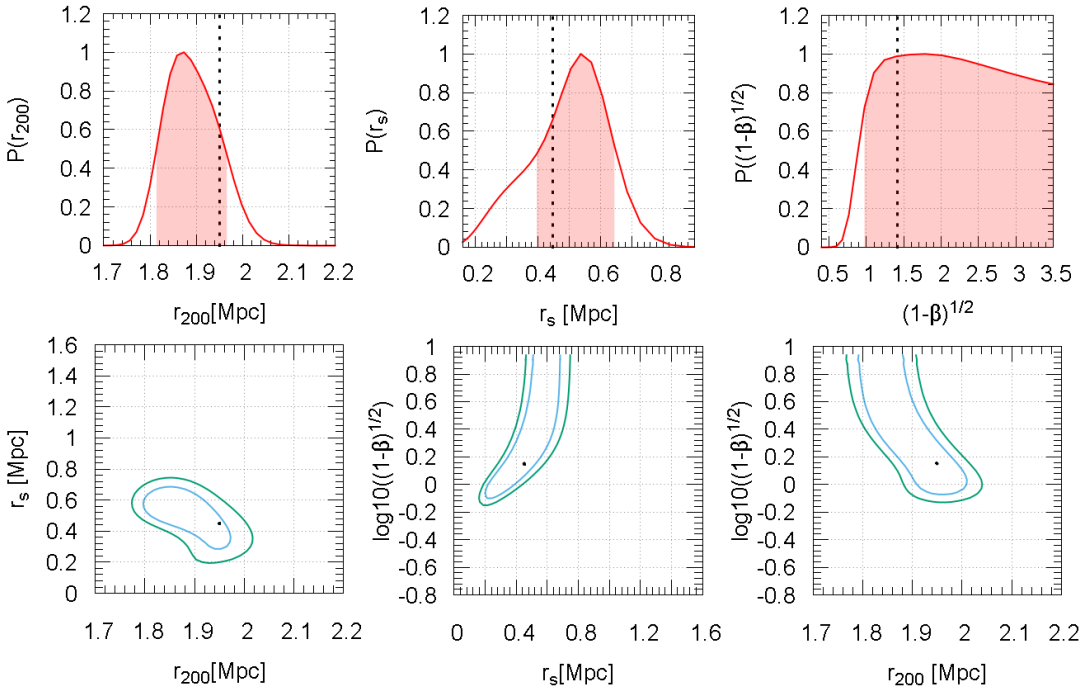

Figure 8.2: Upper plots: marginalized probability distributions of the parameter r_{200} (left) rs (central) and $\mathcal{A} = (1 - \beta_\infty)^{-1/2}$ (right) from the *MAMPOSSt* fit in GR. The red shaded areas correspond to the 68% confidence level for r_{200}, r_s and to the $\Delta\chi^2 = 1.0$ region for $\mathcal{A}$. Black vertical dotted lines are the true values of each parameter. Bottom plots: iso-probability contours of the 2-dimensional likelihood obtained integrating over the third parameter. The blue contours indicates $\Delta\chi^2 = 2.3$, while the green curves correspond to $\Delta\chi^2 = 4.6$. True parameter values are marked as the black point in each plot.

black vertical dotted lines and the black points indicate the true values of the parameters.

I then apply the *MG-MAMPOSSt* method to the synthetic clusters sample in linear $f(R)$ gravity, fitting together the scalaron mass $m \equiv m_{f,R} = 1/\lambda$, the mass profile parameters r_s and r_{200} and the anisotropy normalization β_∞ in the same projected radial range $[0.05\,\mathrm{Mpc}, r_{200}]$.

The 2-dimensional marginalized likelihoods in the plane $(r_{200}, \log(m))$, $(r_s, \log(m))$ and the 1d distribution of the scalaron mass $P[\log(m)]$ are shown in Fig. 8.4 for the halo number 1 (upper plots), the halo number 8 (central plots) and the halo number 15 (bottom plots). In each 2-dimensional distribution the red contours indicate points lying within $\Delta\chi^2 = 2.3$ from the *MAMPOSSt* best fit, while the black solid contours correspond to $\Delta\chi^2 = 4.6$. Note that here I am considering the parameter $\log(m)$ instead of λ: this means that GR is virtually recovered for $\log(m) \gtrsim 1.8$, which corresponds to $\lambda \gtrsim 1.8\,\mathrm{Mpc}$. Indeed, for larger values of

the modified gravity parameter the relative change in the marginalized likelihood is on average less than 0.1% (see Figure 8.3). The results from *MG-MAMPOSSt* show the same behavior as for the analysis of MACS 1206 and RXJX 2248, discussed in Chapter 7; even in the ideal case, no constraints can be obtained on the scalaron mass. This fact is a consequence of the degeneracy between the mass profile parameters and the modified gravity parameter in this particular class of models. The velocity dispersion of a self-gravitating system of particles in GR can be mimicked by a modification of gravity with a suitable combination of r_{200}, r_s and m producing the same effect on the phase space of the tracers. In particular, from the structure of eq. (2.23) one can see that an increase of the value of $\lambda = 1/m$ (i.e. larger departure from GR) corresponds to an increment in ϕ_{mg} which can be compensated by lowering r_{200}. In the same way, a shift from GR could be obtained by increasing r_s; this is responsible for the peak in the marginalized distribution of m. Moreover, since the term $m\, r_s$ always appear as an exponent, a small variation in the scale radius is sufficient to move the maximum of $P(m)$ away from the GR expectation $m \to \infty$. Nonetheless, GR is always included within 1σ, and the results are independent from the values of r_s and r_{200}; I remark that the same behavior has been found for all the phase spaces analyzed.

As an additional test, I investigate the effect of increasing the statistics by doubling the number of tracers used in the *MAMPOSSt* fit. I thus generate 8 new halos, all with the same values of the NFW parameters $r_{200} = 1.96\,\mathrm{Mpc},\ r_s = 0.27\,\mathrm{Mpc}$, which can be interpreted as different random realizations of the same cluster; each halo is built with 2000 particles within the virial radius. I furthermore fix the anisotropy parameter to the true value $\beta_\infty = 0.5$ in order to reduce the number of free parameters. Figure 8.5 shows the contours at $\Delta\chi^2 = 2.3$ in the space $(r_{200}, \log(m))$ and $(r_s, \log(m))$ for all the 8 realizations. Despite the large number of points in the fit and the idealized control of all the assumptions, m remains unconstrained, even if GR is never excluded within 1σ; this result indicates that the analysis of the dynamics of galaxies in a cluster with the *MAMPOSSt* method alone is not sufficient to constrain deviation from standard gravity in $f(R)$ models. It is worth to notice that the results obtained in this part are independent of the anisotropy model used to generate the synthetic cluster. However, in the *MAMPOSSt* analysis I found that the profile labeled as "O" (see eq. (3.35)) produces a slightly stronger degeneracy between the scale radius r_s and the mass scale of the scalaron m in the Likelihood distribution; this is a consequence of the different dependence of $\beta(r)$ from r_s, which is exponentially enhanced in eq. (3.36).

One can now assess how strong should be a prior on the NFW parameters, such as the one

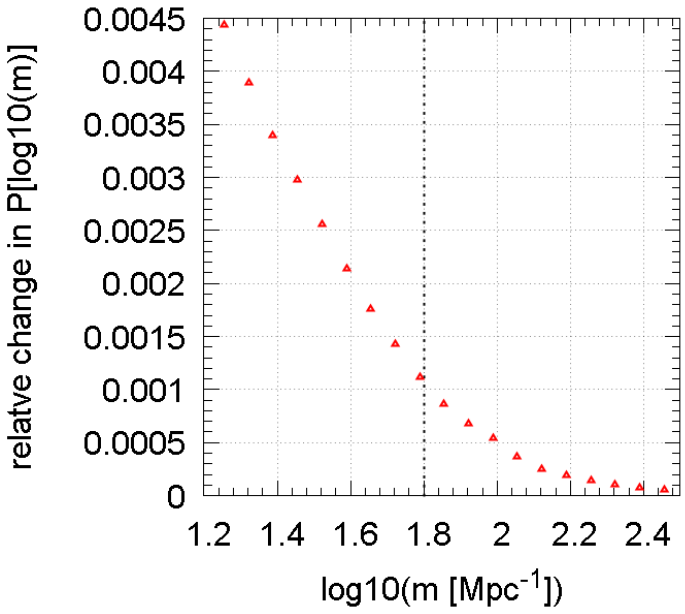

Figure 8.3: Relative changes in the marginalized likelihood $P[log(m)]$ for the *MG-MAMPOSSt* analysis of the galaxy cluster RXJ 2248 with the "T" anisotropy model and NFW mss profile. The vertical dotted line corresponds to the limit chosen in this work above which GR is assumed to be totally recovered.

provided by a lensing probe (which, as shown in the previous chapter, is not sensitive to the additional parameter m), in order to break the degeneracy in the dynamics likelihood and produce competitive constraints on the modified gravity parameter.

8.1.2 Effect of priors on the NFW parameters

I simulate the availability of additional information on r_s and r_{200} as a bivariate Gaussian distribution:

$$P_L(r_s, r_{200}) = \frac{1}{2\pi\sigma_{r_s}\sigma_{r_{200}}\sqrt{1-\rho^2}} \exp\left\{-\frac{1}{2(1-\rho^2)}\left[\frac{(r_s-\bar{r}_s)^2}{\sigma_{r_s}^2}+\right.\right.$$

$$\left.\left.+\frac{(r_{200}-\bar{r}_{200})^2}{\sigma_{r_{200}}^2}-\frac{2\rho(r_s-\bar{r}_s)(r_{200}-\bar{r}_{200})}{\sigma_{r_s}\sigma_{r_{200}}}\right]\right\}, \tag{8.3}$$

centered on the true values of the NFW parameters $\bar{r}_s, \bar{r}_{200}$ shown in Table 8.1. In the above equation, ρ indicates the correlation. I then obtain the joint likelihood distribution $\log\mathcal{L}_{tot} = \log\mathcal{L}_{dyn} + \log P_L$, where $\mathcal{L}_{dyn}(r_{200}, r_s, \beta, m)$ is the likelihood from the *MAMPOSSt* analysis.

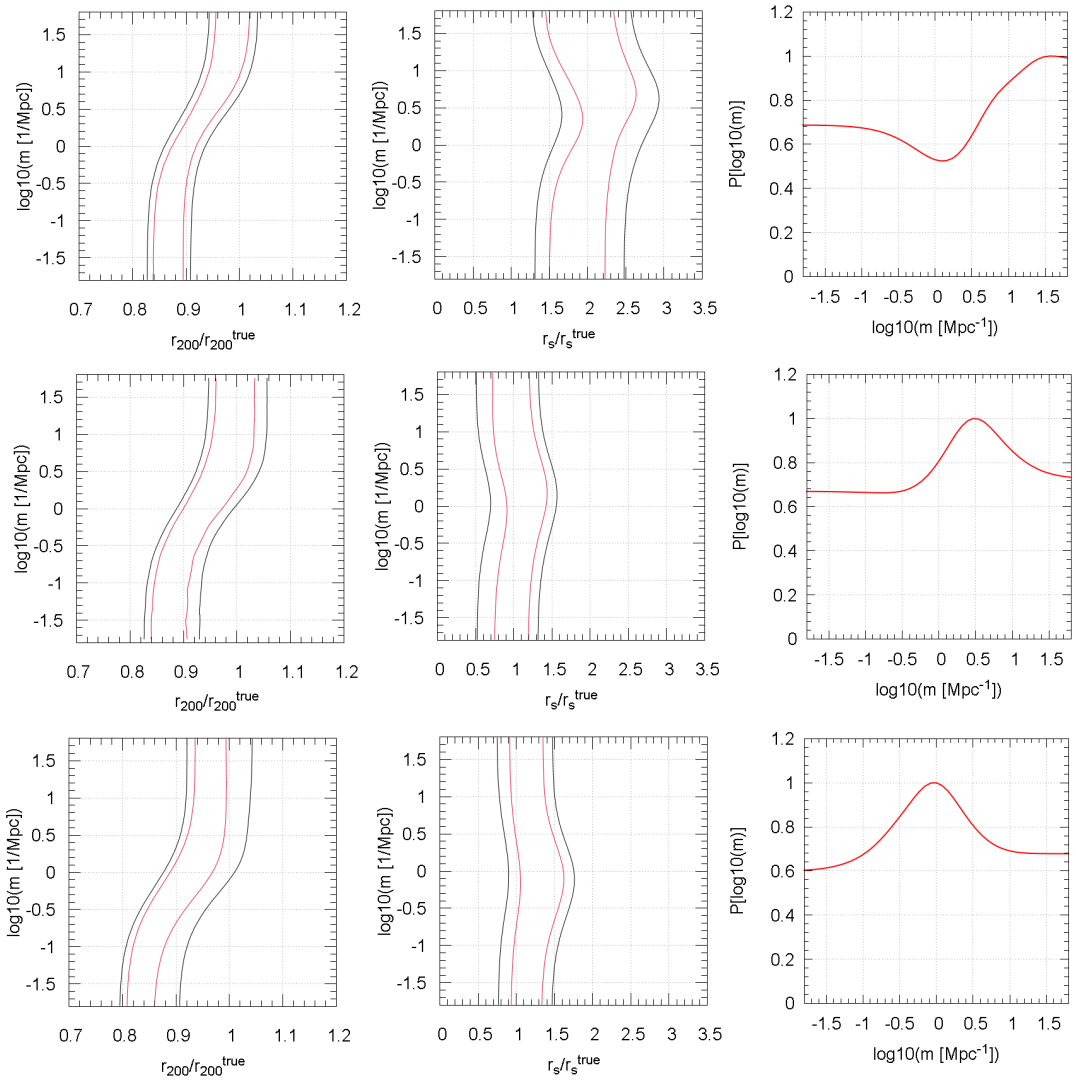

Figure 8.4: In each row: 2-dimensional likelihood distributions in the plane $(r_{200}, \log(m))$ (left plot), $(r_s, \log(m))$ (central plot) and the marginalized distribution $P[\log(m)]$ obtained by the emphMG-MAMPOSSt analysis of the synthetic halo number 1, 8 and 15. the red contours in the left and central plots refer to points at $\Delta\chi^2 = 2.3$, while the black contours indicate points at $\Delta\chi^2 = 4.0$. First line: halo 1. Central line: halo 8. Bottom line: halo 15.

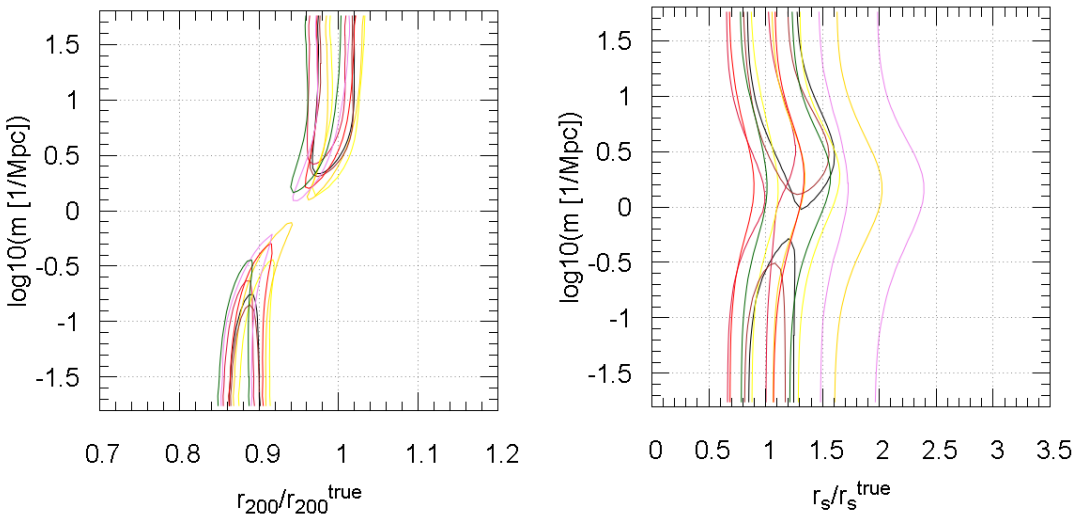

Figure 8.5: 2-dimensional contours at $\Delta\chi^2 = 2.3$ in the plane $(r_{200}, \log(m))$ (left plot) and $(r_s, \log(m))$ (right plot), obtained by the *MG-MAMPOSSt* analysis of 8 halos with 2000 particles within r_{200}. Different colors refer to different clusters.

In general, the virial radius r_{200}, which is related to the total cluster mass, can be constrained much better than the shape of the halo mass profile, expressed in terms of r_s. As shown e.g. in Table 2 of ref. [35], typical uncertainties on the scale radius given by a lensing probe are of the order of $\sim 30 \div 40\%$, while r_{200} can be recovered up to $\sim 5 \div 10\%$; I thus assume a fixed $\sigma_{r_s} = 0.4 \times r_s$, while I change $\sigma_{r_{200}}$ to investigate the variation of the bounds on the modified gravity parameter as a function of the additional constraints on the virial radius. As for the correlation ρ between r_s and r_{200} in $P_L(r_s, r_{200})$ I use the value $\rho = 0.67$ found by fitting a bivariate Gaussian on the posterior distribution of the Strong+Weak lensing analysis of MACS 1206 discussed in the previous Chapter. It is worth to notice that, despite different values of the correlation mildly change the shape of the confidence regions for each cluster, the overall qualitative behavior resulting from our analysis is independent of the choice of ρ.
In Fig. 8.6 I plot the contours at $\Delta\chi^2 = 2.3$ in the 2-dimensional plane $(r_{200}, \log(m))$ (left) and $(r_s, \log(m))$ (right) for halo 1 (upper plots), 8 (central plots) and 15 (bottom plots), increasing the strength of the prior on r_{200}.

This simple exercise shows that an additional information on r_s, r_{200} with 40% and $7 \div 10\%$ uncertainties respectively is on average sufficient to produce constraints on m by the joint "lensing"+dynamics analysis of a single ideal cluster when the number of galaxies in the

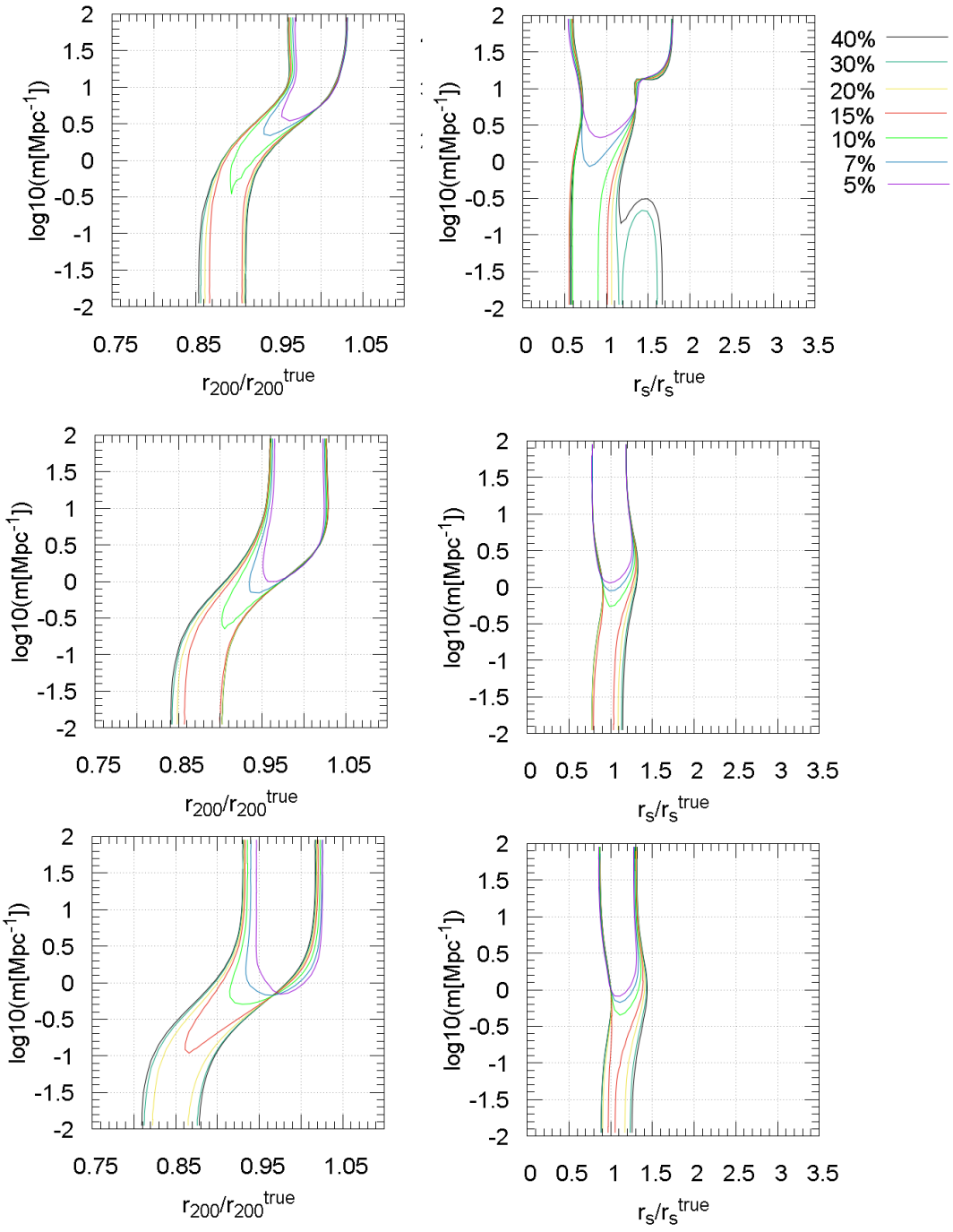

Figure 8.6: 2-dimensional contours at $\Delta\chi^2 = 2.3$ in the parameter space $(r_{200}, \log(m))$ (left) and $(r_s, \log(m))$ (right) for different values of $\sigma_{r_{200}}$ in $P_L(r_s, r_{200})$, from 40% (black curves) to 5% (purple curves). Upper line: halo 1. Central line: halo 8. Bottom line: halo 15

dynamics analysis is $\sim 10^3$. It is worth to notice that this result doesn't change significantly with the number of dynamical tracers in the phase space; moreover, each synthetic phase space never excludes the GR limit within 1σ. The contours in the plane $(r_s, \log(m))$ for halo 1 (right upper plot) are a consequence of the fact that the likelihood from dynamics in r_s is largely biased with respect of true value, as already shown in Table 8.1 for the GR analysis, producing a joint distribution almost bimodal in the scale radius; nonetheless, the constraints on m are unaffected by such behavior.

The dependence of the averaged lower limits in the marginalized distributions of m on the strength of the prior on r_{200} at $\Delta\chi^2 = 1.0$ (red bars) and $\Delta\chi^2 = 4.0$ (blue bars) is shown in the left panel of Figure 8.7. Each point is obtained by averaging the lower limits for every halo, while the associated errorbars correspond to the dispersion around the mean value.

In order constrain m at 95% confidence level with one cluster, one need at least $\sigma_{r_{200}} = 0.07 \times r_{200}$. The right panel of the same Figure displays instead the distributions obtained by combining the marginalized total likelihoods of all the 15 clusters as a function $\sigma_{r_{200}}$. In this case, a prior of 40% in r_s and r_{200} for a relatively small number of halos is already enough to provide stringent bounds on the scalaron mass. I obtain:

$$m \geq 7.6\,\mathrm{Mpc}^{-1} \qquad \Delta\chi^2 = 4.0,$$

$$m \geq 18.8\,\mathrm{Mpc}^{-1} \qquad \Delta\chi^2 = 1.0, \tag{8.4}$$

corresponding to $\lambda \leq 0.053\,\mathrm{Mpc}$ at $\Delta\chi^2 = 1.0$ which is close to the lower limit of the radial range considered in this analysis ($R = 0.05\,\mathrm{Mpc}$), and thus it is the tightest constraint reachable with our method. Indeed, decreasing $\sigma_{r_{200}}$ produces negligible effects on the combined distribution, as shown in Fig. 8.7; clearly, this result relies on the perfect control of the assumptions in the analysis. I will discuss deviations from the ideal situation of a spherically symmetric halo in perfect equilibrium as a possible source of systematics in the next section.

8.2 Analysis of ΛCDM cosmological simulations

The results from the analysis of the synthetic halos indicate that, in the ideal case, a combination of lensing and dynamics with reliable uncertainties and number of tracers for about a dozen objects is enough to constrain the interaction range up to $\sim 50\,\mathrm{kpc}$. In order to understand what

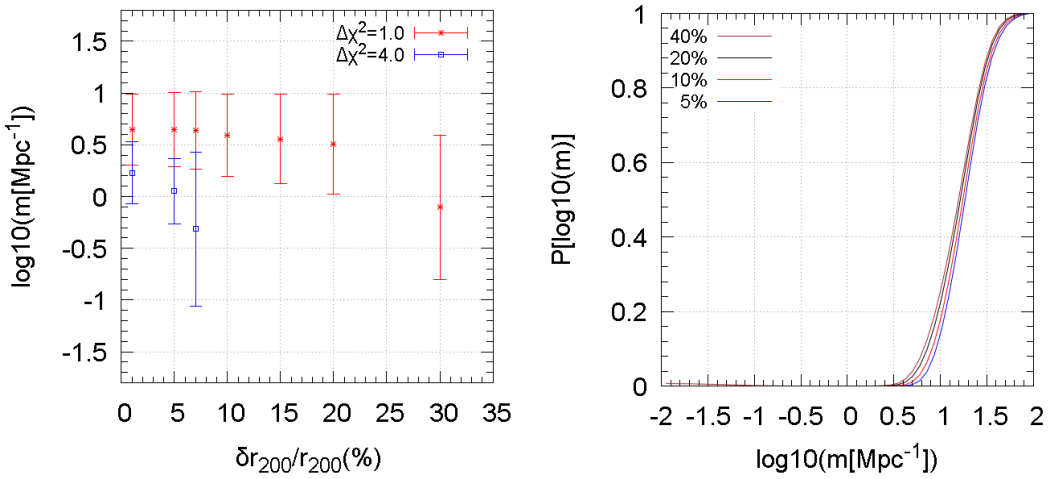

Figure 8.7: Left: lower limit on m obtained averaging the lower limits of each marginalized distribution from the analysis of the 15 synthetic halos as a function of $\sigma_{r_{200}}$ in $P_L(r_s, r_{200})$ (points); the error bars indicate the scatter around the mean value computed over this ensemble of synthetic halos. Red: $\Delta\chi^2 = 1.0$. blue: $\Delta\chi^2 = 4.0$. Right: all-halos-combined distribution of m. Different lines correspond to different values of the prior in r_{200}

kind of clusters in the real Universe should be observationally selected as testbed for constraining deviations from GR, one needs to investigate how departures from the main assumptions of the analysis affects the constraints on m. To this purpose, I consider a set of 29 simulated DM halos selected as the most massive clusters at the center of 29 Lagrangian regions from a cosmological ΛCDM simulation carried out with the parallel Tree-PM SmoothedParticle-Hydrodynamics (SPH) code GADGET-3 of ref. [37]. The parent simulation consists in a periodic box of size $1\,h^{-1}Gpc$ and assumes a flat cosmology with $\Omega_m = 0.24$, $\Omega_\Lambda = 0.76$, $h = 0.72$ and $\sigma_8 = 0.8$ (see e.g. refs. [208, 209, 156]). Each Lagrangian region is re-simulated with the Zoomed Initial Condition (ZIC) technique of ref. [210]; particles of mass increasing with distance are used outside the region to correctly reproduce the tidal field on large scales. In the high-resolution region the mass of DM particles is $m_{DM} = 10^9\,h^{-1}M_\odot$; the simulation is performed in such a way that at $z = 0$ the central halo in not contaminated by low-resolution particles at least out to $5 \times r_{200}$.

Among the central halos, 24 over the 29 in the sample have masses $M_{200} > 8 \times 10^{14}\,h^{-1}M_\odot$, while the remaining 5 are less massive ($M_{200} \sim 1 \div 4 \times 10^{14}\,h^{-1}M_\odot$). In order to increase the statistics in the mass range spawned, I consider also other 20 DM halos, selected among the second massive clusters in each Lagrangian region, requiring that no low resolution particles

are included out to $3 \times r_{200}$. I additionally restrict the analysis only to those halos for which $r_{200} \geq 1\,\mathrm{Mpc}$ at $z = 0$ (corresponding to $M_{200} > 9 \times 10^{13}\, h^{-1} M_{\odot}$). I refer to the first sample as "group 0", while I call "group 1" the halos belonging to the second sample.

I parametrize the mass profile of each simulated cluster as a NFW model, which is shown to provide a good description for dark matter halos in cosmological simulations as discussed in Chapter 1. In the first two columns of Table 8.2 I list the best fit values of the NFW parameters r_{200}, r_s, obtained by a Maximum Likelihood fit over the total 3-dimensional distribution of particles in every cluster. The other four columns indicate the best fit values of the velocity anisotropy free parameter, resulting from the 3D fit of $\beta(r)$ over the particle velocity distribution for each model adopted in this analysis (see below). In the "O" and "T" profile, the fit is done considering the anisotropy scaling radius $r_c \equiv r_s$, as assumed in the *MAMPOSSt* procedure.

Since I am now interested only in calibrating the effect induced by systematics in our constraints on $m = 1/\lambda$, I fix the parameters r_s and r_{200} of the mass profile in the *MAMPOSSt* procedure to be equal to the "true" values of Table 8.2. As shown in Sec. 8.1, for a halo for which all the assumptions are satisfied MAMPOSSt provides results that are always compatible with GR within 1σ, independently of the mass of the cluster and the anisotropy model used to generate the object. Therefore, any departure from this condition is a measure of the systematic uncertainties affecting the analysis.

I randomly select 5 subsamples of 1200 DM particles from each halo in the radial range $[0, 1.2\, r_{200}]$ (so that $\sim$ 1000 particles are included in the *MAMPOSSt* fit from $0.05\,\mathrm{Mpc}$ to r_{200}), considering every bi-dimensional projection as an independent phase space. This fact takes into account our ignorance about the orientation with which a generic cluster is observed on the sky as well as possible biases in the completeness of the tracers distribution.

I run the *MG-MAMPOSSt* code on a total of 735 projected phase spaces to fit together the scalaron mass m and the velocity anisotropy parameter β, adopting 4 different anisotropy models, namely the "T", "ML", "O" and "C" profiles of eqns. (3.34), (3.33), (3.35) and (3.32) respectively. Looking at the marginalized distribution of m, I classify the phase spaces as "regular" (R) if the *MAMPOSSt* analysis does not exclude GR at 68% C.L., "semi-regular" (SR) if GR is included within 95% C.L. and "irregular" (IR) if the tension with standard gravity is larger than 2σ. The percentage of each class is shown in Table 8.3 for all the β profile models assumed in our analysis. As discussed above, we assume that GR is recovered for $\log(m) \gtrsim 1.8$, which corresponds to a galaxy-scale interaction range $\lambda \leq 0.015\,\mathrm{Mpc}$. The

ID	r_{200} [Mpc]	r_s [Mpc]	c_{200} [Mpc]	r_β("ML") [Mpc]	σ_θ/σ_r("T")	σ_θ/σ_r("O")	σ_θ/σ_r("C")
group 0							
1	2.443	0.727	3.360	0.147	>20	0.971	0.407
2	1.612	0.466	3.459	0.127	2.016	1.235	0.393
3	1.767	0.549	3.219	0.28	1.738	1.107	0.316
4	1.639	0.755	2.171	0.198	2.293	0.905	0.343
5	1.178	0.464	2.539	0.473	1.392	1.092	0.261
6	2.328	0.706	3.298	0.089	>20	0.94	0.443
7	2.308	0.656	3.518	0.27	1.677	0.909	0.307
8	2.458	1.205	2.040	>10	0.904	0.958	-0.031
9	1.016	0.220	4.618	0.096	1.617	1.862	0.413
10	2.281	0.549	4.154	0.324	1.621	1.065	0.3
11	2.140	0.781	2.740	1.446	1.241	0.916	0.158
12	2.690	1.157	2.325	0.196	>20	0.837	0.359
13	2.450	2.240	1.094	5.317	1.155	0.971	0.049
14	2.573	0.731	3.520	0.277	2.444	0.992	0.327
15	2.511	0.831	3.022	0.133	3.181	0.841	0.373
16	3.211	1.231	2.608	0.616	2.18	0.907	0.226
17	2.554	1.516	1.678	0.236	>20	0.84	0.345
18	2.124	0.703	3.021	0.58	1.435	0.897	0.242
19	2.297	0.687	3.344	0.051	>20	0.916	0.486
20	2.503	0.806	3.106	0.111	>20	0.918	0.446
21	2.419	0.477	5.412	0.285	1.487	1.046	0.302
22	2.644	0.519	5.094	0.032	>20	1.249	0.539
23	2.297	0.525	4.375	5.267	1.067	0.912	0.09
24	2.328	0.490	4.751	0.089	2.823	1.287	0.437
25	2.102	0.869	2.418	3.317	1.119	0.953	0.082
26	2.404	0.782	3.074	0.527	1.589	0.936	0.241
27	2.458	1.003	2.451	0.292	2.671	0.859	0.31
28	2.658	0.546	4.869	0.657	1.378	1.054	0.229
29	2.452	1.199	2.045	0.805	1.749	0.91	0.2

ID	r_{200} [Mpc]	r_s [Mpc]	c_{200} [Mpc]	r_β("ML") [Mpc]	σ_θ/σ_r("T")	σ_θ/σ_r("O")	σ_θ/σ_r("C")
group 1							
1	1.069	0.247	4.328	0.615	1.234	1.213	0.239
2	1.060	0.199	5.327	0.141	1.44	1.549	0.364
3	1.349	0.316	4.269	0.236	1.397	1.255	0.313
4	0.850	0.204	4.167	0.255	1.413	1.681	0.333
5	1.104	0.208	5.308	0.277	1.305	1.321	0.297
6	1.095	0.332	3.298	0.83	1.213	1.099	0.211
7	1.701	0.533	3.191	0.741	1.298	1.006	0.214
8	1.581	0.644	2.455	0.403	1.612	0.99	0.274
9	1.028	0.855	1.202	2.722	1.144	0.971	0.089
10	1.962	0.433	4.531	0.253	1.581	1.271	0.323
11	1.772	0.427	4.150	2.379	1.129	0.928	0.158
12	1.189	0.935	1.278	>20	0.998	1.001	-0.002
13	1.546	0.350	4.417	>20	0.969	0.909	-0.014
14	0.887	0.532	1.667	0.176	2.272	1.3	0.381
15	1.987	0.782	2.541	0.94	1.326	0.897	0.194
16	1.086	0.334	3.216	>20	0.927	0.815	-0.04
17	1.508	0.374	4.032	4.369	1.05	1.078	0.044
18	1.671	0.235	7.111	0.146	1.458	1.517	0.357
19	1.403	0.302	4.646	1.274	1.161	1.118	0.17
20	1.381	0.377	3.663	0.752	1.251	1.134	0.215

Table 8.2: Best fit values of the NFW mass profile parameters (second and third column) and of the velocity anisotropy parameter (last four column) obtained by a fit over the 3D particles and velocities distribution of all the dark matter halos considered in this analysis. The "T" anisotropy model (5^{th} column) provides the lowest χ^2 for $\sim 60\%$ of the sample

β	R(%)	SR(%)	IR(%)
T	42	13	45
ML	26	11	63
O	27	16	57
C	33	10	57

Table 8.3: Percentage of simulated phase spaces which give a marginalized likelihood of m compatible with GR at 1σ (R), at 2σ (SR) and excluding GR at more than 2σ (IR) when running *MAMPOSSt* with 4 different anisotropy models.

results are slightly different when varying the ansatz on $\beta(r)$; as already discussed in Chapters 6 and 7, changing the model of β is an additional source of systematics in the dynamical analysis. On average, given a generic population of clusters in a universe described by General Relativity, $\sim 30\%$ of the sample is suitable to be used as a test for gravity, regardless of the choice of the anisotropy profile. Interestingly, the "T" model, which provides the highest number of distributions in agreement with GR predictions, is also the parametrization with the lower χ^2 from the fit to the the 3-dimensional anisotropy profile for more than half of the halo sample analyzed.

In order to identify the main sources of spurious departures from standard gravity, as well as to characterize the properties of the "regular" projections, I consider two observational criteria based on the informations that can be directly extracted form the projected phase space.

Anderson Darling Coefficient

The first criterion expresses deviations from Gaussianity rest frame velocity distribution of the tracers along the line of sight which, as discussed in e.g. ref. [38], is a good indicator of the dynamical relaxation state of a galaxy cluster. Indeed, observations and theoretical studies of relaxed systems point out that at equilibrium the l.o.s distribution of galaxies is well described by a Gaussian distribution, while unrelaxed objects show large departures from normality (see e.g. refs [211, 212]); furthermore, ref. [38] found that this indicator highly correlates with other relaxation proxies from X-ray analyses, suggesting that it is a suitable criterion to describe the overall dynamical configuration of a cluster.

Deviations from Gaussianity are quantified by the so called Anderson-Darling (AD) test (T. Anderson & A. Darling, 1952), which determines how different are the cumulative distribution functions of the data set and of the ideal Gaussian case. The AD coefficient A^2 is defined as:

$$A^2 = -n - \frac{1}{n}\sum_{i=1}^{n}\left\{\left[\log\Phi(x_i) + \log(1-\Phi(x_{n+1-i}))\right](2i-1)\right\}. \tag{8.5}$$

In the above equation x_i is the i^{th}-element of the data set, in ascending order, which in our case corresponds to the velocity of the i^{th} particle; $\Phi(x_i)$ is the value of the cumulative Gaussian distribution function[3] at x_i. A large value of A^2 means large deviation from Gaussianity. The left panel of Figure 8.8 illustrates the shape of the l.o.s. velocity distribution for two projected

[3]The AD statistics can be used to test other known distributions, such as flat or exponential, changing the form of $\Phi(x)$

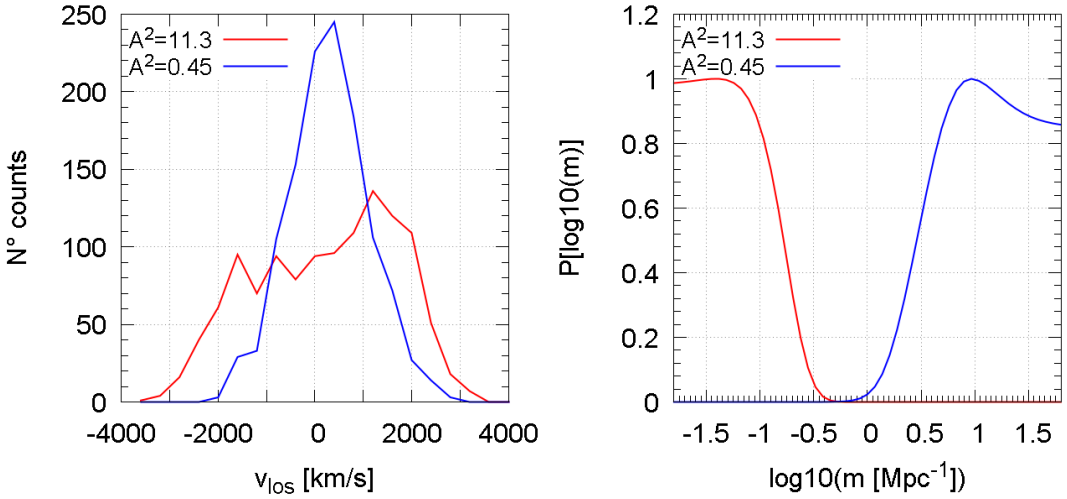

Figure 8.8: Left panel: line of sight velocity distributions of two projected phase spaces characterized by a large and a small value of the AD coefficient (red and blue solid curves respectively). Right panel: corresponding distributions $P[\log(m)]$ obtained by applying *MG-MAMPOSSt* procedure on these projected phase spaces assuming a "T" velocity anisotropy model in the fit.

phase spaces in our sample characterized by a value of $A^2 = 11.3$ (red curve) and $A^2 = 0.45$ (blue curve); on the right panel I show the corresponding marginalized distributions $P[\log(m)]$ from the *MG-MAMPOSSt* analysis with a Tiret model for $\beta(r)$. As we can see, while the phase space with $A^2 < 1$ produce a constrain on m in agreement with GR, the analysis of the projected phase space with large A^2 excludes standard gravity at more than 4σ.

Projected Chi Square

The second parameter used in this analysis is the reduced χ^2 resulting from fitting the projected numerical distribution of galaxies $\nu(r)$ in the phase space with a projected NFW density profile. The value of χ^2_ν incorporates the effect of several systematics, such as departures from spherical symmetry, the presence of substructures in the phase space and the uncertainties in the choice of the parametrization of the number density profile.

In Figure 8.9 I plot the probability $p(GR)$ of finding a cluster consistent with GR predictions within 1σ as a function of χ^2_ν (left plot) and of A^2 (right plot) for the 4 models of $\beta(r)$. Interestingly, I found an overall increase of $p(GR)$ towards lower values of both parameters, with a stronger effect for the AD statistics, and the result does not depend on the chosen ansatz in the velocity anisotropy. This means that phase spaces suitable for the application of our method should be identified among those clusters characterized by an almost Gaussian l.o.s.

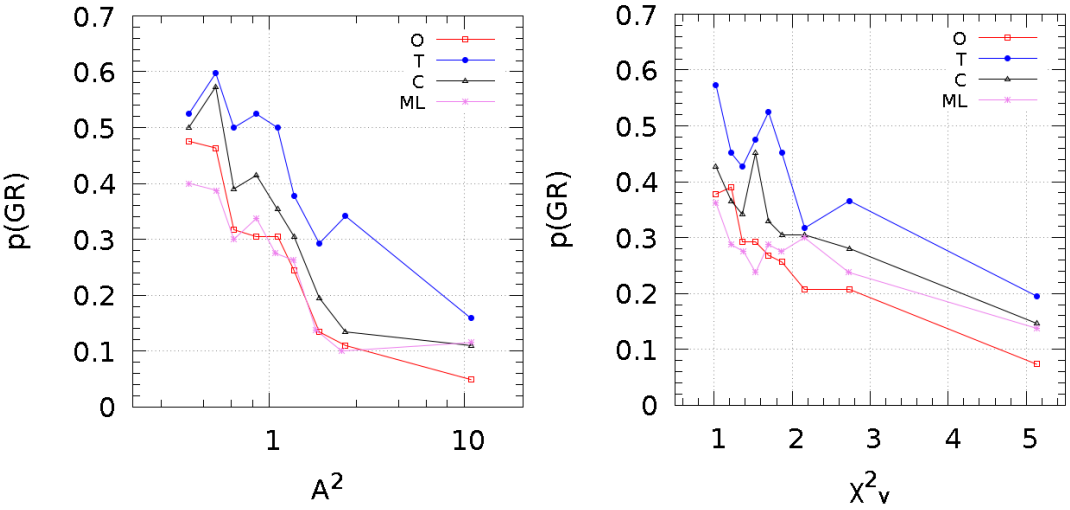

Figure 8.9: Probability that, given a generic phase space, the *MG-MAMPOSSt* analysis produces results compatible with GR predictions within 1σ, expressed as a function of the reduced χ^2_ν (left plot) and the AD coefficient A^2 (right plot). Different colors and point types refer to different anisotropy models. The binning is computed such that each bin contains the same number of clusters.

velocity distribution ($A^2 < 1$) and a reduced chi square in the fit of the projected number density profile $\chi^2_\nu < 1.5$.

To further highlight this behavior, Fig.8.10 shows the 2-dimensional variation of $p(GR)$ for a grid of values of A^2 and χ^2_ν. As expected, the probability rises in the region corresponding to the lower values of chi square and AD coefficient, reaching $\sim 70\%$ for the "T" model (left upper panel). It is worth to notice that $p(GR)$ drops to zero for $A^2 < 1$ and large χ^2_ν; this is due to the fact that there are no clusters with those particular combinations of parameters. In other words, phase spaces with a small AD coefficient tend also to be better described by a NFW profile.

I also explore 2 more theoretical criteria, which rely on the knowledge of the 3-dimensional structure of the halo. As such, they cannot be used as a discriminant to select clusters from observational data; however, since they are linked to the dynamical state of the halos, they can help in understanding the effect of the major systematics. Those criteria are the *center shift* δr, defined as the relative position between the center of mass of the system, computed considering all the particles within the virial radius, and the most gravitationally bound particle, in unit of r_{200}:

$$\delta r = \frac{|\mathbf{r}_{CM} - \mathbf{r}_{bound}|}{r_{200}}, \tag{8.6}$$

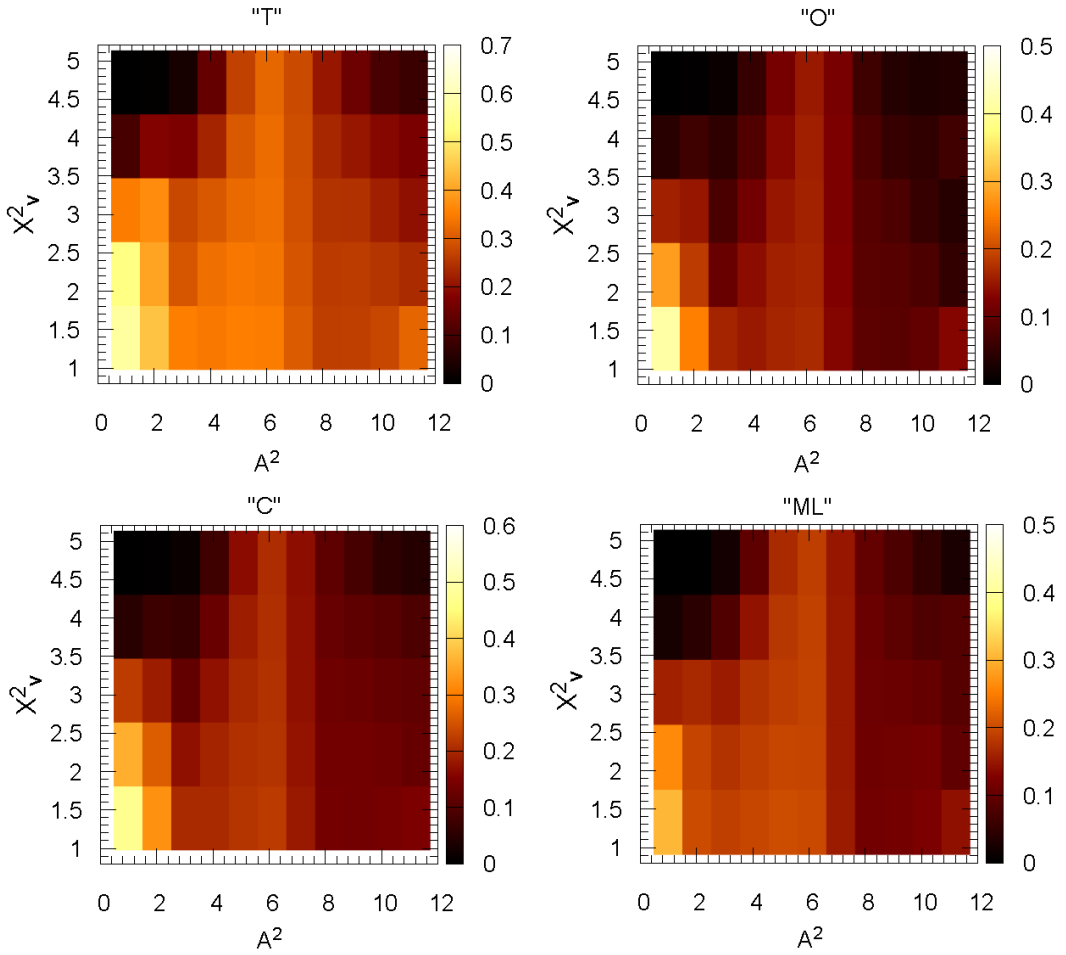

Figure 8.10: Color map of $p(GR)$ as a joint function of A^2 and χ^2_ν for the 4 anisotropy profile models. Each i^{th} bin is colored according to the probability of finding a "regular" phase space in the range of values $[A_{(i-1)}, A_{(i)}]$ and $[\chi^2_{\nu(i-1)}, \chi^2_{\nu(i)}]$.

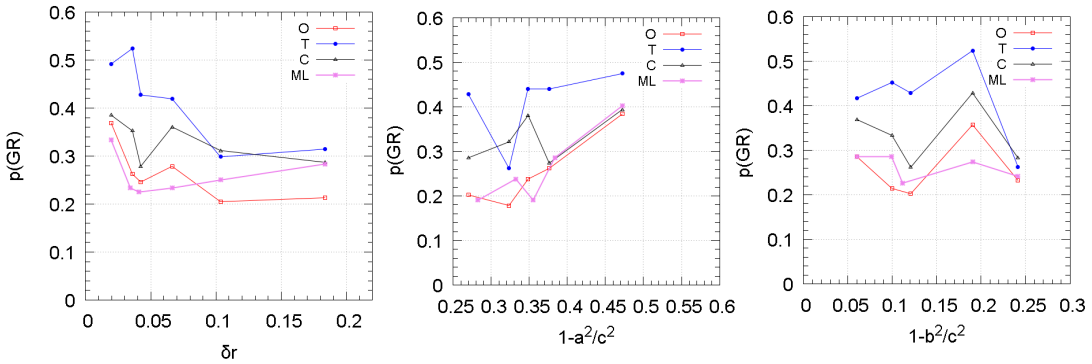

Figure 8.11: Left plot: $p(GR)$ as a function of the center shift δr. Central and right plot: $p(GR)$ as a function of the ratio ξ and ζ respectively. Different colors in each plot correspond to different models of the velocity anisotropy profile.

and the shape of the halo inertia ellipsoid, expressed in terms of the eigenvalues of the inertia tensor:

$$\mathcal{I}_{ij} = \frac{1}{M} \sum_k m_k x_i^{(k)} x_j^{(k)}. \tag{8.7}$$

In the above equation, k runs over all the particles within r_{200}, while i, j, label the three spatial dimensions; m_k is the mass of each particles and M the total mass $\sum_k m_k$

The center shift is widely used in numerical simulations to classify the dynamical state of a cluster (see e.g. ref. [156]), while the eigenvalues of $\mathcal{I}$, $a^2 < b^2 < c^2$, are related to the length of the semi-axes of the inertia ellipsoid a, b, c (e.g. ref. [213]), and thus parametrize deviation from spherical symmetry. I define the ratios $\xi = 1 - a^2/c^2$ and $\zeta = 1 - b^2/c^2$ such that in the case of a perfect sphere $\xi = \zeta = 0$.

In Figure 8.11 $p(GR)$ as a function of δr, ξ and ζ is shown in the left, central and right panels respectively. The center shift appears to correlate with the probability to find a phase space in agreement with GR, in particular for the case of the "T" anisotropy model for $\delta r \lesssim 0.1$, while no evident effects are observed when considering the eigenvalues of the inertia tensor; on the contrary, $p(GR)$ seems to slightly increase with the parameter ξ.

This shows that the shape of the inertia ellipsoid is not a good criteria to identify systematics induced by deviations from spherical symmetry in our analysis; the result is not surprising, since what really enters when building a projected phase space is the orientation of the halo on the plane of the sky with respect to the observer, which has been implicitly taken into account in the definition of the χ^2_ν parameter.

8.3 Discussions

In this Chapter I have examined a set of GR-simulated cluster-size Dark Matter halos in order to estimate the impact of systematics in constraining modification of gravity using a combination of dynamics and lensing mass profile determinations. As a case of study, I have considered the framework of linear $f(R)$ gravity, where deviations from GR are expressed in terms of the (constant) mass of the additional degree of freedom, $m \equiv m_{f_R}$. In the first part of the analysis, I have generated isolated spherically symmetric, self-gravitating distributions of collisionless particles according to a NFW mass profile, spawning approximately two orders of magnitude in masses. I have then analyzed the synthetic phase spaces with the *MG-MAMPOSSt* procedure to constrain m. I found that the dynamics analysis of 15 idealized halos with an additional information of about 40% uncertainties in the NFW parameters r_s and r_{200} (such as the one provided by a lensing probe) is sufficient to produce bounds on the modified gravity parameter which are close to the limit reachable when using cluster mass profiles. Combining the marginalized distributions $P(\log m)$ from the 15 synthetic clusters I have obtained $m \geq 7.6\,\mathrm{Mpc}^{-1}$ at $\Delta\chi^2 = 4.0$ when assuming $\sigma_{r_{200}} = 0.4 \times r_{200}$ and $\sigma_{r_s} = 0.4 \times r_s$ in the Gaussian probability distribution $P_L(r_s, r_{200})$ as given by any additional probe which is sensitive only to the Newtonian part of gravity. Moreover, each single $P(\log m)$ always includes the GR limit within 1σ, regardless of the values of the parameters with which the ideal clusters are generated.

In order to understand how much the breakdown in the assumptions of the analysis affects the constraints on m, I have furthermore considered 735 projected phase spaces of galaxy clusters extracted from cosmological N-body simulations carried out with with the GADGET-3 code. These clusters are taken at $z = 0$ and have masses in the range $9 \times 10^{13}\,h^{-1}M_{\odot} \div 4 \times 10^{15}\,h^{-1}M_{\odot}$; for each halo 5 projected phase spaces have been considered by randomly sampling 1200 Dark Matter particles in the radial range $[0.05\,\mathrm{Mpc}, 1.2\,r_{200}]$. The results show that $\sim 70\%$ of clusters in a ΛCDM Universe (where GR is assumed) produce a spurious detection of modified gravity when no selection criteria are used. This illustrates that the impact of systematics in the proposed method, in particular deviations from spherical symmetry and departures from a dynamical relaxed state of the cluster, plays a dominant role; an accurate control and calibration of such effects is thus required in order to claim our procedure robust.
I define two observational parameters which correlate with the probability to find clusters in

agreement with GR predictions and which can help in identifying the suitable clusters for the application of our method. These parameter are the Anderson-Darling coefficient A^2 of the l.o.s. velocity distribution and the reduced χ^2_ν of the projected number density profile of the tracers, which are connected to the main systematics affecting the analysis and can be directly measured from the projected phase space. The first one identifies deviation from Gaussianity of the l.o.s. velocity distribution, which is connected to the lack of dynamical relaxation, while the second criterion is related to several systematic effects, including deviations from spherical symmetry. The analysis I carried out shows that spurious detections of $\lambda \equiv 1/m > 0$ in the marginalized distribution are correlated with the values of these two observational criteria; in particular, the probability to find spurious detection of modified gravity decreases to $\sim 30\%$ for $A^2 < 1$ and $\chi^2_\nu < 1.5$ and "T" anisotropy model. Moreover, the trend is independent of the parametrization of the velocity anisotropy $\beta(r)$ in the *MAMPOSSt* analysis, which is the major source of uncertainties in the dynamics mass profile reconstruction. This demonstrates that the proposed criteria can be used to help in identifying the suitable clusters for the application of our method, among a generic population of objects.

The analysis presented within this Chapter has important implications for the study of galaxy clusters as test of models of gravity alternative to GR; as already discussed, with the next generation surveys such as Euclid, LSST, DES, a large amount of imaging and spectroscopic data will allow lensing and dynamics mass profile reconstructions for several hundreds clusters in quite large redshift range (e.g. Euclid will collect spectra of galaxies up to $z \sim 1.8$). The results of this work show that few selected clusters, with reasonable number of galaxies used in the dynamics analysis and feasible uncertainties on the additional lensing information, are needed to obtain a constraint on the interaction range $\lambda \leq 0.053\,\mathrm{Mpc}$ for linear $f(R)$ gravity. For viable models where $f_{,RR} \ll R^{-1}$, this corresponds to an average constraint on the second derivative of $f(R)$:

$$|f_{,RR(z=0)}| \lesssim 9.36 \times 10^{-4}\ \mathrm{Mpc}^2, \tag{8.8}$$

which is roughly three order of magnitude smaller than the bound derived from the analysis of a single cluster. For example, in the case of MACS 1206 the constraint $\lambda \leq 1.9\,\mathrm{Mpc}$ translates into $|f_{,RR(z=0)}| \lesssim 1.2\ \mathrm{Mpc}^2$. The detection of such small effects call for a rigorous control of the systematics and a careful selection of the clusters on which carry out our analysis. The criteria I have introduced in this Chapter provide a simple discrimination method which has the noticeable advantage that it requires only the projected information in the phase space. Moreover, even if I considered only halos at $z = 0$, the p.p.s. are independent of the redshift of the

cluster, so that the selection procedure can be applied at any relevant cosmological time.

It is worth to remind that the results of this analysis, although very interesting, are obtained studying only the dynamics of particles in simulated Dark Matter halos; the behavior of galaxies in real clusters can be significantly different from that of DM particles, in particular in the innermost regions where the effects of astrophysical processes become relevant (e.g. ref. [214]). Several developments of the work presented in this Chapter can be made in order to better quantify the effects of the above mentioned systematics. In particular, the analysis of the dynamics of substructures in high resolution simulations, the inclusion of baryons (gas and stars) as well as full lensing mass reconstructions will help in obtaining realistic constraints on modified gravity parameters, at different redshifts, to be compared with real data.

Conclusions

In this PhD Thesis I have presented an extensive analysis aimed at constraining models of gravity alternative to GR by combining mass profiles of galaxy clusters, reconstructed through two different methods: gravitational lensing and internal dynamics as traced by the motion of member galaxies. The analysis carried out focused on those classes of non-standard models which provide a possible explanation for the accelerated expansion of the Universe, one of the most challenging open problems in modern cosmology.

In the last decades, observations of the large-scale structure of the Universe and of the anistropies of the Cosmic Microwave Background have been improving in quantity and quality, reaching an unprecedented level of accuracy; nowadays, the Concordance Model, or ΛCDM model, is found to be in excellent agreement with a large amount of data-sets available from several probes. Nonetheless, in oder to account for the late-time accelerated expansion of the Universe, the Concordance Model introduces a cosmological constant Λ in the Einstein's equations which has no natural explanation in terms of the standard physics. Among the possible alternatives to Λ, one possibility is to modify the theory that describes the gravitational interaction, i.e. GR, in way that such modifications mimic the expansion history of the ΛCDM model without the contribution of the cosmological constant.
With the increasing precision in observational surveys, some analyses have revealed possible tensions between observations and theoretical predictions, whereas other studies has confirmed the expectation of GR. In particular, while the results of CMB analyses in combination with other probes (ref. [1]) indicate a tension between the Concordance Models and data, which in principle can be explained invoking modification of gravity, with the recent observation of a GW signal from a merging of two Neutron stars and its electromagnetic counterpart (ref. [97]), the allowed region of existence of MG models has been consistently reduced, as discussed in Chapter 2. This demands the need of new independent methods to test GR at cosmological

scales, as well as requiring a severe control of systematics. In this picture, galaxy cluster mass profiles offer an alternative and complementary approach to investigate the nature of gravity alongside other cosmological probes.

The space-time around a galaxy cluster is described by a linear perturbation of the Friedman-Robertson-Walker metric; this perturbed metric can be conveniently written in terms of two scalar quantities, Φ and Ψ, called Bardeen potentials, which encoded information about the assumed theory of gravitation. I have discussed how determinations of the mass profile with different methods are differently related to the Bardeen potentials. In particular, Chapter 3 was devoted to describe the reconstruction of the cluster mass profile by the dynamics of the cluster member galaxies, related to the potential Φ through the Jeans' equation, which is based on the assumptions that galaxy clusters are spherically symmetric and dynamically relaxed; in Chapter 4 I have presented reconstruction of cluster mass profile with gravitational lensing analysis, which instead probes the combination of the Bardeen potentials $\Phi_{lens} = \Phi + \Psi$.

The first part of this work, which has been presented in Chapter 6, and Chapter 7, focuses on the analysis of two galaxy clusters, namely MACS J1206.2-0847 at $z = 0.44$ and RXC J2248.7-4431 at $z = 0.35$, for which high-quality imaging and spectroscopic data have been obtained from the Cluster Lensing And Supernova survey with Hubble (CLASH) and the spectroscopic follow-up with the Very Large Telescope (CLASH-VLT). I first combined previous determinations of lensing and dynamics mass profiles for the galaxy cluster MACS J1206.2-0847 to constrain generic deviation from general relativity, parametrized as the ratio $\eta = \Psi/\Phi$, called anisotropic stress, under the assumption of spherical symmetry and dynamical relaxation. In GR $\Phi \equiv \Psi$, thus η should be identically equal to 1. I obtain $\eta(r_{200} = 1.96\,\mathrm{Mpc}) = 1.01^{+0.31}_{-0.28}$ in the cluster outskirt at the 68% C.L., with a negligible radial dependence; the result is in agreement with GR predictions and competitive with constraints obtained from completely independent analyses, such as the combination of CMB data of the Planck mission, large scale structure (LSS) probes and independent determinations of the Hubble parameter H_0.

This first analysis already showed that the combination of lensing and dynamics mass profiles of galaxy clusters is indeed a powerful method to test the nature of gravity at cosmological scales, thus providing interesting bounds on the anisotropic stress η even if the analysis has been carried out on a single cluster. However, it is worth to mention that the quality and the robustness of the results rely on the high quality data-sets used to reconstruct the mass profiles

and on the detailed studies of the internal structure of MACS 1206, which have confirmed that the main assumptions of the method (i.e. spherical symmetry in the matter distribution and dynamical relaxation) are satisfied.

In order to translate the general constraints on η in terms of constraints on specific modified gravity models, the second step of my work took into consideration the class of scalar-tensor theories known as Horndeski Lagrangian. In particular, in order to extend to models of MG the reconstruction of cluster mass profiles from dynamics, I implemented a modified version of the *MAMPOSSt* procedure (Mamon, Biviano and Boué), a method to reconstruct galaxy clusters mass profiles by solving the Jeans' equation. I introduced in the new version of the code, called *MG-MAMPOSSt*, a parametrization of the time-time potential Φ which accounts for the large variety of modified gravity models in the Horndeski framework. The method and the version of the code I have developed have been discussed in Chapter 3. As a case study, I have determined the total mass profiles from dynamics of the two clusters MACS 1206 and RXJ 2248 in the sub-class of $f(R)$ gravity adopting a Navarro-Frenk-White parametrization for the matter density perturbations (which provides the highest Likelihoods in lensing and dynamics analysis for both clusters). It is worth to point out that the two clusters used in this Thesis belong to a sample of few objects selected for their apparent relaxed dynamical state and extensively analyzed within the CLASH and CLASH-VLT collaborations.
I have performed a Maximum Likelihood fit to the data in the projected phase spaces of the member galaxies (R, v_{los}) to constrain the mass profile parameters r_s and r_{200}, the velocity anisotropy parameter β, together with the additional degree of freedom of the theory λ, which is dubbed as interaction range. The larger is λ, the stronger is the departure from GR. As in $f(R)$ photon propagation is determined only by the Newtonian part of gravity, I have then combined the information from the lensing mass profile reconstruction in order to narrow the allowed region in the dynamics parameter space. To simplify the analysis, I have first assumed a constant λ (i.e. a negligible screening contribution over the scale considered in the analysis), working in the so-called linear $f(R)$ gravity, and then I have discussed the chameleon screening effect with an analytical approximation for the Hu & Sawicki functional form of $f(R)$.
In the case of MACSJ 1206 the joint dynamics+lensing analysis is in agreement with GR predictions $\lambda \leq 1.61\,\mathrm{Mpc}$ at $\Delta\chi^2 = 2.71$ in the linear regime, while for RXJ 2248 instead a tension with standard gravity appears when adding lensing information $\lambda \geq 0.14\,\mathrm{Mpc}$ at $\Delta\chi^2 = 2.71$. The results are shown and discussed in Chapter 7.

The discrepancy between the GR expectations and the constraints obtained from the analysis of RXJ 2248 is due to a slight shift between the lensing and dynamics probability distributions in the GR parameter space (r_s, r_{200}); even if the mass profiles derived in GR from lensing and dynamics analyses are not in tension, the lensing likelihood prefers a modestly lower cluster mass with respect to the results from dynamics. Since the effects induced by viable modifications of gravity are in general very small, such modest difference is already enough to provide a preference of modified gravity with respect to GR. As a consequence, the assumptions on which the proposed method relies have to be carefully checked and controlled to avoid the introduction of systematic false detections of modified gravity. This is very important in view of next generation imaging and spectroscopic surveys, both ground-based and in space, that will provide a large amount of data allowing mass profile reconstructions for hundred clusters; the remarkable increase of statistics will however come at the price of a much lower sensitivity on the internal structure of each cluster.

In order to quantify the impact that the violation of the main assumptions has on the constraints derived with this method, in Chapter 8 I presented the study of cosmological simulations of galaxy clusters carried out in the GR framework of the standard LCDM cosmology.To this purpose, I have divided the analysis in two parts; the first analysis has investigated the constraining power of the method in the case where all the assumptions are met. I considered a set of 15 synthetic isolated Dark Matter halos generated over two order of magnitude in mass according to a NFW distribution and with velocity dispersion given by the solution of the Jeans' equation, assuming a specific model for the anisotropy profile.
The *MG-MAMPOSSt* procedure applied on such halos for the example case of linear $f(R)$ gravity shows that with the dynamics mass profile reconstruction alone no constraints on the interaction range λ can be obtained, even when increasing the number of particles used to sample the phase space of the halos. However, when adding additional information on the mass profile parameters r_s, r_{200}, e.g. to be provided by a mass reconstruction from gravitational lensing, I predict that a joint analysis on a dozen objects with reliable uncertainties is already sufficient to saturate the statistical information, obtaining the tightest constraints on GR deviations reachable with our method.
The second part of the study has explicitly determined the systematic effects on the obtained constraints induced by the breakdown of the assumptions. In doing so, I have analyzed more synthetic galaxy clusters drawn from a set of ΛCDM N-body simulations, performed with the

GADGET-3 code, which spawn a mass range from $9\times10^{13}\,M_\odot$ to $8\times10^{15}\,M_\odot$; all the clusters have been considered at $z=0$.

The application of my method on all these halos, regardless of their dynamical status, reveals that a significant spurious detection of modified gravity is present in roughly $\sim 70\%$ of the analyzed clusters, confirming that systematics have a remarkable impact on our procedure. To further investigate the relation between the assumptions of the method and the spurious constraints on the MG parameter λ, I consider two parameters which can be computed from the projected phase space, and thus they can be applied to real data; these parameters are the Anderson Darling coefficient A^2 of the cumulative l.o.s. velocity distribution of the tracers and the chi-square χ^2_ν given by the fit of the projected number density profile with a NFW profile. use to assess to which level the assumptions of dynamical relaxation and spherical symmetry are met; in particular A^2 parametrizes lack of dynamical relaxation while χ^2_ν is connected to deviation from spherical symmetry, systematics in the assumed parametric form of the density profile and the presence of substructures in the projected phase space. I found that both parameters correlate with the probability to find clusters in agreement with GR predictions, and this correlation is independent of the model chosen for the velocity anisotropy profile $\beta(r)$, which is an additional unknown in the dynamics mass profile reconstruction. Once I select those clusters where the assumptions of our method are better satisfied, characterized by low values of A^2 and χ^2_ν, the probability to find halos where λ is consistent with zero rises up to $\sim 70\%$. This demonstrates that these two parameters can be used as selection criteria to discriminate those clusters to be used as a test for GR.

The study of systematic effects carried out in this Thesis has considered only the dynamics of Dark Matter particles, which are collisionless tracers of the gravitational potential, taken from simulated halos in N-body simulation. The natural step further is to perform a similar analysis by using substructures in high-resolution simulations of galaxy clusters, which better reproduce the motion of galaxies with respect to Dark Matter particles; moreover, possible improvements of this work should take into account the effect of baryons in hydrodynamical simulations that could slightly modify the results shown in Chapter 8. As for the lensing part, a detailed ray-tracing reconstruction of the simulated halos (e.g. refs. [215, 216]) is required in order to perform a full joint lensing+kinematic analysis at different redshifts, and to obtain a combined distribution of the new degree of freedom $m(z)$ to be compared with future observations.

Although in my Thesis I focused mainly on linear $f(R)$ gravity, the proposed method can be

easily extended to a large variety of viable modified gravity models; in particular, both the *MG-MAMPOSSt* procedure and the code for the generation of synthetic halos can be run in different environments changing the parametrization of the Bardeen potential $\Phi(r)$ and the number of free parameters in the expression of σ_r^2 of eq. (3.36). Thus, it is possible to investigate the constraining power of our method in a broad range of frameworks; such analysis will be included in a paper in preparation with L. Amendola S. Casas and I. Saltas, in which we will determine the number of ideal clusters needed to constrain the anisotropic stress $\eta(r)$ for several classes of modified gravity models with and without an explicit screening scale.

Recently, full cosmological simulation codes have been developed to work in non-standard frameworks including modified gravity scenarios. In particular, ref. [39] implemented a module based on the P-GADGET3 code (MG-GADGET) which can run both N-body and hydrodynamics simulations in $f(R)$ gravity, assuming the H&S functional form. An application of the procedure proposed in this Thesis to a modified gravity simulation, compared with the results obtained in ΛCDM analyses, will provide crucial information on what one should expect in a Universe where the gravitational interaction is not described by GR theory. A future development of this PhD project will focus on the study of halos extracted from modified gravity simulations; the aim will be to carry out the analysis presented within this Thesis in the most general background, in order to determine the best trade-off between a richer statistics and a high control of the systematics, offering a remarkable comparison scheme between forthcoming data-sets and viable modified gravity models.

In conclusion, within this Thesis I have demonstrated the potential of comparing galaxy cluster mass profiles, reconstructed from dynamics and lensing analyses, as a new independent probe for departures from GR at large scales. Few selected clusters can be used to produce stringent bounds on the parameters of a large variety of modified gravity models at different redshifts, with uncertainties comparable to (or even smaller than) that provided by other cosmological probes. Nevertheless, the expected precision requires a reliable control of all the possible systematics, which can be achieved by a detailed analysis of cosmological simulations. It is worth to remind that mass profiles of galaxy clusters can be estimated also from X-ray and SZ effect observations, by assuming hydrostatic equilibrium of the ICM. With present and next generation surveys (e.g. Athena[4]) new data will be available also for X-ray cluster mass reconstructions which, has already mentioned in Chapter 3, are sensitive to the time-time

[4]https://www.the-athena-x-ray-observatory.eu

potential Φ. Since the hot gas suffers lack of equilibrium differently from the cluster member galaxies, the combination of galaxy cluster dynamics, lensing and X-ray analyses will provide not only more stringent bounds on the MG parameters, but also a more detailed control of the systematics. With the compound of these upcoming data-sets and results from cosmological simulations, the method proposed in my Thesis will allow to test the behavior of gravity at cosmological scales down to an unprecedented level of accuracy.

Bibliography

[1] Planck Collaboration, *Planck 2015 results. XIV. Dark energy and modified gravity*, A&A **594** (Sept., 2016) A14, [arXiv:1502.01590].

[2] A. G. Riess, A. V. Filippenko, P. Challis, A. Clocchiatti, A. Diercks, P. M. Garnavich, R. L. Gilliland, C. J. Hogan, S. Jha, R. P. Kirshner, and others, *Observational Evidence from Supernovae for an Accelerating Universe and a Cosmological Constant*, AJ **116** (Sept., 1998) 1009–1038, [astro-ph/9805201].

[3] S. Perlmutter, G. Aldering, G. Goldhaber, R. A. Knop, P. Nugent, P. G. Castro, S. Deustua, S. Fabbro, A. Goobar, D. E. Groom, and others, *Measurements of* Ω *and* Λ *from 42 High-Redshift Supernovae*, ApJ **517** (June, 1999) 565–586, [astro-ph/9812133].

[4] Planck Collaboration, *Planck 2018 results. VI. Cosmological parameters*, *ArXiv e-prints* (July, 2018) [arXiv:1807.06209].

[5] W. Hu and I. Sawicki, *Models of f(R) cosmic acceleration that evade solar system tests*, Phys. Rev. D **76** (Sept., 2007) 064004, [arXiv:0705.1158].

[6] G. Dvali, S. Hofmann, and J. Khoury, *Degravitation of the cosmological constant and graviton width*, Phys. Rev. D **76** (Oct., 2007) 084006, [hep-th/0703027].

[7] A. Lue, R. Scoccimarro, and G. Starkman, *Differentiating between modified gravity and dark energy*, Phys. Rev. D **69** (Feb., 2004) 044005, [astro-ph/0307034].

[8] B. Hu, M. Liguori, N. Bartolo, and S. Matarrese, *Parametrized modified gravity constraints after Planck*, Phys. Rev. D **88** (Dec., 2013) 123514, [arXiv:1307.5276].

[9] G.-B. Zhao, T. Giannantonio, L. Pogosian, A. Silvestri, D. J. Bacon, K. Koyama, R. C. Nichol, and Y.-S. Song, *Probing modifications of general relativity using current cosmological observations*, Phys. Rev. D **81** (May, 2010) 103510, [arXiv:1003.0001].

[10] K. Yamamoto, B. A. Bassett, R. C. Nichol, Y. Suto, and K. Yahata, *Searching for modified gravity with baryon oscillations: From SDSS to wide field multiobject spectroscopy (WFMOS)*, Phys. Rev. D **74** (Sept., 2006) 063525, [astro-ph/0605278].

[11] E. Jennings, C. M. Baugh, B. Li, G.-B. Zhao, and K. Koyama, *Redshift-space distortions in f(R) gravity*, MNRAS **425** (Sept., 2012) 2128–2143, [arXiv:1205.2698].

[12] G.-B. Zhao, L. Pogosian, A. Silvestri, and J. Zylberberg, *Searching for modified growth patterns with tomographic surveys*, Phys. Rev. D **79** (Apr., 2009) 083513, [arXiv:0809.3791].

[13] S. Ferraro, F. Schmidt, and W. Hu, *Cluster abundance in f(R) gravity models*, Phys. Rev. D **83** (Mar., 2011) 063503, [arXiv:1011.0992].

[14] M. Cataneo, D. Rapetti, F. Schmidt, A. B. Mantz, S. W. Allen, D. E. Applegate, P. L. Kelly, A. von der Linden, and R. G. Morris, *New constraints on f (R) gravity from clusters of galaxies*, Phys. Rev. D **92** (Aug., 2015) 044009, [arXiv:1412.0133].

[15] D. Langlois, R. Saito, D. Yamauchi, and K. Noui, *Scalar-tensor theories and modified gravity in the wake of GW170817*, Phys. Rev. D **97** (Mar., 2018) 061501, [arXiv:1711.07403].

[16] L. Amendola, M. Kunz, I. D. Saltas, and I. Sawicki, *Fate of Large-Scale Structure in Modified Gravity After GW170817 and GRB170817A*, *Physical Review Letters* **120** (Mar., 2018) 131101, [arXiv:1711.04825].

[17] C. M. Will, *The Confrontation between General Relativity and Experiment*, *Living Reviews in Relativity* **9** (Mar., 2006) [gr-qc/0510072].

[18] J. Khoury, *Theories of Dark Energy with Screening Mechanisms*, *ArXiv e-prints* (Nov., 2010) [arXiv:1011.5909].

[19] L. Amendola, *Coupled quintessence*, *Phys. Rev. D* **62** (Jul, 2000) 043511.

[20] A. L. Serra and M. J. L. Domínguez Romero, *Measuring the dark matter equation of state*, MNRAS **415** (July, 2011) L74–L77, [arXiv:1103.5465].

[21] B. Sartoris, A. Biviano, P. Rosati, S. Borgani, K. Umetsu, M. Bartelmann, M. Girardi, C. Grillo, D. Lemze, A. Zitrin, and others, *CLASH-VLT: Constraints on the Dark Matter Equation of State from Accurate Measurements of Galaxy Cluster Mass Profiles*, ApJ **783** (Mar., 2014) L11, [arXiv:1401.5800].

[22] L. Pizzuti, B. Sartoris, S. Borgani, L. Amendola, K. Umetsu, A. Biviano, M. Girardi, P. Rosati, I. Balestra, G. B. Caminha, B. Frye, A. Koekemoer, C. Grillo, M. Lombardi, A. Mercurio, and M. Nonino, *CLASH-VLT: testing the nature of gravity with galaxy cluster mass profiles*, J. Cosmology Astropart. Phys. **4** (Apr., 2016) 023, [arXiv:1602.03385].

[23] M. Postman, D. Coe, N. Benítez, L. Bradley, T. Broadhurst, M. Donahue, H. Ford, O. Graur, G. Graves, S. Jouvel, and others, *The Cluster Lensing and Supernova Survey with Hubble: An Overview*, ApJS **199** (Apr., 2012) 25, [arXiv:1106.3328].

[24] P. Rosati, I. Balestra, C. Grillo, A. Mercurio, M. Nonino, A. Biviano, M. Girardi, E. Vanzella, and Clash-VLT Team, *CLASH-VLT: A VIMOS Large Programme to Map the Dark Matter Mass Distribution in Galaxy Clusters and Probe Distant Lensed Galaxies*, *The Messenger* **158** (Dec., 2014) 48–53.

[25] A. Biviano, P. Rosati, I. Balestra, A. Mercurio, M. Girardi, M. Nonino, C. Grillo, M. Scodeggio, D. Lemze, D. Kelson, and others, *CLASH-VLT: The mass, velocity-anisotropy, and pseudo-phase-space density profiles of the z = 0.44 galaxy cluster MACS J1206.2-0847*, A&A **558** (Oct., 2013) A1, [arXiv:1307.5867].

[26] K. Umetsu, E. Medezinski, M. Nonino, J. Merten, A. Zitrin, A. Molino, C. Grillo, M. Carrasco, M. Donahue, A. Mahdavi, and others, *CLASH: Mass Distribution in and around MACS J1206.2-0847 from a Full Cluster Lensing Analysis*, ApJ **755** (Aug., 2012) 56, [arXiv:1204.3630].

[27] L. Amendola, M. Kunz, and D. Sapone, *Measuring the dark side (with weak lensing)*, *JCAP* **0804** (2008) 013, [arXiv:0704.2421].

[28] B. Jain and P. Zhang, *Observational tests of modified gravity*, Phys. Rev. D **78** (Sept., 2008) 063503, [arXiv:0709.2375].

[29] F. Schmidt, *Dynamical masses in modified gravity*, Phys. Rev. D **81** (May, 2010) 103002, [arXiv:1003.0409].

[30] G. W. Horndeski, *Second-order scalar-tensor field equations in a four-dimensional space*, *International Journal of Theoretical Physics* **10** (1974), no. 6 363–384.

[31] J. Khoury and A. Weltman, *Chameleon cosmology*, Phys. Rev. D **69** (Feb., 2004) 044026, [astro-ph/0309411].

[32] G. A. Mamon, A. Biviano, and G. Boué, *MAMPOSSt: Modelling Anisotropy and Mass Profiles of Observed Spherical Systems - I. Gaussian 3D velocities*, MNRAS **429** (Mar., 2013) 3079–3098, [arXiv:1212.1455].

[33] J. F. Navarro, C. S. Frenk, and S. D. M. White, *A Universal Density Profile from Hierarchical Clustering*, ApJ **490** (Dec., 1997) 493–508, [astro-ph/9611107].

[34] B. Li, G.-B. Zhao, and K. Koyama, *Haloes and voids in f(R) gravity*, MNRAS **421** (Apr., 2012) 3481–3487, [arXiv:1111.2602].

[35] K. Umetsu, A. Zitrin, D. Gruen, J. Merten, M. Donahue, and M. Postman, *CLASH: Joint Analysis of Strong-lensing, Weak-lensing Shear, and Magnification Data for 20 Galaxy Clusters*, ApJ **821** (Apr., 2016) 116, [arXiv:1507.04385].

[36] L. Pizzuti, B. Sartoris, L. Amendola, S. Borgani, A. Biviano, K. Umetsu, A. Mercurio, P. Rosati, I. Balestra, G. B. Caminha, M. Girardi, C. Grillo, and M. Nonino, *CLASH-VLT: constraints on f(R) gravity models with galaxy clusters using lensing and kinematic analyses*, J. Cosmology Astropart. Phys. **7** (July, 2017) 023, [arXiv:1705.05179].

[37] V. Springel, *The cosmological simulation code GADGET-2*, MNRAS **364** (Dec., 2005) 1105–1134, [astro-ph/0505010].

[38] I. D. Roberts, L. C. Parker, and J. Hlavacek-Larrondo, *Connecting optical and X-ray tracers of galaxy cluster relaxation*, MNRAS **475** (Apr., 2018) 4704–4716, [arXiv:1801.03999].

[39] E. Puchwein, M. Baldi, and V. Springel, *Modified-Gravity-GADGET: a new code for cosmological hydrodynamical simulations of modified gravity models*, MNRAS **436** (Nov., 2013) 348–360, [arXiv:1305.2418].

[40] J. F. Navarro, C. S. Frenk, and S. D. M. White, *A Universal Density Profile from Hierarchical Clustering*, ApJ **490** (Dec., 1997) 493–+, [astro-ph/9].

[41] S. Weinberg, *Gravitation and Cosmology: Principles and Applications of the General Theory of Relativity*. July, 1972.

[42] H. Mo, F. C. van den Bosch, and S. White, *Galaxy Formation and Evolution*. May, 2010.

[43] A. Friedmann, *Über die Krümmung des Raumes*, *Zeitschrift fur Physik* **10** (1922) 377–386.

[44] J. A. Frieman, M. S. Turner, and D. Huterer, *Dark Energy and the Accelerating Universe*, ARA&A **46** (Sept., 2008) 385–432, [arXiv:0803.0982].

[45] A. G. Riess, S. Casertano, W. Yuan, L. Macri, J. Anderson, J. W. MacKenty, J. B. Bowers, K. I. Clubb, A. V. Filippenko, D. O. Jones, and B. E. Tucker, *New Parallaxes of Galactic Cepheids from Spatially Scanning the Hubble Space Telescope: Implications for the Hubble Constant*, ApJ **855** (Mar., 2018) 136, [arXiv:1801.01120].

[46] A. G. Riess, S. Casertano, W. Yuan, L. Macri, B. Bucciarelli, M. G. Lattanzi, J. W. MacKenty, J. B. Bowers, W. Zheng, A. V. Filippenko, C. Huang, and R. I. Anderson, *Milky Way Cepheid Standards for Measuring Cosmic Distances and Application to Gaia DR2: Implications for the Hubble Constant*, ApJ **861** (July, 2018) 126, [arXiv:1804.10655].

[47] D. Camarena and V. Marra, *Impact of the cosmic variance on H_0 on cosmological analyses*, Phys. Rev. D **98** (July, 2018) 023537, [arXiv:1805.09900].

[48] A. G. Riess, A. V. Filippenko, P. Challis, A. Clocchiatti, A. Diercks, and et al., *Observational Evidence from Supernovae for an Accelerating Universe and a Cosmological Constant*, AJ **116** (Sept., 1998) 1009–1038, [astro-ph/9].

[49] S. Perlmutter, G. Aldering, G. Goldhaber, R. A. Knop, P. Nugent, P. G. Castro, S. Deustua, S. Fabbro, A. Goobar, D. E. Groom, and others, *Measurements of* Ω *and* Λ *from 42 High-Redshift Supernovae*, ApJ **517** (June, 1999) 565–586, [astro-ph/9812133].

[50] H. Velten, S. Gomes, and V. C. Busti, *Gauging the cosmic acceleration with recent type Ia supernovae data sets*, Phys. Rev. D **97** (Apr., 2018) 083516, [arXiv:1801.00114].

[51] M. e. a. Kowalski, *Improved Cosmological Constraints from New, Old, and Combined Supernova Data Sets*, ApJ **686** (Oct., 2008) 749–778, [arXiv:0804.4142].

[52] B. S. Haridasu, V. V. Lukovi ć, R. D'Agostino, and N. Vittorio, *Strong evidence for an accelerating Universe*, A&A **600** (Apr., 2017) L1.

[53] J. Magaña, V. Motta, V. H. Cárdenas, and G. Foëx, *Testing cosmic acceleration for w(z) parametrizations using* f_{gas} *measurements in galaxy clusters*, MNRAS **469** (July, 2017) 47–61, [arXiv:1703.08521].

[54] D. H. Weinberg, M. J. Mortonson, D. J. Eisenstein, C. Hirata, A. G. Riess, and E. Rozo, *Observational probes of cosmic acceleration*, Phys. Rep. **530** (Sept., 2013) 87–255, [arXiv:1201.2434].

[55] R. Giostri, M. Vargas dos Santos, I. Waga, R. R. R. Reis, M. O. Calvão, and B. L. Lago, *From cosmic deceleration to acceleration: new constraints from SN Ia and BAO/CMB*, J. Cosmology Astropart. Phys. **3** (Mar., 2012) 027, [arXiv:1203.3213].

[56] M. Vargas dos Santos, R. R. R. Reis, and I. Waga, *Constraining the cosmic deceleration-acceleration transition with type Ia supernova, BAO/CMB and H(z) data*, J. Cosmology Astropart. Phys. **2** (Feb., 2016) 066, [arXiv:1505.03814].

[57] K. Freese, *Review of Observational Evidence for Dark Matter in the Universe and in upcoming searches for Dark Stars*, in *EAS Publications Series* (E. Pécontal, T. Buchert, P. di Stefano, and Y. Copin, eds.), vol. 36 of *EAS Publications Series*, pp. 113–126, 2009. arXiv:0812.4005.

[58] Planck Collaboration, *Planck 2018 results. I. Overview and the cosmological legacy of Planck*, *ArXiv e-prints* (July, 2018) [arXiv:1807.06205].

[59] Planck Collaboration, *Planck 2015 results. I. Overview of products and scientific results*, A&A **594** (Sept., 2016) A1, [arXiv:1502.01582].

[60] P. Meszaros, *The behaviour of point masses in an expanding cosmological substratum*, A&A **37** (Dec., 1974) 225–228.

[61] D. H. Weinberg, J. S. Bullock, F. Governato, R. Kuzio de Naray, and A. H. G. Peter, *Cold dark matter: Controversies on small scales*, *Proceedings of the National Academy of Science* **112** (Oct., 2015) 12249–12255, [arXiv:1306.0913].

[62] S. Borgani and L. Guzzo, *X-ray clusters of galaxies as tracers of structure in the Universe*, Nature **409** (Jan., 2001) 39–45, [astro-ph/0012439].

[63] T. Narikawa and K. Yamamoto, *Characterizing the linear growth rate of cosmological density perturbations in an f(R) model*, Phys. Rev. D **81** (Feb., 2010) 043528, [arXiv:0912.1445].

[64] J. M. Bardeen, *Gauge-invariant cosmological perturbations*, Phys. Rev. D **22** (Oct., 1980) 1882–1905.

[65] I. Milillo, D. Bertacca, M. Bruni, and A. Maselli, *Missing link: A nonlinear post-Friedmann framework for small and large scales*, Phys. Rev. D **92** (July, 2015) 023519, [arXiv:1502.02985].

[66] J. E. Gunn and J. R. Gott, III, *On the Infall of Matter Into Clusters of Galaxies and Some Effects on Their Evolution*, ApJ **176** (Aug., 1972) 1.

[67] W. H. Press and P. Schechter, *Formation of Galaxies and Clusters of Galaxies by Self-Similar Gravitational Condensation*, ApJ **187** (Feb., 1974) 425–438.

[68] D. F. Mota and C. van de Bruck, *On the spherical collapse model in dark energy cosmologies*, A&A **421** (July, 2004) 71–81, [astro-ph/0401504].

[69] R.-H. Lin, X.-H. Zhai, and X.-Z. Li, *Spherical collapse and virialization in f (t) gravities*, *Journal of Cosmology and Astroparticle Physics* **2017** (2017), no. 03 040.

[70] Y. B. Zel'dovich, *Gravitational instability: An approximate theory for large density perturbations.*, A&A **5** (Mar., 1970) 84–89.

[71] M. C. Neyrinck, *Quantifying distortions of the Lagrangian dark-matter mesh in cosmology*, MNRAS **428** (Jan., 2013) 141–153, [arXiv:1204.1326].

[72] K. Dolag, S. Borgani, S. Schindler, A. Diaferio, and A. M. Bykov, *Simulation Techniques for Cosmological Simulations*, Space Sci. Rev. **134** (Feb., 2008) 229–268, [arXiv:0801.1023].

[73] R. S. Somerville and R. Davé, *Physical Models of Galaxy Formation in a Cosmological Framework*, ARA&A **53** (Aug., 2015) 51–113, [arXiv:1412.2712].

[74] D. Daverio, Y. Dirian, and E. Mitsou, *A numerical relativity scheme for cosmological simulations*, *Classical and Quantum Gravity* **34** (Dec., 2017) 237001, [arXiv:1611.03437].

[75] J. Adamek, D. Daverio, R. Durrer, and M. Kunz, *General relativistic N-body simulations in the weak field limit*, Phys. Rev. D **88** (Nov., 2013) 103527, [arXiv:1308.6524].

[76] J. F. Navarro, C. S. Frenk, and S. D. M. White, *The assembly of galaxies in a hierarchically clustering universe*, MNRAS **275** (July, 1995) 56–66, [astro-ph/9].

[77] J. F. Navarro, C. S. Frenk, and S. D. M. White, *The Structure of Cold Dark Matter Halos*, ApJ **462** (May, 1996) 563–+, [astro-ph/9].

[78] D. H. Zhao, Y. P. Jing, H. J. Mo, and G. Börner, *Mass and Redshift Dependence of Dark Halo Structure*, ApJ **597** (Nov., 2003) L9–L12, [astro-ph/0309375].

[79] M. A. Sánchez-Conde and F. Prada, *The flattening of the concentration-mass relation towards low halo masses and its implications for the annihilation signal boost*, MNRAS **442** (Aug., 2014) 2271–2277, [arXiv:1312.1729].

[80] F. Prada, A. A. Klypin, A. J. Cuesta, J. E. Betancort-Rijo, and J. Primack, *Halo concentrations in the standard Λ cold dark matter cosmology*, MNRAS **423** (July, 2012) 3018–3030, [arXiv:1104.5130].

[81] A. V. Macciò, A. A. Dutton, and F. C. van den Bosch, *Concentration, spin and shape of dark matter haloes as a function of the cosmological model: WMAP1, WMAP3 and WMAP5 results*, MNRAS **391** (Dec., 2008) 1940–1954, [arXiv:0805.1926].

[82] A. R. Duffy, J. Schaye, S. T. Kay, and C. Dalla Vecchia, *Dark matter halo concentrations in the Wilkinson Microwave Anisotropy Probe year 5 cosmology*, MNRAS **390** (Oct., 2008) L64–L68, [arXiv:0804.2486].

[83] A. A. Klypin, S. Trujillo-Gomez, and J. Primack, *Dark Matter Halos in the Standard Cosmological Model: Results from the Bolshoi Simulation*, ApJ **740** (Oct., 2011) 102, [arXiv:1002.3660].

[84] C. De Boni, S. Ettori, K. Dolag, and L. Moscardini, *Hydrodynamical simulations of galaxy clusters in dark energy cosmologies - II. c-M relation*, MNRAS **428** (Feb., 2013) 2921–2938, [arXiv:1205.3163].

[85] S. Ettori, F. Gastaldello, A. Leccardi, S. Molendi, M. Rossetti, D. Buote, and M. Meneghetti, *Mass profiles and c-M_{DM} relation in X-ray luminous galaxy clusters*, A&A **524** (Dec., 2010) A68.

[86] S. Amodeo, S. Ettori, R. Capasso, and M. Sereno, *The relation between mass and concentration in X-ray galaxy clusters at high redshift*, A&A **590** (May, 2016) A126, [arXiv:1604.02163].

[87] J. Merten, M. Meneghetti, M. Postman, K. Umetsu, A. Zitrin, E. Medezinski, M. Nonino, A. Koekemoer, P. Melchior, D. Gruen, and others, *CLASH: The Concentration-Mass Relation of Galaxy Clusters*, ApJ **806** (June, 2015) 4, [arXiv:1404.1376].

[88] M. Meneghetti, E. Rasia, J. Vega, J. Merten, and M. e. a. Postman, *The MUSIC of CLASH: Predictions on the Concentration-Mass Relation*, ApJ **797** (Dec., 2014) 34, [arXiv:1404.1384].

[89] K. Umetsu, E. Medezinski, M. Nonino, J. Merten, M. Postman, M. Meneghetti, M. Donahue, N. Czakon, A. Molino, S. Seitz, and others, *CLASH: Weak-lensing Shear-and-magnification Analysis of 20 Galaxy Clusters*, ApJ **795** (Nov., 2014) 163, [arXiv:1404.1375].

[90] B. Moore, F. Governato, T. Quinn, J. Stadel, and G. Lake, *Resolving the Structure of Cold Dark Matter Halos*, ApJ **499** (May, 1998) L5–L8, [astro-ph/9709051].

[91] B. Moore, *Evidence against dissipation-less dark matter from observations of galaxy haloes*, Nature **370** (Aug., 1994) 629–631.

[92] R. A. Swaters, B. F. Madore, F. C. van den Bosch, and M. Balcells, *The Central Mass Distribution in Dwarf and Low Surface Brightness Galaxies*, ApJ **583** (Feb., 2003) 732–751, [astro-ph/0210152].

[93] A. Pontzen and F. Governato, *How supernova feedback turns dark matter cusps into cores*, MNRAS **421** (Apr., 2012) 3464–3471, [arXiv:1106.0499].

[94] J. F. Navarro, *The Inner Density Cusp of Cold Dark Matter Halos*, in *Dark Matter in Galaxies* (S. Ryder, D. Pisano, M. Walker, and K. Freeman, eds.), vol. 220 of *IAU Symposium*, p. 61, July, 2004. astro-ph/0311361.

[95] L. Gao, J. F. Navarro, S. Cole, C. S. Frenk, S. D. M. White, V. Springel, A. Jenkins, and A. F. Neto, *The redshift dependence of the structure of massive Λ cold dark matter haloes*, MNRAS **387** (June, 2008) 536–544, [arXiv:0711.0746].

[96] E. Berti, E. Barausse, V. Cardoso, L. Gualtieri, P. Pani, U. Sperhake, L. C. Stein, N. Wex, K. Yagi, T. Baker, and others, *Testing general relativity with present and future astrophysical observations*, *Classical and Quantum Gravity* **32** (Dec., 2015) 243001, [arXiv:1501.07274].

[97] B. P. Abbott, R. Abbott, T. D. Abbott, F. Acernese, K. Ackley, C. Adams, T. Adams, P. Addesso, R. X. Adhikari, V. B. Adya, and others, *GW170817: Observation of Gravitational Waves from a Binary Neutron Star Inspiral*, *Physical Review Letters* **119** (Oct., 2017) 161101, [arXiv:1710.05832].

[98] A. S. Eddington, *Can Gravitation be Explained?*, JRASC **17** (Dec., 1923) 387.

[99] A. Padilla, *Lectures on the Cosmological Constant Problem*, *ArXiv e-prints* (Feb., 2015) [arXiv:1502.05296].

[100] B. Ratra and P. J. E. Peebles, *Cosmological consequences of a rolling homogeneous scalar field*, Phys. Rev. D **37** (June, 1988) 3406–3427.

[101] E. Sefusatti and F. Vernizzi, *Cosmological structure formation with clustering quintessence*, J. Cosmology Astropart. Phys. **3** (Mar., 2011) 047, [arXiv:1101.1026].

[102] R. de Putter, D. Huterer, and E. V. Linder, *Measuring the speed of dark: Detecting dark energy perturbations*, Phys. Rev. D **81** (May, 2010) 103513, [arXiv:1002.1311].

[103] D. Huterer and D. L. Shafer, *Dark energy two decades after: observables, probes, consistency tests*, *Reports on Progress in Physics* **81** (Jan., 2018) 016901, [arXiv:1709.01091].

[104] T. Clifton, P. G. Ferreira, A. Padilla, and C. Skordis, *Modified gravity and cosmology*, Phys. Rep. **513** (Mar., 2012) 1–189, [arXiv:1106.2476].

[105] A. Joyce, L. Lombriser, and F. Schmidt, *Dark energy versus modified gravity*, *Annual Review of Nuclear and Particle Science* **66** (2016), no. 1 95–122, [https://doi.org/10.1146/annurev-nucl-102115-044553].

[106] D. Lovelock, *The fourâĂŘdimensionality of space and the einstein tensor*, *Journal of Mathematical Physics* **13** (1972), no. 6 874–876, [https://doi.org/10.1063/1.1666069].

[107] R. Maartens, *Brane-World Gravity*, *Living Reviews in Relativity* **7** (June, 2004) 7, [gr-qc/0312059].

[108] K. Koyama, *Cosmological tests of modified gravity*, *Reports on Progress in Physics* **79** (Apr., 2016) 046902, [arXiv:1504.04623].

[109] C. Armendariz-Picon, V. Mukhanov, and P. J. Steinhardt, *Essentials of k-essence*, Phys. Rev. D **63** (May, 2001) 103510, [astro-ph/0006373].

[110] P. Creminelli and F. Vernizzi, *Dark Energy after GW170817 and GRB170817A*, *Physical Review Letters* **119** (Dec., 2017) 251302, [arXiv:1710.05877].

[111] V. Mukhanov, *Physical Foundations of Cosmology*. Mar., 2001.

[112] L. Amendola, M. Kunz, M. Motta, I. D. Saltas, and I. Sawicki, *Observables and unobservables in dark energy cosmologies*, Phys. Rev. D **87** (Jan., 2013) 023501, [arXiv:1210.0439].

[113] A. de Felice, T. Kobayashi, and S. Tsujikawa, *Effective gravitational couplings for cosmological perturbations in the most general scalar-tensor theories with*

second-order field equations, *Physics Letters B* **706** (Dec., 2011) 123–133, [arXiv:1108.4242].

[114] H. A. Buchdahl, *Non-linear Lagrangians and cosmological theory*, MNRAS **150** (1970) 1.

[115] T. P. Sotiriou and V. Faraoni, *f(R) theories of gravity*, *Reviews of Modern Physics* **82** (Jan., 2010) 451–497, [arXiv:0805.1726].

[116] T. P. Sotiriou and V. Faraoni, *f(R) theories of gravity*, *Reviews of Modern Physics* **82** (Jan., 2010) 451–497, [arXiv:0805.1726].

[117] M. Cataneo, D. Rapetti, L. Lombriser, and B. Li, *Cluster abundance in chameleon $f(R)$ gravity I: toward an accurate halo mass function prediction*, *ArXiv e-prints* (July, 2016) [arXiv:1607.08788].

[118] L. Pogosian and A. Silvestri, *Erratum: Pattern of growth in viable f(R) cosmologies [Phys. Rev. D 77, 023503 (2008)]*, Phys. Rev. D **81** (Feb., 2010) 049901.

[119] Y.-S. Song, W. Hu, and I. Sawicki, *Large scale structure of f(R) gravity*, Phys. Rev. D **75** (Feb., 2007) 044004, [astro-ph/0610532].

[120] H. Oyaizu, *Nonlinear evolution of f(R) cosmologies. I. Methodology*, Phys. Rev. D **78** (Dec., 2008) 123523, [arXiv:0807.2449].

[121] M. Ishak, *Testing General Relativity in Cosmology*, *ArXiv e-prints* (June, 2018) [arXiv:1806.10122].

[122] M. Amarzguioui, Ø. Elgarøy, D. F. Mota, and T. Multamäki, *Cosmological constraints on f(R) gravity theories within the Palatini approach*, A&A **454** (Aug., 2006) 707–714, [astro-ph/0510519].

[123] L. Taddei, M. Martinelli, and L. Amendola, *Model-independent constraints on modified gravity from current data and from the Euclid and SKA future surveys*, J. Cosmology Astropart. Phys. **12** (Dec., 2016) 032, [arXiv:1604.01059].

[124] S. Basilakos and S. Nesseris, *Conjoined constraints on modified gravity from the expansion history and cosmic growth*, Phys. Rev. D **96** (Sept., 2017) 063517, [arXiv:1705.08797].

[125] R. C. Nunes, S. Pan, E. N. Saridakis, and E. M. Abreu, *New observational constraints on f (r) gravity from cosmic chronometers*, *Journal of Cosmology and Astroparticle Physics* **2017** (2017), no. 01 005.

[126] H. Hildebrandt, M. Viola, C. Heymans, S. Joudaki, and others, *KiDS-450: cosmological parameter constraints from tomographic weak gravitational lensing*, MNRAS **465** (Feb., 2017) 1454–1498, [arXiv:1606.05338].

[127] S. Joudaki, A. Mead, C. Blake, A. Choi, and others, *KiDS-450: testing extensions to the standard cosmological model*, MNRAS **471** (Oct., 2017) 1259–1279, [arXiv:1610.04606].

[128] F. Schmidt, M. Lima, H. Oyaizu, and W. Hu, *Nonlinear evolution of f(R) cosmologies. III. Halo statistics*, Phys. Rev. D **79** (Apr., 2009) 083518–+, [arXiv:0812.0545].

[129] S. Alam, H. Miyatake, S. More, S. Ho, and R. Mandelbaum, *Testing gravity on large scales by combining weak lensing with galaxy clustering using CFHTLenS and BOSS CMASS*, MNRAS **465** (Mar., 2017) 4853–4865, [arXiv:1610.09410].

[130] P. J. E. Peebles, *The large-scale structure of the universe*. Research supported by the National Science Foundation. Princeton, N.J., Princeton University Press, 1980. 435 p., 1980.

[131] E. V. Linder, *Cosmic growth history and expansion history*, Phys. Rev. D **72** (Aug., 2005) 043529, [astro-ph/0507263].

[132] T. Okumura, C. Hikage, T. Totani, M. Tonegawa, and H. e. a. Okada, *The Subaru FMOS galaxy redshift survey (FastSound). IV. New constraint on gravity theory from redshift space distortions at* $z \sim 1.4$, PASJ **68** (June, 2016) 38, [arXiv:1511.08083].

[133] A. Ferté, D. Kirk, A. R. Liddle, and J. Zuntz, *Testing gravity on cosmological scales with cosmic shear, cosmic microwave background anisotropies, and redshift-space distortions*, *ArXiv e-prints* (Dec., 2017) [arXiv:1712.01846].

[134] B. Jain, V. Vikram, and J. Sakstein, *Astrophysical Tests of Modified Gravity: Constraints from Distance Indicators in the Nearby Universe*, ApJ **779** (Dec., 2013) 39, [arXiv:1204.6044].

[135] L. Xu, *Constraints on $f(r)$ gravity through the redshift space distortion*, *Phys. Rev. D* **91** (Mar, 2015) 063008.

[136] J. Binney and S. Tremaine, *Galactic dynamics*. 1987.

[137] A. H. Gonzalez, D. Zaritsky, and A. I. Zabludoff, *A Census of Baryons in Galaxy Clusters and Groups*, ApJ **666** (Sept., 2007) 147–155, [arXiv:0705.1726].

[138] J. M. Budzynski, S. E. Koposov, I. G. McCarthy, S. L. McGee, and V. Belokurov, *The radial distribution of galaxies in groups and clusters*, MNRAS **423** (June, 2012) 104–121, [arXiv:1201.5491].

[139] I. King, *Density Law in Spherical Stellar Systems.*, AJ **67** (June, 1962) 274–275.

[140] Y. Suto, S. Sasaki, and N. Makino, *Gas Density and X-Ray Surface Brightness Profiles of Clusters of Galaxies from Dark Matter Halo Potentials: Beyond the Isothermal β-Model*, ApJ **509** (Dec., 1998) 544–550, [astro-ph/9807112].

[141] F. Lacasa and R. Rosenfeld, *Combining cluster number counts and galaxy clustering*, J. Cosmology Astropart. Phys. **8** (Aug., 2016) 005, [arXiv:1603.00918].

[142] M. Sahlén and J. Silk, *Cluster-Void Degeneracy Breaking: Modified Gravity in the Balance*, *ArXiv e-prints* (Dec., 2016) [arXiv:1612.06595].

[143] A. Kashlinsky, F. Atrio-Barandela, D. Kocevski, and H. Ebeling, *A measurement of large-scale peculiar velocities of clusters of galaxies: Results and cosmological implications*, *The Astrophysical Journal Letters* **686** (2008), no. 2 L49.

[144] S. Borgani, L. N. da Costa, W. Freudling, R. Giovanelli, M. P. Haynes, J. Salzer, and G. Wegner, *Peculiar velocities of clusters in cold dark matter models*, *The Astrophysical Journal Letters* **482** (1997), no. 2 L121.

[145] S. Ettori, A. Morandi, P. Tozzi, I. Balestra, S. Borgani, P. Rosati, L. Lovisari, and F. Terenziani, *The cluster gas mass fraction as a cosmological probe: a revised study*, A&A **501** (July, 2009) 61–73, [arXiv:0904.2740].

[146] G. B. Caminha, C. Grillo, P. Rosati, I. Balestra, W. Karman, M. Lombardi, A. Mercurio, M. Nonino, P. Tozzi, A. Zitrin, and others, *CLASH-VLT: A highly precise*

strong lensing model of the galaxy cluster RXC J2248.7-4431 (Abell S1063) and prospects for cosmography, A&A **587** (Mar., 2016) A80, [arXiv:1512.04555].

[147] J. Ruel, G. Bazin, M. Bayliss, M. Brodwin, R. J. Foley, B. Stalder, K. A. Aird, R. Armstrong, M. L. N. Ashby, M. Bautz, and others, *Optical Spectroscopy and Velocity Dispersions of Galaxy Clusters from the SPT-SZ Survey*, ApJ **792** (Sept., 2014) 45, [arXiv:1311.4953].

[148] J. Binney and G. A. Mamon, *M/L and velocity anisotropy from observations of spherical galaxies, or must M87 have a massive black hole*, MNRAS **200** (July, 1982) 361–375.

[149] O. Host, S. H. Hansen, R. Piffaretti, A. Morandi, S. Ettori, S. T. Kay, and R. Valdarnini, *Measurement of the Dark Matter Velocity Anisotropy in Galaxy Clusters*, ApJ **690** (Jan., 2009) 358–366, [arXiv:0808.2049].

[150] O. Host, *Measurement of the dark matter velocity anisotropy profile in galaxy clusters*, *Nuclear Physics B Proceedings Supplements* **194** (Oct., 2009) 111–115, [arXiv:0810.3676].

[151] S. H. Hansen and B. Moore, *A universal density slope Velocity anisotropy relation for relaxed structures*, New A **11** (Mar., 2006) 333–338, [astro-ph/0411473].

[152] G. A. Mamon, A. Biviano, and G. Murante, *The universal distribution of halo interlopers in projected phase space. Bias in galaxy cluster concentration and velocity anisotropy?*, A&A **520** (Sept., 2010) A30, [arXiv:1003.0033].

[153] A. Diaferio and M. J. Geller, *Infall Regions of Galaxy Clusters*, ApJ **481** (May, 1997) 633–643, [astro-ph/9701034].

[154] C. L. Sarazin, *Gas Dynamics in Clusters of Galaxies*, in *A Pan-Chromatic View of Clusters of Galaxies and the Large-Scale Structure* (M. Plionis, O. López-Cruz, and D. Hughes, eds.), vol. 740 of *Lecture Notes in Physics, Berlin Springer Verlag*, p. 24, 2008.

[155] S. Ettori, A. Donnarumma, E. Pointecouteau, T. H. Reiprich, S. Giodini, L. Lovisari, and R. W. Schmidt, *Mass Profiles of Galaxy Clusters from X-ray Analysis*, Space Sci. Rev. **177** (Aug., 2013) 119–154, [arXiv:1303.3530].

[156] V. Biffi, S. Borgani, G. Murante, E. Rasia, S. Planelles, G. L. Granato, C. Ragone-Figueroa, A. M. Beck, M. Gaspari, and K. Dolag, *On the Nature of Hydrostatic Equilibrium in Galaxy Clusters*, ApJ **827** (Aug., 2016) 112, [arXiv:1606.02293].

[157] D. Martizzi and H. Agrusa, *Mass modeling of galaxy clusters: quantifying hydrostatic bias and contribution from non-thermal pressure*, *ArXiv e-prints* (Aug., 2016) [arXiv:1608.04388].

[158] D. Nagai and E. T. Lau, *Gas Clumping in the Outskirts of ΛCDM Clusters*, ApJ **731** (Apr., 2011) L10, [arXiv:1103.0280].

[159] S. Borgani, G. Murante, V. Springel, A. Diaferio, K. Dolag, L. Moscardini, G. Tormen, L. Tornatore, and P. Tozzi, *X-ray properties of galaxy clusters and groups from a cosmological hydrodynamical simulation*, MNRAS **348** (Mar., 2004) 1078–1096, [astro-ph/0310794].

[160] R. Wojtak and E. L. Łokas, *The importance of interloper removal in galaxy clusters: saving more objects for the Jeans analysis*, MNRAS **377** (May, 2007) 843–854, [astro-ph/0606618].

[161] A. Biviano and P. Salucci, *The radial profiles of the different mass components in galaxy clusters*, A&A **452** (June, 2006) 75–81, [astro-ph/0511309].

[162] G. A. Mamon and E. L. Łokas, *Dark matter in elliptical galaxies - II. Estimating the mass within the virial radius*, MNRAS **363** (Nov., 2005) 705–722, [astro-ph/0405491].

[163] O. Tiret, F. Combes, G. W. Angus, B. Famaey, and H. S. Zhao, *Velocity dispersion around ellipticals in MOND*, A&A **476** (Dec., 2007) L1–L4, [arXiv:0710.4070].

[164] M. Falco, S. H. Hansen, R. Wojtak, and G. A. Mamon, *Why does the Jeans Swindle work?*, MNRAS **431** (Apr., 2013) L6–L9, [arXiv:1210.3363].

[165] R. Narayan and M. Bartelmann, *Lectures on Gravitational Lensing*, *ArXiv Astrophysics e-prints* (June, 1996) [astro-ph/9606001].

[166] T. Faber and M. Visser, *Combining rotation curves and gravitational lensing: how to measure the equation of state of dark matter in the galactic halo*, MNRAS **372** (Oct., 2006) 136–142, [astro-ph/0512213].

[167] H. Hoekstra, M. Bartelmann, H. Dahle, H. Israel, M. Limousin, and M. Meneghetti, *Masses of Galaxy Clusters from Gravitational Lensing*, Space Sci. Rev. **177** (Aug., 2013) 75–118, [arXiv:1303.3274].

[168] T. Treu and P. J. Marshall, *Time delay cosmography*, A&A Rev. **24** (July, 2016) 11, [arXiv:1605.05333].

[169] P. Schneider, J. Ehlers, and E. E. Falco, *Gravitational Lenses*. 1992.

[170] M. Kilbinger, *Cosmology with cosmic shear observations: a review*, *Reports on Progress in Physics* **78** (July, 2015) 086901, [arXiv:1411.0115].

[171] A. Zitrin, T. Broadhurst, R. Barkana, Y. Rephaeli, and N. Benítez, *Strong-lensing analysis of a complete sample of 12 MACS clusters at z > 0.5: mass models and Einstein radii*, MNRAS **410** (Jan., 2011) 1939–1956, [arXiv:1002.0521].

[172] G. B. Caminha, C. Grillo, P. Rosati, M. Meneghetti, A. Mercurio, S. Ettori, I. Balestra, A. Biviano, K. Umetsu, E. Vanzella, and others, *Mass distribution in the core of MACS J1206. Robust modeling from an exceptionally large sample of central multiple images*, A&A **607** (Nov., 2017) A93, [arXiv:1707.00690].

[173] A. Monna, S. Seitz, I. Balestra, P. Rosati, C. Grillo, A. Halkola, S. H. Suyu, D. Coe, G. B. Caminha, B. Frye, A. Koekemoer, A. Mercurio, M. Nonino, M. Postman, and A. Zitrin, *Precise strong lensing mass profile of the CLASH galaxy cluster MACS 2129*, MNRAS **466** (Apr., 2017) 4094–4106, [arXiv:1605.08784].

[174] J. Richard, G. P. Smith, J.-P. Kneib, R. S. Ellis, A. J. R. Sanderson, L. Pei, T. A. Targett, D. J. Sand, A. M. Swinbank, H. Dannerbauer, and others, *LoCuSS: first results from strong-lensing analysis of 20 massive galaxy clusters at z = 0.2*, MNRAS **404** (May, 2010) 325–349, [arXiv:0911.3302].

[175] A. Leauthaud, R. Massey, J.-P. Kneib, J. Rhodes, D. E. Johnston, P. Capak, C. Heymans, R. S. Ellis, A. M. Koekemoer, O. Le Fèvre, and others, *Weak*

Gravitational Lensing with COSMOS: Galaxy Selection and Shape Measurements, ApJS **172** (Sept., 2007) 219–238, [astro-ph/0702359].

[176] N. Kaiser and G. Squires, *Mapping the dark matter with weak gravitational lensing*, ApJ **404** (Feb., 1993) 441–450.

[177] F. Schmidt, A. Leauthaud, R. Massey, J. Rhodes, M. R. George, A. M. Koekemoer, A. Finoguenov, and M. Tanaka, *A Detection of Weak-lensing Magnification Using Galaxy Sizes and Magnitudes*, ApJ **744** (Jan., 2012) L22, [arXiv:1111.3679].

[178] T. L. Johnson and K. Sharon, *The Systematics of Strong Lens Modeling Quantified: The Effects of Constraint Selection and Redshift Information on Magnification, Mass, and Multiple Image Predictability*, ApJ **832** (Nov., 2016) 82, [arXiv:1608.08713].

[179] R. A. Kimble, J. W. MacKenty, R. W. O'Connell, and J. A. Townsend, *Wide Field Camera 3: a powerful new imager for the Hubble Space Telescope*, in *Space Telescopes and Instrumentation 2008: Optical, Infrared, and Millimeter*, vol. 7010 of Proc. SPIE, p. 70101E, July, 2008.

[180] H. Ebeling, A. C. Edge, A. Mantz, E. Barrett, J. P. Henry, C. J. Ma, and L. van Speybroeck, *The X-ray brightest clusters of galaxies from the Massive Cluster Survey*, MNRAS **407** (Sept., 2010) 83–93, [arXiv:1004.4683].

[181] G. O. Abell, H. G. Corwin, Jr., and R. P. Olowin, *A catalog of rich clusters of galaxies*, ApJS **70** (May, 1989) 1–138.

[182] O. LeFevre, M. Saisse, D. Mancini, S. Brau-Nogue, O. Caputi, L. Castinel, S. D'Odorico, B. Garilli, M. Kissler-Patig, C. Lucuix, and others, *Commissioning and performances of the vlt-vimos*, 2003.

[183] M. Girardi, A. Mercurio, I. Balestra, M. Nonino, A. Biviano, C. Grillo, P. Rosati, M. Annunziatella, R. Demarco, A. Fritz, and others, *CLASH-VLT: Substructure in the galaxy cluster MACS J1206.2-0847 from kinematics of galaxy populations*, A&A **579** (July, 2015) A4, [arXiv:1503.05607].

[184] D. Lemze, M. Postman, S. Genel, H. C. Ford, I. Balestra, M. Donahue, D. Kelson, M. Nonino, A. Mercurio, A. Biviano, and others, *The Contribution of Halos with*

Different Mass Ratios to the Overall Growth of Cluster-sized Halos, ApJ **776** (Oct., 2013) 91, [arXiv:1308.1675].

[185] D. S. Hudson, R. Mittal, T. H. Reiprich, P. E. J. Nulsen, H. Andernach, and C. L. Sarazin, *What is a cool-core cluster? a detailed analysis of the cores of the X-ray flux-limited HIFLUGCS cluster sample*, A&A **513** (Apr., 2010) A37, [arXiv:0911.0409].

[186] A. Zitrin, A. Fabris, J. Merten, P. Melchior, M. Meneghetti, A. Koekemoer, D. Coe, M. Maturi, M. Bartelmann, M. Postman, and others, *Hubble Space Telescope Combined Strong and Weak Lensing Analysis of the CLASH Sample: Mass and Magnification Models and Systematic Uncertainties*, ApJ **801** (Mar., 2015) 44, [arXiv:1411.1414].

[187] A. Monna, S. Seitz, N. Greisel, T. Eichner, N. Drory, M. Postman, A. Zitrin, D. Coe, A. Halkola, S. H. Suyu, and others, *CLASH: $z \sim 6$ young galaxy candidate quintuply lensed by the frontier field cluster RXC J2248.7-4431*, MNRAS **438** (Feb., 2014) 1417–1434, [arXiv:1308.6280].

[188] T. L. Johnson, K. Sharon, M. B. Bayliss, M. D. Gladders, D. Coe, and H. Ebeling, *Lens Models and Magnification Maps of the Six Hubble Frontier Fields Clusters*, ApJ **797** (Dec., 2014) 48, [arXiv:1405.0222].

[189] J. Richard, M. Jauzac, M. Limousin, E. Jullo, B. Clément, H. Ebeling, J.-P. Kneib, H. Atek, P. Natarajan, E. Egami, R. Livermore, and R. Bower, *Mass and magnification maps for the Hubble Space Telescope Frontier Fields clusters: implications for high-redshift studies*, MNRAS **444** (Oct., 2014) 268–289, [arXiv:1405.3303].

[190] D. Gruen, F. Brimioulle, S. Seitz, C.-H. Lee, J. Young, J. Koppenhoefer, T. Eichner, A. Riffeser, V. Vikram, T. Weidinger, and A. Zenteno, *Weak lensing analysis of RXC J2248.7-4431*, MNRAS **432** (June, 2013) 1455–1467, [arXiv:1304.0764].

[191] J. Merten, M. Meneghetti, M. Postman, K. Umetsu, A. Zitrin, E. Medezinski, M. Nonino, A. Koekemoer, P. Melchior, D. Gruen, and others, *CLASH: The Concentration-Mass Relation of Galaxy Clusters*, ApJ **806** (June, 2015) 4, [arXiv:1404.1376].

[192] P. Melchior, E. Suchyta, E. Huff, M. Hirsch, T. Kacprzak, E. Rykoff, D. Gruen, R. Armstrong, D. Bacon, K. Bechtol, and others, *Mass and galaxy distributions of four massive galaxy clusters from Dark Energy Survey Science Verification data*, MNRAS **449** (May, 2015) 2219–2238, [arXiv:1405.4285].

[193] P. L. Gómez, L. E. Valkonen, A. K. Romer, E. Lloyd-Davies, T. Verdugo, C. M. Cantalupo, M. D. Daub, J. H. Goldstein, C. L. Kuo, A. E. Lange, and others, *Optical and X-Ray Observations of the Merging Cluster AS1063*, AJ **144** (Sept., 2012) 79.

[194] K. W. Cavagnolo, M. Donahue, G. M. Voit, and M. Sun, *Intracluster Medium Entropy Profiles for a Chandra Archival Sample of Galaxy Clusters*, ApJS **182** (May, 2009) 12–32, [arXiv:0902.1802].

[195] V. Presotto, M. Girardi, M. Nonino, A. Mercurio, C. Grillo, P. Rosati, A. Biviano, M. Annunziatella, I. Balestra, W. Cui, and others, *Intracluster light properties in the CLASH-VLT cluster MACS J1206.2-0847*, A&A **565** (May, 2014) A126, [arXiv:1403.4979].

[196] L. Hernquist, *An analytical model for spherical galaxies and bulges*, ApJ **356** (June, 1990) 359–364.

[197] A. Burkert, *The Structure of Dark Matter Halos in Dwarf Galaxies*, ApJ **447** (July, 1995) L25, [astro-ph/9504041].

[198] B. Binggeli, *The shape and orientation of clusters of galaxies*, A&A **107** (Mar., 1982) 338–349.

[199] P. A. M. de Theije, P. Katgert, and E. van Kampen, *The shapes of galaxy clusters*, MNRAS **273** (Mar., 1995) 30–46, [astro-ph/9409011].

[200] K. Umetsu, A. Zitrin, D. Gruen, J. Merten, M. Donahue, and M. Postman, *CLASH: Joint Analysis of Strong-Lensing, Weak-Lensing Shear and Magnification Data for 20 Galaxy Clusters*, *ArXiv e-prints* (July, 2015) [arXiv:1507.04385].

[201] L. Xu, *Constraints on $f(r)$ gravity through the redshift space distortion*, *Phys. Rev. D* **91** (Mar, 2015) 063008.

[202] G.-B. Zhao, T. Giannantonio, L. Pogosian, A. Silvestri, D. J. Bacon, K. Koyama, R. C. Nichol, and Y.-S. Song, *Probing modifications of general relativity using current*

cosmological observations, Phys. Rev. D **81** (May, 2010) 103510, [arXiv:1003.0001].

[203] S. F. Daniel, E. V. Linder, T. L. Smith, R. R. Caldwell, A. Cooray, A. Leauthaud, and L. Lombriser, *Testing general relativity with current cosmological data*, Phys. Rev. D **81** (June, 2010) 123508, [arXiv:1002.1962].

[204] M. Bartelmann, *Arcs from a universal dark-matter halo profile.*, A&A **313** (Sept., 1996) 697–702, [astro-ph/9602053].

[205] T. C. Beers, K. Flynn, and K. Gebhardt, *Measures of location and scale for velocities in clusters of galaxies - A robust approach*, AJ **100** (July, 1990) 32–46.

[206] L. Lombriser, K. Koyama, G.-B. Zhao, and B. Li, *Chameleon f(R) gravity in the virialized cluster*, Phys. Rev. D **85** (June, 2012) 124054, [arXiv:1203.5125].

[207] H. Kim, *Brans-Dicke theory as a unified model for dark matter-dark energy*, MNRAS **364** (Dec., 2005) 813–822, [astro-ph/0408577].

[208] A. Bonafede, K. Dolag, F. Stasyszyn, G. Murante, and S. Borgani, *A non-ideal magnetohydrodynamic GADGET: simulating massive galaxy clusters*, MNRAS **418** (Dec., 2011) 2234–2250, [arXiv:1107.0968].

[209] S. Planelles, S. Borgani, K. Dolag, S. Ettori, D. Fabjan, G. Murante, and L. Tornatore, *Baryon census in hydrodynamical simulations of galaxy clusters*, MNRAS **431** (May, 2013) 1487–1502, [arXiv:1209.5058].

[210] G. Tormen, F. R. Bouchet, and S. D. M. White, *The structure and dynamical evolution of dark matter haloes*, MNRAS **286** (Apr., 1997) 865–884, [astro-ph/9603132].

[211] A. Yahil and N. V. Vidal, *The Velocity Distribution of Galaxies in Clusters*, ApJ **214** (June, 1977) 347–350.

[212] A. L. B. Ribeiro, R. R. de Carvalho, M. Trevisan, H. V. Capelato, F. La Barbera, P. A. A. Lopes, and A. C. Schilling, *SPIDER - IX. Classifying galaxy groups according to their velocity distribution*, MNRAS **434** (Sept., 2013) 784–795, [arXiv:1306.4722].

[213] N. E. Chisari, N. Koukoufilippas, A. Jindal, S. Peirani, R. S. Beckmann, S. Codis, J. Devriendt, L. Miller, Y. Dubois, C. Laigle, A. Slyz, and C. Pichon, *Galaxy-halo alignments in the Horizon-AGN cosmological hydrodynamical simulation*, MNRAS **472** (Nov., 2017) 1163–1181, [arXiv:1702.03913].

[214] M. Schaller, C. S. Frenk, R. G. Bower, T. Theuns, J. Trayford, R. A. Crain, M. Furlong, J. Schaye, C. Dalla Vecchia, and I. G. McCarthy, *The effect of baryons on the inner density profiles of rich clusters*, MNRAS **452** (Sept., 2015) 343–355, [arXiv:1409.8297].

[215] M. Killedar, S. Borgani, M. Meneghetti, K. Dolag, D. Fabjan, and L. Tornatore, *How baryonic processes affect strong lensing properties of simulated galaxy clusters*, MNRAS **427** (Nov., 2012) 533–549, [arXiv:1208.5770].

[216] M. Meneghetti, P. Natarajan, D. Coe, E. Contini, G. De Lucia, C. Giocoli, A. Acebron, S. Borgani, M. Bradac, J. M. Diego, and others, *The Frontier Fields lens modelling comparison project*, MNRAS **472** (Dec., 2017) 3177–3216, [arXiv:1606.04548].

[217] T. Watanabe and M. J. Hayashi, *General Relativity with Torsion*, *ArXiv General Relativity and Quantum Cosmology e-prints* (Sept., 2004) [gr-qc/0409029].

[218] A. D. I. Latorre, G. J. Olmo, and M. Ronco, *Observable traces of non-metricity: new constraints on metric-affine gravity*, *ArXiv e-prints* (Sept., 2017) [arXiv:1709.04249].

[219] C. W. Misner, K. S. Thorne, and J. A. Wheeler, *Gravitation*. 2017.

Appendix A

Basic notions of differential geometry

In this appendix I review some useful concepts of differential geometry which have been used within this Thesis and the basis of the theory of General Relativity. In the following I will adopt natural units $c = 1$ and the Einstein convention for summed indexes:

$$V_\mu W^\mu = \sum_{\mu=0}^{3} V_\mu W^\mu.$$

In GR, the spacetime is identified by a four-dimensional differentiable manifold (M, g) on which a metric g is defined (see below). Considering a point $x \in M$ and a function $V^\mu(x)$ defined in an open neighborhood U, if a coordinate transformation to another neighborhood U' is such that $U \cap U' \neq \oslash$ it follows that:

$$V'^\mu(x') = V^\nu(x)\frac{\partial x'^\mu}{\partial x^\nu}.$$

V^μ is called *contravariant vector*. A quantity $W_\mu(x)$ which change under coordinate transformation as:

$$W'_\mu(x') = W_\nu \frac{\partial x^\nu}{\partial x'^\mu},$$

is called *covariant vector*.

A *Tensor of rank* $\binom{n}{m}$ is defined as an object with n contravariant indexes and m covariant

indexes, which transform as:

$$T'_{\nu_1.....\nu_m}{}^{\mu_1....\mu_n} = T_{\rho_1.....\rho_m}{}^{\sigma_1....\sigma_n} \frac{\partial x^{\rho_1}}{\partial x'^{\nu_1}} ..... \frac{\partial x^{\rho_m}}{\partial x'^{\nu_m}} \frac{\partial x'^{\mu_1}}{\partial x^{\sigma_1}} ..... \frac{\partial x'^{\mu_n}}{\partial x^{\sigma_n}}. \tag{A.1}$$

A.1 Covariant derivative and Parallel transport

Let us consider a curve $\gamma(\lambda)$ defined on M between the points P e Q, where $\lambda \in [p, q] \subset \mathbb{R}$ is a parameter describing the curve such that $\gamma(p) = P$ and $\gamma(q) = Q$.
Given a point $x(\lambda) \in \gamma$, which is locally identified by the coordinates $x^\mu(\lambda)$, I define the *tangent vector* to γ on x the quantity

$$t(x) \equiv t^\mu \partial_\mu(x) = \frac{d}{d\lambda} x.$$

Supposing to have another vector field $V = V^\mu \partial_\mu$, the *covariant derivative* of V along $\gamma(\lambda)$ is defined as:

$$t^\nu \nabla_\nu V^\mu = t^\nu \partial_\nu V^\mu + t^\nu \Gamma^\mu{}_{\nu\rho} V^\rho, \tag{A.2}$$

which can be rewritten as:

$$\frac{dx^\nu}{d\lambda} \frac{\partial}{\partial x^\nu} V^\mu + \Gamma^\mu{}_{\nu\rho} \frac{dx^\nu}{d\lambda} V^\rho = \frac{D}{d\lambda} V^\mu, \tag{A.3}$$

where $\Gamma^\mu{}_{\nu\rho}$ are called Christoffel Symbols or *Affine Connection* and they are related to the geometrical structure of the manifold.
A vector field V is said to be *Parallel Transported* along a curve $\gamma(\lambda)$ if, given $\frac{d}{d\lambda}$ the tangent vector field of γ, the following relation is satisfied:

$$\frac{D}{d\lambda} V^\mu = f(x) V^\mu, \tag{A.4}$$

meaning that the covariant derivative of V along the curve is proportional to the vector field itself up to an arbitrary function $f(x)$.

A.2 The equivalence principle

The theory of GR is built upon the so-called *equivlance principle*, which can be expressed in three different forms:

The **weak equivalence principle** (WEP) states that the inertial mass and the gravitational mass are equivalent, $m_i = m_g$. Thuis means that the local effects induced by the presence of a gravitational field are indistinguishable from those of an accelerated observer in flat spacetime.

The **Einstein equivalence principle** (EEP) assumes the validity of WEP and that any local non-gravitational experiment made by an observer in a freely falling system is independent of the velocity of the system and its location in spacetime.

The **strong equivalence principle** (SEP) extends the EEP to any local experiment (including the effect of gravitation); it can be rephrased as the fact that in the presence of a gravitational field is always possible to find a locally inertial coordinate system.
As an example, consider an observer freely-falling in a constant gravitational field g. Assuming that the WEP holds, in the laboratory coordinate system, the equation of motion reads:

$$m\frac{d^2x}{dt^2} = mg,$$

The description in the observer reference frame can be obtained by a coordinate transformation $x(t) \to x'(t) = x(t) - \frac{1}{2}gt^2$. In this case the equation of motion becomes:

$$\frac{d^2x'}{dt^2} = 0. \tag{A.5}$$

Thus, a freely-falling observer does not perceive external forces, and the physics is that of a (locally) inertial frame. Gravity assumes a pure geometric connotation; the effects of a gravitational field are encoded in the coordinate transformations between two different coordinate systems.

A.2.1 The geodesics equation

The motion of a particle in a locally inertial frame, identified by the set of coordinates $\xi^\alpha = (\xi^0, \xi^1, \xi^2, \xi^3)$, is described by eq. (A.5), which can be rewritten in four dimensions as:

$$\frac{d^2\xi^\alpha}{d\tau^2} = 0, \tag{A.6}$$

where $d\tau^2 \equiv ds^2 = \eta_{\alpha\beta} d\xi^\alpha d\xi^\beta$ is the *proper time* for an observer at rest in the particle frame; $\eta_{\alpha\beta} = diag[1, -1, -1, -1]$ is a rank 2 tensor whose meaning will be clarified below. From the point of view of a second observer in the coordinate system x^μ, eq. (A.6) reads:

$$\frac{d}{d\tau}\left(\frac{\partial\xi^\alpha}{\partial x^\mu}\frac{dx^\mu}{d\tau}\right) = 0;$$

$$\frac{\partial\xi^\alpha}{\partial x^\mu}\frac{d^2x^\mu}{d\tau^2} + \frac{\partial^2\xi^\alpha}{\partial x^\mu \partial x^\nu}\frac{dx^\mu}{d\tau}\frac{dx^\nu}{d\tau} = 0. \tag{A.7}$$

Multiplying both sides of eq. (A.7) by $\frac{\partial x^\beta}{\partial \xi^\alpha}$ and using the fact that $\frac{\partial\xi^\alpha}{\partial x^\mu}\frac{\partial x^\beta}{\partial \xi^\alpha} = \delta_\mu{}^\beta$, we obtain:

$$\frac{d^2x^\beta}{d\tau^2} + \Gamma^\beta{}_{\mu\nu}\frac{dx^\mu}{d\tau}\frac{dx^\nu}{d\tau} = 0, \tag{A.8}$$

where I have identified the affine connection defined in eq. (A.2) with:

$$\Gamma^\beta{}_{\mu\nu} = \frac{\partial x^\beta}{\partial\xi^\alpha}\frac{\partial^2\xi^\alpha}{\partial x^\mu \partial x^\nu}.$$

Eq. (A.8) is called *geodesics equation* and can be related to the concept of parallel transport; considering that $t^\beta = \frac{dx^\beta}{d\tau}$ is the tangent vector of the curve parametrized by τ:

$$\frac{d}{d\tau}t^\beta + \Gamma^\beta_{\mu\nu}\frac{dx^\mu}{d\tau}t^\nu = 0, \tag{A.9}$$

which corresponds to eq. (A.4) for the tangent vector t^β with $f(x) = 0$. Thus, a geodesic is a curve for which the tangent vector is parallel transported along the curve itself. The parameter τ for which $f(x) = 0$ is called *affine parameter*.

Geodesics can be classified in three categories, according to the properties of the tangent vector:

1. *Timelike geodesics* ($t^\mu t_\mu > 0$) describe trajectories of massive bodies in a gravitational field.

2. *Null geodesics* ($t^\mu t_\mu = 0$) represent the trajectory of a particle with null rest mass in a gravitational field.

3. *Spacelike geodesics* ($t^\mu t_\mu < 0$) describe a series of events which are simultaneous as seen by an appropriate observer.

A.3 The metric tensor

Consider now the interval ds^2, which in the locally inertial frame coincides with the proper time $d\tau^2 = \eta_{\mu\nu} d\xi^\mu d\xi^\nu$; since it is a scalar, it should be invariant under generic coordinate transformations. In an arbitrary coordinate system $\{x^\mu\}$:

$$ds'^2 \equiv ds^2 = \frac{\partial \xi^\alpha}{\partial x^\mu} \frac{\partial \xi^\beta}{\partial x^\nu} \eta_{\alpha\beta} dx^\mu dx^\nu = g_{\mu\nu} dx^\mu dx^\nu, \tag{A.10}$$

where the *metric tensor*, defined as:

$$g_{\mu\nu} = \frac{\partial \xi^\alpha}{\partial x^\mu} \frac{\partial \xi^\beta}{\partial x^\nu} \eta_{\alpha\beta},$$

is a rank $\binom{0}{2}$ symmetric tensor which in 4 dimensions is represented by a 4×4 locally non-singular matrix. Eq. (A.10) expressed the infinitesimal distances between two events in a generic 4-dimensional manifold. In Minkowski spacetime $g \equiv \eta = diag[1, -1, -1, -1]$ is constant, but in general the components of the metric are functions of the points in the manifold $g_{\mu\nu} = g_{\mu\nu}(x)$.

The fact that the metric has a non-vanishing determinant for any local coordinate system provides some important consequences. First of all, the number of positive, negative and null eigenvalues (the *signature*) is the same in all the manifold. Moreover, is possible to define an inverse metric $g^{\nu\alpha}$ such that $g_{\mu\nu} g^{\nu\alpha} = \delta_\mu{}^\alpha$; finally a non-singular metric allows the construction of a non-degenerate scalar product between two vectors $S \equiv V \cdot W = g_{\mu\nu} V^\mu W^\nu$. The contraction of the metric tensor with a vector produces a rank $\binom{0}{1}$ tensor (i.e. a covector); analogously, the contraction of the inverse metric with a covector is a vector.

From the infinitesimal interval of eq. (A.10), the 4-dimensional path between two points A, B in M can be written as:

$$s = \int_A^B ds = \int_A^B \sqrt{g_{\mu\nu} dx^\mu dx^\nu} = \int_{\chi_A}^{\chi_B} \sqrt{g_{\mu\nu} \frac{dx^\mu}{d\chi} \frac{dx^\nu}{d\chi}} d\chi, \tag{A.11}$$

where $\chi \in [\chi_A, \chi_B]$ parametrizes the curve s. Imposing $\delta s = 0$ for small variation of the coordinates δx^μ, it follows that

$$g_{\mu\nu} \frac{d^2 x^\nu}{d\tau^2} + g_{\mu\nu} g^{\nu\alpha} \left[\partial_\gamma g_{\alpha\beta} - \frac{1}{2} \partial_\alpha g_{\beta\gamma} \right] \frac{dx^\beta}{d\tau} \frac{dx^\gamma}{d\tau} = 0, \tag{A.12}$$

which coincides with eq. (A.8) if connection is given by:

$$\Gamma^\mu{}_{\gamma\beta} = \Gamma^\mu{}_{\beta\gamma} = \frac{1}{2} g^{\mu\alpha} \left[\partial_\gamma g_{\alpha\beta} + \partial_\beta g_{\gamma\alpha} - \partial_\alpha g_{\beta\gamma} \right]. \tag{A.13}$$

Eq. (A.13) defines an unique relation between the metric tensor and the Christoffel symbols; in this case, the metric is the only independent variable. This particular connection is known as *Levi-Civita connection* and often indicated by $\left\{ {\mu \atop \gamma\beta} \right\}$.
Formally, the above equation can be derived imposing that the Chirstoffel Symbols are symmetric with respect to the exchange of the lower indexes and assuming $\nabla^\mu g_{\mu\nu} = 0$. This means that the *torsion tensor* $\mathcal{T}^\mu_{\gamma\beta} = \Gamma^\mu{}_{\gamma\beta} - \Gamma^\mu{}_{\beta\gamma}$ and the *non-metricity tensor* $\mathcal{C}_{\mu\nu\alpha} = \nabla_\mu g_{\nu\alpha}$ are identically equal to zero. Some extensions of GR relax these assumptions by introducing both torsion and non-metricity components (see e.g. refs. [217, 218] and references therein), such that the connection can be generally decomposed as:

$$\Gamma_{\mu\beta\gamma} = \{_{\mu\gamma\beta}\} + \frac{1}{2} \mathcal{C}_{\mu\beta\gamma} + \frac{1}{2} \left(\mathcal{T}_{\mu\beta\gamma} + \mathcal{T}_{\beta\mu\gamma} + \mathcal{T}_{\beta\gamma\mu} + \mathcal{C}_{\gamma\beta\mu} - \mathcal{C}_{\beta\gamma\mu} \right).$$

A.4 The weak field limit

Consider a particle with coordinates $\{x^\mu\}$ freely-falling in a gravitational field described by the metric:

$$g_{\mu\nu} = \eta_{\mu\nu} + h_{\mu\nu},$$

where η is the Minkowski metric and h is a small perturbation $|h_{\mu\nu}| \ll 1$. If the speed of the particle is much smaller than the speed of light $v \ll c$, the spatial components of $\frac{dx^\mu}{d\tau}$ are

negligible with respect to the time component $\frac{dx^0}{d\tau} = \frac{dt}{d\tau}$. In this way, the geodesic equation, eq. (A.8), can be rewritten as:

$$\frac{d^2x^\mu}{d\tau^2} + \Gamma^\mu{}_{00}\left(\frac{dt}{d\tau}\right)^2 =$$

$$\frac{d^2\vec{x}}{d\tau^2} - \frac{1}{2}\left(\frac{dt}{d\tau}\right)^2 \eta^{ij}\partial_j h_{00}; \tag{A.14}$$

$$\frac{d^2t}{d\tau^2} = 0, \tag{A.15}$$

where we used the fact that $\Gamma^\mu{}_{\alpha\beta}$ is given by eq. (A.13), and that the metric is independent of time. The solution of the last equation is given by $\frac{dt}{d\tau} = cost$; dividing eq. (A.14) by $\left(\frac{dt}{d\tau}\right)^2$, we obtain:

$$\frac{d^2\boldsymbol{x}}{d\tau^2} = \frac{1}{2}\nabla h_{00}. \tag{A.16}$$

Thus, in the limit of non-relativistic particles and weak gravitational field, the geodesic equation reduce to the Newtonian equation of motion where the acceleration is sourced by the potential $\phi = -2h_{00} + cost$. Note that for a linearly perturbed FLRW metric h_{00} is given by the Bardeen potential Φ.

Appendix B

Fermat Theorem in GR and effective refractive index

I present the derivation for the effective refractive index in a generic stationary curved space-time by applying the method of ref [166]. This result is applied in Chapter 4 to the case of the linearly perturbed FLRW metric. Consider a static gravitational field for which the metric could be written as:

$$\partial_t g_{\mu\nu} = 0; \qquad g_{0i} = g_{i0} = 0. \tag{B.1}$$

The light ray propagation in this metric is described by null curves

$$ds^2 = 0 = g_{\mu\nu} dx^\mu dx^\nu,$$

from which one has

$$dt^2 = -\frac{g_{ij}}{g_{00}} dx^i dx^j. \tag{B.2}$$

I define the *Fermat metric* in a 3-dimensional Riemanian manifold as $\hat{g}_{ij} = -\frac{g_{ij}}{g_{00}}$. As shown in ref. [166], the null geodesic equation:

$$g_{\mu\nu} \frac{d^2 x^\nu}{d\chi^2} + \Gamma_{\mu\nu\rho} \frac{dx^\nu}{d\chi} \frac{dx^\rho}{d\chi} = 0, \tag{B.3}$$

with affine parameter χ, is equivalent to a geodesic equation in the 3-dimensional Riemanian space in which $\hat{g}_{ij}$ is defined with affine parameter t[1]. After some passages I obtain:

$$g_{jk}\frac{d^2x^k}{dt^2} + \left[\partial_m \hat{g}_{jl} - \frac{1}{2}\partial_j \hat{g}_{lm}\right]\frac{dx^l}{dt}\frac{dx^m}{dt} = 0, \tag{B.4}$$

where the term inside the square parentheses is the Christoffel symbol for the Fermat metric $\hat{\Gamma}_{jml}$. By means of the definition of geodesics, the affine parameter t satisfies

$$\delta\tau = \delta\int_C dt = 0 = \delta\int_C \sqrt{\hat{g}_{ij}dx^i dx^j}; \tag{B.5}$$

τ represents the length of the path C in the Riemanian manifold, or equivalently the time coordinate $x^0 = \tau$ as measured by an observer in the 4-dimensional spacetime. Eq. (B.5) is exactly the formulation of the Fermat principle in General Relativity:

Theorem. *Let S be an source event and l the worldline of an observer in a spacetime $(M, g_{\mu\nu})$. Then a curve γ from S to l describes a light ray if and only if the arrival time τ on l is stationary for first order variations $\delta\gamma$.*

For a detailed proof, the interested reader could refer to ref. [219] pages 100-103.
It is possible to obtain a more general result for the case of a conformal stationary spacetime described by a metric:

$$ds^2 = e^{2f(t,x^i)}\left[-(dt + \hat{\phi}_i dx^i)^2 + \hat{g}_{ij}dx^i dx^j\right], \tag{B.6}$$

where $\hat{\phi}_i(x^\mu)$ is called Fermat 1-form. The Fermat principle can be rephrased as:

$$\delta\int\left[\sqrt{\hat{g}_{ij}dx^i dx^j} - \hat{\phi}_i dx^i\right] = 0. \tag{B.7}$$

Eq. (B.7) reduces to eq. (B.5) for a static spacetime where $\hat{\phi}_i = \partial_i h$, with h a scalar function of the space coordinates $\vec{x}$.
Let's now focus on a light ray propagating over a background spacetime (e.g. Minkowski spacetime) which is perturbed by the presence of a gravitational field described by the metric $g_{\mu\nu}$; considering that the speed of light across a medium can be defined as $v_n = \frac{c}{n}$, where

[1]Note that t is not an affine parameter in the 4-dimensional spacetime with metric $g_{\mu\nu}$

n indicates the refraction index of the medium, I express the Fermat principle in terms of the optical distance instead of time:

$$\delta \int cdt = \delta \int n(x,y,z)v_n dt = \delta \int n(x,y,z)dl = 0, \tag{B.8}$$

where I used the fact that $v_n = dl/dt$, with $dl = \sqrt{\delta_{ij}dx^i dx^j}$ the 3-dimensional distance element the background metric (Euclidean in this case). If the unperturbed light ray passes through a region in which there is a stationary gravitational field described by $g_{\mu\nu}$, with a corresponding Fermat metric $\hat{g}_{ij}$ conformally equivalent to the 3-dimensional background metric:

$$\hat{g}_{ij} = \Omega^2(x,y,z)\delta_{ij},$$

then eq. (B.5) can be written as

$$\delta \int \sqrt{\hat{g}_{ij}dx^i dx^j} = \delta \int \Omega(x,y,z)\sqrt{\delta_{ij}dx^i dx^j} = \delta \int \Omega(x,y,z)ds = 0. \tag{B.9}$$

The above equation coincides with eq. (B.8) if I set $\Omega = n$.
Thus, in a stationary spacetime with metric $g_{\mu\nu}$, one can recast the effect of gravity defining an *effective refractive index* as the coefficient of the conformal transformation connecting the spatial part of the background unperturbed metric to the Fermat metric. If $\hat{g}_{ij}$ is not conformally equivalent to the background metric, the effective refractive index will be a tensor:

$$n_{ij} = \sqrt{\hat{g}_{ij}}.$$